THE USE OF NUMERICAL METHODS TO INTERPRET POLYMER DECOMPOSITION DATA

by

Artur Witkowski

A thesis submitted in partial fulfilment for the requirements of the degree of
Doctor of Philosophy
at the
University of Central Lancashire

May 2012

Abstract

Polymer decomposition is the key to understanding fire behaviour. It is a complex process involving heat transfer, breakdown of the polymer chain, volatile fuel formation and gasification occurring as a moving interface through the polymer bulk. Two techniques, chemical analysis using STA-FTIR, and pyrolysis modelling have been combined as a tool to better understand these processes.

This work covers the experimental investigation of polymer decomposition using the STA-FTIR technique. Several polymers including polyacrylonitrile (PAN), polypropylene (PP) and ethylene-vinyl acetate (EVA) alone, and as potential fire retardant composites have been studied in different conditions to optimise the methodology and analysis of results. Polyacrylonitrile was used to optimise the experimental technique. Polypropylene, containing nanoclay and ammonium phosphate, was decomposed and the composition of the decomposition products analysed in order to investigate the fire retardant effects of the additives on the thermal decomposition. Ethylene-vinyl acetate copolymer containing nanoclay and/or either aluminium hydroxide or magnesium hydroxide was decomposed, with vapour phase FTIR analysis showing a change in the initial decomposition pathway with a shift from acetic acid evolution, to acetone production.

In parallel, this experimental data has been used to perform early attempts towards validation of numerical models developed by the use of a 1-dimensional pyrolysis computational tool called ThermaKin. As ThermaKin is relatively new and still not widely used for fire modelling, a detailed description of its capabilities has been provided. A detailed study of heat transfer of cardboard, leading to thermal decomposition, accompanied by pyrolysis and char formation has been described. Several microscale kinetics models have been proposed with different levels of complexity. Not only do the numerical approximations reflect the experimental results of single compounds, describing the material's behaviour (expressed in terms of mass loss) when exposed to external heat, but also predictive models of fire retardant mixtures have been developed for different atmospheres and heating rates.

In addition, the powerful combination of pyrolysis modelling and chemical analysis by STA-FTIR has provided new insights into the decomposition and burning behaviour of both PP protected with nanoclay and ammonium phosphate, but also the industrially important cable sheathing materials based on EVA. The novelty of this work stems from the first use of the

pyrolysis models to study fire retardant behaviour; the first reported combination of STA-FTIR with ThermaKin pyrolysis model, and a deep understanding of the pre-ignition behaviour of cardboard.

Table of Contents

Index of Figures

Index of Tables

Acknowledgments

I would like to thank the following for the assistance given, without which this would not have been possible:

Professor T. Richard Hull at the University Of Central Lancashire's Centre of Fire and Hazard's Science for his inspiration, dedication and guidance throughout this project.

Dr Stanislav Stoliarov at the University of Maryland's Department of Fire Protection Engineering, my numerical modelling advisor for the opportunity to visit and be part of his group of researchers and to experience the hidden gem on the east coast: Maryland and D.C.

The Centre of Fire and Hazard Science for granting the PhD Studentship.

All the research team of the Centre of Fire and Hazard Science past and present, namely Parina, Jen and Cameron for having good time between studies, and David and Luke for interesting discussions. Eternal gratitude is expressed to John Milnes and Steve Harris for taking on maintenance challenges in the Material's Laboratory.

All the members of the Department of Fire Protection Engineering at University of Maryland especially Mark McKinnon for his collaboration during research on cardboard.

Finally, my family and friends, whose combined support has been invaluable, I would like to thank my mother and father for instilling ambition and motivation, my sister for the years of constant support in my early education, and my wife Ania who convinced me to come back to academic life, broaden my horizons and change my life.

1 INTRODUCTION

The overall aim of this research project is to develop tools to unravel the complex behaviour of decomposing polymers tested in the fire laboratory, and hence identify the processes occurring during burning. This has been done by a combination of experimental work, numerical analysis and by the use of versatile, one dimensional, mathematical modelling tool called ThermaKin. In the experimental work a Thermogravimetric Analysis (TGA) apparatus, was used to generate mass loss data as a function of temperature at fixed heating rates, and combined with a Fourier Transform Infrared Spectrometer (FTIR) was used to generate decomposition products by exposing a specimen of the material to heating under well-defined thermal and environmental conditions. TGA mass loss curves were used to propose steps (chemical reactions) in the models together with kinetic parameters and stoichiometry, the FTIR technique was used to identify gas phase products from those reactions. Using a gas phase infrared cell, an FTIR instrument can identify and quantify volatile products dynamically, thus creating absorption/concentration versus time profiles for each species. The use of Fourier Transform Infrared (FTIR) spectroscopy can quantify multiple gases quickly with high accuracy in real time. However, while analysis based on FTIR spectroscopy is conceptually straightforward, the practical implementation has several potential problems. For example, using a high spectral resolution setting increases noise making accurate low-level determinations difficult, while using lower resolution makes identification difficult. Additionally, vapours must be transferred from the TGA test apparatus to the spectrometer at a known temperature and rate to obtain accurate concentration versus time data.

The experimental part of the program starts with STA-FTIR method optimization and validation. This study aimed to optimize the accuracy of decomposition gas analysis from different products by identifying and improving STA-FTIR operating parameters, establishing reliable sampling and recording methods, and using numerical techniques for data analysis using OMNIC software. The first step in achieving this was to find and verify different parameter settings; in TGA, such as heating rate and sample weight; in gas phase Fourier Transform Infrared Spectroscopy (FTIR) establishing optimum relationship between spectrometer operating parameters such as resolution, scanning time, and data acquisition for

different tests. After considering each parameter in isolation the optimised parameters were then combined in order to maximize the range of species detected.

FTIR analysis of polymer decomposition products presents numerous problems, not only in sampling of the gases, but also in the identification and quantitative measurements. The major problem is the range and number of different chemical species that are present. For these reasons FTIR, which yields large and complex data sets, was investigated for possible identification and quantification of a larger range of chemical species present in decomposition products. Series of samples containing for example polymer with, and without flame retardant and nanofiller were investigated and qualitative analysis carried out in order to get familiarised with the existing OMNIC software. With robust data on polymer decomposition rates and chemistry, it was decided to investigate the factors controlling polymer decomposition. This required testing and development of ThermaKin's abilities to build sophisticated mathematical models based around experimental data obtained in the fire laboratory using the optimised sampling methodology. The need for multiple tests arises from the complexity of fire phenomena and their sensitivity to environmental conditions. However ThermaKin is a computational tool that predicts the behaviour of materials exposed to fire. It can help to reduce the number and complexity of these tests in order to obtain comprehensive characterization of the materials of interest. The bases of ThermaKin are mathematical algorithms that describe transient thermal energy transport, chemical reactions, and the transport of gases through the condensed phase. The model also is able to capture important aspects of a material's fire behaviour, such as charring and intumescence.

The objective of the first part of this work is to develop methods for reliable quantification of FTIR data from thermogravimetric analysis. At present there are two problems.

- Firstly thermogravimetric analysis (TGA) or simultaneous thermal analysis (STA), which combines TGA with exo/endothermicity data provides an excellent microscale model of the thermal decomposition of polymers, and is an essential input to models of polymer burning behaviour. Complemented by gas phase FTIR of the products (where the complex vibration-rotation spectra are precisely defined by their quantum mechanical

origins), mixtures of a small number of volatiles can take several days to deconvolute manually into profiles of the individual products. This problem is exacerbated by the need to identify key species from fire retardants, which may be present at low concentrations. A survey of available software systems has highlighted the deficiency in this area.

- Secondly, the kinetics of condensed phase decomposition is complex and requires sophisticated mathematical analysis to resolve into individual processes. Rein et al. at the University of Edinburgh[1] have demonstrated the potential of this techniques using convergent genetic algorithms to produce interesting results. However in this work the modelling was done by the use of ThermaKin which is relatively new, powerful computational tool. ThermaKin is a versatile numerical model of pyrolysis and combustion of polymeric materials formulated by R.E Lyon and S. I Stoliarov[2].

2 TECHNIQUES FOR STUDYING THERMAL DECOMPOSITION AND FLAMMABILITY OF POLYMERS

Thermal degradation of polymers involves physical and chemical property changes as a result of overheating. It often involves changes to the molecular weight of the polymer by the separation of the long chain into shorter fragments by the different mechanisms (see Chapter 3).

Thermal decomposition is extensive and irreversible chemical reaction caused by heat. As heat is required to break chemical bonds in the compound the reaction is usually endothermic. However, reaction with oxygen is normally exothermic providing heat from further decomposition.

Pyrolysis can be viewed as a special type of thermal decomposition, in this study, mainly focused on the formation of volatile products during heating. The process is applied to chemical transformations induced by thermal energy when a compound is heated at a temperature significantly higher than ambient and when the decomposition of the initial compound forms smaller molecules[3]. Pyrolysis and analysis of pyrolysates may be included in the group of thermal analysis techniques; however, overlap exists between analytical pyrolysis for identification, quantification or quality control, and other thermoanalytical techniques[3].

In both analytical and applied applications, knowledge about the chemical processes taking place during pyrolysis is essential[4]. Many techniques have been used to study the thermal degradation of polymers, some having general applicability, like polymer characterisation, and others being used to correlate degradation to parameters sensitive to the decomposition processes[5]. In most cases parameters used for monitoring degradation are based on changes in molecular weight[6]. However, other parameters, such as changes in crystallinity, formation of functional groups in degrading products or changes in the concentration of terminal groups have also been used[7]. To monitor these parameters as a function of reaction time, the methods reported in the literature include thermogravimetric analysis, thermal volatilization analysis, pyrolysis mass spectroscopy, analysis by infrared spectroscopy[8], summarised in Table 1.

Table 1 Thermoanalytical techniques

Type of technique	**Analytical Technique**	**Measured Parameters**
Thermal analysis	TGA (Thermagravimetric Analysis)	Mass loss as a function of temperature during controlled heating
	DTA (Differential Thermal Analysis)	Heat flow to the sample and reference are identical, so any thermal processes cause a difference in temperature between the sample and reference
	STA (Simultaneous Thermal Analysis)	Combined TGA with DTA (or DSC)
	DSC (Differential Scanning Calorimetry)	Heat flow as a function of temperature; observing the difference in heat flow between the sample and reference (measuring the amount of heat absorbed or released to maintain sample and reference at the same temperature)
Techniques for Evolved Gas Analysis (EGA)	TGA - FTIR (Fourier Transform Infrared)	Measuring how much radiation a sample absorbs at each different wavelength
	pyGCMS (Pyrolysis gas chromatography mass spectrometry)	Volatilisation with direct identification by GCMS of the volatile products

2.1 Thermal Analysis

Thermal properties, including glass transition temperature, crystalline melting point, thermal stability, thermal decomposition, etc., are measured using dedicated instrumentation. Thermal analysis includes thermogravimetric analysis (TGA), differential thermal analysis (DTA), differential scanning calorimetry (DSC), and evolved gas analysis (EGA)[9].

In thermogravimetric analysis (TGA) the weight is continuously measured as a polymer sample is heated at a fixed rate in air or in an inert atmosphere. The weight loss occurs initially due to the evaporation of residual volatile compounds in the polymer (water, solvents) and then due to the polymer decomposition and elimination of volatile fragments. This technique allows the determination of the thermal stability of the polymer[3].

The determination of glass transition temperature is typically measured using DTA or DSC. In DTA the polymer sample and an inert reference usually an empty crucible are continuously heated and the temperature difference is recorded as a function of temperature. When endothermic or exothermic processes occur in the polymer, its temperature of the sample pan becomes lower or higher respectively than that of the inert material[3]. In DSC the sample and the reference are heated at a constant rate and the difference in energy required to maintain identical temperatures is recorded. Similarly to DTA, the change in the shape of the graph can indicate glass transition, an exothermic process may indicate crystallization or an oxidation reaction, an endothermic process may indicate melting or vaporization[3].

Evolved gas analysis (EGA) is a useful tool for the investigation of thermal decomposition mechanisms as, in addition to the mass loss of the heated product, information about the identity of the evolved substances are obtained. Among several techniques, coupling a TGA with infrared spectroscopy appears to be more and more common[8].

2.2 Analytical applications of polymer pyrolysis

The qualitative and quantitative analysis of the pyrolysis products often serves as a definitive proof of the identity of unknown polymer samples[4]. Analytical pyrolysis is a technique used for the characterization of a material (or a chemical process) based on the results of chemical degradation reactions induced by thermal energy[3,10].

Analytical pyrolysis has significant advantages requiring only a very small amount of sample[11]. The first step in this technique is the pyrolysis reaction. Pyrolysis itself only provides analytical data if it is associated with some kind of measurement process. This can provide information related to the polymer analysis, thermal decomposition mechanisms of polymers

and pyrolytic conversion of polymeric precursors[4]. A summary of analysis methods applicable to thermal analysis are summarised below.

2.2.1 Spectroscopic methods

Controlled heating of the sample inside the analytical instrument is a possible way to obtain direct information on the thermally induced chemical reactions in polymers[4]. The spectroscopic methods of analysis are used for the determination of polymer identification (chemical composition). Infrared (IR) spectroscopy has the advantages, among other techniques, of requiring a relatively short time (a few seconds are enough to collect the spectrum) and to be non-destructive, so that the same sample can be used to monitor the time resolved evolution of degradation products[7].

IR absorption is produced by the transition of the molecules from one vibrational quantum state into another, and most decomposing polymers generate characteristic spectra[3].

2.2.1.1 FTIR

The physical properties of polymeric systems depend upon the chemical constituents and the configuration of the macromolecules, and also on the relationships among the morphology the parameters defining such as crystallinity and phase segregation[12]. Many spectroscopic techniques are available to access these features, and FTIR spectroscopy is perhaps the most widely used due to its versatility in determining composition and conformation among others. Spectrometers measure the interaction of radiation with experimental samples. They record the frequencies or wavelength at which the atoms or molecules contained in sample absorbs radiation and intensities of the absorptions. Frequency, or wavelength, and intensity of sample absorption are depicted in a two-dimensional plot called a spectrum.

Interpretation of the infrared spectrum, in the condensed phase, is based on the table of group absorption frequencies[13]. For small molecules in the gas phase each molecule produces its own unique spectrum, which is often complex. Positive identification and quantification can best be obtained by comparison of the whole spectrum. In general, all the absorptions fall within the range 4000 – 400 cm^{-1}. Positions of the principal decomposition gases in cm^{-1} are

presented in Figure 1. This shows the sharp and well-defined absorption peaks of many simple molecules, providing a wealth of data, in a complex form, for interpretation.

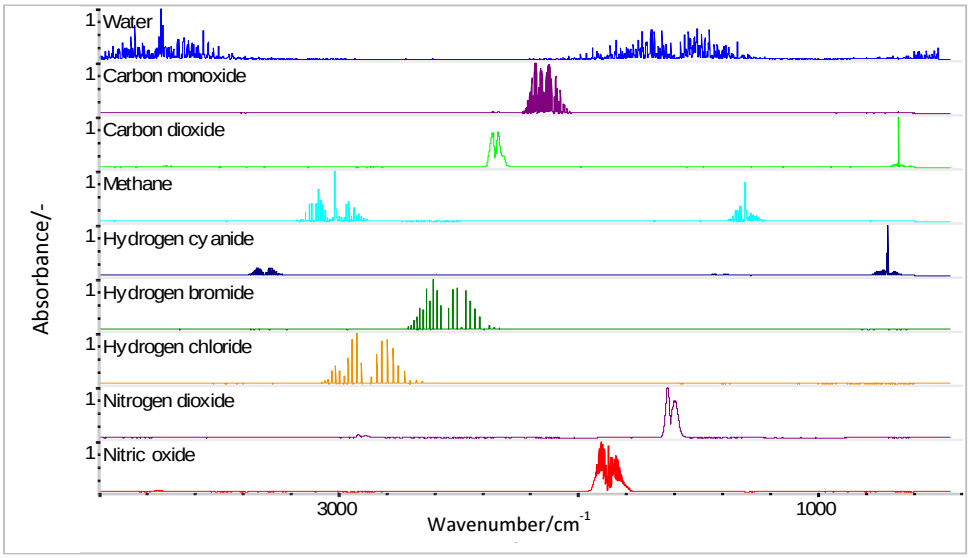

Figure 1 FTIR spectra of common gaseous decomposition products

Gas phase FTIR has been developed to identify and quantify most of the chemical species present in gases, such as those generated by various polymers under different decomposition conditions. Protocols for the use of FTIR for fire gas analysis primarily for studies of fire effluent toxicity have been described in ISO 19702[14]. The most obvious advantage of the FTIR system is that, it will detect all species (except homonuclear diatomics: oxygen, nitrogen, chlorine, etc) in real time, and, at least in theory, each of the known components can then be subtracted from the spectrum, simultaneously for the whole of the measuring period, there is no wastage of information, analogous to a blanked-off part of the spectrum, and so the sensitivity achievable in a real time is very much greater than from dispersive instruments[15]. Nevertheless, to fully exploit the potential of this method, some skill is needed in developing a methodology that will permit optimization of the analysis since IR absorption of the decomposition products is difficult because of the strong IR absorption of water[3] (one of the main problems).

2.3 Coupled techniques or combination of analytical instruments

Thermogravimetric analysis is also considered to be an analytical pyrolysis method when carried out in an inert atmosphere and coupled to a volatile product analysis instrument[4].

2.3.1 TGA-DSC

Usually the elucidation of degradation is based solely on thermogravimetric analysis (TGA)[16,17,18,19,20,21]. In TGA a loss of mass is measured, whereas the thermal effects of degradation of polymeric materials begins frequently with enthalpy changes which cannot be detected by use of this technique. These changes can be obtained by DTA or DSC measurements in order to record the phase transitions such as melting[22]. Simultaneous measurements by DSC and TGA methods allow the study of the thermooxidative and thermal stability of different materials or products together in parallel with the mass loss over a wide temperature range resulting in specific mechanisms of degradation. It is possible to analyse both the thermogravimetric and calorimetric data collected over a large temperature range at similar heating rates and other conditions.

2.3.2 STA-FTIR

Thermogravimetric analysis or Simultaneous thermal analysis coupled to Fourier transform infrared spectroscopy (STA-FTIR) has proved a powerful tool to obtain information about the general characteristics of a pyrolysis process[8,23,24,25,26,27].

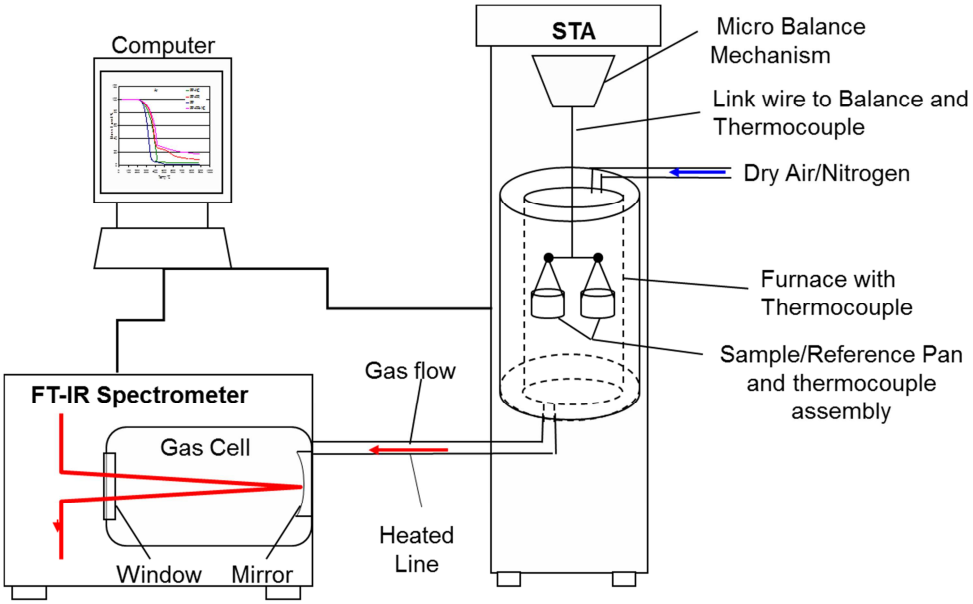

Figure 2 STA-FTIR diagram

Thermogravimetry (TG) measures sample weight as a function of temperature, but gives no information on the chemical basis of the weight change process. The introduction of FTIR spectrometry as a hyphenated technique with TG allows for the real time collection of spectra of gases evolved during sample heating, so that one can make assignments of the evolved gases to the detected mass losses. The main advantage of the coupled technique STA-FTIR is the identification of gaseous products, which together with the thermal effects (DTA) and mass changes (TG) allow interpretation of the course of the reactions investigated. Qualitative analysis is routinely done by comparing the relative intensities of recorded spectra with those of known compounds[69,28,29].

The gaseous compounds are removed by the carrier gas through a heated transfer line to the FTIR spectrometer. The spectrum obtained is a mixture of individual components[23].

2.3.3 Pyrolysis Gas Chromatography and Mass Spectrometry

As an alternative to STA-FTIR pyrolysis gas chromatography and mass spectrometry (pyGCMS) provides a more robust identification of the individual volatile species but less reliable quantification information on their relative concentration. After thermal decomposition, usually at a controlled heating rate in a controlled atmosphere, gas chromatographic separation of the volatiles occurs by passing through a capillary column lined with a suitable sorbent liquid. Each component then passes separately into the ion source of a mass spectrometer, where it is fragmented and ionised, giving rise to a characteristic mass spectrum. The spectrum is matched by library software interrogating a database, giving the identity of each species evolved.

2.3.4 Microscale Combustion Calorimeter

Although it is not strictly a thermal analysis technique, the microscale combustion calorimeter, as a TVA-EGA technique, where the EGA is oxygen depletion calorimetry to determine heat release rate. TVA is thermal volatilisation analysis and generally involves heating the polymer trapping the volatiles, and analysing them e.g. with mass spectrometer. Developed in Glasgow in 1960's it is still in use in Strathclyde (in Glasgow).

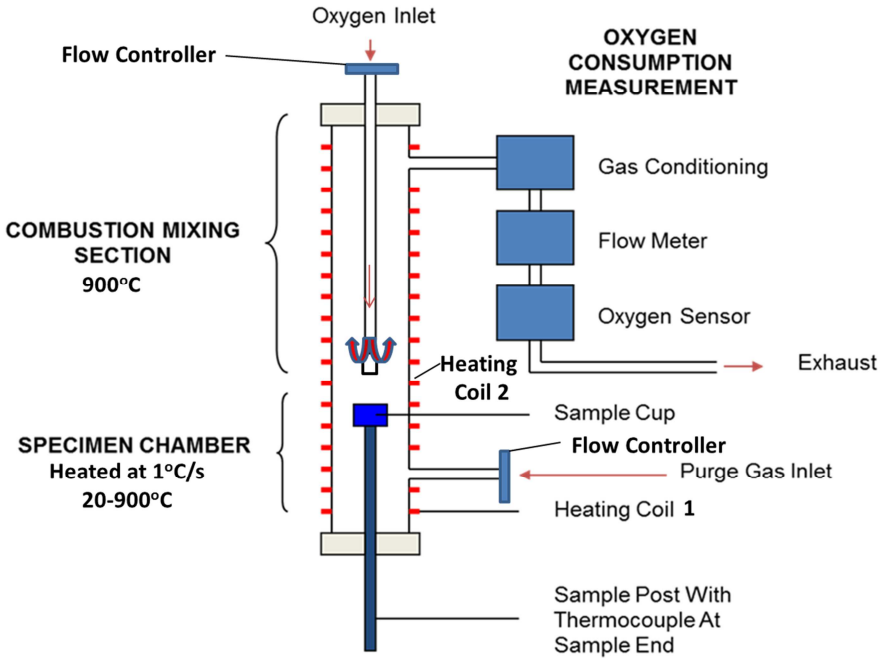

Figure 3 Schematic view of a MCC

The Pyrolysis Combustion Flow Calorimeter (PCFC) also known as Micro Combustion Calorimeter (MCC) apparatus is utilised to determine the flammability characteristics of polymeric materials by use of combustion calorimeter on a micro-scale. The apparatus is used according to ASTM D 7309[30]. The method was developed by the Federal Aviation Administration (FAA)[31,32], and uses the principle of oxygen consumption as its basis. Similar to the cone calorimeter, the method can determine several of the parameters related to flammability including the heat release rate, the heat of combustion, char yield and ignition temperature, however unlike the cone calorimeter, the apparatus requires only milligram quantities of sample. As the technique utilises oxygen consumption calorimeter for determining heat release rate (similar to the cone calorimeter) using these techniques together can provide valuable heat release data at both the micro and bench scale.

2.4 Measurement of Flammability

There are a large number of different techniques for measuring different aspects of flammability. The cone calorimeter is the most popular method for determination of heat release rates under controlled condition.

2.4.1 Cone Calorimeter

A laboratory-scale method for measuring several of the parameters related to flammability is by use of the cone calorimeter as shown in Figure 4[33,34].

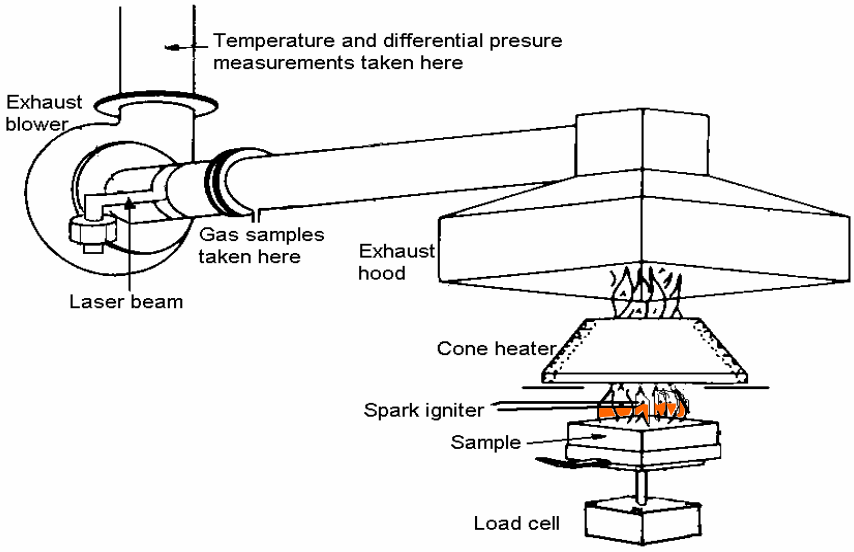

Figure 4 Schematic view of a Cone Calorimeter[34]

The method is based on the principle that the net heat of combustion is proportional to the amount of oxygen required for combustion. It has been established that approximately 13.1×10^3 kJ of heat are released per kilogram of oxygen that is consumed. The specimens are subjected to a radiant heat source and measurements are made of oxygen concentration and exhaust gas flow rates. Specimens are 100 mm by 100 mm and may be up to 50 mm thick. The thermal radiation can be set for any heat flux between 0 and 100 kWm^{-2}. The method is particularly useful for fire retardant polymer formations which may not be ignited initially by a direct source by thermal radiation from nearby flames such as wall or ceiling materials[35,36].

The cone calorimeter is used to measure the heat release rate, mass loss rate, smoke production, flame spread and ignition properties[37]. The material is heated uniformly by a radiant heating source and then ignited. The ignition source within the cone calorimeter is a spark igniter. The sample is weighed constantly to determine mass loss as a parameter in its own right, and as a function of time. Smoke obscuration can also be measured using a laser photometer system. The cone calorimeter can be operated according to ISO 5660-1 or other standard protocols[38,39].

3 THERMAL DECOMPOSITION OF POLYMERS

A polymer is a chain molecule composed of repeating structural units. There are hundreds of different types of polymers, both natural and synthetic, and the chains may be linear, branched, or cross-linked where bonds are formed between two adjacent polymer chains.

Thermal decomposition is a process where polymeric materials undergo both physical and chemical changes when heat is applied[40]. It may proceed by oxidative processes which are often accelerated by oxidants, such as air or oxygen. The rate, mechanism, and product composition of thermal decomposition processes depend both on the physical properties of the original material and on its chemical composition. For example, the chemical processes (melting, charring etc.) where the generation of flammable volatiles is observed can alter the decomposition and burning characteristics of a material. There are a number of generalised mechanisms used to characterise the thermal decomposition of polymers:

1. Chain Scission

a) Random-chain scission, in which the polymer chain is broken at apparently random locations.

b) End-chain scission, in which individual monomer units are successively removed from the chain end.

2. Chain stripping, in which atoms or groups, not part of the main polymer chain (or backbone), are cleaved. It occurs via one of two main reaction types: side chain elimination or side chain cyclisation[9].

a) Side Chain Elimination involves the breaking of the bond between the functional group and the main polymer chain. The eliminated group often reacts with other eliminated functional groups[42]; sometimes the eliminated group catalyses further chain stripping, as in the ease of HCl coming off PVC.

b) Side Chain Cyclisation- occurs when two functional groups which are adjacent react such that a bond is formed resulting in a cyclic structure. This mechanism is important to char formation, due to the cyclic nature of the resulting group, and the residue being much more stable and richer in carbon than prior to the reaction[41].

3. Cross-linking, in which bonds are created between polymer chains[40]. The resulting molecule is of higher molecular weight, and is less easily volatilised, thus cross-linking is an important step in the formation of char[42].

It is important to note that the thermal decomposition of a polymer often involves more than one of these mechanisms[42,43]. Some examples of polymers and their main polymer decomposition mechanism are presented in Table 2.

Table 2 Generalised mechanisms of polymer decomposition

Mechanism		**Examples of Polymer**	**Typical products**
Chain Scission	Random Chain Scission	Polyethylene Polypropylene Polystyrene	Alkanes, alkenes, very little monomer Alkanes, alkenes, very little monomer Styrene monomer, dimer and trimer
	End Chain Scission	Polymethylmethacrylate Polytetrafluoroethylene	90 - 100% monomer 90 - 100% monomer
Chain Stripping		Polyvinyl chloride Polyvinyl alcohol	Hydrogen chloride, aromatic hydrocarbons and char Water and char
Cross-linking		Polyacrylonitrile	Char (and HCN)

3.1 Kinetics of Polymer Decomposition

Both chemical and physical changes occur when a polymeric material is exposed to excessive heating. Once the polymer is heated, it starts to decompose and begins yielding volatile products that are usually combustible. Additionally, the polymer can melt before decomposition what is dependent upon the degree of crosslinking and its stability.

Decomposition involves breakdown of the polymer chain which can occur through a variety of mechanisms – chemical or thermal attack, ultraviolet and ultrasonic radiation etc.[44]. The energy required for a particular chemical reaction to occur is referred to as the activation energy. The process is shown graphically in Figure 5. The initial energy required for the reaction to proceed from X to Y is greater than the difference in energy (referred to as the

enthalpy of reaction (ΔH)). The activation energy (E_a) is the energy molecules must posses in order to overcome the barrier to reaction. Statistically, only those few molecules possessing very large amounts of energy can undergo reaction.

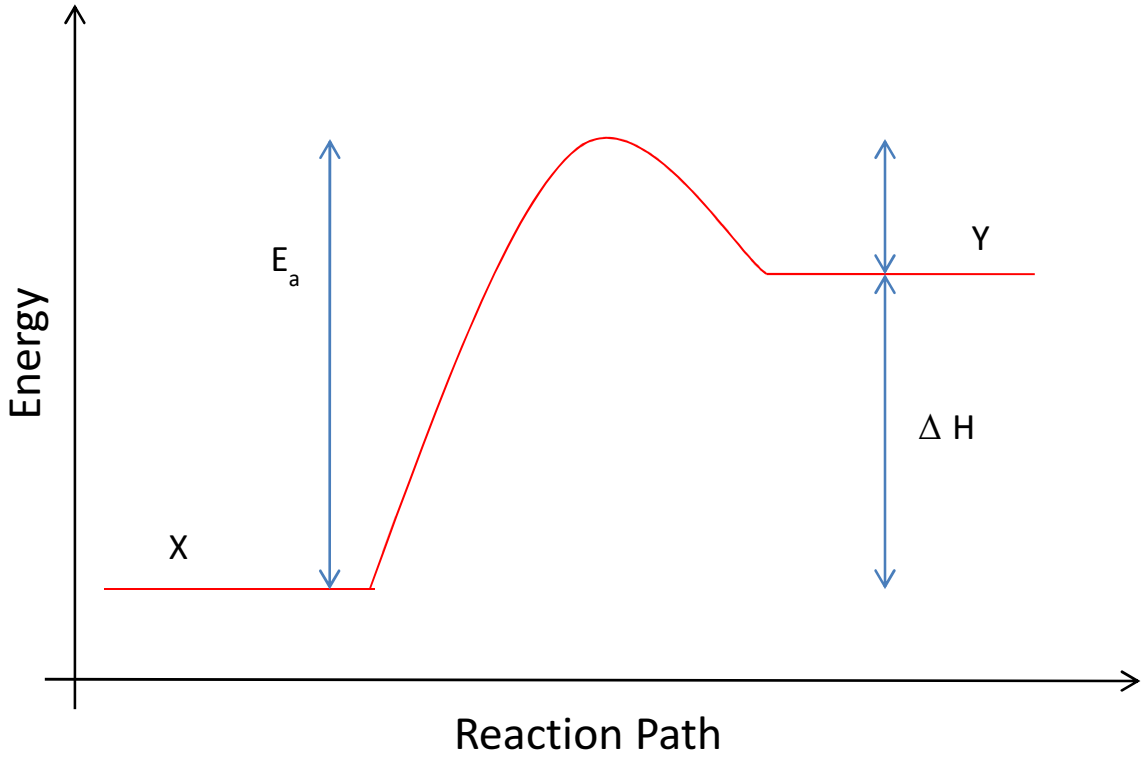

Figure 5 Activation Energy

Classical chemical kinetics also describes the Arrhenius factor (A) relating to the number of molecular collisions and their orientations. The experimentally determined Arrhenius equation shows the relationship between the fundamental reaction rate A and its temperature dependence $e^{-E_a/RT}$, on the rate of the reaction, k:

$$k = Ae^{-E_a/RT}$$

Equation 1

Where

R is the universal gas constant (8.314 JK^{-1} mol^{-1})
T is the temperature (in K)
k is the reaction rate coefficient

3.2 Behaviour of Individual Polymers

Polymers are often classified based on physical properties or in terms of polymers chemical composition. The main hydrocarbon polymers are polyolefins such as polyethylene and polypropylene which are two of the most widely used polymers. The most important oxygen-containing polymers are polyacrylics, and polyesters. Nitrogen-containing materials include polyurethans, polyamides, and polyacrylonitrile. Some polymers, such as polypropylene have a specific structure, others such as polyamides or polyesters represent a class of materials with similarities in their repeating units.

A small selection of some of the most widely used materials, have been studied as part of this thesis. Their decomposition and combustion behaviour is briefly discussed below.

3.2.1 Polyethylene

The decomposition of polyethylene has been illustrated schematically in Figure 6, and illustrates the generalised processes of thermal decomposition by random chain scission[43]. The temperature increase causes random scission of the polymer backbone resulting in the formation and release of a larger amount of cyclic hydrocarbons and aromatic rings by Diels-Alder cyclisation reactions of alkenes (olefins or molecules with C=C double bonds). The aromatic content increases with increasing temperature. The thermal decomposition in air produces not only hydrocarbons and aromatic compounds, but also partially oxygenated products such as aldehydes, ketones and also major combustion products: carbon monoxide, carbon dioxide, and water[43,45].

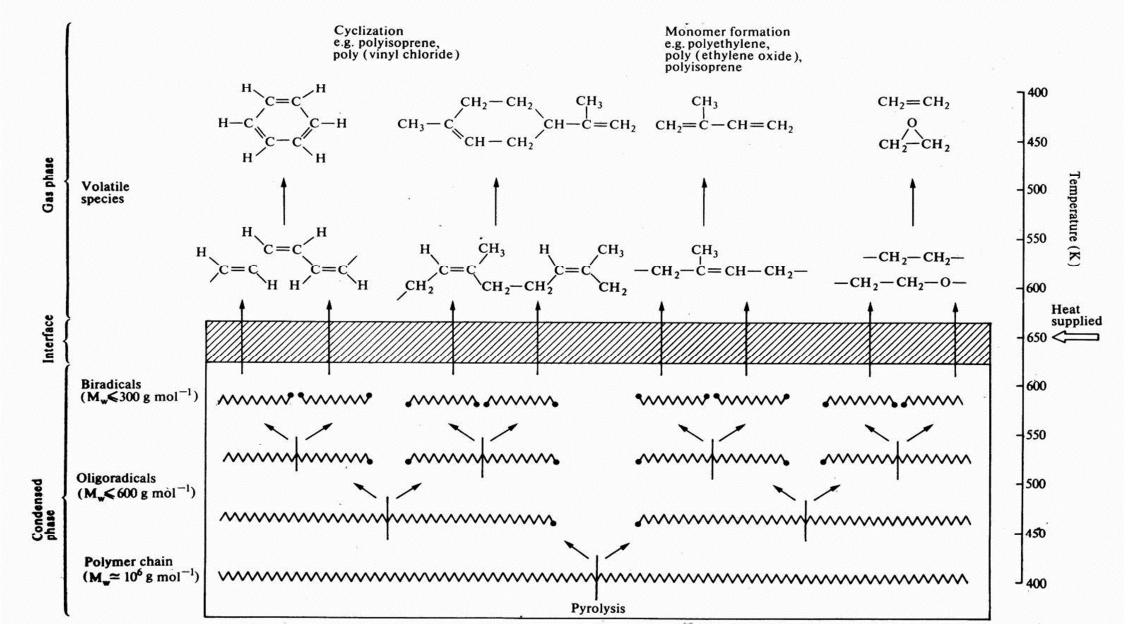

Figure 6 Thermal degradation for LDPE

3.2.2 Polypropylene

With around 18% of the world plastic consumption, polypropylene (PP), Figure 7, is one of the most used commodity polymers representing a huge market[46]. Polypropylene has good mechanical properties and is easily processed. It is used in many applications, for example, car, furniture, electronics housing, interior decoration, insulation, architectural material, and so on. However, it is highly flammable and this often limits its application[47].

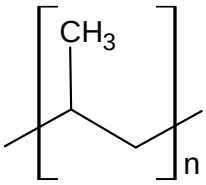

Figure 7 Polypropylene structure

The degradation of PP has been the subject of extensive studies[3,48,49]. Polypropylene pyrolysis is dominated by initial chain scissions. The thermal degradation of PP under non-isothermal conditions revealed that the recovery of carbon as organic volatile products comprised dienes, alkanes, and alkenes. Major compounds include C9 hydrocarbons, like 2-methyl-4-octene; 2-methyl-2-octane; 2,6-dimethyl-2,4-heptadiene; 2,4-dimethyl-1-heptene; and 2-methyl-1-octene[50]. During the oxidation of polypropylene, the following volatile products have been identified: water, formaldehyde, acetaldehyde, acetone, methanol, hydrogen, carbon

monoxide and carbon dioxide. Decomposition of the polypropylene chain is also oxidatively sensitized and occurs by breaking the weaker bonds at the polymer surface in the presence of chemisorbed oxygen. In TGA even 1% oxygen is sufficient to significantly lower the onset of decomposition. In the inner oxygen-free zone, C–C bond scission begins resulting in formation of shorter radicals and biradicals.

Polypropylene has similar chemical and physical properties to polyethylene (Figure 6) [43].

3.2.3 Polyacrylonitrile

Polyacrylonitrile (PAN), Figure 8, has high rigidity and low gas permeability, and with good resistance to solvents. The pure polymer is difficult to dissolve, and exhibits exceptional barrier properties to oxygen and carbon dioxide[51].

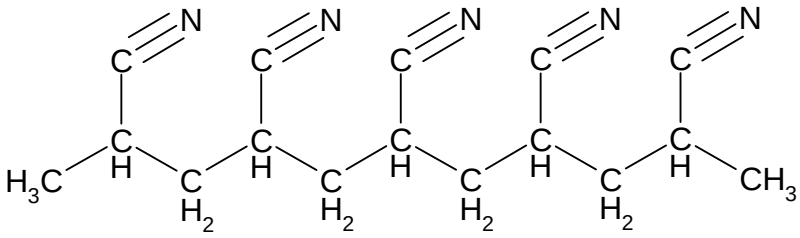

Figure 8 Chemical structure of the repeating unit of polyacrylonitrile[52]

Polyacrylonitrile begins to decompose between 251°C and 352°C with the evolution of small amounts of ammonia and hydrogen cyanide[41]. These products accompany cyclisation reactions involving the creation of linkages between nitrogen and carbon on adjacent side groups. In the cyclization reaction the nitrile groups open, resulting in a material containing segments of short, ladder molecules connected by sequences of unchanged PAN polymer. Additionally, nitrogen in the nitrile group is bound with the carbon of neighbouring nitrile groups in the polymer chain forming six-element rings (hydronaphthiridine rings)[52,53,54]. The hydronaphthiridine rings may undergo oxidative dehydrogenation leading to acridone and other structures increasing the aromaticity[52.] The result is a ladder polymer containing a mixture of acridone, pyridine, hydronaphiridine and other structures, Figure 9[52].

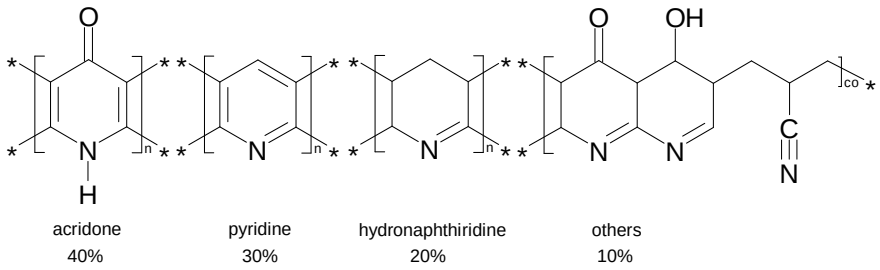

Figure 9 Typical ladder polymer structure of PAN[52]

The gaseous products are not the result of the cyclisation of itself, but arise from the splitting off of side or end groups not involved in the cyclisation. The ammonia is derived principally from terminal imine groups (NH) while HCN results from side groups that do not participate in the polymerisation-like cyclisation reactions. At temperatures of 350°C to 700°C, hydrogen is evolved as the cyclic structures carbonise. At higher temperatures, nitrogen is evolved as the char becomes nearly pure carbon[41,55].

Table 3 PAN decomposition products in air during heating at 10°C/min

Decomposition Products from PAN	
Carbon dioxide	Water
Ammonia	Carbon monoxide
Acrylonitrile	Benzonitrile
Acetonitrile	2-methyl-2-propenitrile
Hydrogen cyanide	Propanenitrile
3-methylbenzonitrile	Pentadinitrile
Pyridine	1-cyano-2-butene

3.2.4 Ethylene-vinyl acetate copolymer

Ethylene-vinyl acetate (EVA) copolymer, Figure 10, represents the largest-volume segment of the ethylene copolymer market. Over 150 grades are available with applications in automotive industry, household objects, electrical cable insulation and jacketing, etc.[3]. This class of materials has attracted attention because of their unique combination of enhanced properties, including improved barrier, mechanical and fire properties. It is highly elastomeric, and tolerates high filler loadings while retaining its flexible properties[56,57,58,59].

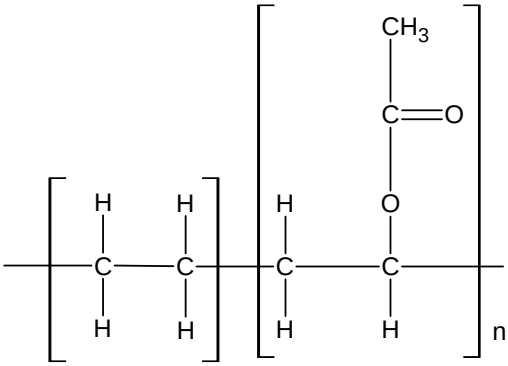

Figure 10 Ethylene-vinyl acetate structure

Some the most common products from EVA thermal degradation are listed in Table 4. In air during heating at 10°C/min, EVA decomposes by a two-step mechanism, with the loss of acetic acid during the first step (300–350°C), resulting in the formation of unsaturated polyenes. Other studies on the degradation of EVA copolymers showed also that the initial step involving the formation of acetic acid was enhanced with increasing vinyl acetate content. It is also mentioned that a competing reaction occurs at the same temperature range and CO, CO_2 and CH_4 is produced[58,60].

Table 4 EVA degradation products

Products found from EVA thermal degradation	
Carbon dioxide	Carbon monoxide
Acetic acid	Water
Methane	Butadiene
Butene	Ethylene
Benzene	Naphthalene
Toluene	Indene

The second decomposition step involves random chain scission of the remaining material, forming unsaturated vapour species (~430°C), such as butene and ethylene, and generating all volatile hydrocarbon chains from C8 to C26 grouped in a series of α-dienes, 1-alkenes and n-alkanes. Further breaking of double bonds in the backbone of the polymer results in volatilisation of some aromatic compounds such as benzene, toluene, naphthalene, indene, etc.[3]. During thermal degradation, the surface of the polymer crosslinks rapidly which lead to

the formation of a protective layer which limits the access of oxygen to the remaining material, and impedes the flow of fuel to the gas phase[56,58,59].

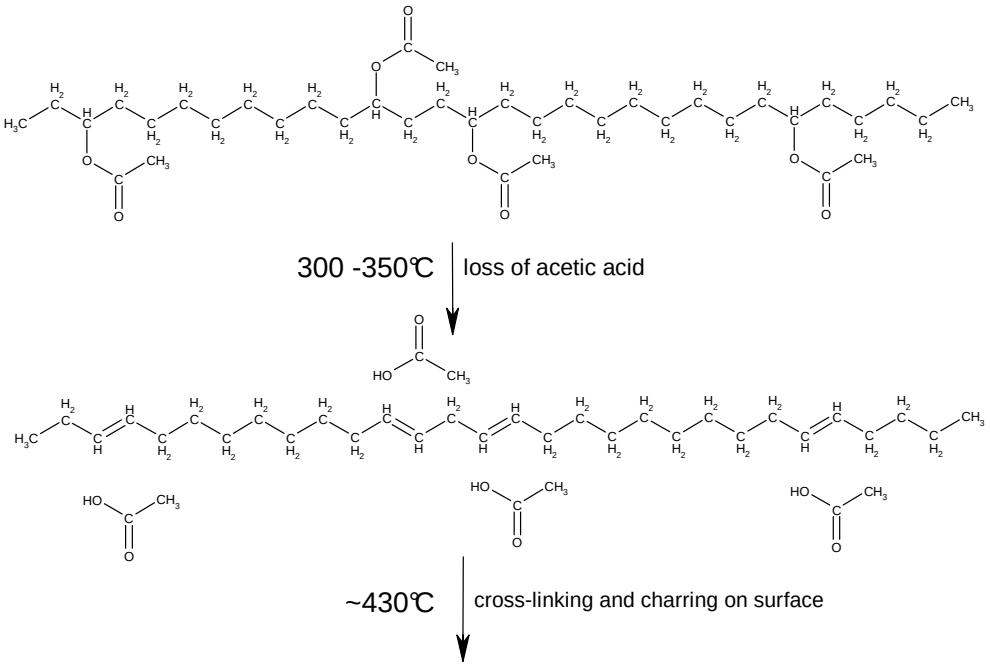

Figure 11 EVA decomposition mechanism

4 OPTIMISATION METHODS FOR STA-FTIR EXPERIMENTAL DATA COLLECTION

In this section, accuracy and precision parameters of STA-FTIR will be covered for pyrolysis of various samples. STA-FTIR measurements were performed on polyacrylonitrile (PAN) sample and the dependence of the spectral response (in the form of Gram Schmidt reconstruction, or integrated absorbance) on experimental parameters such as resolution, scanning time and heating rate, mass, and carrier gas flow rate is explained in following sections.

Simultaneous Thermal Analysis (STA) was carried out using a Stanton Redcroft STA 780 simultaneous thermal analyser. Samples (with different masses: 5, 10, 15mg) were decomposed at a heating rate of 5°C/min, 10°C/min and 20°C/ min in air, from ambient temperature to 900°C. This produced a record of the mass changes (TGA) and sample temperature changes (differential thermal analysis DTA) during the furnace heating programme.

Fourier Transform Infrared Analysis of Volatiles (FTIR) Evolved volatile species were analysed by direct connection of a heated sampling line (at 250°C) to an infrared cell (heated up to 280°C) using a Thermo Electron STA interface located in a Nicolet Magna 550 FTIR spectrometer. The STA-FTIR interface is equipped with a built-in, temperature-controlled flow cell connected to the thermogravimetric analyser (STA) furnace. It is possible to analyse the evolved gases from STA experiments using the OMNIC Series software (version 7.3) developed by Thermo Scientific. Omnic software provides user friendly graphical environment to analyse FTIR data quickly and efficiently. Dry air, purged with a Whatman purifier, was used as a reference and purge gas.

Photometric factors affecting accuracy in FTIR Spectrometry

FTIR yields large and complex data set which was investigated for possible identification and quantification of a larger selection of chemical species present in decomposition products[61]. Many factors affect the accuracy of Fourier transform spectrometers[62]. They include the effect of resolution and apodisation. Apodisation is a mathematical computation that compensates for the fact that the interferogram is not an infinite set of data and it is used to smooth the discontinuities at the beginning and end of the sampled time record. Apodisation is performed

automatically before the Fourier transform. Strong apodisation reduces the resolution of the data and broadens the peaks[63] on the spectrum. FTIR analysis of decomposition products presents also other problems[64], not only in sampling of the gases, separation of solid particles such as soot without also removing species of interest, but also in the identification and quantitative measurements.

At present, most of the publications on polymer decomposition present FTIR analysis, in terms of the bonds contained within the molecule, rather than fully interpreting the gas phase spectra, where the patterns are unique to particular molecules[65, 66,67]. Those that do use gas phase spectra present only whole FTIR spectra without analysis of time (or temperature) resolved profiles.

A single 90 minute STA-FTIR run can take over a week to deconvolute. Also, quantitative calibration requires care since many gases are nonlinear with concentration and, if interferences are present in the spectral region may require a suitable reference method in order to provide time resolved profiles of the individual species. One of the main problems with the FTIR technique is obscuration of absorbance of one species by another in the spectrum. Water is a very strong absorber of infra-red radiation over a wide range of frequencies and obscures many other species, increasing the detection limit and increasing the noise in the absorbance signal of the compounds that overlap with water[68]. Some successful quantification has been achieved recently, applying FTIR spectrometry[69,70,71,72]. However, ideally, calibration methods require selection of regions free from interferences from different species, and there is a need to be careful in choosing the wavenumbers of the gas to be analysed, otherwise these problems will increase the limit of detection and uncertainties. Such quantification is especially important when investigating multistage decomposition reactions, or, when two or more gases evolve simultaneously.

Effect of Spectral Resolution

The spectral resolution, along with the number of scans, affects the total collection time. Increasing the resolution and number of scans will result in an increase of the total collection time[63]. The smaller the resolution width, the better the resolution. Increasing the resolution (use a smaller width) will better distinguish the narrow bands of vibration-rotations

spectra as the points in the spectrum are closer together (higher peak differentiation), but can be still identified as separate peaks. On the other hand, setting the highest resolution will not provide additional information, and the smaller signal can result in increased noise. Also, the higher the resolution, the longer it takes to collect the data and the memory that is required to save the spectrum[63].

Effect of Scanning Time

The number of scans determines how many repeats are performed during each data collection stage, before where the system averages them. The number of scans, along with the resolution and mirror velocity, affect the total collection time. For a given resolution, increasing the number of scans increases the total collection time. Increasing the number of scans reduces the noise level of the data (increases the signal-to-noise ratio) and increases the sensitivity; that is, the ability to distinguish small peaks from noise. However, a large number of scans have already been collected; it will take many more scans to achieve a significant increase in sensitivity[63]. Generally n repeated measurements give $\sqrt{n}$ improvement in accuracy.

Signal to Noise Ratio

Studying samples that produce small spectral peaks, it is important to make sure that the signal-to-noise ratio is high enough to distinguish spectral features from the noise inherent in all experimental data.

RMS (root mean square) noise

RMS is a measure of the variation in a spectral region. Before the RMS noise is computed, the best linear fit to the baseline is removed from the signal in the spectral region of interest[63]. This removes the effect of offset on the noise measurement. Then the RMS noise level is equal to the square root of the average of the square of the linearly corrected values. The formula for RMS noise is shown below.

$$RMS \quad noise = \sqrt{\frac{\sum \left(y_i - \bar{y}\right)^2 - \frac{\left(\sum \left(x_i - \bar{x}\right)\left(y_i - \bar{y}\right)\right)^2}{\sum \left(x_i - \bar{x}\right)^2}}{n-2}}$$

Equation 2

Where:

y_i is the intensity at a data point within the region,

x_i is the *X* value of the data point,

and *n* is the total number of data points in the region.

A bar over a variable indicates the arithmetic mean of the values of that variable at the data points within the region[63].

Classification of FTIR spectroscopy

Bonds have different levels of energy, which result in the pattern and intensity of the spectrum. In a simple diatomic molecule, there is only one band of infra-red absorption resulting from stretching the bond. If there are more atoms, there will be more bonds, and therefore more modes of vibrations, more complex spectrum. The gases studied in this project have different behaviour patterns and only SO_2 and acrolein are reported to have approximately linear infrared absorption/concentration. Many of the gases: CO, CO_2, NO, NO_2, HCl, HCN show non-linearity. The major problem connected with the FTIR technique is overlapping with other gas species in the same spectrum. Water is a very strong absorber of infra-red radiation over a wide range of frequencies and obscures many other species[15]. There are also many other factors which will influence the qualitative analysis, heating rate, sample masses, resolution, scanning time etc. are a few of the most important and will be detailed and discussed in practical part of this work.

Classification of gases with FTIR spectroscopy requires the use of sophisticated kind of pattern recognition mathematical algorithms. In order to classify gas species that overlap in the infrared spectra different mathematical algorithms are tested within Omnic package.

4.1 PAN Decomposition

In the case of polymers, there are only a few main patterns of breakdown: depolymerisation or loss of side groups (substituents). In some cases, the polymer molecular weight will fall rapidly as degradation proceeds and often there is only one stage of degradation as the temperature is gradually raised[73]. Side group or substituent reactions can often lead to a more complex pattern of degradation. The resulting unsaturated chain (with double C=C bonds) may break down to create volatiles or lose further substituents and undergo carbonisation or char formation[43]. Under these circumstances, more than one stage of degradation is normally observed as the temperature is gradually increased.

Polyacrylonitrile (PAN) was decomposed using STA-FTIR. Tests were carried out in air with heating rate 10°C/min up to 900°C. FTIR analysis was performed either at 0.5 cm^{-1} or 4.0 cm^{-1} resolution (as some products like HCN are not seen on spectra for higher resolutions, as explained in later sections). Decomposition products and their profiles are presented in Figure 12 and Figure 13.

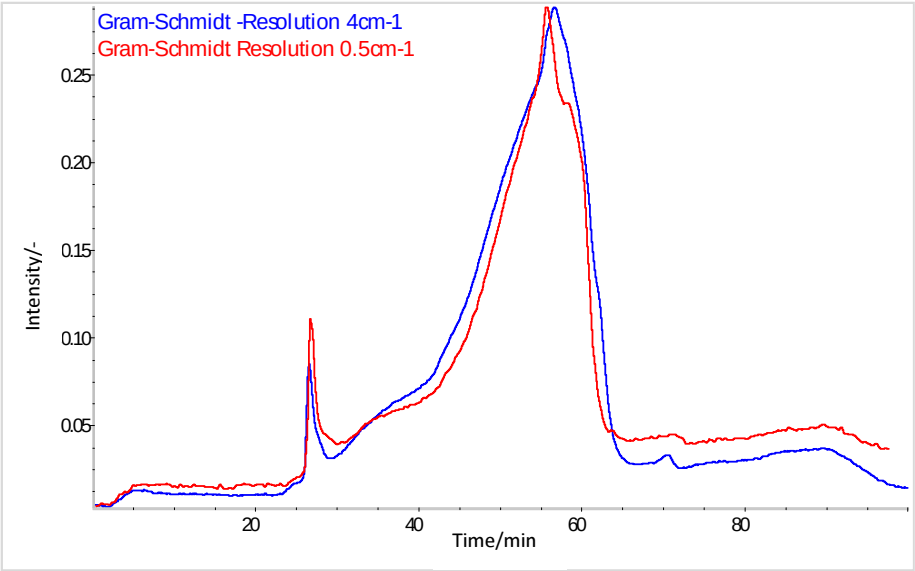

Figure 12 Intensity (Gram-Schmidt) curve of PAN decomposition

Gram-Schmidt reconstruction is a graphical representation of series data that shows how the overall relative spectral response changed over the duration of the experiment. As expected, the Gram-Schmidt profile for PAN is not different at the resolutions. There are two

major peaks where products are evolved. The first change is seen as a sharp peak occurring at 25 – 30 min (which responds to 270 – 320°C as heating rate is 10°C/min plus ambient temperature). Second peak is much longer and broader and occurs between 35 – 65 min (corresponding to 370 – 670°C).

Figure 13 presents spectra of PAN, at resolution 4 cm^{-1}, at different times and with different decomposition products. PAN decomposes either by cyclisation, or chain stripping with the release of hydrogen cyanide and ammonia. Then the structure may either decompose further producing volatiles like carbon monoxide (CO), carbon dioxide (CO_2) and other aromatics[52].

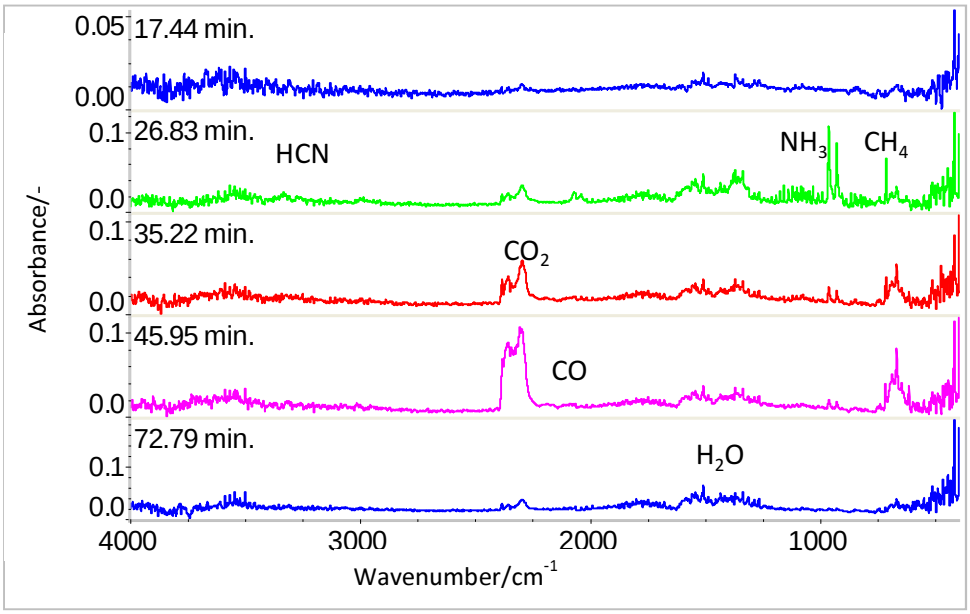

Figure 13 Spectra of PAN decomposition in air with heating rate 10°C/min

Table 5 presents baseline and gas species wavenumbers used to create profiles of PAN decomposition products. Within the chosen wavenumbers the baseline must be clear of any peaks and, for comparison must remain the same. All product profiles are based on peak height and also they should be clear of interferences or overlap with other peaks.

Table 5 Selected wavenumbers for PAN decomposition products

Decomposition product	**Wavenumber/cm^{-1}**
Baseline	2550-2450
CO_2	668
CO	2099
HCN	3333
NH_3	930

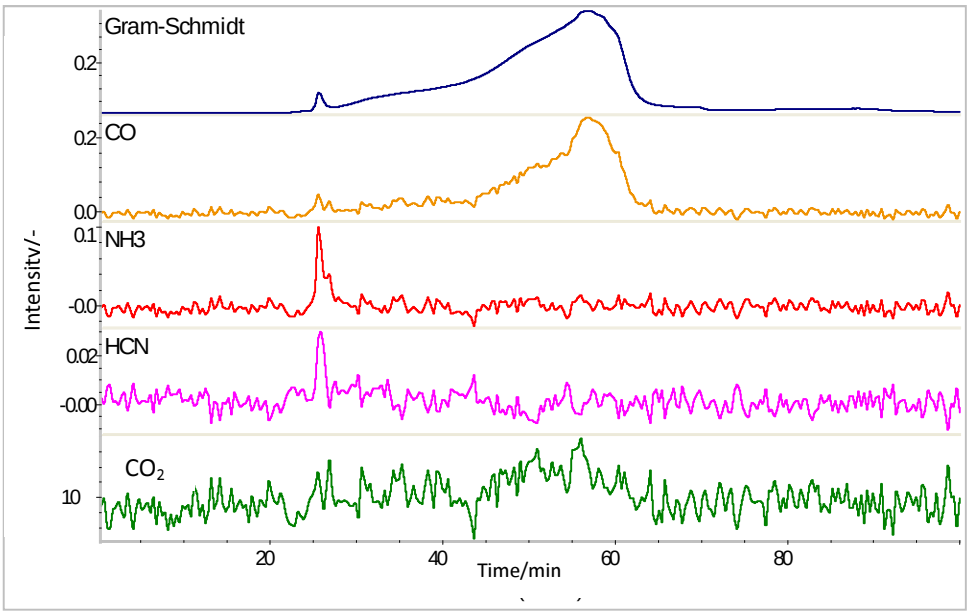

Figure 14 Products and profile of PAN decomposition

From FTIR spectra it is seen that heating PAN in air for around 25 min resulted in the formation of hydrogen cyanide and ammonia (first peak in Figure 14) and a charring residue. Then heating the residue 500-650°C (45-65min) resulted in further decomposition producing volatiles such as carbon monoxide, carbon dioxide (second broad peak observed in Figure 14). As well as the major products identified, there are still some unidentified volatiles with absorbances at 2982, 2805, 2105, 2054, 1902, 1754, 1585, 1438, and 1083 cm^{-1} respectively, Figure 15. Some suggestions of species are given in Table 6 as they fit into wavenumbers region. However there is no assurance as different compounds occurred in this region and further analysis is required either with more specific settings (increased scan number) or other confirmation technique should be used to identify these volatiles (pyGCMS). This highlights the

problem of FTIR – the inevitable compromise between resolution (easier identification of unknown molecules) and reduction of noise (better resolution of intensities of absorption).

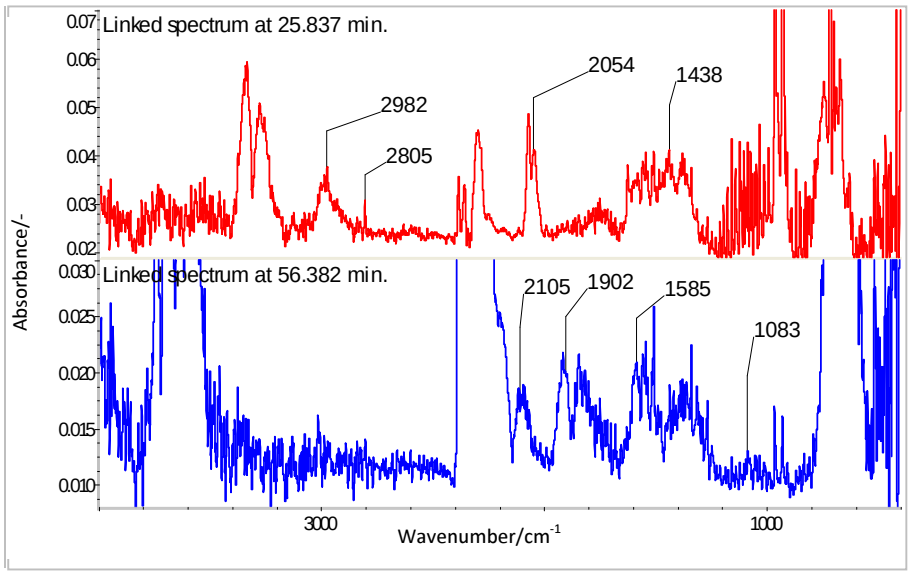

Figure 15 Unidentified peaks from PAN decomposition in air 10°C/min heating rate

Table 6 Unidentified peaks and possible products

Unidentified Peak wavenumbers/cm^{-1}	**Possible product**
2982	Hydrocarbons or Propionitrile
2805	Not identified
2105	Not identified
2054	Not identified
1902	Nitric oxide
1754	Acetamide or Formaldehyde
1585	Nitroethane
1438	Not identified
1083	Not identified

4.2 FTIR different optimisation parameters

In these studies, different parameters for FTIR and STA were set. All the spectral correlations are done using the combination of settings shown in Table 7. Different settings of heating rates, resolution and scanning are tested and compared to obtain the best results.

Table 7 Combination of settings for PAN samples

Sample name	**FTIR Settings**		**STA settings**		
	Resolution/ cm^{-1}	No of Scans	Heating rate/ $^{\circ}C \cdot min^{-1}$	Air Flow/ $cm^{3} \cdot min^{-1}$	Mass/ mg
PAN_5_5_05	0.5	5	5	30	14.70
PAN_5_10_05		10			15.00
PAN_5_20_05		20			14.80
PAN_10_5_05bis	0.5	5	10	30	10.08
PAN_10_10_05bis		10			10.30
PAN_10_20_05bis		20			10.31
5-R05	0.5	5	10	50	15.20
PAN_10_5_05	0.5	5	10	30	14.60
PAN_10_10_05		10			14.20
PAN_10_15_05		15			14.80
PAN_10_20_05		20			14.30
PAN_20_5_05	0.5	5	20	30	10.08
PAN_20_10_05		10			10.23
PAN_20_20_05		20			9.90
10-R1	1.0	10	20	50	9.90
PAN_15_5_2	2.0	5	20	50	14.10
10-R2		10			10.40
PAN_5_5_4	4.0	5	5	30	10.29
PAN_5_10_4		10			10.21
PAN_5_20_4		20			10.19
PAN_20_R4	4	20	10	50	14.60
PAN_10_5_4	4	5	10	30	10.14
PAN_10_10_4		10			10.01
PAN_10_20_4		20			10.16
PAN_20_5_4	4	5	20	30	9.53
PAN_20_10_4		10			10.33
PAN_20_20_4		20			10.07
PAN_20_30_10	4	10	20	30	10.20
PAN_20_30_5		15			5.10
PAN_20_50_5	4	10	20	50	5.10
PAN_20_50_10		10			10.60
PAN_20_50_15		15			15.50

4.2.1 Resolution

To optimise the resolution setting, the samples were scanned first at a low resolution (4 wavenumbers). Then the resolution was increased to 2, 1, and 0.5 wavenumbers respectively (cm^{-1}). The spectra were overlaid and quality was compared in Figure 16. Tests were carried out in air with heating rate 10°C/min, $30cm^3$ of air flow and 5 scans per output spectrum. It can be seen that the two higher resolutions (0.5 and 1.0 cm^{-1}) are the preferred settings.

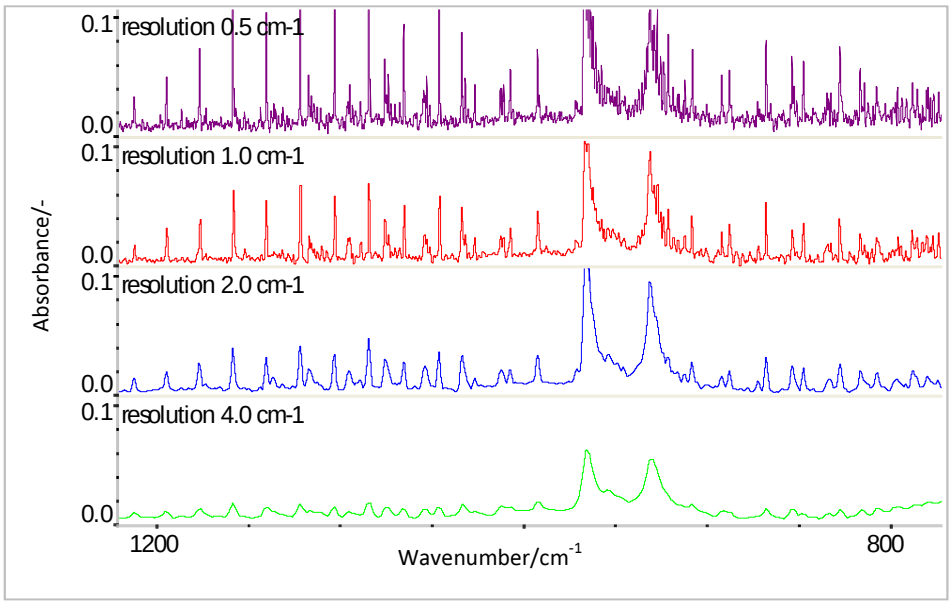

Figure 16 Resolution influence on the spectra quality

However it was observed that with the lower resolution settings it is visually easier to see the changes in the spectra and different pyrolysates (at different times). Figure 17 shows an example of spectra for different resolutions. For the higher resolutions (0.5 or 1 cm^{-1}) much thicker lines are observed compared to the lower ones (4.0 cm^{-1}). What is interesting is that for higher resolutions it is very difficult to see, for example, HCN bands occurring in 3200-3300 cm^{-1} region, when for lower resolutions it is very clearly visible.

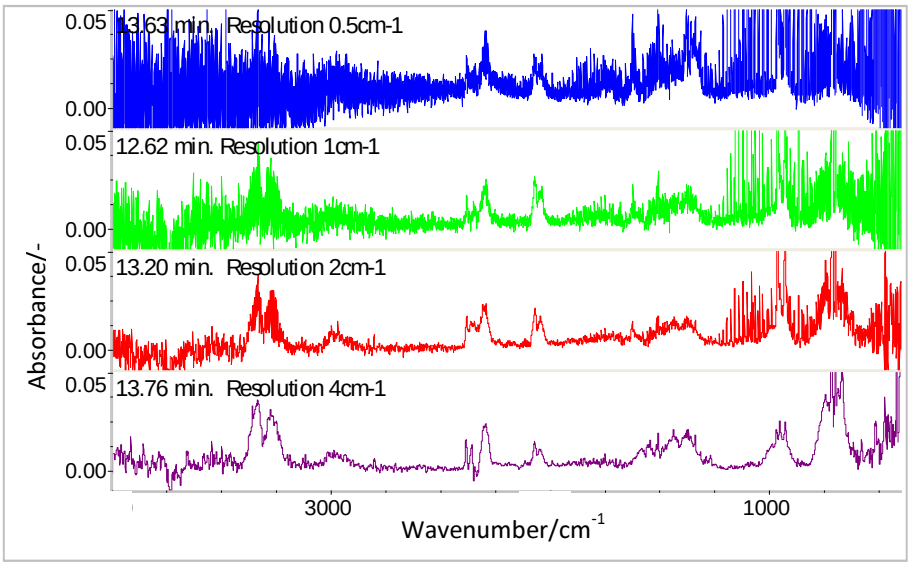

Figure 17 Visual differences for spectra lines for different resolutions (heating rate 20°C/min, number of scans: 10)

4.2.2 Effect of Scanning Time (Signal to Noise Ratio)

There are several ways to improve the signal-to noise ratio. The most commonly used method is to increase the number of scans. This both reduces the noise level and makes small absorptions easier to distinguish. It is also possible to improve the ratio by reducing the resolution (using a higher resolution setting).

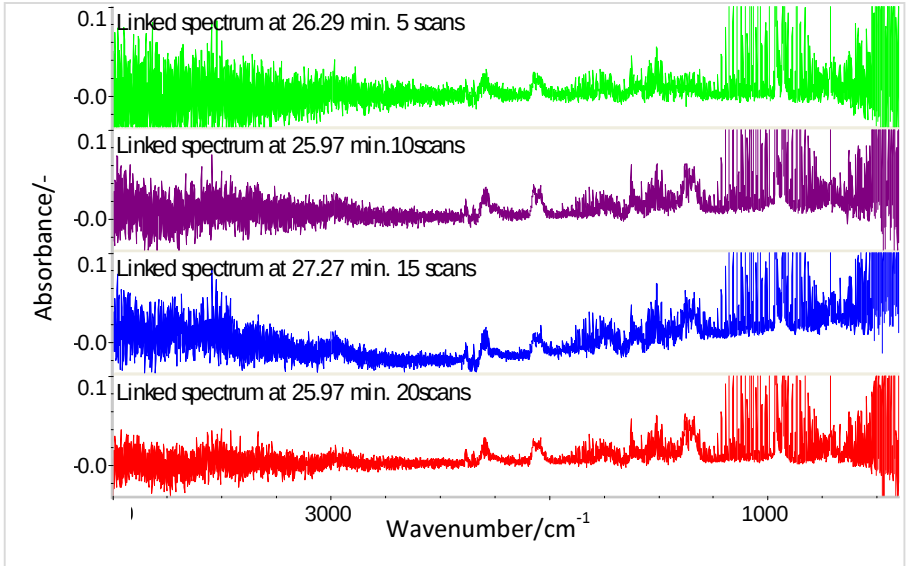

Figure 18 FTIR spectra collected with various number of scans (5, 10, 15, and 20) while other settings remain unchanged (heating rate 10°C/min, air flow 30cm^3 and resolution 0.5cm^{-1})

Different tests were carried on PAN in air to measure Root Mean Square noise values (RMS) (see Equation 2) from tests with different scanning times (5, 10, and 15) and resolutions (0.5 and 4.0 wavenumbers). RMS noise measurement is a statistical analysis of the noise variation and together with peak to peak noise is given in Table 8.

RMS values, similar to peak-to-peak noise are the highest when higher resolution settings are used (0.5 cm^{-1}). The RMS values decrease with the resolution decrease (4.0 cm^{-1}), resulting in an increase in the noise level which makes small absorptions more difficult to distinguish. A similar effect is observed for the number of scans where RMS values decrease with the higher scan number. Heating rate or mass does not seem to have any effect on the quality of the spectrum and noise values.

Table 8 Examples of RMS and peak-to-peak noise values for PAN tests

			RMS values x 10^{-3}				Peak to peak noise x 10^{-3}			
Heating Rate/ °C·min^{-1}	**Resolution/ cm^{-1}**	**Mass/ mg**	**Number of scans**				**Number of scans**			
			5	**10**	**15**	**20**	**5**	**10**	**15**	**20**
5	0.5	~15.00	4	3		2	27	17		10
10	0.5	~15.00	5	3	4	2	27	17	22	12
20	2.0	~15.00	1				4			
10	0.5	~10.00	4	3		2	23	15		11
20	0.5	~10.00	4	3		2	22	15		12
20	1.0	~10.00		2				7		
20	2.0	~10.00		1				4		
5	4.0	~10.00	1	1		0	0	2		2
10	4.0	~10.00	1	1		1	6	2		2
20	4.0	~10.00	1	1		1	3	2		3
20	4.0	~5.00	2				1			

2450-2500 cm^{-1} wavenumber region is used for all calculations.

4.3 Omnic Classification techniques

OMNIC gives the choice of using different searching algorithms and spectral regions to classify recorded signals. The FTIR spectra of PAN samples are compared with the library resources using five different algorithms such as: Absolute Difference, Squared Difference, Absolute Derivative, Squared Derivative, and Correlation. The above methods determine the minimum match value expressed in % for searching and displaying results (100% means perfect match). Omnic uses an evaluation algorithms that compare experimental and library reference spectra. The accuracy between spectra is called match value or just fitness, ξ. The improvement of fitness means a better fitting between experiments and reference data. Optimal testing methods are found with the maximisation of ξ.

A brief description of each classification algorithm is formulated to associate search method to quality of experimental data:

- Absolute Difference - this algorithm focuses on the small differences between the unknown spectrum and library spectra. This means that impurities will have a larger effect on the search results.

- Squared Difference - emphasizes the large peaks in the unknown spectrum. This algorithm is mainly used if a noisy spectrum is being identified.

- Absolute Derivative - gives small peaks and peak shifts an increased effect on the search results. The algorithm removes any differences between the unknown and library spectra caused by an offset in the unknown spectrum. This algorithm is useful when a user wants to emphasize peak positions rather than peak intensities.

- Squared Derivative - emphasizes large peaks as well as peak shape. The algorithm removes any differences between the unknown and library spectra caused by an offset in the unknown spectrum. This algorithm works well with spectra of poor quality.

- Correlation - normally gives the best results and is recommended for most applications. The algorithm removes any effect of offset in the unknown spectrum, thus eliminating the effects of baseline variation.[63]

The match values of the FTIR spectra of all PAN samples are shown in Table 9. The comparison was made in two spectral regions: 4000-400 cm^{-1} and 1000-900 cm^{-1}. Where region 4000-400 cm^{-1} gives overall information about the decomposition products and the spectral region 1000–900 cm^{-1} was chosen because in this area characteristic groups absorb and the 'fingerprint' region for ammonia is included. Consequently in this region any differences between the spectra can be detected.

Table 9 Results of different searching methods based on all tests performed. Presented match values expressed in % are related with ammonia spectrum from Vapour Phase Library

Sample name (heating -scanning-resolution)	Absolute Difference	Squared Difference	Absolute Derivative	Squared Derivative	Correlation in region 4000-400cm^{-1}	Correlation in region 1000-900cm^{-1}
PAN_5_5_05	16	23	57	62	66	89
PAN_5_10_05	-	11	50	55	44	90
PAN_5_20_05	16	23	57	62	48	90
PAN_10_5_05	13	21	54	59	57	**91**
PAN_10_10_05	13	20	56	61	62	**91**
PAN_10_20_05	15	25	56	63	68	90
PAN_20_5_05	7	8	53	53	36	89
PAN_20_10_05	10	15	54	58	55	90
PAN_20_20_05	3	2	51	51	18	89
PAN_5_5_4	-	-	52	51	16	85
PAN_5_10_4	-	-	52	51	18	88
PAN_5_20_4	-	-	52	51	16	87
PAN_10_5_4	-	3	53	54	40	89
PAN_10_10_4	-	-	53	53	32	89
PAN_10_20_4	6	7	55	60	60	89
PAN_20_5_4	-	-	52	51	19	87
PAN_20_10_4	8	10	55	57	52	90
PAN_20_20_4	10	17	56	62	65	90

The data in Table 9 show a summary of all the results of STA-FTIR comparison tests. It was determined that configurations giving the sharpest and strongest infrared signal during PAN pyrolysis are: 10°C/min heating rate, 5 or 10 scanning time and 0.5 cm^{-1} resolution. At the same set of data also indicate the best classification algorithm.

Different heating rates results are presented in Table 10.

Table 10 Comparison of six searching methods according to different heating rates. Results are filtered by heating rates and match values are averaged and expressed in terms of %

Heating rate/ $°C \cdot min^{-1}$	Absolute Difference	Squared Difference	Absolute Derivative	Squared Derivative	Correlation in region 4000-400cm^{-1}	Correlation in region 1000-900cm^{-1}
5	16	19	53	55	35	88
10	12	15	55	58	53	90
20	8	10	54	55	41	89

Although in real fires heating rates are much higher than 10°C/min, for TGA apparatuses this value seems to be optimal to keep the temperature uniform (no temperature gradient) inside the sample without heating the sample so slowly that ageing effects predominate. In such conditions samples are considered to be thermally thin. It is worth noting that heating rates of 5°C/min or lower could also affect the TGA's microbalance precision to detect mass loss correctly. However, slower heating helps to separate large numbers of chemical reactions occurring close to each other in time. This could potentially reduce the number of gas phase products in FTIR's gas cell making infrared signal less complex, hence easier to analyse, but lowering the concentration of individual species in the gas cell would also reduce the sensitivity.

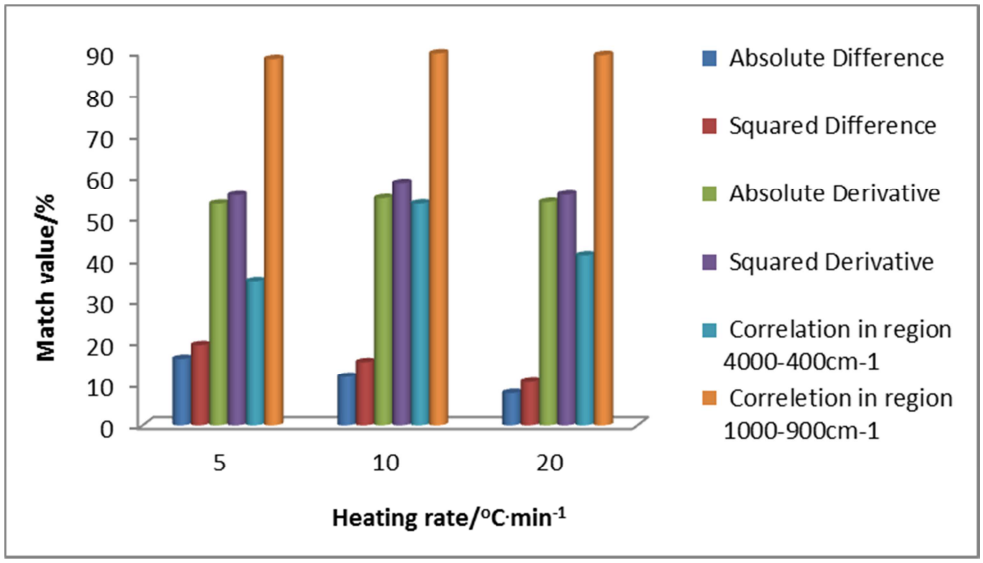

Figure 19 Evaluation of efficiency of each search algorithm according to heating rate (graphical summary of Table 10)

The best results (almost 90% matches) are obtained by the use of correlation algorithm in a specific region for all heating rates as presented in Figure 19. However when the region is not known and whole range is searched then it is preferable to use Squared Derivative or Absolute Derivative algorithms, with matching efficiency between 50-60%. Also the Correlation method could be still permissible but only for heating rate of 10°C/min. It is observed that the higher the heating rate, the less efficient Absolute Difference and Squared Difference methods are.

Table 11 shows how the algorithms are suited to variation in scanning time. To be more precise scanning time (or just scanning) is presented here as a number of scans used to produce a single spectrum therefore scanning does not have a unit. It is important to know that scanning time not only depends on the number of scans but also on the resolution used. The higher the resolution the longer the required scanning time for the same number of scans.

Table 11 Comparison of six searching methods according to different scanning time. Results are filtered by scanning time and match values are averaged and expressed in terms of %

Scanning	Absolute Difference	Squared Difference	Absolute Derivative	Squared Derivative	Correlation in region 4000-400cm^{-1}	Correlation in region 1000-900cm^{-1}
5	12	14	54	55	39	88
10	10	14	53	56	44	89
20	10	15	55	58	46	89

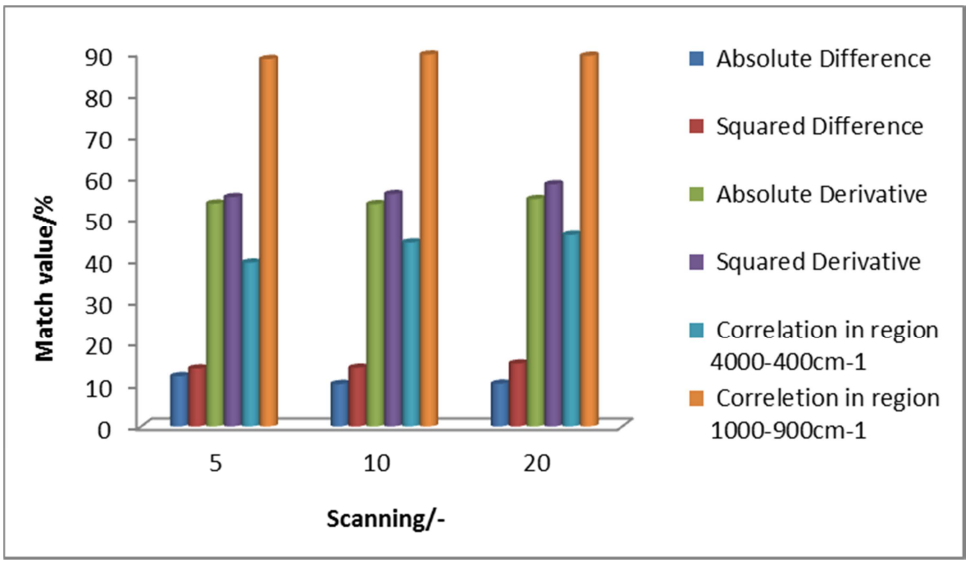

Figure 20 Evaluation of efficiency of each search algorithm according to scanning time (graphical summary of Table 11)

When the scanning time varies, the Correlation algorithm in specific search region is the best match. The sensitivity of algorithms according to scanning time is not significant; however the efficiency of the Squared Derivative (which is ranked as a second choice method) grows with increasing scanning time.

Table 12 presents which algorithm gives the best results when resolution is changed.

Table 12 Comparison of six searching methods according to different resolutions performed by average match values

Resolution	Absolute Difference	Squared Difference	Absolute Derivative	Squared Derivative	Correlation in region 4000-400cm^{-1}	Correlation in region 1000-900cm^{-1}
0.5	12	16	54	58	51	90
4	8	9	53	54	36	88

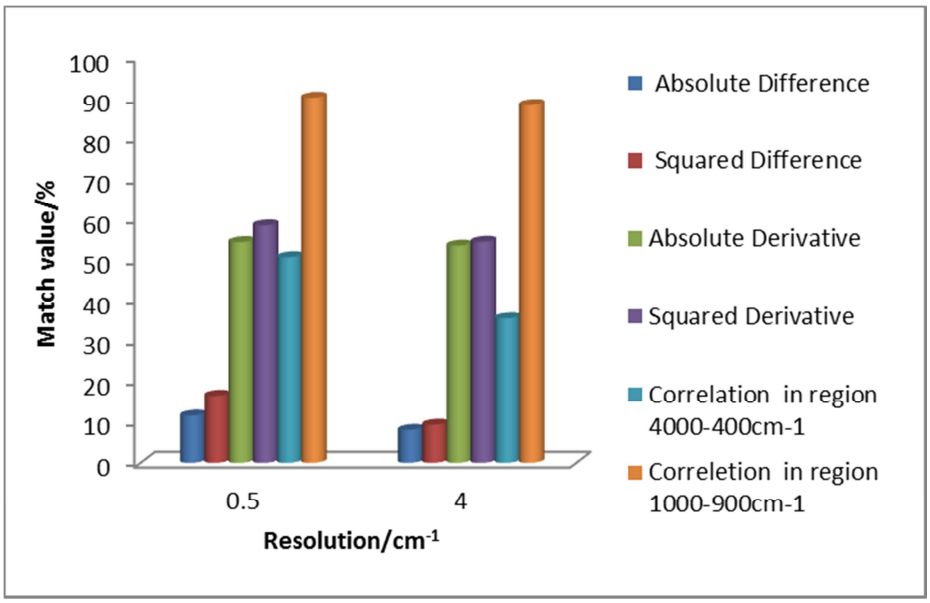

Figure 21 Evaluation of efficiency of each search algorithm according to resolution (graphical summary of Table 12)

Again, in this case the specific region is crucial for the Correlation algorithm efficiency, which is the best choice when the resolution is changed. Also the Squared Derivative and Absolute Derivative techniques are acceptable. The Correlation method in whole range gives satisfactory results, but only for the resolution 0.5 cm^{-1}. It is observed that all algorithms are sensitive to resolution change – the performance is decreased with the lower resolution.

4.3.1 Summary of classification techniques

The five different algorithms, provided by Omnic software, such as: Absolute Difference, Squared Difference, Absolute Derivative, Squared Derivative, and Correlation were used to perform recognition tests on 18 PAN samples with different STA-FTIR test configurations. Every time spectrum with the presence of ammonia peaks was chosen to test all 5 algorithms to establish its efficiency. At the same time, the most optimal STA-FTIR

configuration settings were identified from the "best searching" results. The best searching algorithm, in this type of comparison, was the method based on correlation, but used together with a narrowed searching region. As the most optimal STA-FTIR setting configuration, from the perspective of the most efficient searching algorithm (and probably the strongest FTIR signal) was: 10 scans, 5 or 10°C/min heating rate and resolution 0.5 cm^{-1}.

4.4 TGA Optimisation parameters

Decomposition processes are often highly dependent on the conditions, particularly the atmosphere. The sensitivity of changes under different conditions (e.g. air, nitrogen or oxygen), heating rate or sample shape and size, can help to identify the processes occurring. Moreover, sensitivity to these parameters gives away vital clues needed to interpret the fire behaviour[74]. Thermogravimetry is a technique in which the mass of a test specimen is measured as a function of temperature or time, while the test specimen is subjected to a controlled temperature program. It is used to determine the temperature and rate of decomposition of polymers, and to identify the steps involved. In addition, coupled with suitable analytical equipment, it can be used to identify and quantify the amounts of volatile matter in real time during the heating process[74].

4.4.1 Heating rate

Figure 22 presents the difference between mass loss curves of PAN measured in TGA and Gram-Schmidt Intensity from FTIR instrument. Samples were tested at three different heating rates: 5˚C/min, 10˚C/min and 20˚C/min. The first rapid mass loss increases with increase in heating rate from 5˚C/min to 20˚C/min. This is confirmed by FTIR curves where the slower heating rate will produce less decomposition products within a longer time period. However, it is well known that heating rates affect the decomposition chemistry, and therefore it is not appropriate to change the heating rate merely to get data with better resolution.

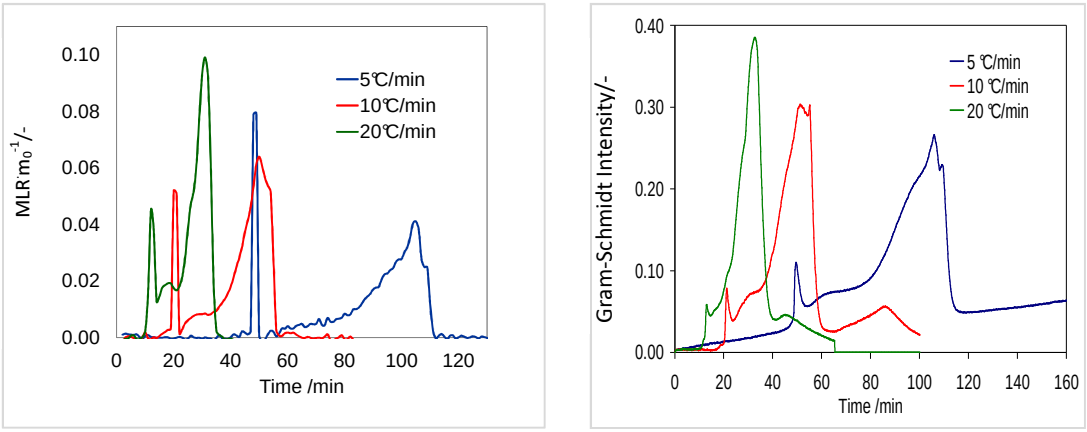

(a) (b)

Figure 22 TGA (a) and FTIR (b) curves of PAN samples with different heating rates

FTIR spectra comparison with TGA heating rates: 5˚C, 10˚C and 20˚C. TGA mass loss rate (MLR) is normalised by initial sample mass (m_0). Wavenumber region of 1200-900 cm^{-1} is used for the comparisons. This region is characteristic for ammonia peaks presence.

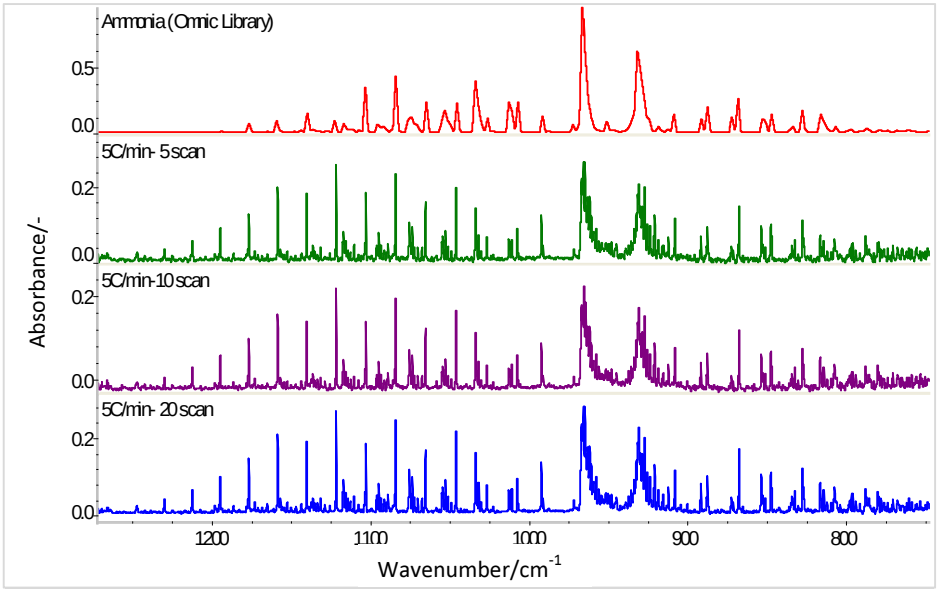

Figure 23 PAN spectra in region characteristic for ammonia presence. Spectra collected while PAN samples were pyrolysed with different heating rates (5, 10, 20°C/min) resolution 0.5 cm^{-1}

There is no observed difference in quantity of spectra for different heating rates. However, as explained above, heating rate will affect the intensities and time of products generation.

4.4.2 Sample Initial Mass

Another factor which will affect the spectrum quality next to heating rate is initial mass placed in a TGA crucible. An example is given below where three different masses were used and compared in Figure 24.

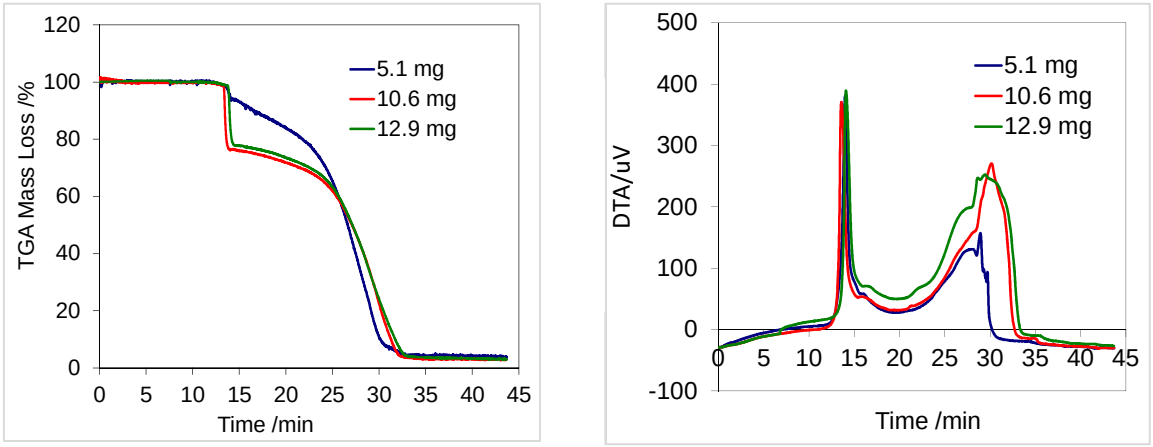

(a) (b)

Figure 24 TGA-DTA curves for PAN at 20˚C/min and different masses

Looking at TGA–DTA data different masses will affect decomposition processes, lower masses will have much shorter time for forming volatiles in the lower range of temperatures (first decomposition stage) and higher masses will not only have higher DTA peaks, but also much higher mass losses over the range 200 - 400˚C and much broader second peaks at 550-650˚C resulting from CO_2 production.

Comparing TGA-DTA data with FTIR Gram-Schmidt intensities very similar conclusions can be drawn. For test carried out with 5.1 mg it is much harder to see the first decomposition stage occurring around 10-15 min compared to higher masses used in this study. Increasing masses to 15 mg, bigger differences are observed for two decomposition stages as well as much broader Gram-Schmidt peaks for this stage which are slightly shifted to higher temperatures (longer time).

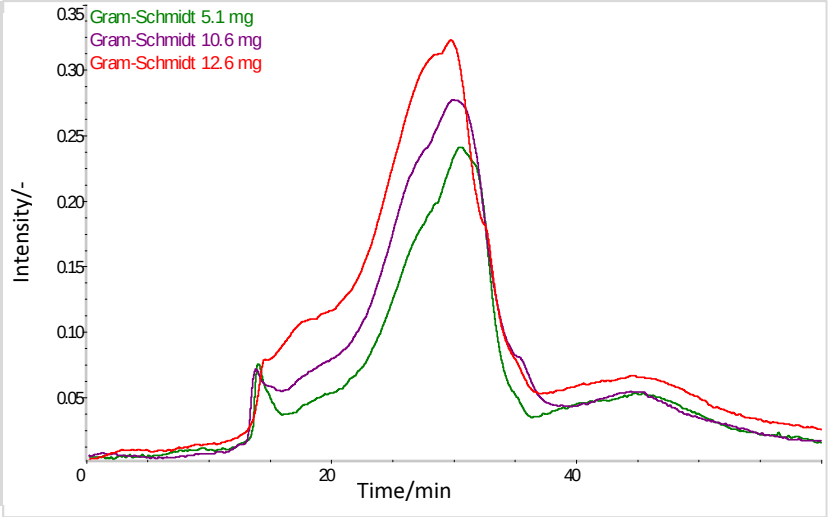

Figure 25 TGA curves of PAN samples with different mass

The influence of different sample masses on FTIR intensities of different products is presented in Figure 25 and Figure 26. It is seen that sample masses have an effect on the intensity, and higher masses will lead to higher absorbances (concentrations) recorded on spectrum. It is worth noting that 5 mg sample masses will increase difficulties for qualitative analysis as the absorbances may not be above the noise level, so it may be difficult to recognise and associate species to a corresponding calibration spectrum. An example is shown, in Figure 27, for the low intensity of the ammonia peak (at 993cm^{-1}) which is absent at 2982 or 1902 cm^{-1} where the differences within different masses are clearly observed. These differences may vary for different samples and STA-FTIR settings: mass, heating rate, resolution are probably the most important factors driving good quality analytical data.

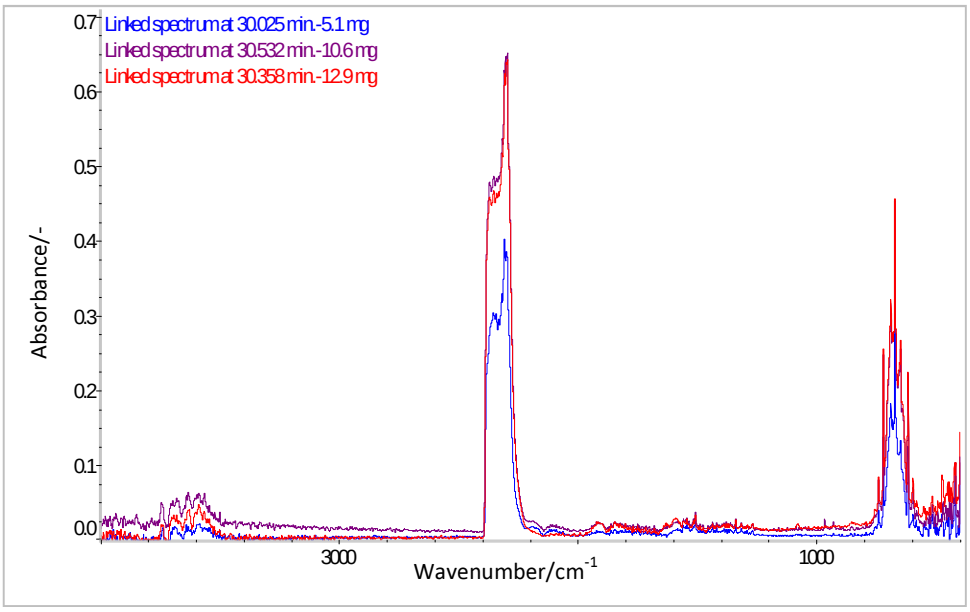

Figure 26 Different mass influence on the major FTIR absorbance peaks

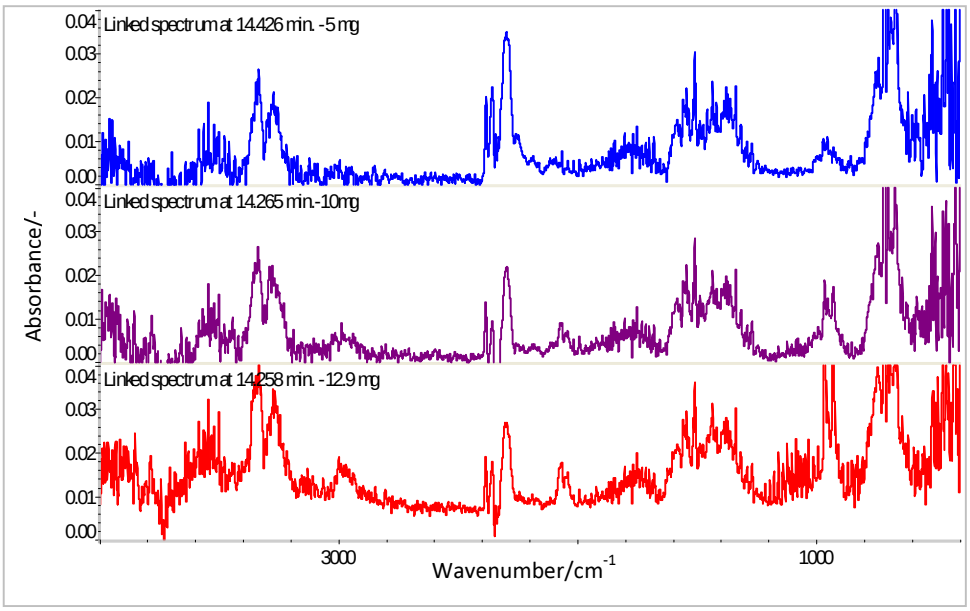

Figure 27 Mass influence on the minor FTIR absorbance peaks

4.5 STA-FTIR Response Time

STA results are presented in terms of temperature dependence. Therefore, in order to provide STA-FTIR results, it was necessary to estimate the transport time between evolution of gases in the STA and detection in the FTIR instrument, so FTIR results can be deconvoluted from time to temperature units. Figure 28 presents the first PAN decomposition peak for STA (represented by DTA) and FTIR first peak on Gram-Schmidt reconstruction curve. Typically, for this type of comparison MLR curves would be used instead of DTA. However for this data, for the simple reason of the better quality of data, DTA curves were used to identify the time of peak decomposition. The noise in MLR curves occurred following numerical differentiation of the mass loss, but it was confirmed that MLR and DTA correspond to each other for these reactions.

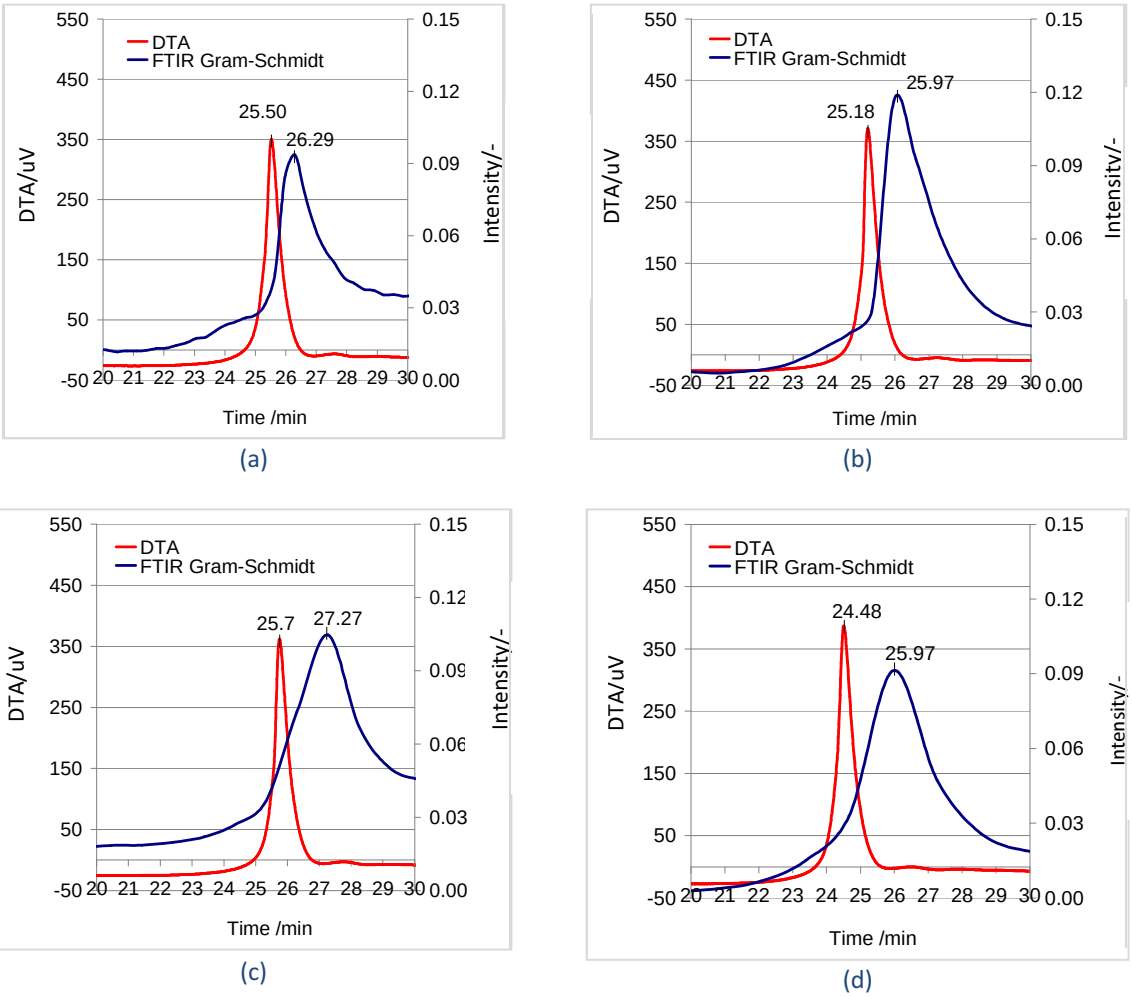

Figure 28 DTA and Gram-Schmidt Responses time for FTIR (a) 5 scans (b) 10 scans (c) 15 scans and (d) 20 scans

The STA-FTIR response time was compared for the same sample masses (~15mg) with air flow 30cm^3, and 10°C·min^{-1} and FTIR resolution 5cm^{-1} for different scanning time: 5, 10, 15 and 20 (Table 7). It can be seen that there is no significant difference in delay time between 5 and 10 scans and 15 and 20 scans. The FTIR response time is 1 min and 29sec and 1 min 31sec, for 5 and 10 scans respectively. The delay time is almost half when the scan number is increased to 15 and 20 scans, when FTIR response time is only 47 seconds after TGA.

Another comparison was made with air flow change from 30 to 50 cm3/min, Figure 29. All the other parameters were the same and for FTIR: 10 scans, 4cm^{-1} resolution was selected, for TGA: ~10mg sample, 20°C/min heating rate was chosen.

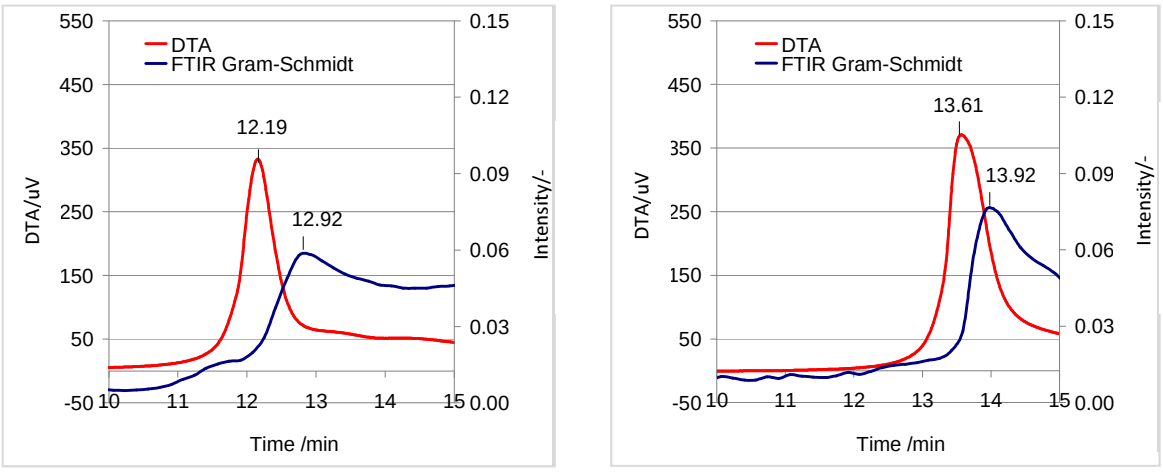

Figure 29 DTA and Gram-Schmidt Responses time for air flow a) 30 cm^3/min and a) 50 cm^3/min

Increasing TGA gas flow rate has an effect on the response time between TGA and FTIR instruments. Having the same FTIR parameters, it can be observed that increasing the flow from 30 to 50 cm^3 decreases the response time from 44 to 18 seconds in FTIR instrument. The signal to noise ratio for different spectra at different times was checked for different gas flow rates, and is summarised below. It is difficult to estimate the noise ratio at higher or lower flows and no clear correlation between scanning time and gas flow rates for the signal to noise ratio was observed.

Table 13 Signal to noise ratio or different air flow rates and scanning time

Scanning Rate	Air Flow Rate/ $cm^3 \cdot min^{-1}$	Signal to noise ratio x 10^{-3}	
		Spectrum at 13th min	Spectrum at 30th min
5 scans	30	2.872	1.855
	50	2.103	2.460
10 scans	30	2.378	1.855
	50	1.888	2.084

It is important to remember that for any testing and comparison purposes each parameter should be checked at once, while the other factors should stay the same in all STA and FTIR experiments.

4.6 Summary of STA-FTIR Investigation

Many different factors have influence on the quality of FTIR spectra. It was found that from all selected resolutions (4, 2, 1, and 0.5 wavenumbers respectively) the best results are seen for 0.5 and 1 cm^{-1}. Additionally, it should be pointed out that the higher resolution settings it is visually easier to see the changes in the spectra and different pyrolysates (at different times). Higher resolutions decrease the sensitivity by decreasing the signal-to-noise ratio and thus increase the minimum detection limits, which makes small absorptions more difficult to distinguish. Also, it will increase the selectivity and discrimination between different gases. A similar effect is observed for the number of scans where the RMS value decreases with the higher number of scans. Heating rates and sample masses do not seem to have significant effect on the quality of the spectra and noise levels. However, it is recommended to keep sample mass around 10 mg and use heating rate $10°C \cdot min^{-1}$. In terms of interpretation, FTIR technique and analysis provides very useful sets of data, however obscuration of absorbance of one species by another in the spectrum, or water, are the main issues which increase a problem with FTIR analysis. Water is a very strong absorber of infra-red radiation over a wide range of frequencies and obscures many other species increasing the detection limit and increasing the noise of the compounds that overlap with water.

In terms of TGA optimisation, it was found that higher masses of samples increase FTIR absorbances and therefore makes easier to interpret FTIR peaks. Similarly decreasing flow rate of air or nitrogen makes easier interpretation. In terms of quality of spectra, heating rates do not affect results. It was found that it is better in terms of FTIR interpretation to use 15mg mass and 30cm^3 flow rate.

5 NUMERICAL MODELLING OF COMPOSITE DECOMPOSITION

5.1 Introduction to ThermaKin

A substantial number of studies[1,75,76,77,78,79] have demonstrated that numerical pyrolysis modelling (using e.g. Gpyro[80], the general pyrolysis model of FDS[81] or ThermaKin[2]) can describe degradation of solid materials exposed to external heat flux and determine the relationships between the fundamental physical and chemical properties of polymeric materials and their gasification behaviour. Most of the models calculate the mass loss rate of a sample exposed to heat source in one-dimension. ThermaKin has been used in this work for the prediction of the results of micro-scale and bench-scale fire experiments[2,82,83,84]. The model combines the transport of thermal energy with Arrhenius kinetics for the decomposition of the polymer and predicts the overall behaviour of a pyrolysing object by solving a set of mass and energy conservation equations:

Conservation of condensed-phase mass:

$$\frac{\partial \xi_i}{\partial t} = \sum_{1}^{N_r} \theta_r r_r$$

Equation 3

Conservation of gas-phase mass:

$$\frac{\partial \xi_g}{\partial t} = -\frac{\partial J_g}{\partial z} + \sum_{1}^{N_r} \theta_r^g r_r$$

Equation 4

Conservation of condensed-phase energy:

$$\sum_{i}^{N} \xi_i c_{p_i} \frac{\partial T}{\partial t} = -\frac{\partial \dot{q}''_{cond}}{\partial z} + \sum_{1}^{N_r} r_r h_r + \alpha_M I \left(1 - \frac{\sigma_S T^4}{I_s}\right) - \sum_{g}^{N_g} J_g \frac{\partial}{\partial z}\left(\int_0^T c_{p_g} dT\right)$$

Equation 5

Where

$\dot{q}''_{cond} = -\frac{\partial}{\partial z}\left(k_M \frac{\partial T}{\partial z}\right)$ is the conduction heat flux calculated using mixture conductivity k_M;

$J_g = -\frac{\partial}{\partial z}\left(D_M \frac{\partial \xi_g}{\partial z}\right)$ is the species-mass flux with mixture diffusivity D_M;

$r_r = \xi_r k'$ is the reaction rate with the Arrhenius rate coefficient, $k' = A\ exp(-E_a/RT)$.

ξ, c_p, T are the concentration, heat capacity and temperature;

θ and h are the stoichiometric coefficient and heat of reaction, respectively;

α_M and σ_S are the mixture radiation absorption coefficient and Stefan-Boltzmann constant;

I_s and I are the external heat flux and the radiation flux inside the material computed using Beer-Lambert law[85].

These equations are formulated in terms of rectangular finite elements. Each element is characterised by component mass and temperature. The model describes the transport of gases through the condensed phase and tracks changes in the volume of the bulk material. The level of complexity of the model can be modified by introducing or removing chemical reactions and material components. Each component is characterized by temperature-dependent physical and chemical properties, such as density, heat capacity, thermal conductivity, emissivity and absorption coefficient. The processes modelled by ThermaKin are presented in Figure 30. Absorption of radiant perpendicular heat produced by the cone calorimeter can be simulated, emission and reflect. In this way, condensed phase heat transfer processes are modelled through the solid. As a result of the temperature increase, the endothermic or exothermic decomposition processes lead to the gasification of volatile fuel components. Ignition occurs when a critical mass flux to the vapour phase is reached, where upon the incident heat flux is added to by the radiation produced by the flame. Therefore, quasi-steady state conditions pertain, until the sample is so thin that it has no more capacity to absorb heat, and the rate of pyrolysis increases.

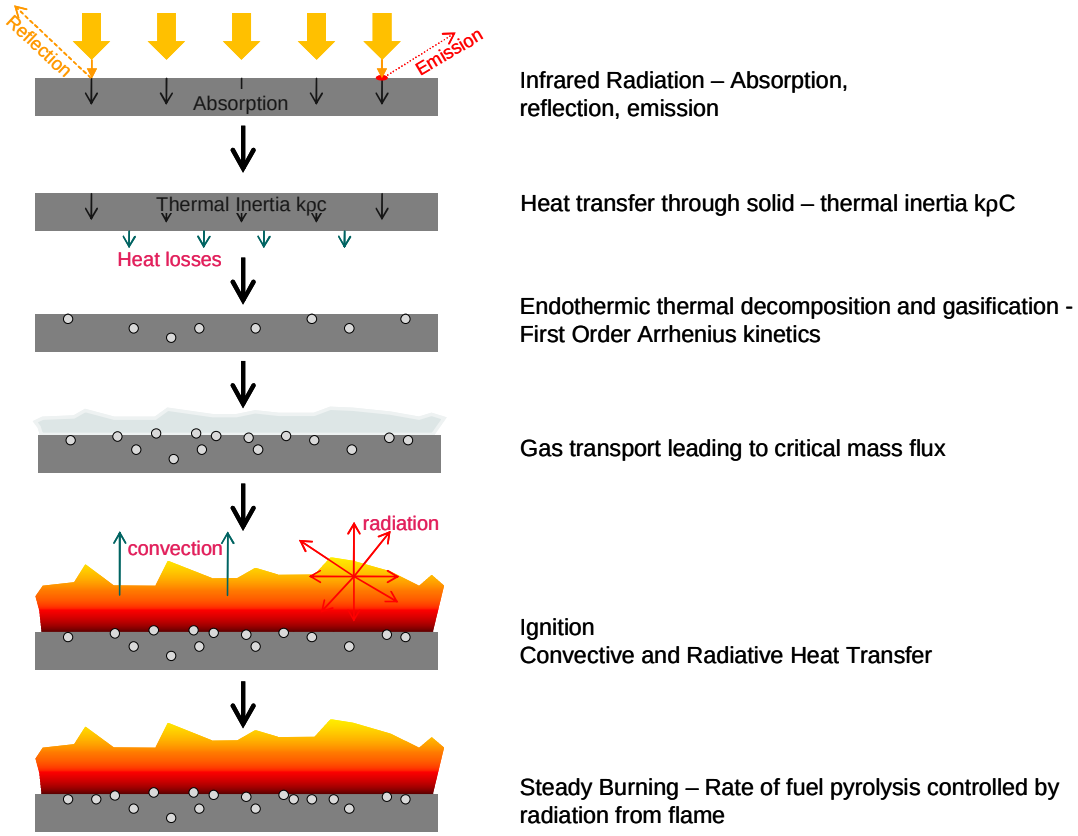

Figure 30 ThermaKin schematic model of the processes occurring in the cone calorimeter

The outputs of the ThermaKin model show the concentration of each component distributed in each ”layer” of material and the mass of the sample as a function of time. Mass loss rate curve can be obtained by numerical differentiation of mass. MLR multiplied by the appropriate heat of combustion of the material being studied can be used to predict its heat release rate.

5.2 Sensitivity Analysis of ThermaKin

In order to introduce the key parameters driving the ThermaKin model, the following parametric study, which was undertaken as part of this project is described. The sensitivity analysis was performed on ThermaKin, which was employed to calculate the rate of burning (expressed in terms of mass loss) of a one-dimensional material object exposed to steady radiative heat. The sensitivity of the burning rate to variations (±5%) in physical and chemical properties of PEEK polymer has been examined in order to understand the relative importance of these properties. The results of the calculations indicate that the values of decomposition

reaction parameters (including the Arrhenius pre-exponential factor, activation energy, heat, (Table 14) are of key importance for prediction of the peak and average burning rates[84].

The purpose of this analysis was to understand the input parameters of a computational tool capable of modelling pyrolysis and combustion of a wide range of materials including composites.

5.2.1 Model Setup

For input, ThermaKin requires thermal, optical, and chemical properties of the material. For this analysis values of PEEK properties determined by Lyon et al. were used as indicated in Table 14.

The energy and mass conservation equations, which form the foundation of ThermaKin, were solved numerically by subdividing the object into 5×10^{-5}m thick elements and using 5×10^{-3}s time steps. Mass loss rate (MLR) curves were obtained by numerical differentiation of the sample mass output by the model in time. A detailed description of the solution methodology implemented in ThermaKin can be found elsewhere[2,86].

Table 14 List of factors and values used for sensitivity analysis

Factors Tested	Abbrv.	Standard PEEK value[a]	Value increased by 5%	Value decreased by 5%
Thickness of PEEK/(m)	τ	0.0025	0.002625	0.002375
Gas component flow (PEEK_g Lin)/(kg/s)	GCF_{Lin}	0.05	0.0525	0.0475
Convective heat transfer coefficient (Convection coeff)/(W/m^{2}K)	ν	10	10.5	9.5
Initial flux (Time prog 1)/(W/m^2)	f_i	5.00E+04	5.25E+04	4.75E+04
Critical mass flux MLR for gas(PEEK_g)/ (kg/m^{2}s)	ξ_g	5.00E-05	5.25E-05	4.75E-05
Radiation/(kW/m^2)	R	1.50E+04	1.58E+04	1.43E+04
Density (PEEK solid)/(kg/m^3)	ρ_s	1300	1365	1235
Heat capacity (PEEK solid)/(J/kgK)	c_s	2160	2268	2052
Conductivity (PEEK solid)/(W/mK)	κ_s	0.25	0.26	0.24
Transport (PEEK solid, internal mass transport, diffusivity)/(m^2/s)	D_s	2.00E-05	2.10E-05	1.90E-05
Emissivity (PEEK solid, dimensionless)	ε_s	0.9	0.945	0.855
Absorption (PEEK solid)/(m^2/kg)	α_s	2.5	2.625	2.375
Density (PEEK Char)/(kg/m^3)	ρ_{ch}	650	682.5	617.5
Heat capacity (PEEK char)/(J/kgK)	c_{ch}	1720	1806	1634
Conductivity (PEEK char)/(W/mK)	κ_{ch}	1.50E-09	1.575E-09	1.425E-09
Transport (PEEK char, Internal mass transport, diffusivity)/(m^2/s)	D_{ch}	2.00E-05	2.10E-05	1.90E-05
Emissivity (PEEK char, dimensionless)	ε_{ch}	0.9	0.945	0.855
Absorption (PEEK char)/(m^2/kg)	α_{ch}	100	105	95
Density (PEEK gas)/(kg/m^3)	ρ_g	1180	1239	1121
Heat capacity (PEEK gas)/(J/kgK)	c_g	1000	1050	950
Conductivity (PEEK gas)/(W/mK)	κ_g	0.22	0.231	0.209
Transport (PEEK gas, Internal mass transport)/ (m^2/s)	D_g	2.00E-05	2.10E-05	1.90E-05
Emissivity (PEEK gas, dimensionless)	ε_g	0.9	0.945	0.855
Absorption (PEEK gas)/(m^2/kg)	α_g	2.5	2.625	2.375
Parall conductivity (fraction of parallel conductivity)	κ_{par}	0.5	0.525	0.475
Parall transport (fraction of parallel transport)	T_{par}	0.5	0.525	0.475
Arrhenius pre-exponential factor, A/(m^3/kgs)	A	1.00E+24	1.05E+24	9.5E+23
Arrhenius activation energy, E_a/(J/mole)	E_a	4.23E+05	4.44E+05	4.02E+05
Heat produced by reaction/(J/kg)	h_r	-8.30E+05	-8.72E+05	-7.89E+05

[a] Supplied by R. E. Lyon et. al. in private communication October 2010

5.2.2 Results and discussion

The simulations were performed using 29 sets of conditions whose values were increased and decreased separately by 5%. Each MLR history obtained from the simulations was characterized by four fire response parameters: time to mass loss (t-ML), peak mass loss rate (pMLR), time to peak mass loss rate (t-pMLR), and average mass loss rate (avgMLR). The t-ML was defined as the time when MLR exceeds the threshold of 1×10^{-3} kgm^{-2} s^{-1} for the first time. This value of the threshold corresponds to the onset of piloted ignition for combustible polymers under mild convective conditions[87]. The pMLR was presented as the maximum value of MLR. The t-pMLR was taken to be the time to pMLR. The avgMLR was calculated as a sum of MLR from t-ML to the time of the end of mass loss and subsequent division this value by the length of the time period used in the sum. The time of the end of mass loss was defined as the time of the final drop of MLR below 1×10^{-3} kgm^{-2} s^{-1}.

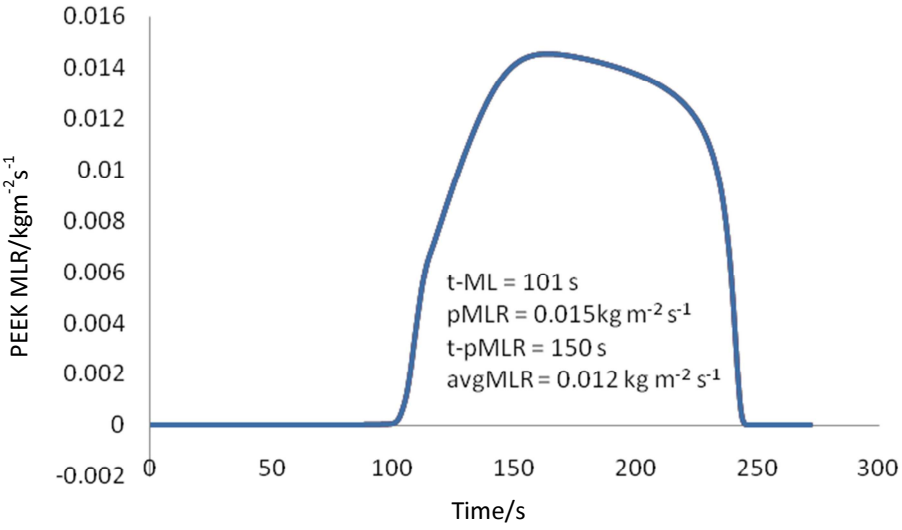

Figure 31 Simulation of burning PEEK sample

First, avg-MLR histories of the PEEK polymer were calculated. Subsequently, all 29 properties were increased and decreased by 5% of their original values so 58 simulations were performed. 7 sets of properties affected the avg-MLR significantly, which are shown in Figure 32. Activation energy (E_a) caused the biggest changes - more than 17%, next was initial flux (f_i) with more than 5% change, another 5 factors varied the property from 1% to 5%. For pMLR, the changes are shown in Figure 33, the situation is similar. The value of E_a, f_i, h_r, R, ε_{ch}, τ is very important for predicting this parameter; small changes in the value of the other parameters

have little or no effect. Figure 34 presents t-ML changes and contains the biggest number of factors. For t-pMLR, the changes are shown in Figure 35, and the knowledge of 7 properties is important.

The effects of variation of the rest of the properties were examined in the same manner, but less than 1% change was observed.

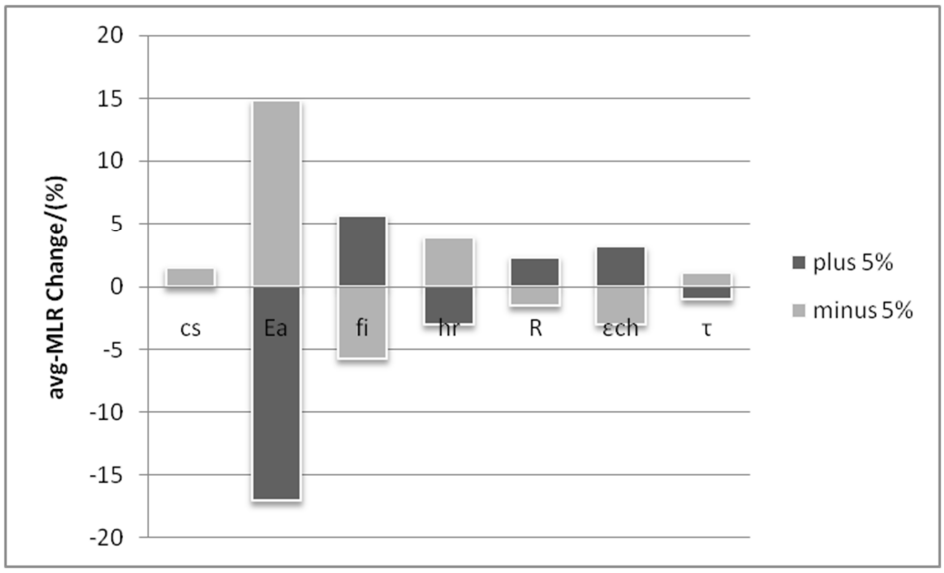

Figure 32 Effects of 5% increase/decrease of PEEK properties on avg-MLR

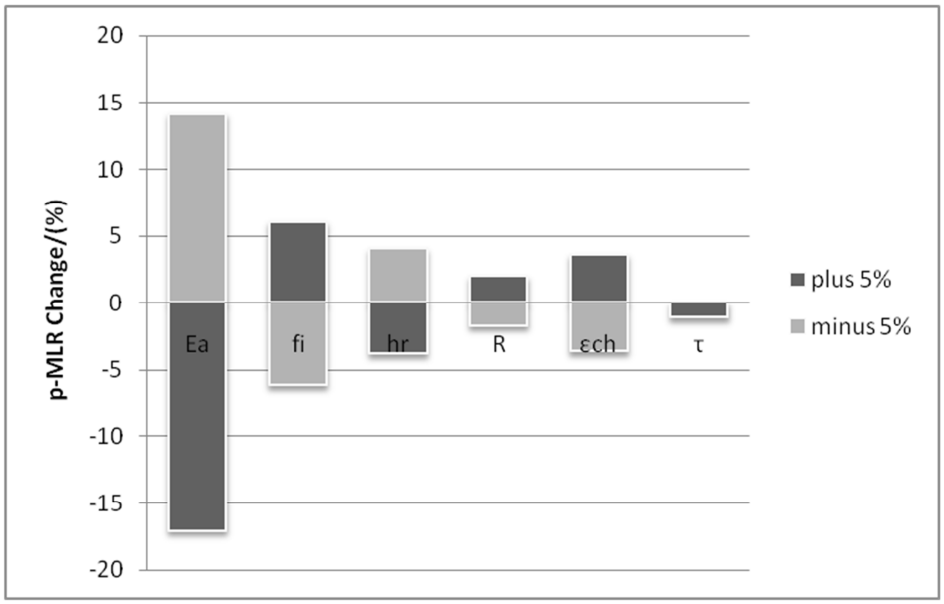

Figure 33 Effects of 5% increase/decrease of PEEK properties on p-MLR

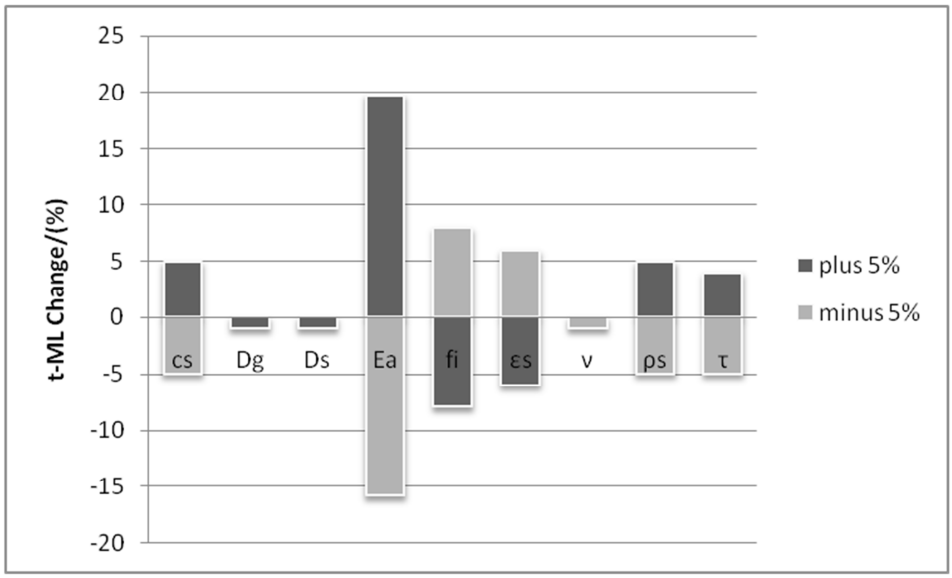

Figure 34 Effects of 5% increase/decrease of PEEK properties on t-ML

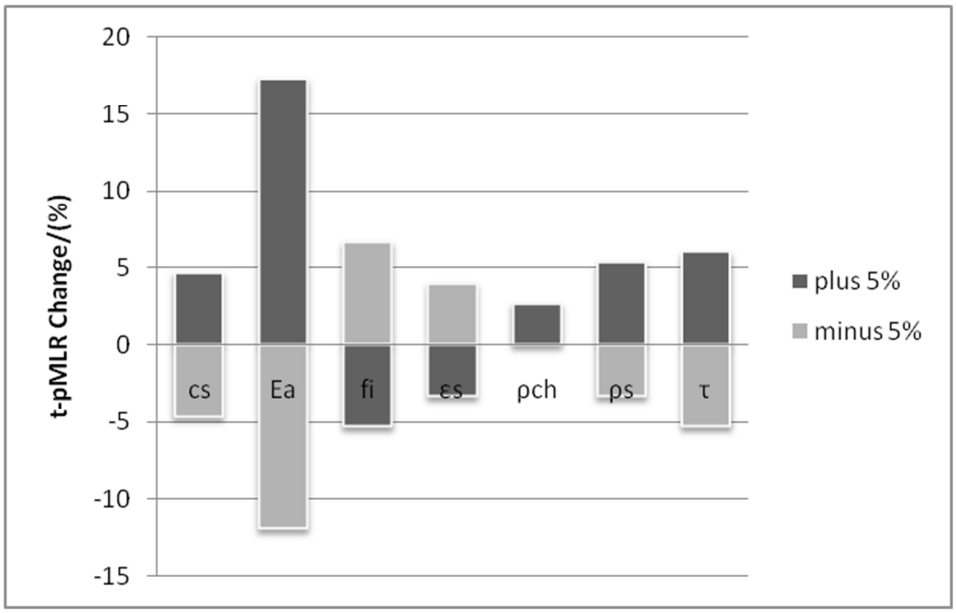

Figure 35 Effects of 5% increase/decrease of PEEK properties on t-pMLR

5.2.3 Influence of Physical Properties on PEEK decomposition and burning behaviour

The physical properties input into the ThermaKin model which will be described first are density (ρ), thermal conductivity (k) and heat capacity (c) where the product of these three parameters is called thermal inertia. For thermally thick solids with thicknesses above 15 mm[88] the thermal inertia has a significant impact on material's surface temperature and time to

ignition and flame spread properties. The time to ignition (t_{ig}) of a thermally thick solid exposed to an external heat flux ($\dot{Q}_{\acute{R}}{}^2$) is presented in Equation 6[89].

$$t_{ig} = \frac{\pi}{4} k\rho c \frac{\left(T_{ig} - T_0\right)^2}{\dot{Q}_{\acute{R}}{}^2}$$

Equation 6

where T_{ig} and T_0 are the ignition and ambient temperatures, respectively. The time to ignition of a thermally thin material exposed to perpendicular heat flux can be found in Equation 7.

$$t_{ig} = \rho c\tau \frac{\left(T_{ig} - T_0\right)^2}{\dot{Q}_{\acute{R}}}$$

Equation 7

Where τ refers to sample thickness.

The above models of time to ignition are based on the simple assumption that the parameters are described by constant values rather than by temperature dependent functions and any heat losses are completely ignored.

Study of a range of common polymers demonstrated that the thermal decomposition temperature or peak pyrolysis temperature (T_p), has influence on ignition and burning[90] and is the temperature at the maximum specific heat release rate, as indicated by the Pyrolysis Combustion Flow Calorimeter (PCFC)[32].

The ThermaKin input requires the volume and density to be defined, from which mass of the sample is calculated. The lower the density the higher the surface temperature and the faster the critical pyrolysis flux is reached, but also larger the thermal gradient through its bulk, and therefore more heat is required for the rest of the sample to reach the pyrolysis temperature. This is confirmed by the longer time to reach the peak heat release rate than for the higher density polymer. The effects of 5% change of density (ρ) of solid PEEK and PEEK char causes approximately 5% change of t-ML and t-pMLR (Figure 34 and Figure 35).

The effect of changing thermal conductivities by 5% in this model does not affect the results significantly, so these properties can be assigned to their average values without a significant loss of accuracy. Thermal conductivity reflects the ability to conduct heat and transfer energy through a material where a temperature difference exists. In lower thermal conductivity materials heat is concentrated more at the surface and therefore the ignition occurs earlier.

When thermal conductivity is high, heat is dispersed through the bulk so ignition will be delayed but the concentration of heat within the system will accelerate the burning rate. A material with a low thermal conductivity is more likely to show thermally thick burning behaviour. Similarly, a material with a greater thermal conductivity is more likely to show thermally thin burning. As a result, this gives a longer t-pMLR as each layer ignites and burns as a separate entity.

The effect of heat capacity on Figure 34 shows strong influence on t-ML, and Figure 35 on t-pMLR. The heat capacity of a material refers to the amount of energy required to raise the temperature of the bulk by 1°C. A lower heat capacity indicates that less energy is required to raise the temperature of the surface to ignition temperature. A low heat capacity material will have a low thermal inertia (*kpc*) and hence the upper layers will reach the critical surface temperature for ignition more quickly than a material with higher heat capacity (or greater thermal inertia). At a constant external heat flux, this is governed by the time of exposure, which is balanced by the energy required for gasification (the heat of decomposition). The peak heat release rate and the time of test remain constant[91].

5.2.3.1 Radiation

According to Stefan-Boltzmann equation, the total energy emitted by a body is proportional to T^4, where T is temperature in Kelvin: the total emissive power is

$$\mathbf{E} = \boldsymbol{\varepsilon\sigma T^4} \quad [\mathbf{W/m^2}]$$

Equation 8

where σ is the Stefan-Boltzmann constant (5.67×10^{-8} W/m^2K^4) and ε is a measure of the efficiency of the surface as radiator, known as the emissivity. The perfect emitter – the 'black body' – has an emissivity of unity. The intensity of radiant energy (q") falling on a surface remote from the emitter can be found by using the appropriate 'configuration factor' ϕ which takes into account the geometrical relationship between the emitter and the receiver.

$$(\dot{\boldsymbol{q}}'') = \boldsymbol{\phi\varepsilon\sigma T^4}$$

Equation 9

This shows that the PEEK ThermaKin simulation is not significantly sensitive to radiation - only p-MLR and avg-MLR show slight changes. Such behaviour can be explained by the low

initial temperature used in this experiment which is 300˚C. Studies show that above around 400˚C radiation becomes increasingly dominant[89].

5.2.3.2 Diffusivity – internal mass transport in solids D_s, char D_{ch} and gas D_g.

Diffusivity or diffusion coefficient is proportionality constant between the molar flux due to molecular diffusion and the gradient in the concentration of the species (or the driving force for diffusion). Diffusivity is encountered in Fick's law and numerous other equations of physical chemistry.

It is generally prescribed for a given pair of species. For a multi-component system, it is prescribed for each pair of species in the system.

The higher the diffusivity (of one substance with respect to another), the faster they diffuse into each other.

Internal mass transport of solids and gas are noticed by the analysis of t-ML (Figure 34). The higher the diffusivity the faster mass loss is observed, however a lower level of diffusivity does not change t-ML.

5.2.3.3 Convection coefficient (v)

As indicated in Equation 10, convective heat transfer (convection) is that mode of heat transfer to or from a solid by movement of a surrounding fluid. The empirical relationship first discussed by Newton is:

$$\dot{q}'' = v\Delta T \ [W/m^2]$$

Equation 10

where v is known as the convective heat transfer coefficient. This equation defines v which, unlike thermal conductivity, is not a material constant. It depends on the characteristics of the system, the geometry of the solid and the properties of the fluid including the flow parameters, and is also a function ΔT. The evaluation of v for different situations has been one of the major problems in heat transfer and fluid dynamics. Typical values lay in the range 5-25 W/m^2K for free convection and 10-500 W/m^2K for forced convection in air[89].

As seen in Table 14, the value of v used for PEEK is 10 W/m^{2}K around the lower limit for forced convection in air. This value seems to be critical for the ThermaKin model because a slight decrease of this value affects t-ML when the same amount of increase does not affect any of the observed properties.

5.2.3.4 Initial flux

Initial flux (kJ/m^3) is important factor directing thermal decomposition of polymers. In other words the amount of heat delivered to sample (or more simply – temperature) has huge impact on its fire behaviour. Temperature dependence is present in most if not all of fire dynamics equations. While analysing 'behaviour' of ThermaKin it is not surprising that higher/lower values of f_i are increasing/decreasing the values of all four observed factors, however t-ML seems to be the most affected.

5.2.3.5 Critical mass flux MLR for Gas (ξ_g) in modelling polymer combustion

Thermally thin samples

The idea of modelling ignition and extinction of a flame by a critical mass flux is supported by experimental and theoretical studies. This hypothesis has been used as a modelling approach of flammability of thermally thin polymers[92,93,94,95,96,97]. Nelson et al have used the critical mass flux assumption to study the flammability of thermoplastics and to model the efficiency of solid-phase active fire-retardants by assuming that the incorporation of the additive leaves the criticality state unaffected. In these publications and also in ThermaKin the dynamics of the flame are not modelled, the critical mass flux is used to turn a flame on and off.

Thermally non-thin samples

Thermally non-thin materials were modelled by Staggs and Nelson[98]. Presented results quantify the effect of the thickness of the sample on the mass-loss rate curve. The authors concluded that thermally thick materials are categorized by an area of steady burning which does not rely on the initial sample thickness.

5.2.3.6 Thickness

Thickness of sample is a significant factor in fire modelling. It is strictly connected with heat transfer, conduction and overall fire behaviour. The relationship between heating time and thickness and also the temperature profiles below the surface of a slab of thickness τ, heated instantaneously on one face, until the rear face becomes heated to a temperature significantly above ambient (T_0), can be defined by equation (Welty et al., 1976):

$$\frac{\theta}{\theta_\infty} = 1 - \mathrm{erf}\frac{\tau}{\sqrt{(\alpha t)}}$$

Equation 11

where the error function $\mathrm{erf}\beta$ is defined as:

$$\mathrm{erf}\beta \equiv \frac{2}{\sqrt{\pi}}\int_0^\beta e^{-\phi^2} d\phi$$

Equation 12

where $\theta = T - T_0$ and α is thermal diffusivity of the material[89].

This analysis shows that sample thickness mainly affects t-ML and t-pMLR in ThermaKin model. The relationship between these factors seems to be directly proportional as seen on Figure 34 and Figure 35 respectively.

5.2.4 Influence of Chemical Properties

The chemical properties employed by the ThermaKin model and analysed here are activation energy and Arrhenius factor.

The Arrhenius equation is a powerful mathematical tool for fitting numerical values to decomposition behaviour. The two parameters A, describing the rate of the chemical process and E_a, the change in the rate of the process with temperature, cannot be treated independently. Instead, it is better to group them as a single term, pyrolysis temperature, defined in Equation 13. This is the peak of the mass loss curve in the Thermogravimetric Analysis (TGA) (expressed as a Differential Thermogravimetric (DTG) curve) provided the decomposition step results in fuel release.

Equation 13 shows that the peak pyrolysis temperature is defined by activation energy (E_a) and Arrhenius factor (A) and that E_a and A are not independent:

$$T_p = \frac{E_a}{R \ln\left[\frac{A}{k_p}\right]}$$

Equation 13

Where R is the Universal Gas Constant and k_p is the kinetic rate constant for pyrolysis. Equation 13 is a simple rearrangement of logarithmic form of the Arrhenius equation, applied to pyrolysis process. It has been proposed that uncertainty in the Arrhenius parameters manifests itself as uncertainty in modelling the fire response of polymers.[90]

The thermal decomposition kinetic parameters of the condensed phase, the Arrhenius pre-exponential factor A and activation energy E_a, define the rate of generation of combustible volatiles at a particular temperature in the material. Thus, these parameters are significant for fire modelling. These parameters can be measured using TGA where sample mass is recorded as a function of time over a range of temperatures at a constant heating rate.[99]

Sensitivity analysis of these factors shows the importance of E_a in modelling using ThermaKin. Any change of E_a causes exponential change of heat release rate, avg-MLR (Figure 32) and p-MLR (Figure 33). At the same time significant changes are made to t-ML (Figure 34) and t-pMLR (Figure 35).

5.2.4.1 Heat produced by reaction (h_r)

Heat of reaction is the amount of heat added or removed by a chemical reaction with the initial and final states of all substances present being at the same temperature. When the pressure in the reacting system is constant, the heat of reaction also represents the change in the thermodynamic quantity called enthalpy. Heat of reaction shows the difference between the enthalpy of the substances present at the end of the reaction and the enthalpy of the substances present at the start of the reaction. Therefore, the heat of reaction measured at constant pressure is also designated the enthalpy of reaction, represented by the symbol ΔH_r. A reaction is said to be endothermic if the reactants gain energy, so the heat of reaction is positive or exothermic if the reactants lose energy to the surroundings, when it is negative.

In ThermaKin the heat of reaction refers to the polymer gasification process. Polymer gasification is an endothermic process, which must occur prior to ignition, and which may be followed by combustion, or reaction with oxygen, a highly exothermic process.

The calculation and prediction of the heat effects that come with chemical changes are important to the understanding and use of chemical reactions. If the reacting system is thermally insulated, the heat from the reaction may increase or decrease the temperature of the substances present.

In practice it is often difficult to isolate and measure the heat for a particular reaction, such measurement may not be feasible for certain reactions. However, in many cases such immeasurable quantities may be obtained indirectly from standard tables of data. These data usually take the form of standard heats of formation and heats of combustion. The standard heat of reaction is defined as the amount of heat absorbed or evolved at 25°C and at one atmosphere pressure when one mole of a compound is created from its constituent elements being in its normal physical state - gas, liquid, or solid. The heat of formation of an element in its standard state is arbitrarily assigned a value of zero. The standard heat of combustion is correspondingly defined as the amount of heat evolved at 25°C and at one atmosphere pressure when one mole of a substance is burned in excess oxygen. The method of calculating heats of reactions from measured values of heats of formation and combustion is based on Hess's law of heat summation.[100]

A 5% change in the heat of reaction (h_r) affects p-MLR and avg-MLR significantly. The enthalpy of PEEK decomposition should be established with high precision.

5.2.5 Influence of Optical Properties

The optical properties present in the ThermaKin model are reflectivity and absorption coefficient. The process of absorption of radiant heat depends on the optical properties of the sample. Shiny materials would not absorb much radiation, and so would not ignite easily. Absorption is basically a molecular process where a photon of radiation results in the excitation of a specific atom or molecule. The infrared radiation from the cone heater at 50 kW m^{-2} results in vibration and excitation which eventually relaxes down to increased thermal energy, observed a higher temperature. Reflectivity refers to interaction of the material's surface with

external heat fluxes from the cone heater and then from the flame. The upper limit for reflectivity shows a longer time to ignition. This is due to the fact that more energy is reflected and not absorbed by the surface. A lower peak of heat release rate is observed because less heat is available for decomposition and volatilisation and the overall process is slower. Accordingly, the low reflectivity surface shows a shorter time to ignition, higher peak heat release rate and an overall shorter burning time. The addition of a fire retardant or a different sample preparation (surface roughening) could have a significant effect on the heat release rate curve just because of changes in the reflectivity. High accuracy in measuring emissivity (ε = 1-reflectivity) of solid and char are important in ThermaKin model. t-ML as a feature describing the early stage of the decomposition is affected by the emissivity of the solid (Figure 34 and Figure 35), as char is not present yet and later when charring of the sample starts, the emissivity of char starts to play important role (Figure 32 and Figure 33).

A material's absorption coefficient refers to the amount of energy absorbed the material is capable of absorbing over a certain thickness. Some polar bonds are good absorbers of infrared radiation and most of the heat will be absorbed by the surface layers when these bonds are present. The absence of such absorbers will allow more heat to go through the bulk of the polymer. Large absorption coefficient surfaces will heat up much quicker than those of a material with a lower absorption coefficient. However, the radiation which penetrates the species without being absorbed will cause heating in lower layers. Therefore, highly absorbing materials have shorter time to ignition; however the lower absorbing materials will have an earlier peak heat release rate. The heat release rate associated with lower absorption shows a longer time to ignition and a more progressive decrease from its peak of heat release rate to 0kWm^{-2}. This happens because an increasing part of the radiation goes through samples as the thickness decreases. In most cases, the absorption of polymers is changing during decomposition as the bonding changes, increasing the number of absorbing points, so this type of behaviour is rarely observed.

Changes of absorption show minor effect in this analysis. Probably 5% change in absorption coefficient could be too little to make significant changes in ThermaKin simulation.

5.2.6 Conclusions

Sensitivity analysis of ThermaKin was performed to predict peak and average burning rates. Similar comparison was undertaken by Stoliarov et. al.[84] However, different criteria of variations in polymer properties were used. Here, constant, ±5% variation in properties was used instead of using values based on actual variations of other polymers as limits. It is worth adding that here not only were the initial sample properties changed in this analysis but also the product properties.

Polymer flammability has been characterised by the peak and average rate of heat release measured in a fire calorimetry test[101]. The heat release rate (HRR) curve can be obtained by multiplying ThermaKin's mass loss rate curve by the effective heat of combustion of volatile decomposition products. The results of this study indicate that the knowledge of the rate of decomposition (defined by the E_a, f_i, h_r, R, ε_{ch}, τ, etc) is very important for predicting these parameters. The situation changes when the time to ignition and time to peak heat release rate (or their mass loss equivalents—time to mass loss and time to peak mass loss rate) are added to the list of parameters that need to be predicted. In that case, more properties become important like c_s, ε_s, ρ_s, ρ_{ch} with the Arrhenius parameters clearly dominating (similar to Stoliarov's results[85]). Convective heat transfer coefficient and internal mass transport are somewhat important. Emissivity and absorption (somewhat important in Stoliarov's analysis) or radiation and conductivity are of little importance here, which means that these properties can be assigned their average values without a significant loss of accuracy.

5.2.7 Visualisation of ThermaKin Output

As ThermaKin computational tool is still under development its user interface is not very friendly. The input files have just row text format and the user must correctly input data. Once the input files are constructed there is a need to extract valuable data from ThermaKin output file, which is less straightforward. The first attempt of visualisation of the output ThermaKin file in terms of animation has been undertaken and is presented in this part. The animation of heat transfer through the solid and thickness of the sample as a function of time is presented by the use of Tecplot 360 - visualization software for data simulation. However, before row, ThermaKin text output data could be recognized by Tecplot 360 VBA code needed

to be written to convert it to required data format. The VBA code is included as Appendix C and can be used in an Excel spreadsheet as a macro.

Figure 36 presents screenshots of the animation at three different times.

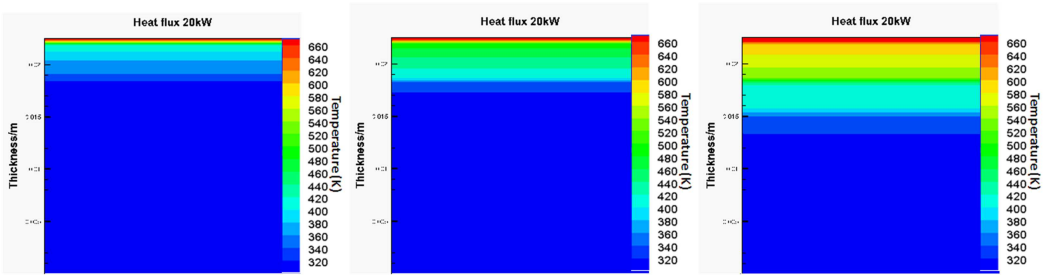

Figure 36 ThermaKin output visualisation

This shows the temperature profile through a cone calorimeter sample of cardboard at a heat flux of 20kW/m^2 at tree times 10s, 25s and 50s respectively.

The plan for future is to develop visualisation interface to present ThermaKin data from output file in automatic way.

5.3 Modelling Methodology – Case Study on Composite Modelling

This part of research was made with collaboration with Dr Stanislav Stoliarov and Mark McKinnon during the author's stay at the University of Maryland, USA, 2011. The project on corrugated cardboard was sponsored by FM Global.

5.3.1 Introduction

It has been stated by Chaos, et. al. that an understanding of the pyrolysis of corrugated cardboard is important in analysing the development and growth of a warehouse fire[102]. It has also been asserted by Chaos, based on an investigation completed by Kashiwagi, et. al. on other cellulosic material samples that the subsequent smouldering of corrugated cardboard char could also be an important contributor to the growth and spread of fire in an area used primarily for storage[103].

One of the major obstacles to accurate comprehensive models describing the pyrolysis and subsequent oxidation or smouldering of corrugated cardboard is a lack of measured

properties to be used as parameters in the models. Though several studies have been completed to determine the flammability and combustibility characteristics of lignocellulosic fuels, there have been few studies directed at corrugated cardboard, which presents a unique set of challenges because of its heterogeneous structure.

This study focuses on collecting the necessary parameters for a comprehensive pyrolysis and oxidation model of corrugated cardboard and subsequent char. Thermogravimetric data have been used to determine the effective Arrhenius parameters to describe the reactions that lead to thermal degradation of cellulosic materials[104,105]. Differential scanning calorimetry was used to find heat capacity (c_p) and heat of reaction (h_r) of cardboard. Cone calorimeter tests have also been conducted in past investigations to verify the results of the combustion model[2]. All of these techniques are employed during this investigation.

The structure of corrugated cardboard presents an interesting physical modelling challenge because of the presence of a complex, non-homogeneous section consisting of the non-planar fluted medium and air. Since the ThermaKin program[2] utilized in this investigation is a one-dimensional model, the curvature of the fluted material cannot be exactly represented and the situation must be simplified. Initially, the effective properties that differ from the real material properties are defined and assigned to the entire composite section to represent the physical situation as accurately as possible.

The cardboard samples specific to this investigation further complicate modelling because the unequal thickness of the two fluted sections. This unequal thickness results in different physical properties. During this study two approaches were tested: homogenous and non-homogenous structure of the cardboard. In the homogenous version, the intensive properties of the component materials do not differ between the three dense liner boards and two fluted sections, which can be counterintuitive. It was determined during modelling that the simplest form of the model was not able to capture all features of the fire modelling. That is why a non-homogenous model had to be developed, where the effective properties of the composite fluted sections and liner boards were assumed to have the actual dimensions and different properties of the cardboard.

5.3.2 Sample Material

The material on which this investigation is focused is a double-wall corrugated cardboard. The cardboard is composed of three sets of parallel liner boards, each with a thickness of approximately 0.64 mm and an area density of approximately 363 g/m^2. The liner boards are separated by a relatively thinner material that is oriented with flutes along the length of the cardboard. The flute material has an approximate thickness of 0.23 mm and an area density of 122 g/m^2. A schematic representation of the cardboard material is provided in Figure 37. The thickness of the entire composite material was measured as 7.5 mm with a density of approximately 174 kg/m^3.

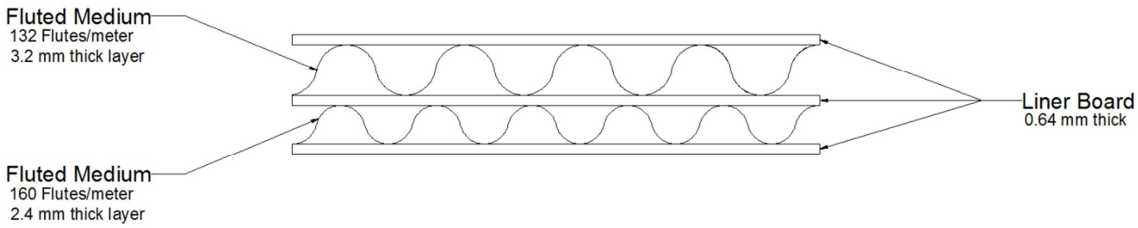

Figure 37 Structure of the corrugated cardboard samples

5.3.3 Cone Calorimeter Tests - Internal Temperatures Profiles

Cone calorimeter tests were conducted by Mark McKinnon of the University of Maryland at heat fluxes of 20 kW/m^2 and 60 kW/m^2 with thermocouples inserted in the fluted sections and below the sample. The thermocouples were unsheathed, butt-welded type K thermocouples and had a diameter of 0.38 mm. Relatively thin, unsheathed thermocouples were used to get the best response time available, while providing the ability to determine the position of the thermocouple within acceptable limits of error by securing the thermocouple from both ends. The thermocouples were inserted in the sample of corrugated cardboard and tension was applied from both ends to make the wires taught. The ends of the wire were wrapped and secured around ceramic posts attached to the sample holder to prevent short circuits. The approximate positions of the thermocouples in the cardboard sample and a picture of the experimental setup are displayed in Figure 38.

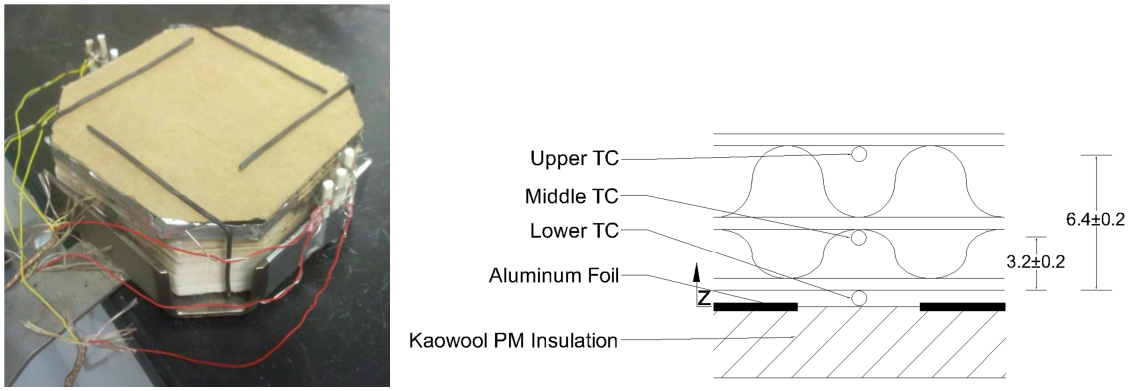

Figure 38 Picture of thermocouple experimental setup and a schematic representation of the locations of the thermocouples in the corrugated cardboard sample

The temperature data was collected from the thermocouples at a rate of 1 Hz. The plots provided in Figure 39 contain the instantaneous mean temperature displayed over the range of time data was collected and the individual data from each of the five tests displayed at a frequency of 0.2 Hz to improve readability. The average error in the curves, defined as two standard deviations of the mean, ranged from 5% to 15% error in all the curves at both heat fluxes.

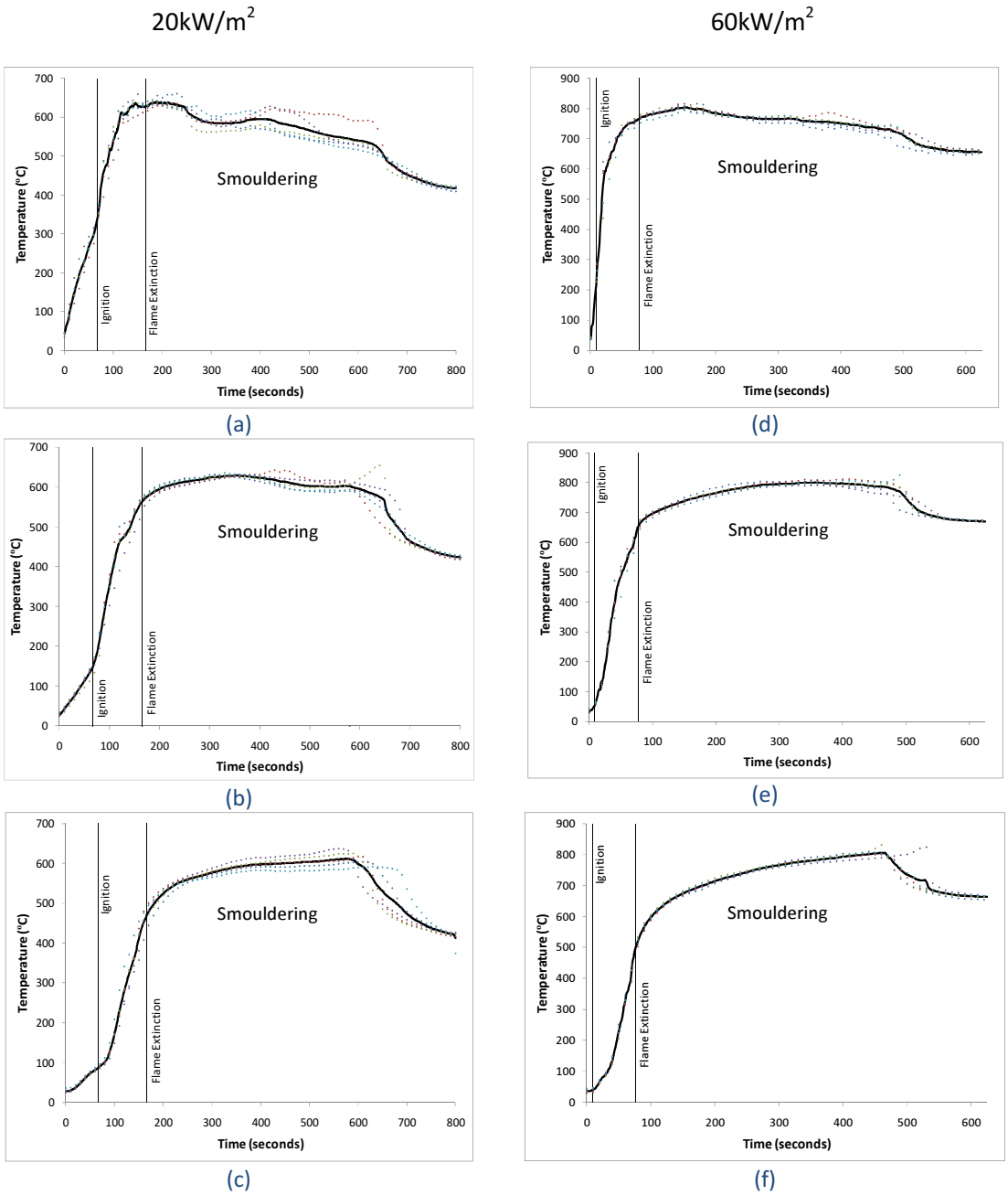

Figure 39 Temperature Data Collected during Cone Calorimeter Tests: (a) Upper Thermocouple at 20 kW/m^2 (b) Middle Thermocouple at 20 kW/m^2 (c) Lower Thermocouple at 20 kW/m^2 (d) Upper Thermocouple at 60 kW/m^2 (e) Middle Thermocouple at 60 kW/m^2 (f) Lower Thermocouple at 60 kW/m^2

5.3.4 Micro-Scale Experiments

Micro-scale experiments were conducted to analyse the thermal decomposition characteristics of the corrugated cardboard material. Thermogravimetric analyses were

completed with various heating programs and reactive and inert atmospheres to determine the chemical kinetics of the pyrolysis and oxidation reactions that occur at an elevated temperature.

A square metalwork file was used to abrade the edge of a cardboard sample to generate a fine powder, and the powder was allowed to dry in a desiccator in the presence of Drierite for a minimum of 48 hours. The corrugated cardboard powder was compacted in an alumina crucible such that approximately half of the crucible was filled. The sample masses prepared in this manner were in the range of 6-10 mg.

5.3.5 TGA Pyrolysis

The pyrolysis reaction was examined by heating the cardboard powder in a pure nitrogen atmosphere from 40°C to 850°C at a rate of 10°C/min. The sample was heated from room temperature to 40°C and allowed to condition in the nitrogen atmosphere at 40°C for twenty minutes. This "conditioning period" was included to ensure the sample was purged of oxygen before data was collected. The data resulting from three tests with a pure nitrogen atmosphere are provided in Figure 40. The data between tests is largely consistent and all variations appear to be random noise caused by the numerical differentiation of the mass data to produce the mass loss rate plots.

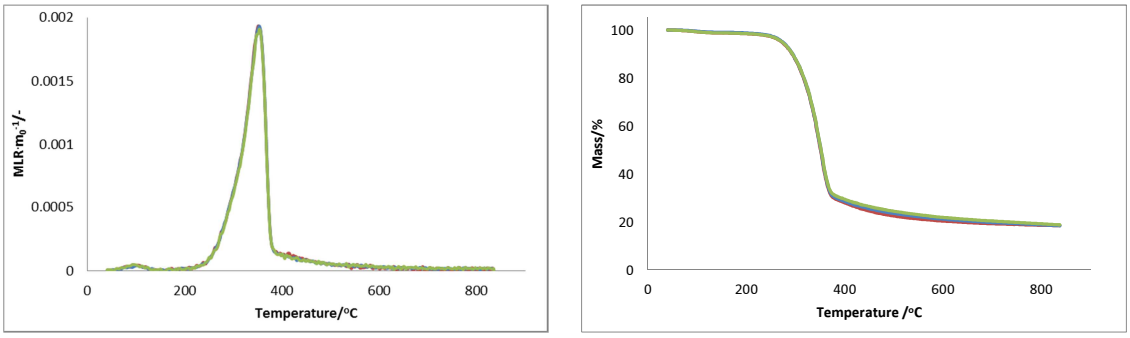

(a) (b)

Figure 40 Thermogravimetric data displayed as mass loss rate (a) and mass loss (b) with cardboard data from three tests in nitrogen

Three distinct processes can be observed in the degradation of corrugated cardboard powder displayed in Figure 40(a). The first occurred in the range 50-110°C and is attributed to the evaporation of moisture from the sample. The second process was evidenced by the large peak ranging 225-375°C when the majority of the mass of the sample was vaporized. The final process started at approximately 375°C and finished at approximately 575°C, generating a tail

that slowly approached zero as the sample pyrolysed to yield char at approximately 18.5% of the original mass.

5.3.6 TGA Pyrolysis in the Presence of Oxygen

Degradation and oxidation of the virgin cardboard samples was examined by testing the cardboard powder in atmospheres with 21% Oxygen and 10% Oxygen, both in a balance of nitrogen. The tests conducted in each atmosphere had the same heating program that consisted of a 20 min conditioning period at 40°C followed by heating from 40°C to 700°C at a rate of 10°C/min. The thermogravimetric data collected in these tests is displayed in Figure 41. The mass loss rate data was calculated as a numerical differentiation of the total mass data, so the experimental curves contain random noise, but the curves from each of the three tests displayed in the plots show consistent, repeatable data.

Thermogravimetric analysis of corrugated cardboard powder was conducted in two, well-defined atmospheres containing oxygen, and resulted in mass loss rate data with two distinct peaks (325^{o}C and 425°C). The first peak associated with the release of moisture was disregarded in the figure, to emphasize the processes that deviated from the pure nitrogen atmosphere data.

Three key differences were observed. First, the first (major) peak was shifted from [~345°C] to [~325°C] but the mass loss at the end of this peak was smaller in simulated air then in nitrogen. Second, a slow decomposition continued from [~325-425°C] in simulated air, and third, the residual char was rapidly oxidised at [~425°C] in simulated air. The residue at [~425°C] is assumed to be predominantly inorganic ash. Little difference is observed between 10% O_2 and 21% O_2.

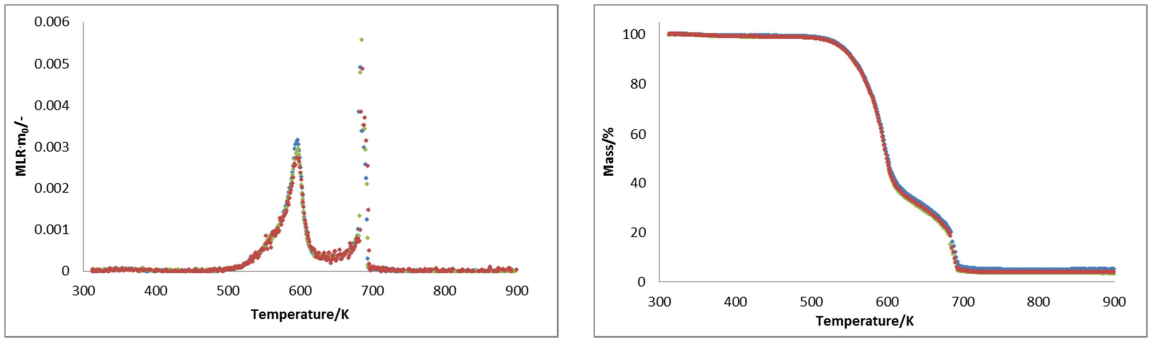

(a) (b)

Figure 41 Thermogravimetric data displayed as mass loss rate (a) and mass loss (b) in 21% oxygen atmosphere

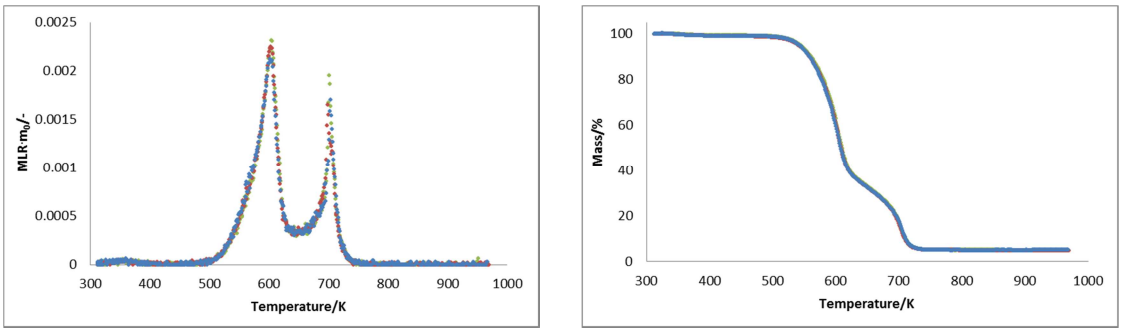

(a) (b)

Figure 42 Thermogravimetric data displayed as mass loss rate (a) and mass loss (b) in 10% oxygen atmosphere

5.3.7 Microscale Combustion Calorimeter in Nitrogen and Air

The Microscale Combustion Calorimeter (MCC) apparatus is shown in Figure 3 and described in section 2.3.4. A sample is placed within the sample cup. The specimen chamber is heated at a constant heating rate (1°C per second) in a flow of nitrogen. Any volatile products enter the combustion mixing chamber, held at 900°C where a flow of oxygen is introduced, to ensure the complete combustion of these products.

Microscale Combustion Calorimeter (MCC) tests in nitrogen and air on corrugated cardboard were performed to investigate heat release rate. MCC data was supplied by Natallia Safronava collected at the Federal Aviation Administration laboratory. The tests were carried out in air in order to obtain heat of combustion values (for the gasification or oxidation of the char).

Table 15 MCC experimental data of corrugated cardboard collected in (a) N_2 atmosphere and (b) in Air

(a)

Sample	Mass/ mg	Char/ %	HRC/ $J \cdot g^{-1} \cdot K^{-1}$	HRR/ $W \cdot g^{-1}$	HR/ $kJ \cdot g^{-1}$	T_{peak}/ °C
#1	4.864	16.8	153	148	10.1	371
#2	4.748	18.4	149	144	10.3	369
#3	4.816	16.9	149	146	10.6	370
#4	4.929	16.8	153	149	10.5	370
#5	4.975	17.0	141	140	10.2	370

(b)

Sample	Mass/ mg	Char/ %	HRC/ $J \cdot g^{-1} \cdot K^{-1}$	HRR/ $W \cdot g^{-1}$	HR/ $kJ \cdot g^{-1}$	T_{peak}/ °C
#6	4.729	1.3	-	257	17.0	354
#7	5.050	1.5	-	400	16.5	334
#8	5.053	1.4	-	292	16.6	347
#9	5.164	1.3	-	347	16.7	339
#10	5.096	1.4	-	267	16.4	354

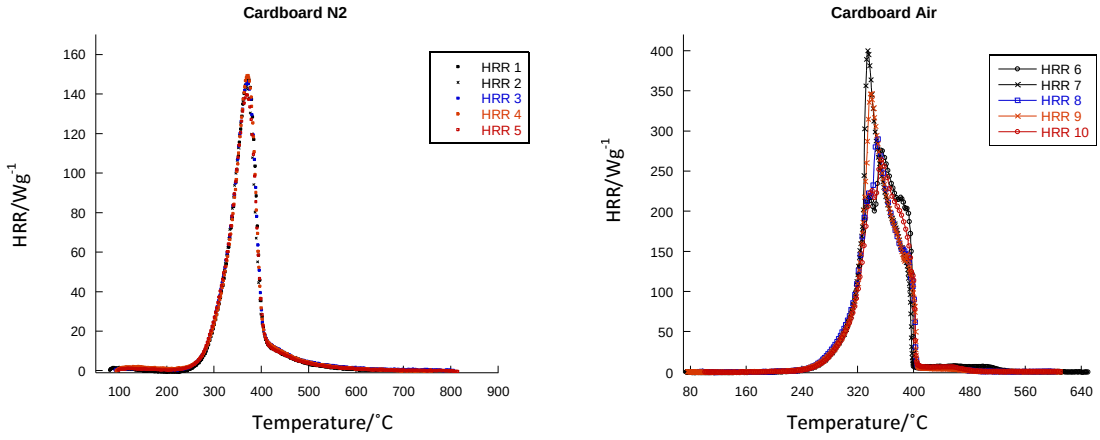

Figure 43 MCC HHR curves of cardboard (a) in nitrogen and (b) in air

MCC tests were performed to investigate the HRR associated with mass loss. Particularly the area between 100-200°C was interesting because mass loss occurred without any heat release.

5.3.8 Pyrolysis Kinetics Modelling

This section provides guidance on how to obtain reaction schemes and kinetics parameters. A detailed, step-by-step method is presented showing how to build a single reaction mechanism and then construct a multiple reaction mechanism. This methodology is used to create all the kinetic models in this work and to determine the kinetic parameters.

In this section temperature may be expressed in Kelvins (K) as ThermaKin temperature dependent parameters are calculated in this unit.

The thermogravimetric data, for decomposition in nitrogen, was used as the basis for the pyrolysis model of corrugated cardboard constructed using the ThermaKin program[2]. When the overall ThermaKin model of the TGA experimental curve is developed, we can predict how the sample mass is changing with time, or temperature but it is also an extremely efficient method for estimating Arrhenius thermal decomposition kinetics parameters, the pre-exponential factor A and activation energy E_a of the sample material, the subject of detailed studies by Rein et al.[1]

For most real materials, such as polymers A and E_a are not tabulated in the literature. For ThermaKin modelling this problem can be relatively easy to overcome. Kinetic parameters are the most important component in modelling the fire behaviour of materials. It has been confirmed by sensitivity analysis that even the small changes can result in significant differences in overall model prediction, even with other parameters well-defined. Both the methodology and results of modelling TGA curves using ThermaKin are described in this section.

The main simplifying assumption is to start with a single reaction approach to keep the model simple. The first model only fits the main peak visible on MLR curve, disregarding the others.

The methodology of finding the best ThermaKin fit is based first on calculating the pairs of kinetics parameters from TGA experimental curves (both MLR and ML) and then using the best values of A and E_a performing series of manual iteration simulations to get the best approximation.

Initially, it is necessary to support the process of finding the first pair of kinetics parameters by such a theoretical approach. The fuel generation rate of a material element in a burning solid is assumed to be equal to the change in mass *m* of the element per unit time *t*. For a first order thermal decomposition process with rate constant *k* the mass loss rate is

$$-\frac{dm}{dt} = k[m]$$

Equation 14

A more convenient form for thermal analysis is obtained when the instantaneous mass is referenced to the initial sample mass, $m(0) = m_0$. Defining an instantaneous mass fraction $x(t) = x = m(t)/m_0$

$$-\frac{dx}{dt} = x' = k[x]$$

Equation 15

If *k* is of the Arrhenius form, $k = A \exp[-E_a/RT_p]$, Equation 15 provides the relationship between the frequency factor *A*, activation energy E_a, universal gas constant R and the residual mass fraction at temperature T_p[106].

It is clear that this method is not giving us unequivocal solution, as the one equation has two unknowns, *A* and E_a. For this reason it is preferable to choose a value for activation energy close to any other known material of similar properties. Having E_a there is only one solution for pre exponential value of factor *A* from Arrhenius equation. Values of dx/dt = 0.0018, x = 0.53 and T_p = 622*K* are read from MLR and ML curves. At this point, it is possible to perform first simulation using ThermaKin.

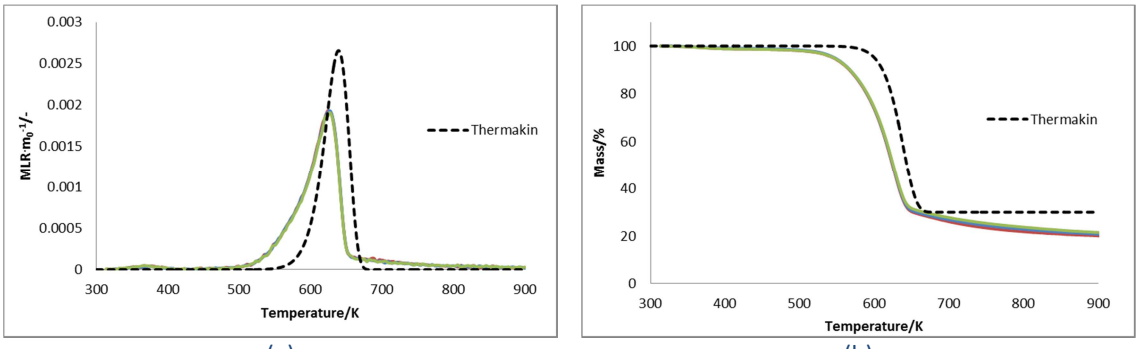

(a) (b)

Figure 44 Example of accuracy using the first choice of kinetic parameters in ThermaKin simulation (a) MLR and (b) ML curves

Figure 44 shows that the first run does not give a satisfactory solution. A series of manual iterative ThermaKin simulations are now required to find the activation energy E_a, pre-exponential factor A, and stoichiometric yields to fit the TGA curve. A new, better pair of kinetics parameters is needed. As stated by Rein et al.[1] these parameters are determined by solving an inverse problem. The inverse problem consists of combining together the mass-loss model and an optimisation technique to identify the set of kinetic parameters that best reproduces the mass loss measured in the TGA experiments. Unfortunately ThermaKin itself has no optimisation algorithm for this purpose. Each pair of A and E_a has to be carefully chosen to come closer to the final solution as each simulation has to be initialized manually. After a number of simulations a simple but very efficient converging method has been established.

The algorithm converging to a final solution is based on the Arrhenius equation's relationship of the parameters. It is observed that increasing/decreasing the value of T_p shifts the approximate curve peak to higher/lower temperature areas while at the same time increasing/decreasing E_a is responsible for the peak going up or down respectively as presented in Figure 45 (a) and (b). Pre-exponential factor $A = f(E_a, T_p)$ is a function of E_a and T_p, calculated from Arrhenius equation. Figure 46 (a) and (b) uses pairs of kinetics generated by proposed method.

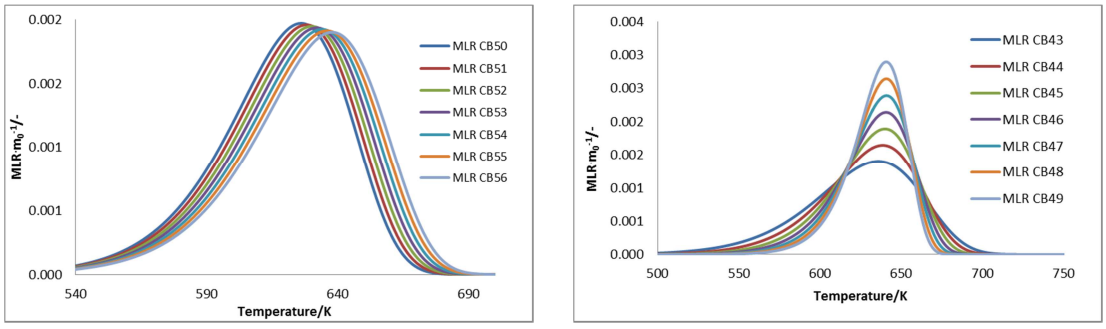

(a) (b)

Figure 45 ThermaKin fitting curve shapes when changing (a) T_p and (b) E_a - while $A = f(E_a, T_p)$

Table 16 (a) and (b) contain values of kinetics used to run simulations presented in Figure 45 (a) and (b).

Table 16 Kinetics parameters values when (a) T_p or (b) E_a is increased

(a)

Simulation	E_a	$A = f(E_a, T_p)$	T_p
CB50	1.40E+05	3.31E+09	610
CB51	1.40E+05	3.02E+09	612
CB52	1.40E+05	2.76E+09	614
CB53	1.40E+05	2.53E+09	616
CB54	1.40E+05	2.31E+09	618
CB55	1.40E+05	2.12E+09	620
CB56	1.40E+05	1.94E+09	622

(b)

Simulation	E_a	$A = f(E_a, T_p)$	T_p
CB43	1.00E+05	7.98E+05	624
CB44	1.20E+05	3.77E+07	624
CB45	1.40E+05	1.78E+09	624
CB46	1.60E+05	8.41E+10	624
CB47	1.80E+05	3.97E+12	624
CB48	2.00E+05	1.88E+14	624
CB49	2.20E+05	8.87E+15	624

After several ThermaKin iterations a single reaction model is described below.

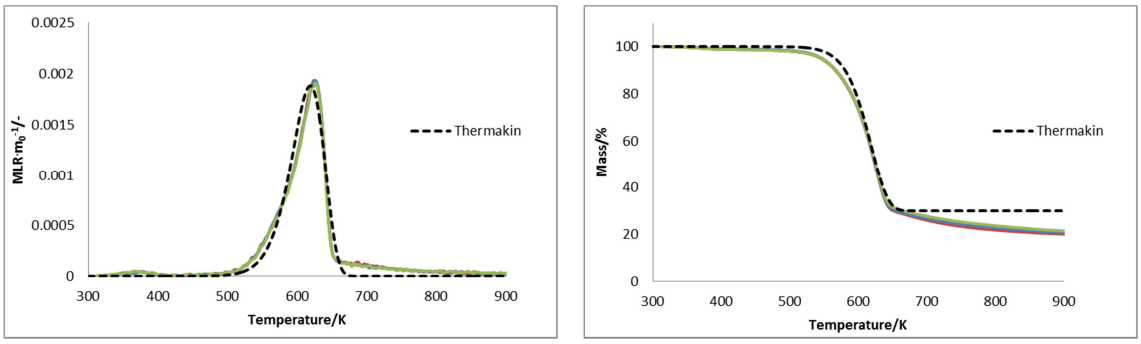

(a) (b)

Figure 46 ThermaKin single reaction model of TGA in nitrogen (a) MLR and (b) ML curves

Thermogravimetric (TG) data was fitted with a first-order reaction curve. The Arrhenius parameters for the reaction are $A = 1.72 \times 10^{-9}$ sec^{-1} and $E_a = 1.36 \times 10^{5}$ J/mol. The ThermaKin plot presents the single reaction simplification. The parameters were determined using a simple algorithm and manually fitting the experimental TG data with a curve or series of curves. The single reaction contains two solids and one gas phase material:

$$CB_a \rightarrow 0.3CB_b + 0.7CB_{volatiles}$$

The mass loss rate curve was initially fitted with a single reaction mechanism for simplicity, but it was determined that a single reaction could not accurately depict the processes involved in the anaerobic degradation of the cardboard sample as presented in Figure 46. A four-reaction mechanism was found to be the simplest curve that could encompass all the features of the curve. It is important to note that the reaction mechanism and the components included in the mechanism are not necessarily physically significant. The mechanism is intended to mathematically mimic the mass loss rate data in the simplest form possible and defines

model-specific kinetics that can reproduce the experimental curve. The ThermaKin framework allows extra reactions to be incorporated by two different methods. Reactions can be parallel:

$$A + B \rightarrow C + D$$

$$E + F \rightarrow G + H$$

or consecutive:

$$A + B \rightarrow C + D$$

$$C + D \rightarrow E + F$$

Usually making the right decision as to which type of the reaction should be applied in the model is not easy, and very often further investigation is required. In such situations a good practice is to perform a Micro-Combustion Calorimeter (MCC) experiment to check the heat release rate (HRR) associated with each mass loss area observed on the TGA curve. The general principle of MCC is similar to TGA, but instead of MLR we obtain HRR and oxygen consumption as a function of temperature. Other words the MCC can provide additional information about the reactions – if they are producing fuel or not at specific temperatures. Also, the amount of flammable volatiles can be measured by analysing the MCC experimental data. Complicated mixtures of volatiles are evolved during each reaction, and assigning a heat of combustion to each set of volatiles helps improve the accuracy of the model.

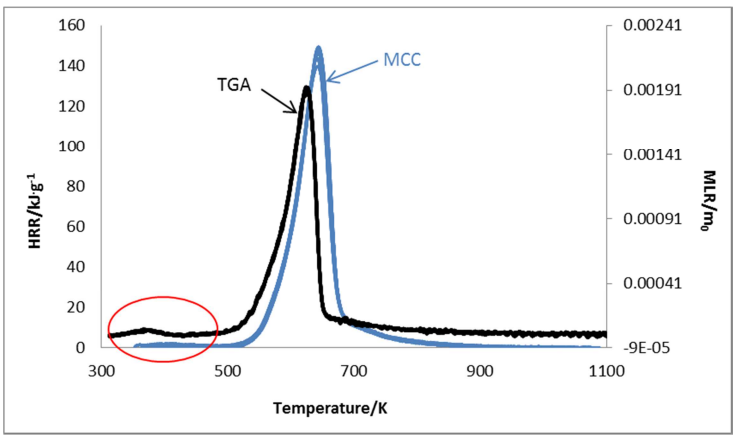

Figure 47 Comparison of MLR and HRR curve of corrugated cardboard generated by TGA and MCC in N_2 atmosphere

Visually, the shapes of both curves look similar except in the area around 370K (100^{o}C), marked by an ellipse on Figure 47. MLR is observed but not HRR. A reasonable explanation for this situation could be the presence of liquid such as water which changed into gas phase at that temperature. The surface of cellulose as coated with water, which is lost over these temperatures.

The plan was to add one parallel reaction at the beginning of the cardboard pyrolysis process, illustrating gasification of the independent component, which is water, and one consecutive reaction at the end corresponding to the cardboard char formation. However, additional consecutive competitive reaction is also considered to fit the asymmetric part of the main peak.

The four-reaction pyrolysis mechanism is depicted in Table 17. It is assumed that the corrugated cardboard sample contains 98% of component CB_a and 2% of H_2O(l). The first reaction corresponds to the release of moisture in the sample and does not contribute considerably to the mass loss. Reactions 2-4 represent cardboard decomposition as a sequential process. Reactions 2 and 3 describe the large peak in the mass loss rate curve. Reaction 4 corresponds to the gradually decreasing tail of the mass loss rate curve. The solution of this inverse problem is complex. The high dimensionality of the problem (12 parameters) produces a large search space and very complicated landscapes for the optimisation target, with many local minima and maxima. Moreover, there is no guarantee of uniqueness of the solution because very complex physical processes are being simulated with a relatively simple mass loss-model. For these reasons genetic algorithms, as a multidimensional optimisation technique, is often used[1]. However, in this work another optimisation method is proposed. The principle of this new method is based on the algorithm used in mathematics called divide-and-conquer method. Here, the solution for a complex problem, such as optimisation of the kinetic-parameter set for a four reaction mechanism can be divided into four sub-solutions, corresponding to each reaction. First, each reaction parameter set (from Reaction 1 to Reaction 4 as presented in Table 17) is estimated separately (by the same methodology as for model presented in Figure 46) then the four solutions are combined to produce an overall model shown in Figure 48. The advantages of this method are that it is more predictable than genetic algorithms, is directly

linked to the physical processes occurring and a model can be found using lower number of iterations (saving time).

Table 17 Pyrolysis Reaction Mechanism

Reaction 1 $H_2O(\ell) \rightarrow H_2O(g)$ $A = 6.14\ sec^{-1}$ $E_a = 2.35 \times 10^4$ J/mol	Reaction 3 $CB_b \rightarrow 0.37CB_{char1} + 0.63CB_{volatiles2}$ $A = 2.0 \times 10^{11}\ sec^{-1}$ $E_a = 1.6 \times 10^5$ J/mol
Reaction 2 $CB_a \rightarrow 0.9CB_b + 0.1CB_{volatiles1}$ $A = 7.95 \times 10^9\ sec^{-1}$ $E_a = 1.3 \times 10^5$ J/mol	Reaction 4 $CB_{char1} \rightarrow 0.59CB_{char2} + 0.41CB_{volatiles3}$ $A = 2.61 \times 10^{-2}\ sec^{-1}$ $E_a = 1.7 \times 10^4$ J/mol

The simulated mass loss rate curve and the contributing reactions are displayed in Figure 48. The average experimental data is depicted in the figure as the thick solid line. The dashed line corresponds to the total simulated mass loss rate based on the reaction mechanism outlined in Table 17. The dotted lines indicate the contribution of each reaction in the mechanism to the total mass loss rate, with each subsequent reaction corresponding to a peak mass loss rate at a higher temperature.

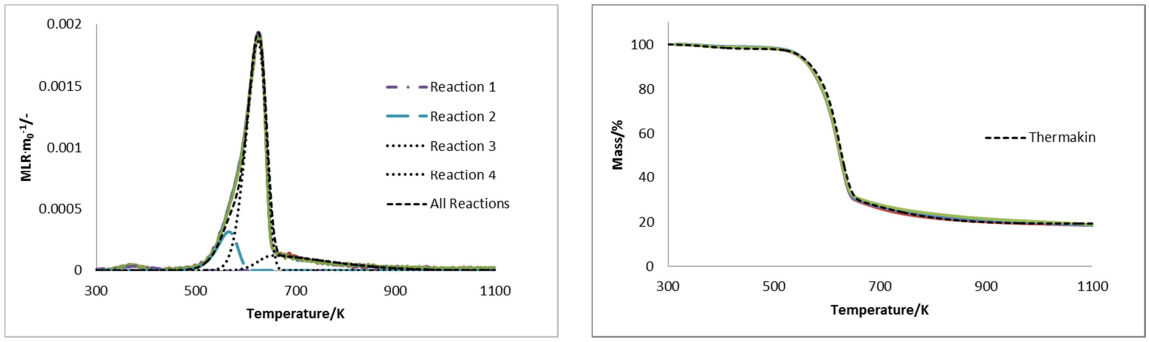

(a) (b)

Figure 48 Thermogravimetric Data Collected in a Pure Nitrogen Atmosphere Plotted with the Curve Fit and Contributing Reactions (a) MLR and (b) ML

The first reaction runs parallel to the next three reactions. Second reaction and third are not only consecutive but also competitive. Forth reaction is based on the product of third one so it is consecutive.

The four reaction model fits all stages of pyrolysis of cardboard in TGA with satisfactory accuracy, as was used to fit the MCC data in nitrogen.

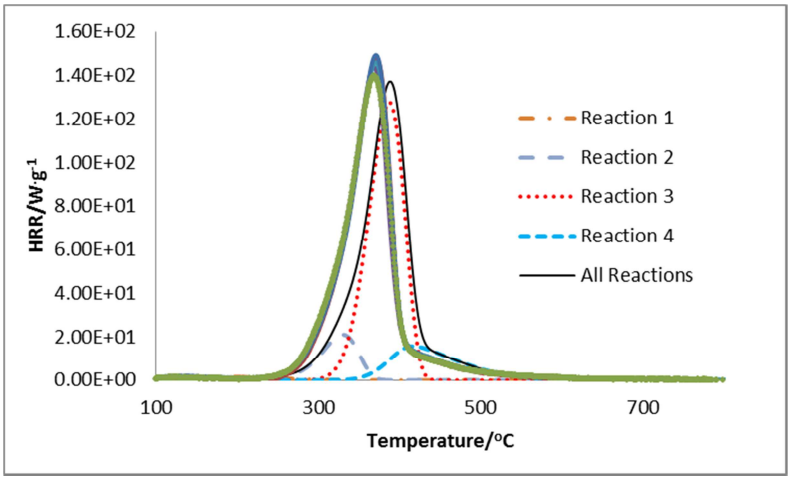

Figure 49 ThermaKin four reactions model of MCC in nitrogen

The heat release (HR) used to fit the MCC curve on Figure 49 using ThermaKin is calculated from the MCC data in Table 18. The average experimental value of HR is 12.1kJ/g by mass loss. The fit is satisfactory apart from the temperature difference of 18°C between the model and the experimental data. Such a situation can be justified by fast heating rate of 1°C/min, and the location of the thermocouple relative to the sample in the MCC apparatus.

5.3.9 Oxidation Kinetics Modelling

The next stage of this research was to investigate the thermal behaviour of cardboard in an atmosphere containing oxygen. The cardboard was degraded in air and in an atmosphere containing 10% oxygen at a heating rate of 10°C/min, up to 700°C. Before numerical models of oxidation models are proposed it is important to analyse the mass loss curves in nitrogen and in the presence of oxygen.

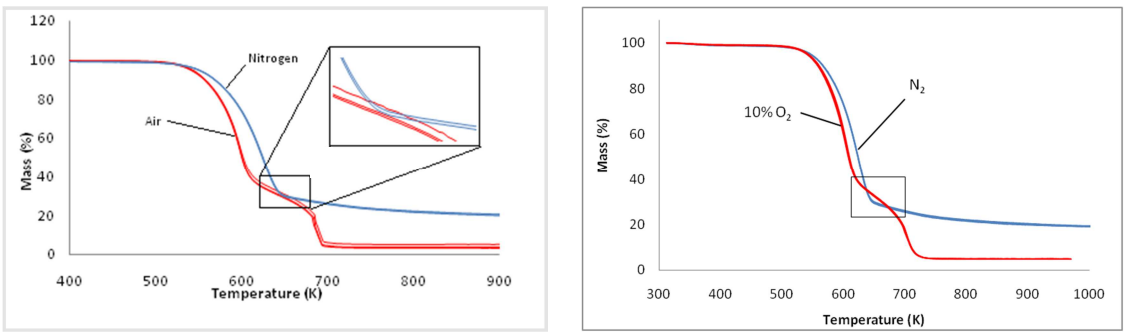

(a) (b)

Figure 50 Comparison of TGA mass loss curves (a) in nitrogen and air and (b) in 10% oxygen atmosphere

It is observed that the presence of oxygen in TGA experiments has an unexpected influence on the mass loss of the cardboard. It is visible on Figure 50 that, up to 600K (325°C), oxygen accelerates the mass loss. Between 600-700K (325-425°C) mass loss in air and 10% O_2 is slowed down and both curves touch or intersect the pyrolysis curve. As a result there is a point at a temperature around 650K (375°C) that the mass of a sample in 10% oxygen is higher than in nitrogen. Although counterintuitive, this situation also arises with some synthetic polymers, such as EVA. The final stage of combustion is oxidation of the char with significant mass loss from about 20% to around 5%.

5.3.10 Oxidation kinetics model in air and 10% oxygen atmosphere

The TGA data in air was fitted to the four reactions assumed to be responsible for the pyrolysis process and another three competitive reactions were added to describe the transition phase oxidation of the cardboard and also oxidation of the char.

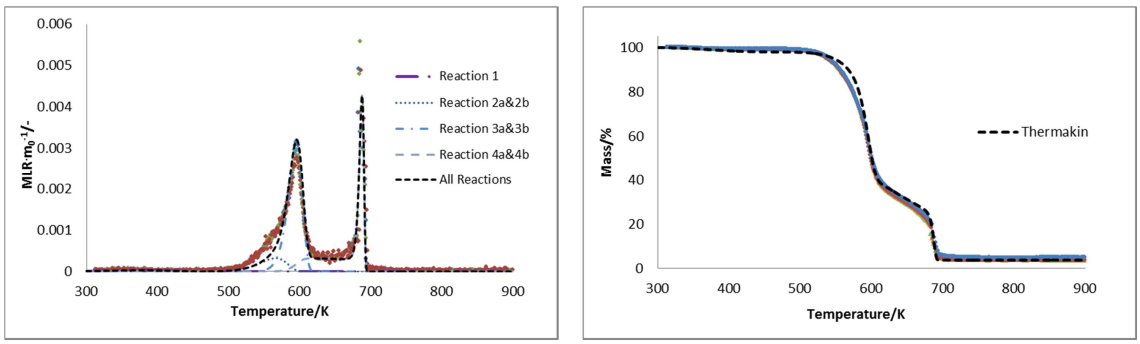

(a) (b)

Figure 51 ThermaKin seven reactions model of TGA in air (a) MLR and (b) ML curve

The ThermaKin model using the data displayed in Figure 51 contains seven reactions as follows:

Table 18 Mechanism for corrugated cardboard reaction in air

Reaction 1 Pyrolysis $CB_a \rightarrow CB_{volatiles1}$ $A = 6.14\ sec^{-1}$ $E_a = 2.35 \times 10^4$ J/mol	Reaction 3 a Pyrolysis - Oxidation $CB_c \rightarrow 0.48CB_{char} + 0.52CB_{volatiles3}$ $A = 2.0 \times 10^{11}\ sec^{-1}$ $E_a = 1.6 \times 10^5$ J/mol
	Reaction 3 b Oxidatian $CB_c \rightarrow 0.48CB_{char} + 0.52CB_{volatiles3}$ $A = 2.86 \times 10^{24}\ sec^{-1}$ $E_a = 3.0 \times 10^5$ J/mol
Reaction 2 a Pyrolysis $CB_b \rightarrow 0.9CB_c + 0.1CB_{volatiles2}$ $A = 7.95 \times 10^9\ sec^{-1}$ $E_a = 1.3 \times 10^5$ J/mol	Reaction 4 a Pyrolysis - Oxidation $CB_{char} \rightarrow 0.09CB_{char2} + 0.91CB_{volatiles4}$ $A = 2.61 \times 10^{-2}\ sec^{-1}$ $E_a = 1.7 \times 10^4$ J/mol
Reaction 2 b Oxidation $CB_b \rightarrow 0.9CB_c + 0.1CB_{volatiles2}$ $A = 2.86 \times 10^{24}\ sec^{-1}$ $E_a = 3.0 \times 10^5$ J/mol	Reaction 4 b Oxidation $CB_{char} \rightarrow 0.09CB_{char2} + 0.91CB_{volatiles4}$ $A = 6.48 \times 10^{95}\ sec^{-1}$ $E_a = 1.28 \times 10^6$ J/mol

A second, seven-reaction ThermaKin model was built to illustrate the behaviour of corrugated cardboard in the TGA in 10% oxygen.

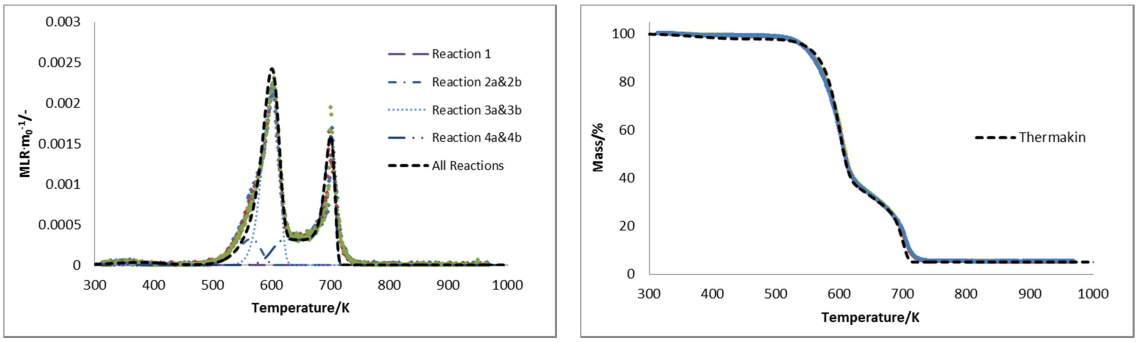

(a) (b)

Figure 52 ThermaKin seven reactions model of TGA in 10% oxygen atmosphere (a) MLR and (b) ML curve

This second ThermaKin model using the data from Figure 52 contains the following seven reactions:

Table 19 Mechanism for corrugated cardboard reaction in 10% oxygen atmosphere

Reaction 1 Pyrolysis $CB_a \rightarrow CB_{volatiles1}$ $A = 6.14\ sec^{-1}$ $E_a = 2.35 \times 10^4$ J/mol	Reaction 3a Pyrolysis – 10% Oxidation $CB_c \rightarrow 0.48CB_{char} + 0.52CB_{volatiles3}$ $A = 2.0 \times 10^{11}\ sec^{-1}$ $E_a = 1.6 \times 10^5$ J/mol
	Reaction 3b 10% Oxidation $CB_c \rightarrow 0.48CB_{char} + 0.52CB_{volatiles3}$ $A = 1.26 \times 10^{17}\ sec^{-1}$ $E_a = 2.20 \times 10^5$ J/mol
Reaction 2a Pyrolysis $CB_b \rightarrow 0.9CB_c + 0.1CB_{volatiles2}$ $A = 7.95 \times 10^9\ sec^{-1}$ $E_a = 1.3 \times 10^5$ J/mol	Reaction 4a Pyrolysis – 10% Oxidation $CB_{char} \rightarrow 0.12CB_{char2} + 0.88CB_{volatiles4}$ $A = 2.61 \times 10^{-2}\ sec^{-1}$ $E_a = 1.7 \times 10^4$ J/mol
Reaction 2b 10% Oxidation $CB_b \rightarrow 0.9CB_c + 0.1CB_{volatiles2}$ $A = 1.26 \times 10^{17}\ sec^{-1}$ $E_a = 2.20 \times 10^5$ J/mol	Reaction 4b 10% Oxidation $CB_{char} \rightarrow 0.12CB_{char2} + 0.88CB_{volatiles4}$ $A = 5.70 \times 10^{37}\ sec^{-1}$ $E_a = 5.30 \times 10^5$ J/mol

The idea was to build two independent models illustrating thermal behaviour of cardboard in these two different atmospheres. However both models were based on a pyrolysis mechanism. The models in air and 10% oxygen contain the same number of reactions. Reaction 1 (in both models) corresponds to moisture evaporation from the sample and is exactly the same as in the pyrolysis model. Also Reaction 2a is taken directly from the pyrolysis model. Reaction 2b was enforced by the presence of oxygen which caused acceleration of mass loss, but no extra mass was lost – the stoichiometry of this reaction is the same as 2a. Reaction 3a is called Pyrolysis – Oxidation because the kinetics parameters are the same as the pyrolysis model, but the stoichiometry was changed due to the presence of oxygen – surprisingly more mass is left after this reaction then in the pyrolysis model (this situation is emphasized in Figure 50). Reaction 3b is called oxidation as it is again accelerating the process of mass loss. Reaction 4a is again the Pyrolysis – Oxidation reaction but this time more mass is consumed then in pure nitrogen. Reaction 4b is a typical reaction corresponding to oxidation of the char – a fast and significant mass loss is observed from about 20% of char to 5% of ash.

The terms pyrolysis and oxidative pyrolysis are used in this section to describe two reactions in the decomposition mechanism. The difference between these two thermal decomposition reactions is the absence or presence of oxygen, respectively. However, the mechanisms in Table 18 and Table 19 show different aspects of oxidative pyrolysis. These

oxidative pyrolysis reactions were sensitive to oxygen concentration - oxygen can either accelerate or retard the mass loss of the decomposing material. This intriguing behaviour was observed when the oxygen concentration was reduced to 10%, shown in Figure 50b. Alternatively this type of oxidative reaction in low oxygen concentrations can be called smouldering. It is reported by Bustamante Valencia[109] that the kinetics of thermal decomposition of materials, such as cardboard, that can undergo smouldering combustion need to be studied, because they occur in environments with reduced oxygen. These smouldering materials present a potential hazard because of the flameless combustion and generation of toxic gaseous products, particularly CO. A detailed description of kinetic modelling of smouldering combustion has been reported by Rein et al[1] work on polyether polyurethane foam (PPUF).

5.3.11 Universal Oxidation Predictive Model

A set of kinetic parameters was determined to describe the degradation of the corrugated cardboard samples in atmospheres containing oxygen. The kinetics were individually determined for the mass loss rate data collected in 10% oxygen and 21% oxygen (see paragraph above) and were defined as a function of the ambient oxygen concentration. The reaction mechanism was constrained by the requirement that the Arrhenius pre-exponential factor was a function of the ambient oxygen concentration, given as a volumetric fraction, and the requirement that at 0% oxygen concentration this mechanism would revert to the pyrolysis mechanism given in Table 17.

The reaction mechanism including oxidation is provided in Table 20. Four oxidation reactions were included that were not present in the pyrolysis mechanism. The mechanism has sequential reactions, similar to the pyrolysis mechanism, but also incorporates parallel reactions that compete with reactions 3 and 4, respectively. The competitive reactions 3a and 3b act to effectively speed reaction 3 without the loss of more mass. Reactions 4a and 4b act to effectively speed reaction 4 and decrease the final char yield from approximately 20% of the initial mass to approximately 5% of the initial mass.

Table 20 The universal reaction mechanism for corrugated cardboard as a function of ambient oxygen volume fraction

Reaction 1 Pyrolysis $H_2O(\ell) \rightarrow H_2O(g)$ $A = 6.14\ sec^{-1}$ $E_a = 2.35 \times 10^4$ J/mol	Reaction 3b Oxidation $CB_b \rightarrow 0.48CB_{char1} + 0.52CB_{volatiles2}$ **$A = 1.11 \times 10^{21}[O_2\%]\ sec^{-1}$** $E_a = 2.8 \times 10^5$ J/mol
Reaction 2 Pyrolysis $CB_a \rightarrow 0.9CB_b + 0.1CB_{volatiles1}$ $A = 7.95 \times 10^9\ sec^{-1}$ $E_a = 1.3 \times 10^5$ J/mol	Reaction 4 Pyrolysis $CB_{char1} \rightarrow 0.59CB_{char2} + 0.41CB_{volatiles3}$ $A = 2.61 \times 10^{-2}\ sec^{-1}$ $E_a = 1.7 \times 10^4$ J/mol
Reaction 3 Pyrolysis $CB_b \rightarrow 0.37CB_{char1} + 0.63CB_{volatiles2}$ $A = 2.0 \times 10^{11}\ sec^{-1}$ $E_a = 1.6 \times 10^5$ J/mol	Reaction 4a Oxidation $CB_{char1} \rightarrow 0.48CB_{char2} + 0.52CB_{volatiles3}$ **$A = 1.24 \times 10^{-3}\ [O_2\%]\ sec^{-1}$** $E_a = 1.7 \times 10^4$ J/mol
Reaction 3a Oxidation $CB_b \rightarrow 0.59CB_{char1} + 0.41CB_{volatiles2}$ **$A = 4.76 \times 10^9[O_2\%]\ sec^{-1}$** $E_a = 1.6 \times 10^5$ J/mol	Reaction 4b Oxidation $CB_{char2} \rightarrow 0.15A_{ASH} + 0.85CB_{volatiles3}$ **$A = 2.31 \times 10^{125}\ [O_2\%]\ sec^{-1}$** $E_a = 1.69 \times 10^6$ J/mol

The mass loss rate curve and mass curve collected in 21% oxygen are provided in (a) and (b) of Figure 53. The experimental data is indicated by dotted lines and the simulation data based on the reaction mechanism given in Table 20 is provided as the dashed line. The mass loss rate curve and mass curve collected in 10% oxygen is provided in (c) and (d) of Figure 53, with the same line type scheme.

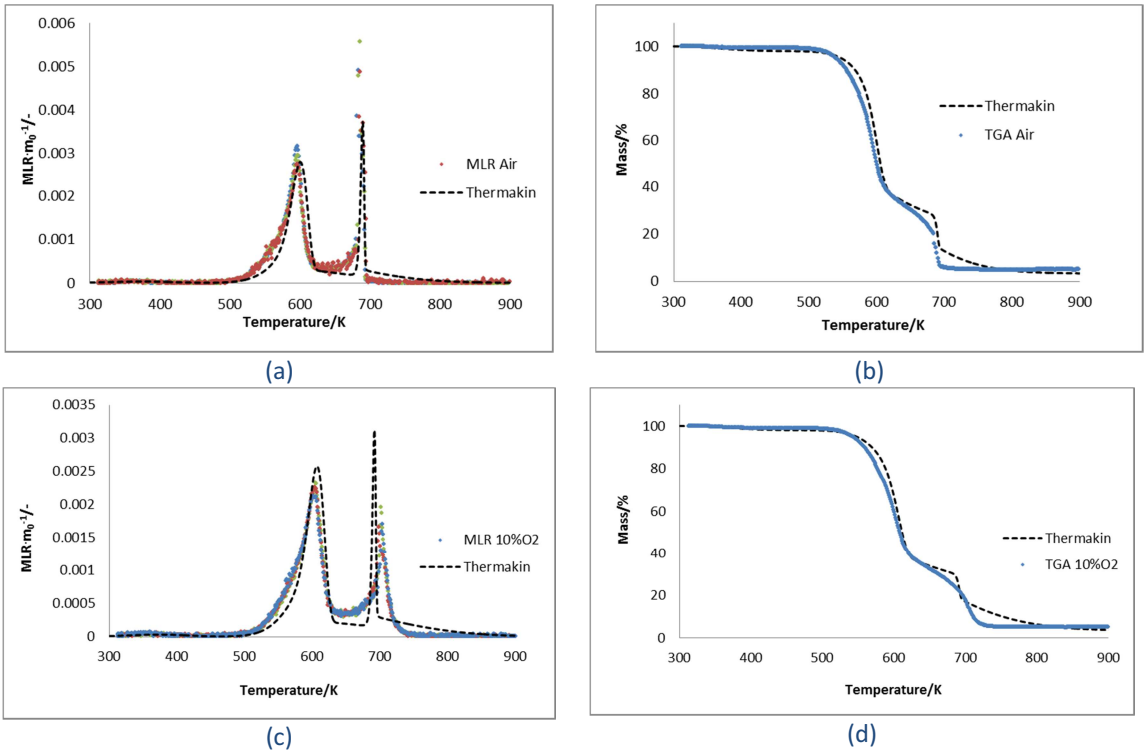

Figure 53 The Universal Reaction Mechanism Fit to (a) The Mass Loss Rate plot in 21% Oxygen (b) The Total Mass Curve in 21% Oxygen (c) The Mass Loss Rate plot in 10% Oxygen (d) The Total Mass Curve in 10% Oxygen

Although it is possible to obtain curve fits that correspond more accurately to the data, the fits displayed in the previous two figures provide good quantitative and qualitative predictions for the reaction kinetics of corrugated cardboard in an atmosphere with oxygen, while keeping the number of reactions relatively small.

5.4 ThermaKin Bench-Scale Modelling

5.4.1 Laboratory technics for parameters optimisation

The heat capacity was calculated from DSC data collected using covered platinum pans with the Netzsch 449 F3 Jupiter. The data were collected in a pure nitrogen atmosphere with a temperature program ranging from 40°C to 840°C heated at a rate of 10°C/min. The DSC data were presented in units of mW/mg and are shown in Figure 54. The heat capacity [$J \cdot g^{-1} \cdot K^{-1}$] was calculated by dividing the DSC signal [mW/mg] by the true heating rate [K/s]. The true heating rate was calculated by a simple interpolation described in the following equation:

$$HR = \frac{T_{n+2} - T_n}{t_{n+2} - t_n}$$

Equation 16

A region between the release of moisture and the onset of the first degradation reaction was identified as the most representative period of time to describe the heat capacity of the virgin cardboard material. The data could not be accurately described with a linear relationship, so the data in the range 125°C to 270°C was averaged and considered the heat capacity of cardboard.

The heat of reaction (polymer gasification) was calculated from the same DSC data that was used to calculate the heat capacity. The reaction mechanism determined in ThermaKin was employed to describe the relative masses of each component and the calculated heat capacities were assigned to each component to generate a baseline curve. The baseline curve described the total heat capacity of the sample as the composition of the sample changed. The baseline was superimposed on the DSC data curve and the integral of the difference between the largest peak of the DSC data and the baseline was considered the heat of reaction.

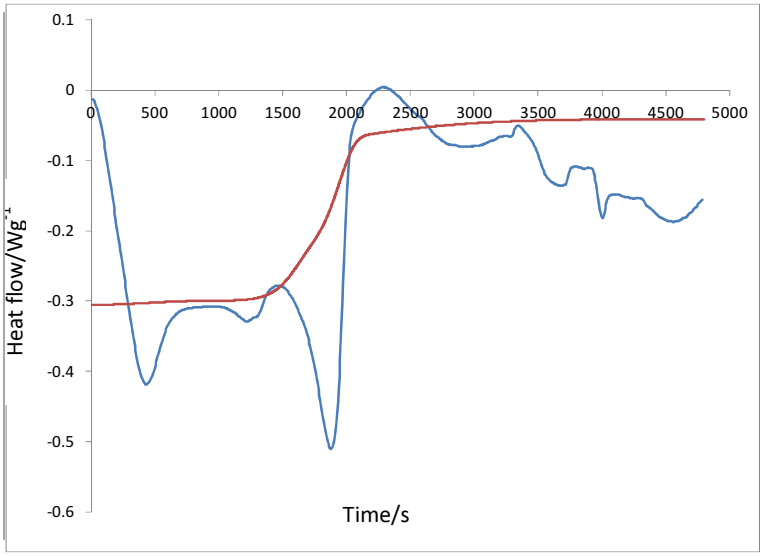

Figure 54 DSC data of the cardboard (blue line) and baseline (red line)

The heat flux from the flame in the cone calorimeter was measured with a Schmidt-Boelter heat flux gauge inserted in the sample such that the surface of the gauge was flush with the top surface of the cardboard. Tests set up in this manner were conducted with

incident heat fluxes of 20 and 60 kW/m^2. The data collected in the tests conducted at each heat flux were averaged to generate a single mean heat flux curve. The steady heat flux before ignition was subtracted from the total heat flux data to effectively produce the flame heat flux.

The average flame heat flux curves collected at 20 and 60 kW/m^2 did not follow a common trend, so it was determined that a mean value would be the best representation of the flame heat flux. A threshold value of 50% of the maximum flame heat flux was used to define the limits of the averaging used to describe the mean flame heat flux at each incident heat flux.

The flame temperature was determined using the Chemical Equilibrium for Applications program developed by NASA[107]. It was assumed that the adiabatic flame temperature for stoichiometric combustion of hydrocarbons with chemical composition similar to cellulose $[(C_6H_{10}O_5)_n]$ would provide a good approximation of the flame temperature of the cone tests with corrugated cardboard. Six compounds with chemical composition similar to cellulose were identified and the adiabatic flame temperatures of combustion of these compounds in sufficient air at 1 atm were averaged to obtain 2270 K.

The fraction of the heat flux that is attributed to radiation can be assumed to range from 0.15 to 0.35 based on the nature of the fuel and the observations of the flame. The flame is considered fairly transparent so it is assumed there is little absorption of radiation by the flame. The remainder of the flame heat flux is considered to be transferred by convection. Depending on whether the radiative fraction (X_r) describing the flame is chosen to be nonzero, the heat flux in the convection equation changes to $\dot{q}''(1 - X_r)$.

The convective heat transfer coefficient (h) from the flame to the cardboard surface was calculated by manipulating the convective heat transfer equation (Equation 17):

$$h = \frac{\dot{q}''}{\left(T_{flame} - T_{surface}\right)}$$

Equation 17

The heat flux was measured directly, the flame temperature was approximated as 2270 K as described above. The temperature of the surface of the heat flux gauge is kept relatively constant based on water circulation, so the surface temperature is approximately between 288 K and 298 K.

The heat of combustion was calculated from data collected with the cone calorimeter. The integral of the heat release rate curve was divided by the integral of the mass loss rate curve. The limits of integration were chosen based on which portion of the process was desired. A similar analysis of MCC data can also be used to yield the heat of combustion data for each step. These are summarised in Table 21. A detailed description of the physical properties of the material is crucial to the process of understanding its burning characteristics including time to ignition, time to flaming, or time to smouldering.

Table 21 Convection coefficient estimation

External heat flux [kW/m^2]	20	40	60
Heat flux from flame (q_{flame}) [W/m^2]	17000	23500	30000
Gauge temperature T_g [K]	290		
Temperature of flame T_{flame} [K]	2270		
Convection coefficient $h=g_{flame}/(T_{flame}-T_g)$ [W/m^{2}K]	**8.58**	**11.86**	**15.14**

5.4.2 Thermal Conductivity and Emissivity Modelling

The thermal conductivity of the corrugated cardboard was evaluated as one of the most important physical properties in fire modelling particularly with respect to the time to ignition[84]. This means it is important to estimate thermal conductivity as accurately as possible, due to its importance. ThermaKin allows modelling of the burning behaviour on a bench-scale, provided the all physical properties are included in the model. The kinetic parameters were estimated by using ThermaKin to fit TGA curves. The majority of the physical properties of the material under investigation were measured in the laboratory. The thermal conductivity and emissivity were estimated using ThermaKin and cone calorimeter. To obtain the best approximation of emissivity, while quantifying thermal conductivity, the surface of the cardboard was painted in black and value of 0.95 for emissivity was used in the model. Once the thermal conductivity was known, the typical surface of the sample was used to find actual emissivity value.

5.4.2.1 Homogeneous Model

A model of the cardboard treating the card and corrugations as low densities homogenous material was initially considered, because it incorporates assumptions that considerably simplify the calculations. With a homogeneous model, the entire sample was assumed to have uniform thermal properties. The models were constructed with the thermal conductivity adjusted to fit the thermal conductive data collected in the cone calorimeter tests undertaken with thermocouples in the samples. The thermal conductivity was assumed to be temperature dependent.

The temperature data was collected during the cone calorimeter tests with incident heat fluxes of 20 kW/m^2 for the black surface sample and additional 60 kW/m^2 data sets for the typical surface sample. Simulations were completed with these incident heat flux values to fit the predictions to the experimental curves. Convective cooling that was present during testing was simulated with a convective heat transfer coefficient of 8.52 $Wm^{-2}K^{-1}$ (for 20 $kW{\cdot}m^{-2}$ heat flux) and 15.14 $Wm^{-2}K^{-1}$ (for 60$kW{\cdot}m^{-2}$ heat flux) and an environmental temperature of 2270K (2000^{o}C) as shown in Table 21. Data corresponding to the temperatures predicted by the ThermaKin model at the same positions as the thermocouples in the physical experiments were extracted from the ThermaKin output. These data were fitted to the physical data collected in the cone calorimeter experiments by adjusting the thermal conductivity of the sample material.

The bottom boundary of the corrugated cardboard sample was insulated by 30 mm of Thermal Ceramics Kaowool PM Low Temperature Board. The insulation was simulated in the ThermaKin model by using a 20 mm layer with the thermal properties reported for Kaowool PM by the manufacturer and listed in Table 22. The thermal conductivity of Kaowool was approximated by the quadratic polynomial as shown in Figure 55.

Table 22 Thermal and material properties for Kaowool PM

Kaowool PM	
Density	256 kg·m^{-3}
Specific heat capacity	1.07 kJ·kg^{-1}K^{-1} (980°C)
Loss on ignition	4.00-7.00%
Thermal conductivity (W/m-K)	0.0576 (at 260°C)
	0.085 (at 538°C)
	0.125 (at 816°C)
	0.183 (at 1090°C)
Melting point	1760°C
Maximum service temperature in Air	1180°C

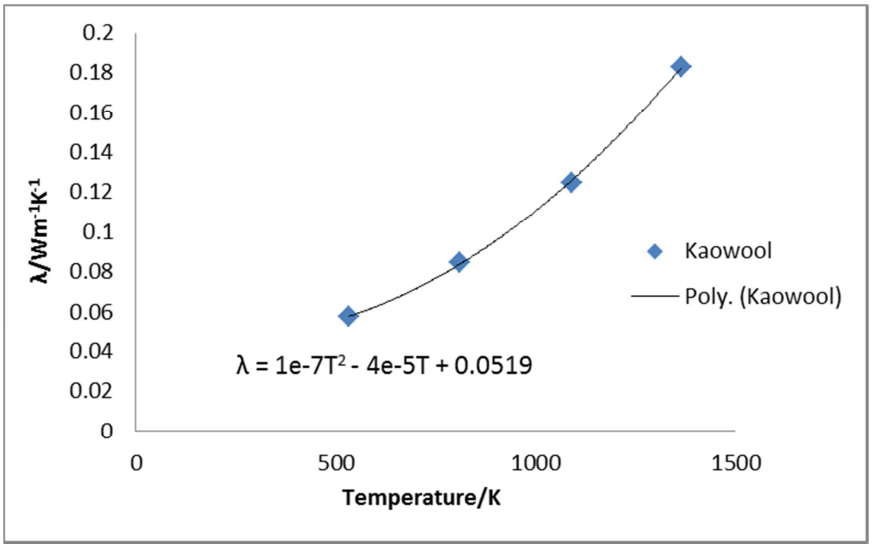

Figure 55 Curve fit of the temperature-dependent thermal conductivity of Kaowool PM

The results of three ThermaKin simulations with black and typical surface at the two heat fluxes 20 kW/m^2 and 60 kW/m^2 and the experimental temperature data from the beginning of the test until ignition (black surface sample) and until flaming (typical surface samples) are provided in Figure 56 and Figure 57. The temperatures simulated by ThermaKin are represented by the lines on the plots. The highest temperature line corresponds to the uppermost thermocouple and the line indicating the lowest temperature corresponding to the bottommost thermocouple. The uncertainty in the position of the thermocouple is assumed to be ± 0.15 mm and is indicated in the plots as broken lines at each thermocouple position. The experimental data is indicated by data points displayed at a rate of 0.2 Hz in the 20 kW/m^2 plots

and at a rate of 1 Hz in the 60 kW/m^2 plots and was calculated as the instantaneous average of five tests as described in a previous section. The error bars on the data points indicate two standard deviations of the mean at each point.

Appendix A contains VBA macro that could be used to extract temperature profiles from ThermaKin output file in Excel spreadsheet.

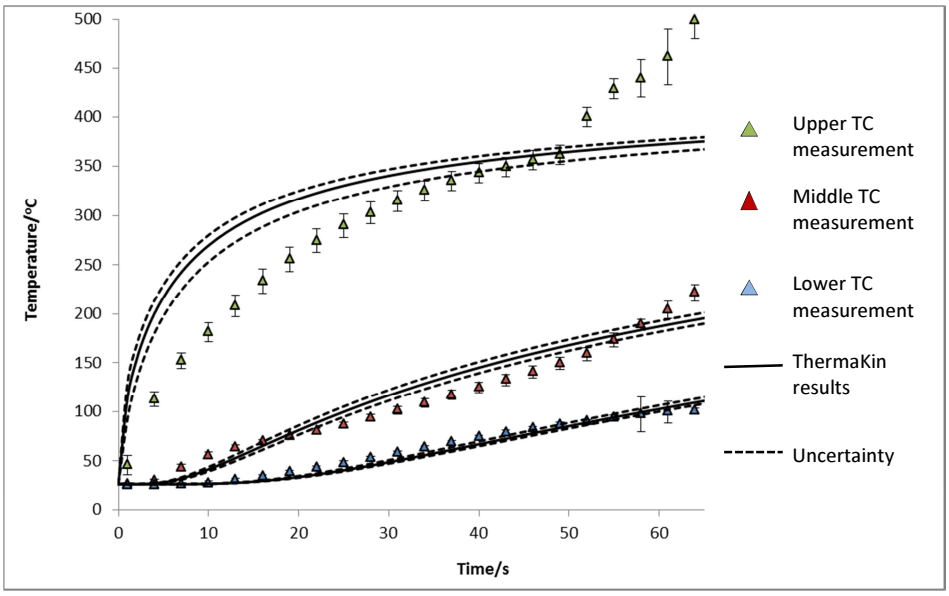

Figure 56 Thermal conductivity fitting for a homogeneous model with black surface with 20 kW/m^2 heat flux

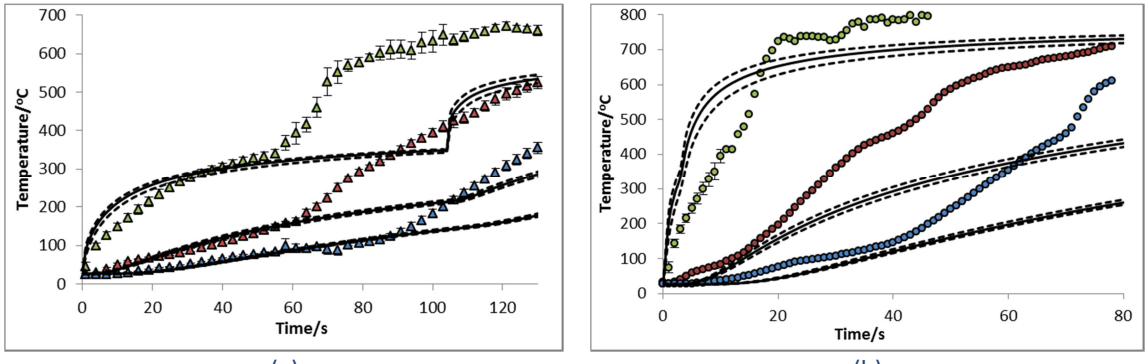

(a) (b)

Figure 57 Emissivity fitting for a homogeneous model with normal surface the ThermaKin prediction shown with solid lines and dashed for upper and lower error limits and the experimental data shown with discrete points with error bars for: (a) 20 kW/m^2 (b) 60 kW/m^2 with α=0.65

Estimated values of thermal conductivity and emissivity were used to generate ThermaKin MLR curves to reproduce MLR behaviour in cone calorimeter.

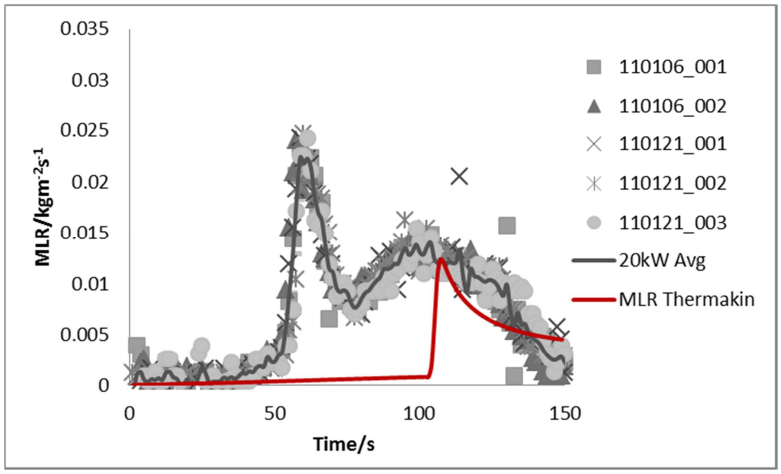

Figure 58 Comparison of ThermaKin homogenous model and Cone Calorimeter MLR profiles with heat flux 20 kW/m^2

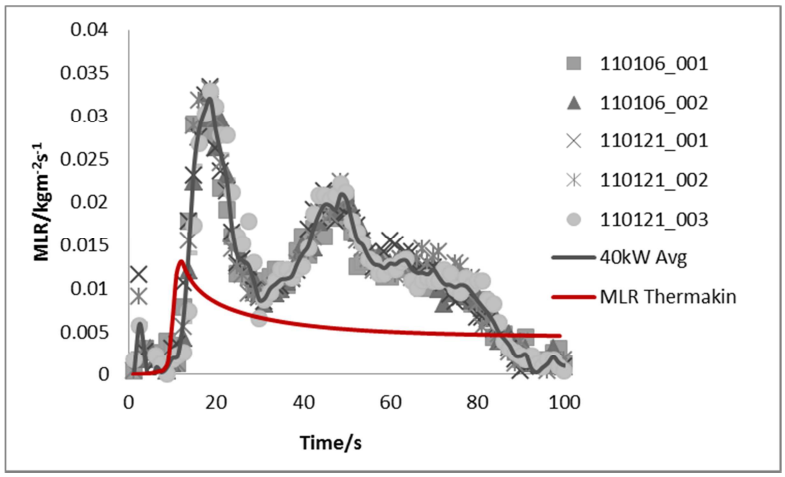

Figure 59 Comparison of ThermaKin homogenous model and Cone Calorimeter MLR profiles with heat flux 40 kW/m^2

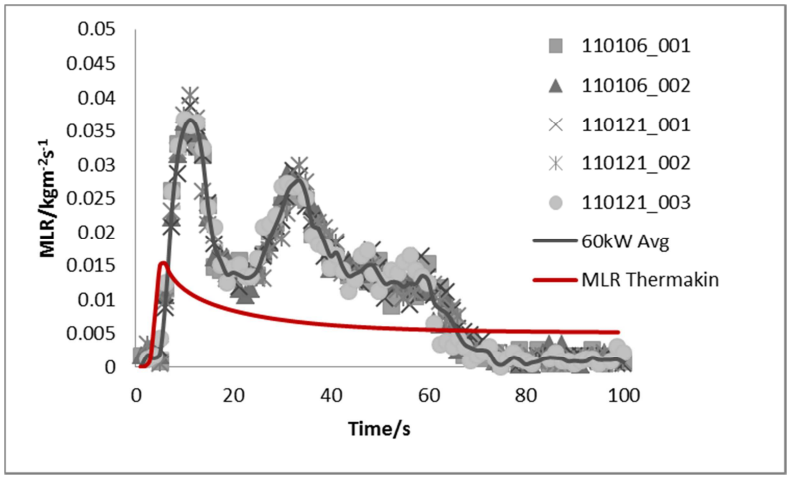

Figure 60 Comparison of ThermaKin homogenous model and Cone Calorimeter MLR profiles with heat flux 60 kW/m^2

The results of the ThermaKin models presented in Figure 58 - Figure 60 do not agree with the data collected in the cone calorimeter tests. As ThermaKin temperature profiles in Figure 56 and Figure 57 show acceptable agreement with experimental measurement (at least to ignition) thus models of MLR curve for homogenous model are far from good agreement.

5.4.2.2 Non-Homogeneous Model

The non-homogeneous model consisted of five layers made of two different materials, similar to the structure of the actual corrugated cardboard sample. The linerboards were simulated by a material with a density equal to the measured density of the linerboards. The fluted sections, physically composed of the fluted medium and air, were simulated by a different, single material with a low density compared to the linerboards. The densities of the entire composite sample and the linerboards were well known from measurements completed on dried samples.

The density of the fluted section was defined with the volume of both fluted sections and the mass as the difference between the mass of the entire composite and the mass of the linerboards. This was determined to be the best method to conserve continuity and yield the most reliable results. The fluted section density was defined as 39 kg/m^3 and linerboard density was defined as 567 kg/m^3. The area-weighted average density of whole sample was measured as 174 kg/m^3 and the simulation produced the same density. Although the effective densities of the two fluted sections were different because of a different flute frequency for each section, it was determined that defining the same properties for both fluted sections would simplify the model at this stage in its evolution.

It was determined that the best results were obtained with the single thermal conductivity for both liner board and the fluted section of $k = 0.08 + 6e\text{-}10T^3$ W/mK and emissivity of $\alpha = 0.67$. The results of these simulations is provided in Figure 62 and compared with experimental data collected at 20 kW/m^2 and 60 kW/m^2. The uncertainties in the plots of are shown in the same manner of those of Figure 57.

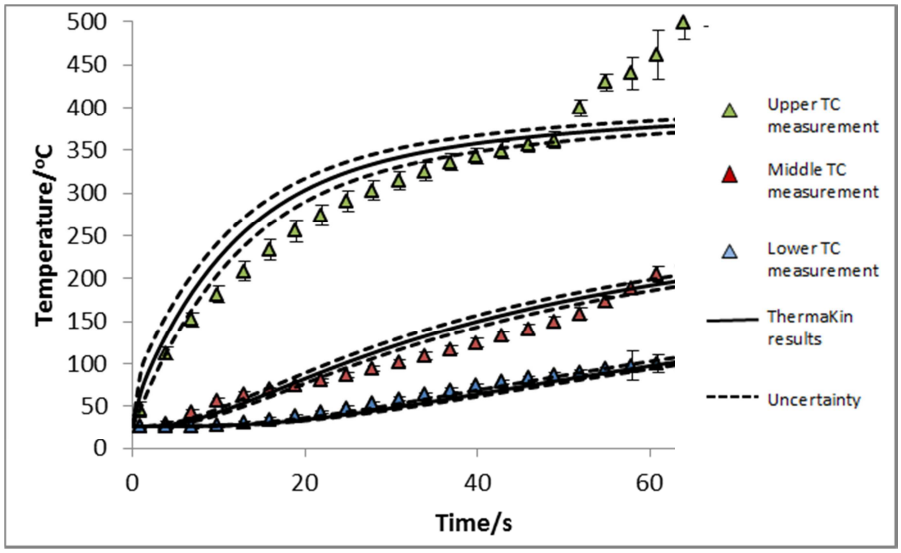

Figure 61 Thermal conductivity fitting for a non-homogeneous model with black surface with 20 kW/m^2 heat flux

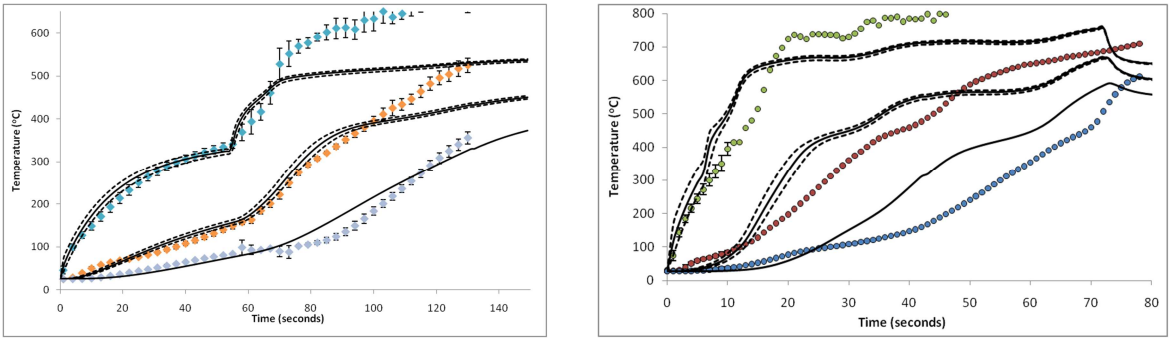

(a) (b)

Figure 62 Emissivity model for non-homogeneous material with the ThermaKin prediction shown with lines and experimental data shown with discrete points for (a) 20 kW/m^2 (b) 60 kW/m^2

Having all parameters estimated it was possible to generate ThermaKin MLR curves equivalent to cone calorimeter MLR results as shown in Figure 63.

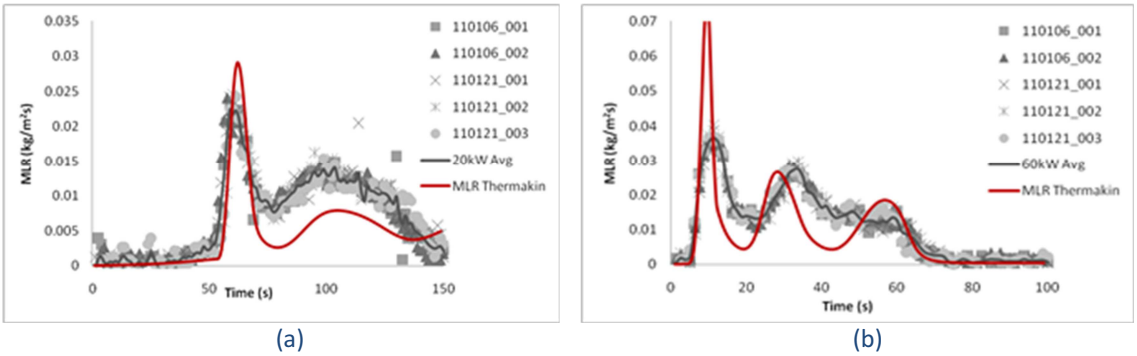

(a) (b)

Figure 63 Comparison of ThermaKin non-homogenous model and Cone Calorimeter MLR profiles with heat flux (a) 20 kW/m^2 and (b) 60 kW/m^2

The non-homogeneous model yields more accurate replication of the actual situation than the homogenous model. Though the fit for each temperature profile does not entirely encompass the experimental data, the simulated curves are considerably closer to the experimental data than those predicted by the homogenous model. Literature data on the thermal conductivity of cardboard is between 0.06-0.17 $W/m \cdot K$[108] which agrees with the results obtained in this work. The time to ignition in the non-homogenous model is captured with high accuracy however the first MLR peak is too large especially for test with a high flux.

5.4.3 Summary of Numerical Modelling of Corrugated Cardboard

Thermogravimetric data was collected for the cardboard samples in atmospheres consisting of pure nitrogen, 10% oxygen, and 21% oxygen with a balance of nitrogen. All the data was repeatable for tests with the same atmosphere. Each set of data was fitted with a multiple reaction mechanism. A universal predictive reaction mechanism that was a function of the ambient oxygen concentration was generated, which fitted the experimental data within acceptable limits of error.

The orientation of the cardboard sample was found to affect the rate of heat release and the mass loss rate of the sample during cone calorimeter testing. It was determined that the results obtained with the thick fluted section facing the heater yielded results comparable to the results obtained when the thin fluted section faced the heater and the edges of the sample were sealed with aluminum tape prior to ignition.

The data collected with thermocouples during cone calorimeter tests was repeatable at each heat flux that was tested. The data collected from the thermocouples was fitted to curves generated by a ThermaKin model with variable thermal conductivity to determine the best model-specific thermal conductivity for a homogeneous and non-homogeneous model of the corrugated cardboard. It was determined that the homogeneous model did not fit the experimental curves well, but the non-homogeneous model fitted most of the thermocouple positions well and was able to predict time to ignition.

The majority of parameters in the ThermaKin model have been measured or modelled. However still some research needs to be done on the thermal conductivity or the emissivity of

the char to improve latest results. This would account for the lower first peak in the experimental data, when compared with the non-homogenous model. All these parameters will allow a full one-dimensional model of corrugated cardboard combustion to be completed. The completed model and simulations may then be compared to the results of cone calorimeter tests to verify the accuracy of the model.

Work on oxidation of the char will be completed in the future to finish the comprehensive model of one-dimensional burning for corrugated cardboard.

For reference, input files describing the model are attached in Appendix B.

5.5 ThermaKin Modelling of PAN

In this section the thermal decomposition of the polyacrylonitrile (PAN) was investigated from the perspective of ThermaKin models. The detailed methodology of ThermaKin modelling is presented on cardboard earlier in this chapter. This time, it is interesting to compare not only two different atmospheres but also three different heating rates, in order to validate the model.

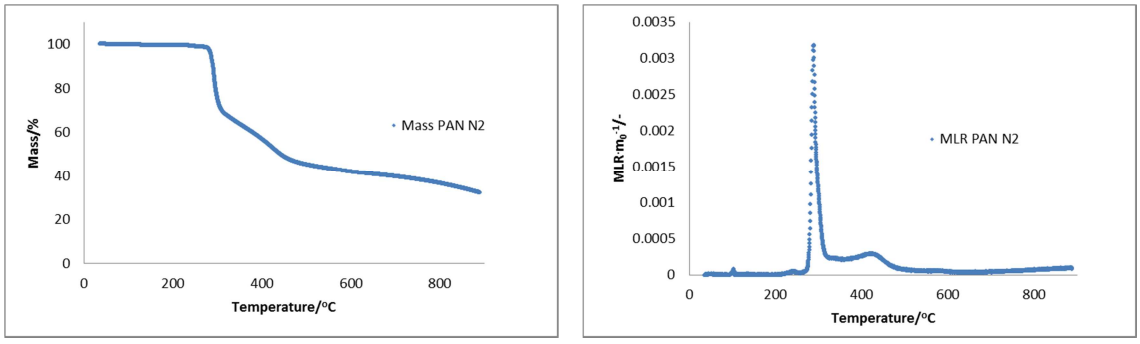

(a) (b)

Figure 64 TGA of PAN in nitrogen atmosphere (a) mass loss and (b) mass loss rate curve

The decomposition of PAN in nitrogen with heating rate 10°C/min is a three-step reaction as seen on Figure 64. At around 385°C a rapid reaction begins consuming about 30% of mass, then a slower reaction lasting till 425°C degrading another 25% of the initial mass, and finally a long shoulder is formed at the end leaving about 30% of residue. The MLR curve in Figure 64(b) shows one dominating peak, then a plateau, followed by a small peak, and

then a flat, low shoulder. The mechanism, containing three reactions, is proposed in Table 23 to model PAN behaviour in N_2, depicted in Figure 65.

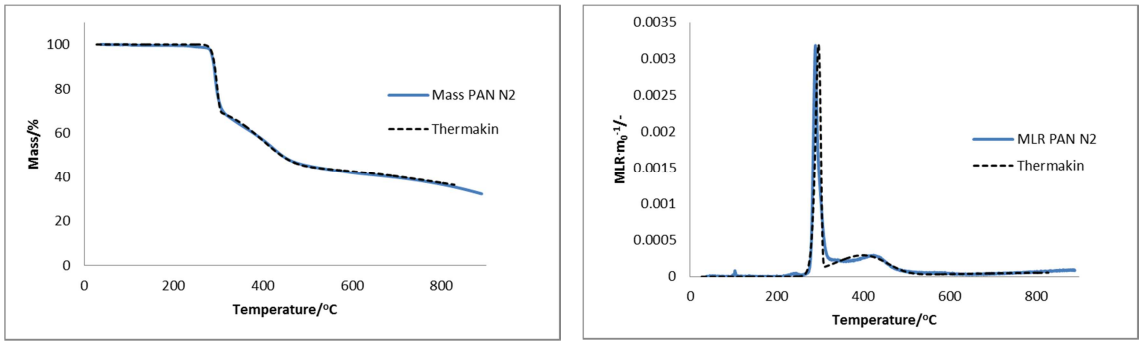

(a) (b)

Figure 65 Three reaction ThermaKin model of PAN decomposition in N_2 (a) mass loss and (b) mass loss rate curve

The dashed line represents the ThermaKin fit function and solid line shows experimental result.

Table 23 Mechanism of PAN decomposition in N_2

Reaction 1	Reaction 2
$PAN \rightarrow 0.7PAN_{residue1} + 0.3PAN_{volatiles1}$ $A = 4.73 \times 10^{39}\ sec^{-1}\ E_a = 4.5 \times 10^5\ J/mol$	$PAN_{residue1} \rightarrow 0.65PAN_{residue2} + 0.35PAN_{volatiles2}$ $A = 4.73 \times 10\ sec^{-1}\ E_a = 5.5 \times 10^4\ J/mol$
Reaction 3	
$PAN_{residue2} \rightarrow 0.35PAN_{residue3} + 0.65PAN_{volatiles3}$ $A = 4.09 \times 10^{-3}\ sec^{-1}\ E_a = 2.5 \times 10^4\ J/mol$	

The first reaction corresponds to a sharp peak on MLR curve, second reaction is a slower mass decomposition between 375-525°C and reaction number three represents the long shoulder at the end.

When atmosphere is changed for air the TGA of PAN decomposition looks like in Figure 66.

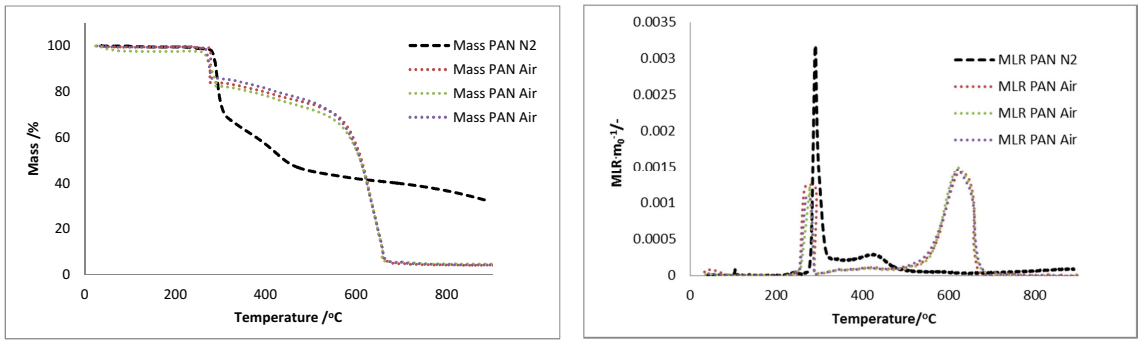

(a) (b)

Figure 66 Comparison of TGA PAN curves in air and nitrogen with 10°C/min heating rate

As seen on Figure 66, oxidative decomposition, expressed by dotted lines, follows a different mechanism from nitrogen. Most mass loss is delayed until almost 625°C, when it is fairly rapid. At about 60% mass loss the PAN air curve crosses the N_2 curve and the mass finally drops to 5%.

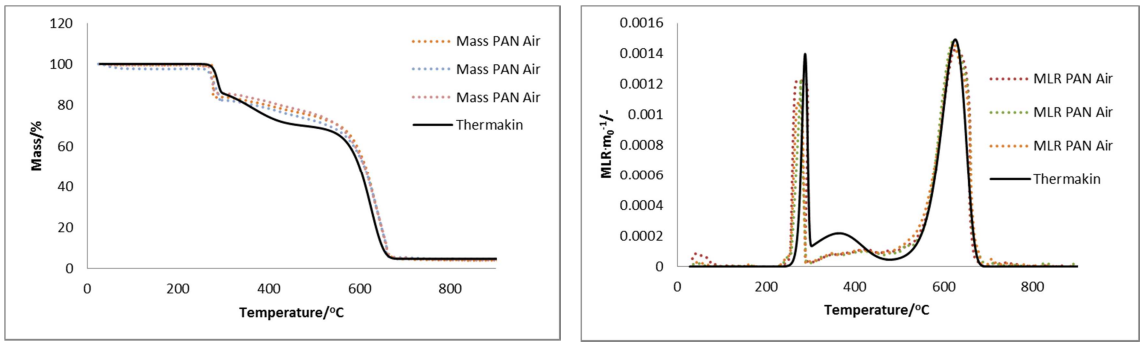

(a) (b)

Figure 67 ThermaKin model of PAN decomposition with 10°C/min heating rate in air (a) mass loss and (b) mass loss rate curve

The ThermaKin model is presented in Figure 67 as a solid line while experimental data are shown as dotted lines.

Table 24 Mechanism of PAN decomposition in air

Reaction 1 Pyrolysis $PAN \rightarrow 0.7PAN_{residue1} + 0.3PAN_{volatiles1}$ $A = 4.73 \times 10^{39}\ sec^{-1}\ E_a = 4.5 \times 10^5$ J/mol	Reaction 1a Oxidation $PAN \rightarrow 0.9PAN_{residue1} + 0.1PAN_{volatiles1}$ $A = 4.75 \times 10^{35}\ sec^{-1}\ E_a = 4.0 \times 10^5$ J/mol
Reaction 2 Pyrolysis $PAN_{residue1} \rightarrow 0.65PAN_{residue2} + 0.35PAN_{volatiles2}$ $A = 4.73 \times 10\ sec^{-1}\ E_a = 5.5 \times 10^4$ J/mol	Reaction 2a Oxidation $PAN_{residue1} \rightarrow PAN_{residue2}$ $A = 4.73 \times 10\ sec^{-1}\ E_a = 5.5 \times 10^4$ J/mol
Reaction 3 Pyrolysis $PAN_{residue2} \rightarrow 0.35PAN_{residue3} + 0.65PAN_{volatiles3}$ $A = 4.09 \times 10^{-3}\ sec^{-1}\ E_a = 2.5 \times 10^4$ J/mol	Reaction 3a Oxidation $PAN_{residue2} \rightarrow 0.03PAN_{residue3} + 0.97PAN_{volatiles3}$ $A = 2.09 \times 10^{12}\ sec^{-1}\ E_a = 2.5 \times 10^5$ J/mol

The reaction mechanism including oxidation is provided in Table 24. Three oxidation reactions were included that were not present in the pyrolysis mechanism. The mechanism has parallel reactions that compete with reactions 1, 2 and 3 respectively. The competitive reactions 1a and 2a act to effectively delay reaction 1 and 2 and also delay degradation of the mass. Reaction 3a acts to effectively speed reaction 3 and also degrade the final yield from 33% to 5%.

Table 25 The universal reaction mechanism for PAN as a function of ambient oxygen volume fraction

Reaction details	Temperature (˚C)	Gas-phase products
Reaction 1 Pyrolysis $PAN \rightarrow 0.7PAN_{residue1} + 0.3PAN_{volatiles1}$ $A = 4.73 \times 10^{39}\ sec^{-1}\ E_a = 4.5 \times 10^5$ J/mol	260-310	Ammonia
Reaction 2 Pyrolysis $PAN_{residue1} \rightarrow 0.65PAN_{residue2} + 0.35PAN_{volatiles2}$ $A = 4.73 \times 10\ sec^{-1}\ E_a = 5.5 \times 10^4$ J/mol	280-450	Hydrogen cyanide
Reaction 3 Pyrolysis $PAN_{residue2} \rightarrow 0.35PAN_{residue3} + 0.65PAN_{volatiles3}$ $A = 4.09 \times 10^{-3}\ sec^{-1}\ E_a = 2.5 \times 10^4$ J/mol	430-850	Methane
Reaction 1a Oxidation $PAN \rightarrow 0.9PAN_{residue1} + 0.1PAN_{volatiles1a}$ **$A = 2.27 \times 10^{34}[O_2\%]$**$sec^{-1}\ E_a = 4.0 \times 10^5$ J/mol	250-280	Hydrogen cyanade, ammonia, methane, hydrocarbons or propionitrile, acetamide or formaldehyde
Reaction 2a Oxidation $PAN_{residue1} \rightarrow PAN_{residue2}$ **$A = 2.26[O_2\%]$**$sec^{-1}\ E_a = 5.5 \times 10^4$ J/mol	270-545	-
Reaction 3a Oxidation $PAN_{residue2} \rightarrow 0.03PAN_{residue3} + 0.97PAN_{volatiles3a}$ **$A = 0.1 \times 10^{11}[O_2\%]$**$sec^{-1}\ E_a = 2.5 \times 10^5$ J/mol	370-660	Cabon dioxide, carbon monoxide, water, aromatics

The reaction mechanism in Table 25 was constrained by the requirement that the Arrhenius pre-exponential factor was a function of the ambient oxygen concentration, given in volumetric fraction, and the requirement that at 0% oxygen concentration this mechanism would revert to the pyrolysis mechanism given in Table 14. It should be noted that this model is tested only for an oxygen level of 21%.

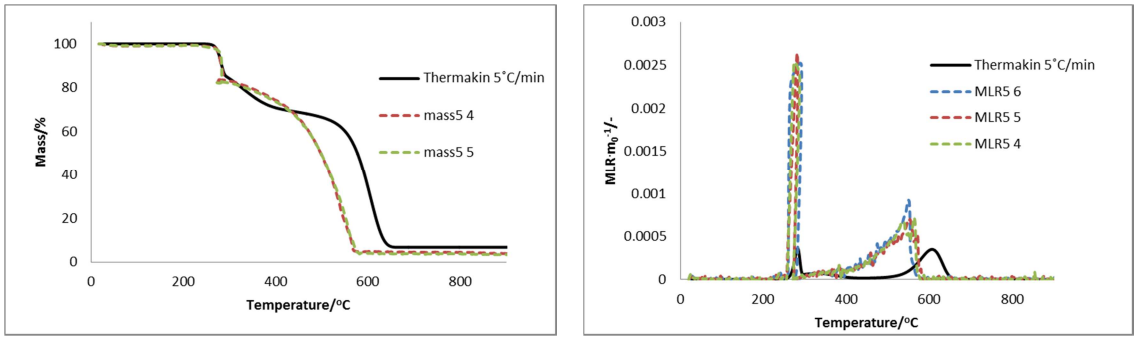

(a) (b)

Figure 68 ThermaKin model of PAN decomposition with 5°C/min heating rate in air (a) mass loss and (b) mass loss rate curve

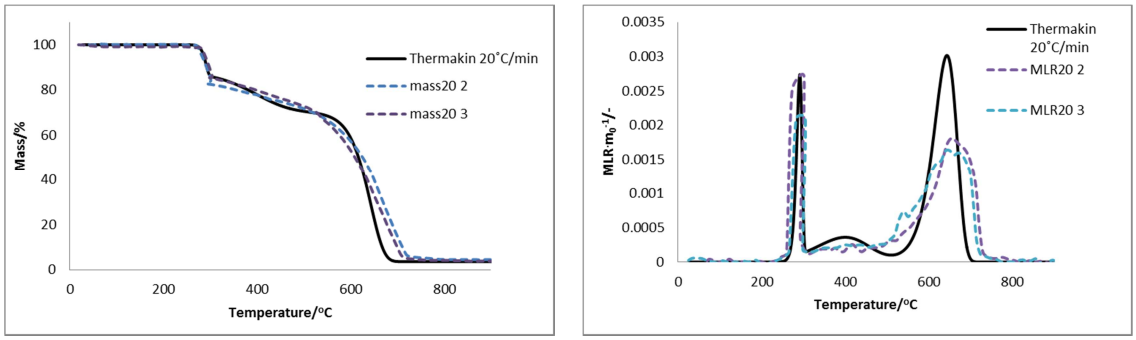

(a) (b)

Figure 69 ThermaKin model of PAN decomposition with 20°C/min heating rate in air (a) mass loss and (b) mass loss rate curve

Performance of universal model to predict PAN decomposition in air with different heating rates is presented in Figure 68 and Figure 69 with heating rates 5°C/min and 20°C/min respectively.

Universal reaction mechanism proposed in Table 25 was used to model PAN behaviour in 4 different testing conditions: two different atmospheres air and nitrogen and three different heating rates were used. Taking into account simplicity of the model (just six reactions were used) its results are at satisfactory level.

6 ANALYSIS OF DECOMPOSITION OF FIRE RETARDED POLYMERS

Simultaneous thermal analysis (STA) is an established technique for measuring the change in weight and thermal properties of a sample during heating and thermal decomposition as a function of temperature, or time, in a controlled atmosphere. This provides a wealth of information on the processes occurring when a polymer (with and without fire retardant) is broken down. A heating rate of 10°C/min, and temperature range from ambient to 700°C, in air, and in nitrogen, with flow rate of 50cm^3/min with sample sizes around 10 mg were used to study the each decomposition stage using a Stanton Redcroft STA 780.

The thermal degradation mechanisms have been investigated with simultaneous thermal analysis (STA) (combined thermogravimetry and differential thermal analysis) interfaced to a Fourier Transform Infrared Spectrophotometer (FTIR). Such combination of pyrolysis modelling with TGA-FTIR was attempted by Bustamante Valencia[109] or Rougaume et al.[29] The thermal degradation of representative specimens of fire retardants and nanofillers were tested separately and together in order to compare the combustion products from the composite materials with those from the virgin polymers using STA-FTIR, as a function of mass loss. The profiles of individual species' evolution as a function of temperature have been reported.

Fourier Transform Infrared Spectroscopy (FTIR) has revolutionised real time, dynamic infrared analysis including measurement of gas concentration changing with time. This allows the total spectrum (the sum of the spectra of each species present) to be recorded at intervals less than 1 per minute (or every 10°C). The individual species and their profiles obtained from a Fourier Transform Infrared Spectrophotometer (FTIR) are reported as a function of time or temperature. The FTIR spectra were collected at resolution of 4 cm^{-1} using a DTGS detector. The gas cell was heated to 280°C and the heated lines to 250°C. Profiles of evolution rates have been derived from the spectra, isolating and identifying the individual processes involved. Gases evolved during the thermal pyrolysis of different materials are reported qualitatively.

In the modelling sections, the proposed mechanisms of pyrolysis, which include chemical reactions with kinetic parameters, and stoichiometry, are based on TGA results. The methodology of finding solutions of these inverse problems describing mass-loss models is

discussed in section 5.3.8. Possible volatile products in ThermaKin models reactions can be found by analysis of FTIR data.

This part of the thesis is about building numerical pyrolysis models of polymers with or without fire retardant additives. STA mass loss data and gas phase products detected by the use of FTIR are analysed. The pyrolysis experiments carried on STA-FTIR on polymers and polymers with additives will be reflected by proposing appropriate numerical mechanisms using ThermaKin. Also, interesting approach where pyrolysis modelling coupled with TGA-FTIR is used on polymer such as polyether polyurethane foam (PPUF) can be found in research reported by Bustamante Valencia in 2009[109] and parallel work was done by Rogaume et al. in 2011[29].

6.1 STA—FTIR Study on the Thermal Degradation of Polypropylene with Fire Retardant and Nanoclay

The samples used in this study were polypropylene (PP) Moplen grade HP500N, supplied by LyondellBasell, blended with 5% Polybond 3200, maleic anhydride-polypropylene oligomers (PPgMA), supplied by Crompton Polybond Co. The fire retardant (FR) was Exolit AP 760 (ammonium polyphosphate) (Figure 70), supplied by Clariant and the nanoclay (NC), Cloisite 20A, a natural montmorillonite modified with a quaternary ammonium organic modifier (Figure 71), supplied by Southern Clay Products. The formulations used to create these composites are detailed in Table 26[46,110].

Table 26 Formulation of PP, polymer materials, with and without FR and NC (in wt %)

Material	*Polymer/%*	*Fire Retardant/%*	*Nanoclay/%*
Polypropylene (PP)	100		
PP+FR	70	30	
PP+NC	95		5
PP+FR+NC	65	30	5

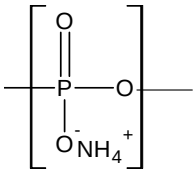

Figure 70 Exolit APP 760

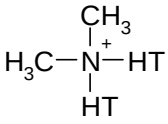

where HT is Hydrogenated Tallow

Figure 71 Organic modifier in Cloisite 20A

6.1.1 Thermal decomposition, degradation products and modelling of Polypropylene

As most bonds in PP are the same strength, they will all break at the same temperature in nitrogen. In air it is believed that peroxo radicals (·OOH) start the decomposition at surface.

6.1.1.1 TGA Thermal Decomposition

Experimental TGA curves of PP decomposition in nitrogen are presented in Figure 72.

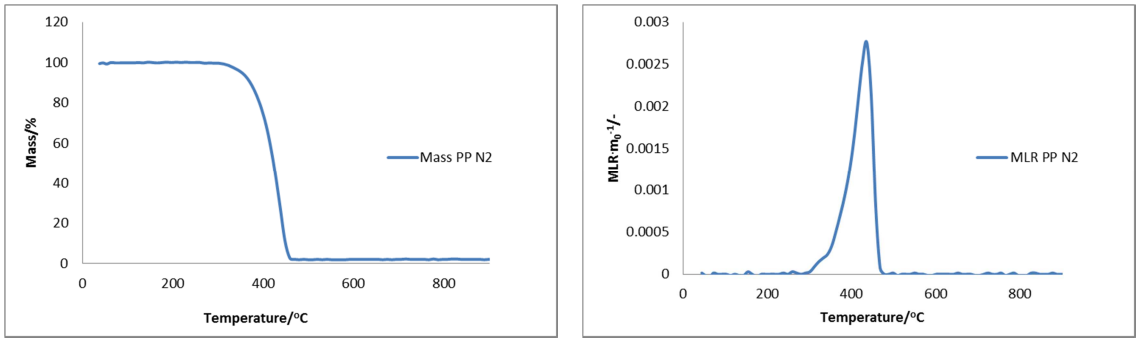

(a) (b)

Figure 72 TGA of PP in nitrogen atmosphere (a) mass loss and (b) mass loss rate curve

The degradation process of PP is different when oxygen is present. Comparison of both processes in terms of mass loss and mass loss rate is shown in Figure 73.

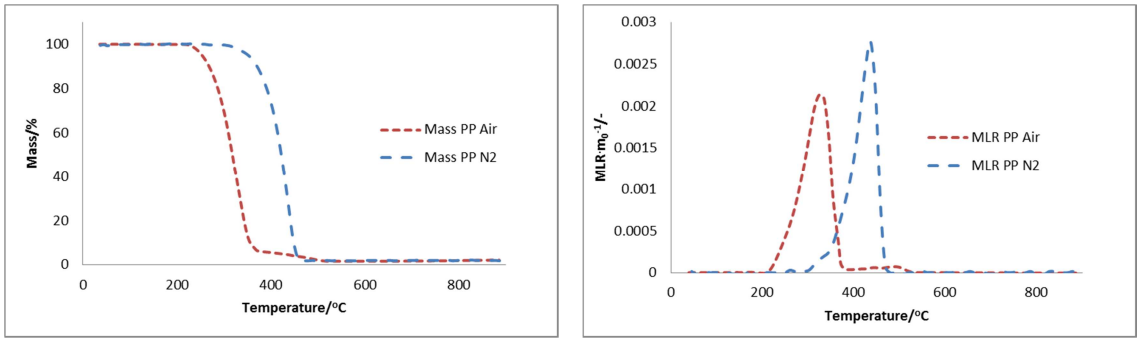

(a) (b)

Figure 73 Comparison of TGA curves in air and nitrogen

As seen on Figure 73 oxidation is accelerating the mass loss of PP. Mass loss starts at 215°C and at 375°C the small shoulder is formed and finally at 525°C is oxidized completely. Such mass loss behaviour is not reported in nitrogen. In nitrogen mass loss occurs later at temperature 335°C but then, surprisingly, mass loss rate is greater (MLR peak is higher) than in air as it is seen on Figure 73(b). Such behaviour in nitrogen can be explained by the fact that most of the mass is pyrolysed without shoulder formation while the presence of oxygen is probably forming a protective layer which is delaying the final mass degradation process.

6.1.1.2 ThermaKin Modelling of PP

The TGA for decomposition of PP in nitrogen suggests a single step reaction, although the MLR curve Figure 72b shows slight asymmetry. However, initially a single reaction mechanism is proposed to model PP behaviour in N_2.

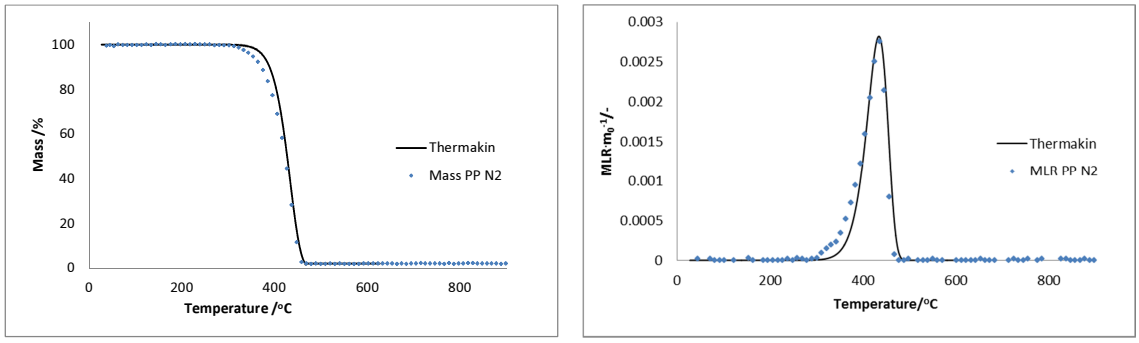

(a) (b)

Figure 74 ThermaKin fit of PP in nitrogen atmosphere (a) mass loss and (b) mass loss rate curve

Single reaction mechanism:

$PP \rightarrow 0.02PP_{residue} + 0.98PP_{volatiles}$

$A = 1.41 \times 10^{11}\ sec^{-1}$ $E_a = 1.8 \times 10^5$ J/mol

Figure 74b shows that a single reaction model is not able to fit the whole process of PP pyrolysis in N_2. It is necessary to introduce second reaction to capture the earlier mass loss at 315°C. ThermaKin's two reaction fit is shown in Figure 75, where dotted lines on the MLR curve represent the contribution of each reaction to overall mass loss.

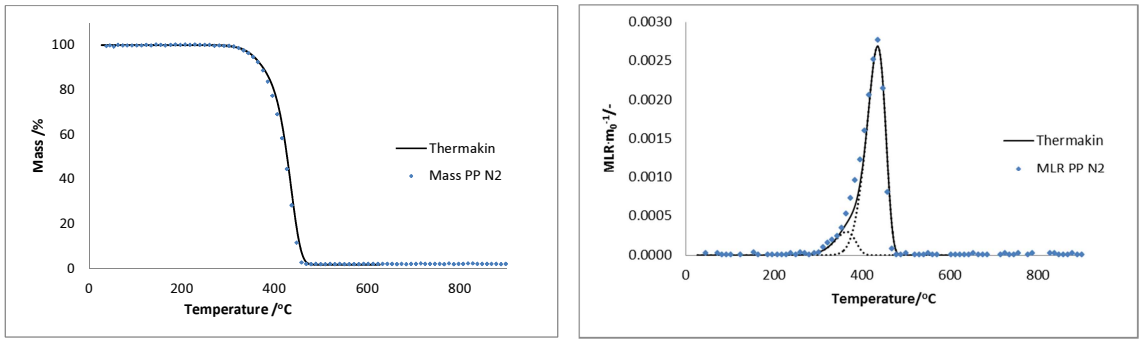

(a) (b)

Figure 75 Two reactions ThermaKin model of PP decomposition in nitrogen atmosphere (a) mass loss and (b) mass loss rate curve

Table 27 Mechanism of PP decomposition in N_2

Reaction 1	Reaction 2
$PP \rightarrow 0.89PP_{residue1} + 0.11PP_{volatiles1}$	$PP_{residue1} \rightarrow 0.02PP_{residue2} + 0.98PP_{volatiles2}$
$A = 2.36 \times 10^9\ sec^{-1}$ $E_a = 1.41 \times 10^5$ J/mol	$A = 1.26 \times 10^{12}\ sec^{-1}$ $E_a = 1.93 \times 10^5$ J/mol

The two reaction mechanism from

Table 27 improves ThermaKin's fit of the PP pyrolysis curve obtained in N_2.

Mixtures of volatiles products in nitrogen are detected by FTIR and can be found in Figure 77. There is some reason to believe that two different mixtures of volatiles were detected such as $PP_{volatiles1}$ and $PP_{volatiles2}$ as indicated in ThermaKin mechanism because the peak at 1261 cm^{-1} is present only in the higher temperature corresponding to reaction 2, however, the evidence from FTIR is not very convincing.

The idea of PP ThermaKin model in air presented in Figure 76 is to maintain 2 pyrolysis reactions from nitrogen simulation and to add another four reactions corresponding to the oxidation mechanism as it is shown in Table 28.

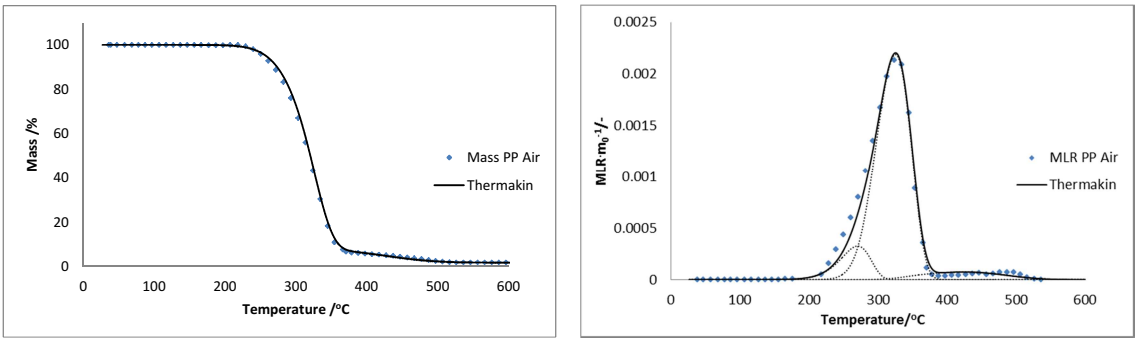

(a) (b)

Figure 76 ThermaKin model of PP decomposition in air (a) mass loss and (b) mass loss rate curve

The fit of the solid ThermaKin MLR line from Figure 76b with experimental results is supported by three grey dotted lines corresponding to each reaction in order respectively to appearance.

Table 28 Mechanism of PP decomposition in air

Reaction 1 Pyrolysis $PP \rightarrow 0.89PP_{residue1} + 0.11PP_{volatiles1}$ $A = 2.36 \times 10^{9}\ sec^{-1}\ E_a = 1.41 \times 10^{5}$ J/mol	Reaction 2a Oxidation $PP_{residue1} \rightarrow 0.2PP_{residue2} + 0.8PP_{volatiles2a}$ $A = 1.26 \times 10^{12}\ sec^{-1}\ E_a = 1.93 \times 10^{5}$ J/mol
Reaction 1a Oxidation $PP \rightarrow 0.89PP_{residue1} + 0.11PP_{volatiles1a}$ $A = 2.73 \times 10^{8}\ sec^{-1}\ E_a = 1.1 \times 10^{5}$ J/mol	Reaction 2b Oxidation $PP_{residue1} \rightarrow 0.09PP_{residue2} + 0.91PP_{volatiles2a}$ $A = 2.45 \times 10^{7}\ sec^{-1}\ E_a = 1.1 \times 10^{5}$ J/mol
Reaction 2 Pyrolysis $PP_{residue1} \rightarrow 0.11PP_{residue2} + 0.89PP_{volatiles2}$ $A = 1.26 \times 10^{12}\ sec^{-1}\ E_a = 1.93 \times 10^{5}$ J/mol	Reaction 3 Oxidation $PP_{residue2} \rightarrow 0.2PP_{residue3} + 0.8PP_{volatiles2a}$ $A = 4.61 \times 10\ sec^{-1}\ E_a = 5.73 \times 10^{4}$ J/mol

The reaction mechanism including oxidation is provided in Table 28. Four oxidation reactions were included that were not present in the pyrolysis mechanism. The mechanism has sequential reactions, similar to the pyrolysis mechanism, but also incorporates parallel reactions that compete with reactions 1 and 2. The competitive reactions 1a and 2a act to effectively speed-up reaction 1 and 2 without the loss of more mass. Reaction 2b acts to

effectively speed-up reaction 2 and decrease the residue yield. Reaction 3 illustrates the oxidation of the tail at the end of PP degradation process. All volatile products from the ThermaKin mechanism such as $PP_{volatiles1a}$ and $PP_{volatiles2a}$ can be found in Figure 78. Although there are 3 oxidative reactions only two different mixtures of volatiles are detected by FTIR.

Table 29 The universal reaction mechanism for PP as a function of ambient oxygen volume fraction

Reaction description	Temp. (˚C)	Gas-phase products
Reaction 1 Pyrolysis $PP \rightarrow 0.89PP_{residue1} + 0.11PP_{volatiles1a}$ $A = 2.36 \times 10^{9}\ sec^{-1}\ E_a = 1.41 \times 10^{5}$ J/mol	270-350	2-methyl-1-butene 2-methyl-1-pentene 2-methyl-1-hexene 2-methyl-1-heptene Double bonded hydrocarbons
Reaction 1a Oxidation $PP \rightarrow 0.89PP_{residue1} + 0.11PP_{volatiles1a}$ **$A = 1.3 \times 10^{7}\ [O_2\%]\ sec^{-1}$** $E_a = 1.1 \times 10^{5}$ J/mol	220-300	H_2O, CO_2, CO, 1-pentene 2-methyl-1-pentene,
Reaction 2 Pyrolysis $PP_{residue1} \rightarrow 0.11PP_{residue2} + 0.89PP_{volatiles2a}$ $A = 1.26 \times 10^{12}\ sec^{-1}\ E_a = 1.93 \times 10^{5}$ J/mol	330-470	2-methyl-1-butene 2-methyl-1-pentene 2-methyl-1-hexene 2-methyl-1-heptene Double bonded hydrocarbons
Reaction 2a Oxidation $PP_{residue1} \rightarrow 0.2PP_{residue2} + 0.8PP_{volatiles2a}$ **$A = 6.01 \times 10^{10}\ [O_2\%]\ sec^{-1}$** $E_a = 1.93 \times 10^{5}$ J/mol	230-360	2-pentanone, 3-pentanone, 3-methyl-2-butanone 3-methyl-2-pentanone, 4-methyl-2-pentanone 4-methyl-2-pentene, pentene, benzaldehyde, ethanal, propanal, propenal, 2-butanal, benzaldehyde, propanol
Reaction 2b Oxidation $PP_{residue1} \rightarrow 0.09PP_{residue2} + 0.91PP_{volatiles2a}$ **$A = 1.17 \times 10^{6}\ [O_2\%]\ sec^{-1}$** $E_a = 1.1 \times 10^{5}$ J/mol		
Reaction 3 Oxidation $PP_{residue2} \rightarrow 0.2PP_{residue3} + 0.8PP_{volatiles2a}$ **$A = 2.2 \times 10^{-1}\ [O_2\%]\ sec^{-1}$** $E_a = 5.73 \times 10^{4}$ J/mol	350-500	

The reaction mechanism in Table 29 was constrained by the requirement that the Arrhenius pre-exponential factor was a function of the ambient oxygen concentration, given as a volumetric fraction, and the requirement that at 0% oxygen concentration this

mechanism would revert to the pyrolysis mechanism given in Table 27. It should be noted that this model is tested only for oxygen level of 21%.

6.1.1.3 FTIR Thermal Degradation Products

Figure 77 presents two decomposition steps for the polypropylene sample in nitrogen at a heating rate of 10°C/min. Approximate temperatures can be calculated from the times, for example 36 minutes corresponds to a 360°C temperature increase, from ambient (about 20°C) so the temperature at 36 minutes is ~380°C. Spectra were matched against spectra taken from TQ library software. In nitrogen, double bonded hydrocarbons show good matching to the selected peaks, but are very similar to each other. Each of the molecules listed in Table 27 consistent with fragments of polypropylene resulting from random chain scission, and thus a mixture of these compounds may have been present. There is a very strong peak for hydrocarbons at 2966cm^{-1} and a few smaller peaks observed for wavenumbers lower than 1700cm^{-1}. As this test is carried out in nitrogen, carbon dioxide and monoxide would not be expected. There is only one noticeable difference between 36th and 46th minute which is assigned to the peak located at 1261cm^{-1} suggesting the presence of a different volatile.

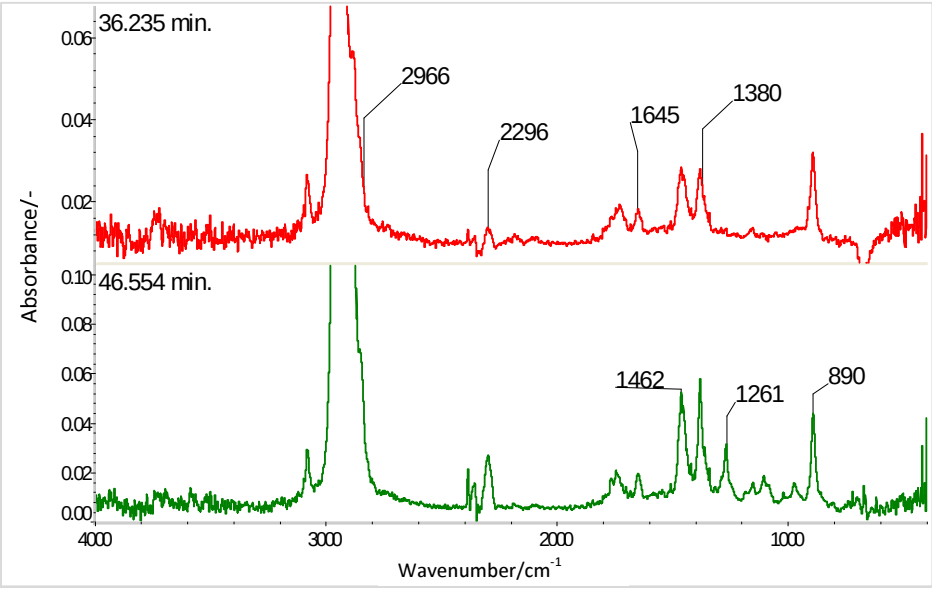

Figure 77 Selected spectra and peak for the PP analysis in nitrogen

Table 30 presents possible hydrocarbons which fit the best to analysed spectra within the 3100-2800 cm^{-1} wavenumber region. In terms of positive identification of which hydrocarbon is present other FTIR settings or other alternative techniques would be required.

Table 30 Possible volatiles for polypropylene decomposition in nitrogen

Wavelength/cm^{-1}	**Possible Compounds**
2966	2-methyl-1-butene
1645	2-methyl-1-pentene
1462	2-methyl-1-hexene
1380	2-methyl-1-heptene
890	

Figure 78 presents decomposition product at different times for PP tested in air atmosphere. The major products are formed at 26 - 38 min region. It seems that peaks at 2967 and 1731cm^{-1} represent hydrocarbons similar to 1-pentene. As tests were carried out in air, CO and CO_2, as well as water (H_2O) tend to dominate the spectra. For peaks occurring at 2967 and 1731cm^{-1}, 2-methyl-1-pentene or 4-methyl-2-pentanone was found. Table 31 presents possible volatiles chosen for 1369 cm^{-1} for polypropylene decomposition. Further analysis (like pyGCMS) is required to unambiguously identify the decomposition products occurring at this wavenumber.

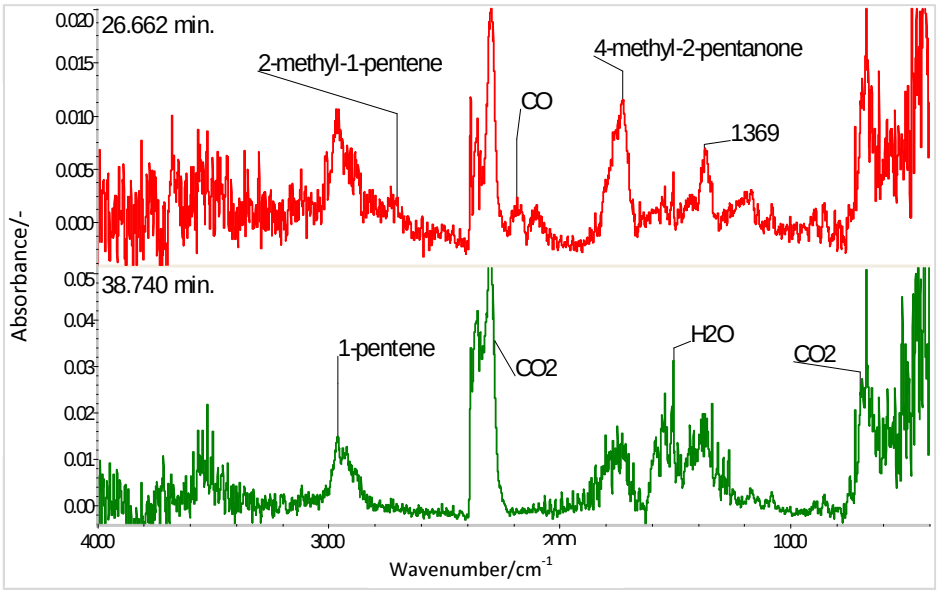

Figure 78 Selected spectra and peaks for the PP analysis in air

Table 31 Possible volatiles for polypropylene decomposition in air

Wavelength/cm^{-1}	**Possible Compounds**
1369	2-pentanone, 3-pentanone, 3-methyl-2-butanone 3-methyl-2-pentanone, 4-methyl-2-pentanone 4-methyl-2-pentene, pentene, benzaldehyde ethanal, propanal, propenal, 2-butanal, benzaldehyde, propanol

6.1.2 Thermal decomposition, degradation products and modelling of polypropylene with nanoclay

6.1.2.1 TGA Thermal Decomposition

TGA curves in Figure 79 and Figure 80 provide information about temperature dependence of the decomposition reactions of polypropylene containing 5% nanoclay in nitrogen and air respectively.

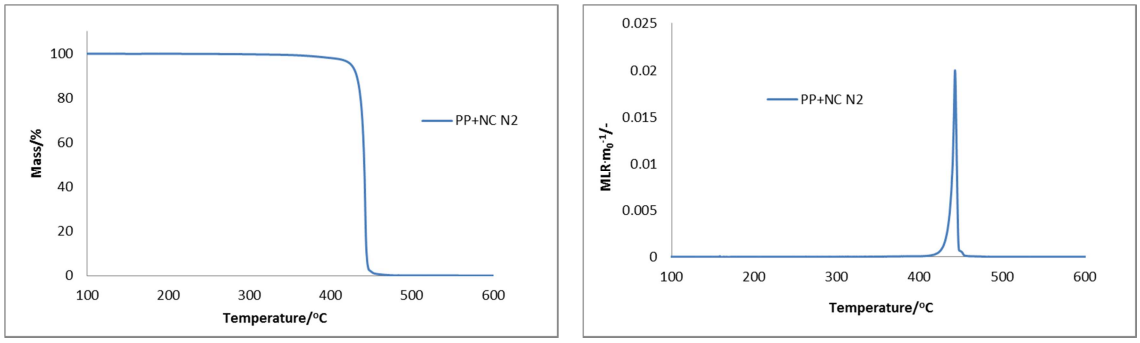

(a) (b)

Figure 79 TGA of PP+NC in nitrogen atmosphere (a) mass loss and (b) mass loss rate curve

The decomposition of PP+NC in N_2 is much sharper, and occurs at a higher temperature than for PP without NC. The presence of oxygen changes the decomposition process of PP+NC as seen on Figure 80.

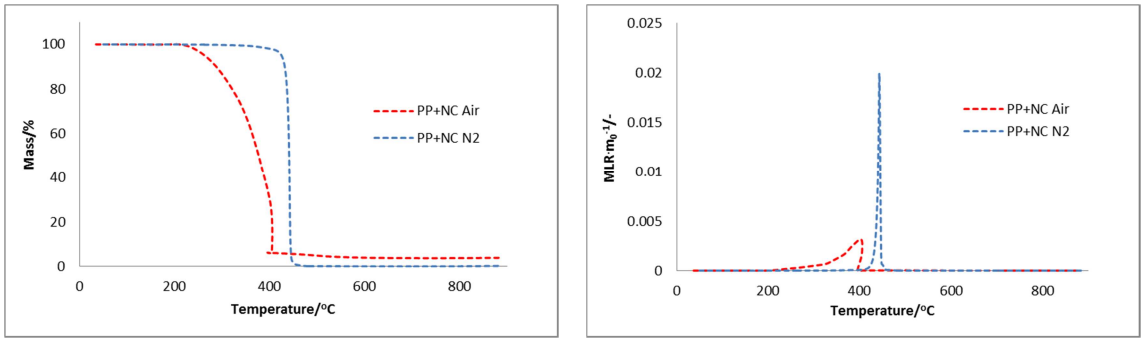

(a) (b)

Figure 80 Comparison of TGA curves in air and nitrogen

It is clear that oxidation is accelerating the mass loss of PP+NC. Mass loss in air starts at 220°C, and at 405°C a small shoulder is formed. Such mass loss behaviour is not observed in nitrogen. In nitrogen mass loss occurs at higher temperature 440°C but is much faster than in air.

6.1.2.2 ThermaKin Modelling of PP with Nanoclay

In this case model assumption is that Nanoclay is well-dispersed in PP and a separate mechanism for polymer and nanofiller decomposition will not be considered. It has been reported that when a well-dispersed system is obtained, loadings of 3 to 5% are sufficient to cause a large improvement in mechanical properties and a significant reduction in the rate of peak heat release[111]. In other words PP+NC model may be entirely independent of the PP model.

Decomposition of PP+NC in nitrogen is a single step reaction as seen on Figure 79 so single reaction mechanism is proposed to model PP+NC behaviour in N_2.

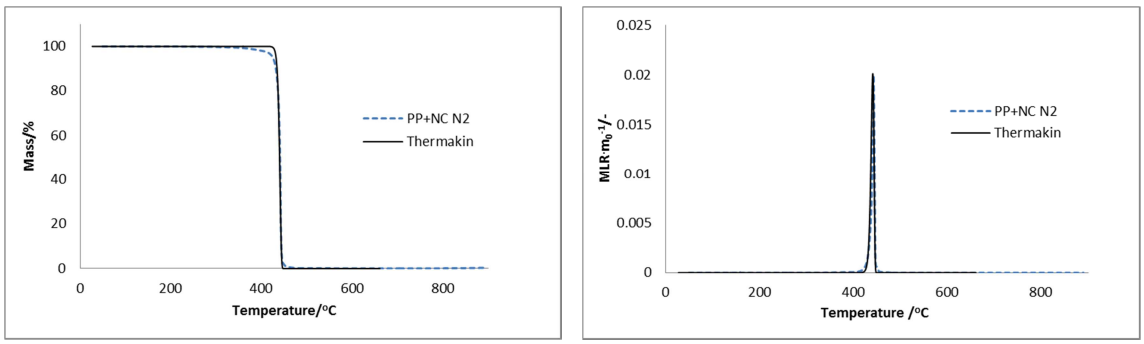

(a) (b)

Figure 81 ThermaKin fit of PP+NC in nitrogen atmosphere (a) mass loss and (b) mass loss rate curve

Single reaction mechanism:

$PP\_NC \rightarrow PP\_NC_{volatiles}$

$A = 4.34 \times 10^{99}\ sec^{-1}\ E_a = 1.38 \times 10^{6}\ J/mol$

As seen on Figure 81 single reaction ThermaKin fit gives satisfactory result. Possible $PP\_NC_{volatiles}$ products can be found in Figure 83.

In the PP+NC ThermaKin model in air (Figure 82), the pyrolysis reaction from the decomposition in nitrogen is still present and another two reactions corresponding to oxidation process are added as shown in Table 32.

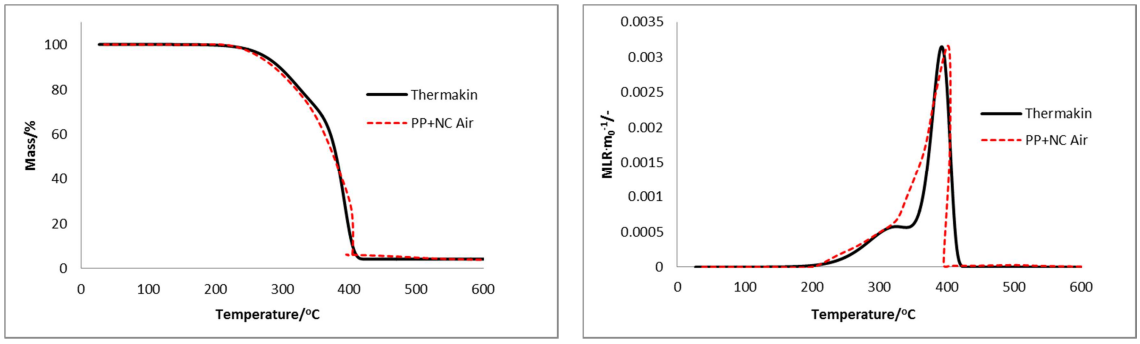

(a) (b)

Figure 82 ThermaKin model of PP+NC decomposition in air (a) mass loss and (b) mass loss rate curve

Table 32 Mechanism of PP+NC decomposition in air

Reaction 1 Oxidation $PP\_NC \rightarrow 0.7PP\_NC_{residue1} + 0.3PP\_NC_{volatiles1}$ $A = 4.98 \times 10^{4}\ sec^{-1}\ E_a = 8.0 \times 10^{4}\ J/mol$	Reaction 3 Pyrolysis $PP\_NC \rightarrow PP\_NC_{volatiles2}$ $A = 4.34 \times 10^{99}\ sec^{-1}\ E_a = 1.38 \times 10^{6}\ J/mol$
Reaction 2 Oxidation $PP\_NC_{residue1} \rightarrow 0.06PP\_NC_{residue2} + 0.94PP\_NC_{volatiles2}$ $A = 1.87 \times 10^{19}\ sec^{-1}\ E_a = 2.7 \times 10^{5}\ J/mol$	

Two oxidation reactions were added to the pyrolysis mechanism. The first oxidation reaction is responsible for starting the decomposition process at lower temperature than in nitrogen, and another oxidative reaction is responsible for creating a protective layer that leaves 4% residue at the end. Possible volatiles products associated with $PP\_NC_{volatiles1and2}$ can be found in Table 35.

Table 33 The universal reaction mechanism for PP+NC as a function of ambient oxygen volume fraction

Reaction description	Temp. (˚C)	Gas-phase products
Reaction 1 Oxidation $PP\_NC \rightarrow 0.7PP\_NC_{residue1}$ + $+0.3PP\_NC_{volatiles1}$ **$A = 2.38 \times 10^3 [O_2\%]\ sec^{-1}$** $E_a = 8.0 \times 10^4$ J/mol	200-300	H_2O, CO_2, CO, 1-pentene, 2-propanone, 4-methyl-2-pentanone, 4-methyl-2- pentene 2-methyl-1-pentene, 2-pentanone, 3-pentanone, 3-methyl-2-butanone, 3- methyl-2-pentanone pentene, benzaldehyde, ethanal, propanal, propenal, 2-butanal, benzaldehyde, propanol
Reaction 2 Oxidation $PP\_NC_{residue1} \rightarrow 0.06PP\_NC_{residue2}$+ $+0.94PP\_NC_{volatiles1}$ **$A = 8.92 \times 10^{17} [O_2\%]\ sec^{-1}$** $E_a = 2.7 \times 10^5$ J/mol	250-420	
Reaction 3 Pyrolysis $PP\_NC \rightarrow PP+NC_{volatiles2}$ $A = 4.34 \times 10^{99}\ sec^{-1}$ $E_a = 1.38 \times 10^6$ J/mol	390-445	2-methyl-1-butene 2-methyl-1-pentene 2-methyl-1-hexene 2-methyl-1-heptene Hydrocarbons, isocyanate

A single universal reaction mechanism in Table 33 showed that it was possible to obtain good fit for two experimental conditions. This shows the Arrhenius pre-exponential factor was a function of the ambient oxygen concentration, given as a volumetric fraction, and the 0% oxygen concentration is equivalent to the pyrolysis mechanism in nitrogen.

As observed, the combination of nanoclay and PP (Table29) has significantly larger kinetic parameters than those for PP in nitrogen (Table 33). The biggest difference is reported for the frequency factor *A*, where value is higher by approximately 87 orders of magnitude! The activation energy difference is about 1 order of magnitude. In air, the difference between the pre-exponential factors is also large, at approximately 7 orders of magnitude, while the activation energies stay close to each other.

An alternative theory of fire retardant performance of polymer nanocomposites containing plate-like clays is that the plates impede the passage of oxygen into, and volatile fuel out of the molten polymer. Although this was not investigated in the current work it is

believed that it could be investigated using ThermaKin and altered gas diffusion parameters. A second component, NC would react to loose its organic coating leaving the clay residue.

6.1.2.3 FTIR Thermal Degradation Products

Figure 83 presents different spectra for PP+NC decomposition carried out in nitrogen. Similarly to all other tests carried out in nitrogen there are very strong peaks observed for hydrocarbons as well as peak located at 2296 cm^{-1} which may be an isocyanate, however this requires further analysis.

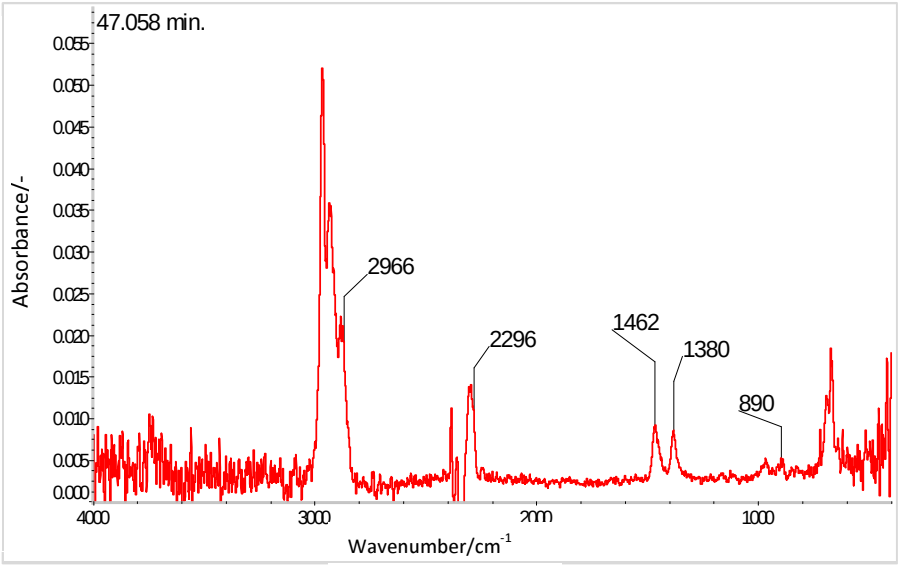

Figure 83 Selected spectra and peaks for the PP+NC analysis in nitrogen

Table 34 present possible hydrocarbons found for the selected spectrum. All products are very similar to PP decomposition products.

Table 34 Possible volatiles for polypropylene and nanoclay, decomposition in nitrogen

Wavenumber / cm^{-1}	**Possible Compounds**
2966	2-methyl-1-butene
1462	2-methyl-1-pentene
1380	2-methyl-1-hexene
890	2-methyl-1-heptene

Figure 84 presents peaks occurring at different times for polypropylene mixed together with nanoclay. Tests were carried out in air, therefore CO, CO_2, and H_2O are found. Similar hydrocarbon peaks, as for polypropylene decomposition (in air), together with additional peaks found for PP+NC are summarised and reported in Table 35.

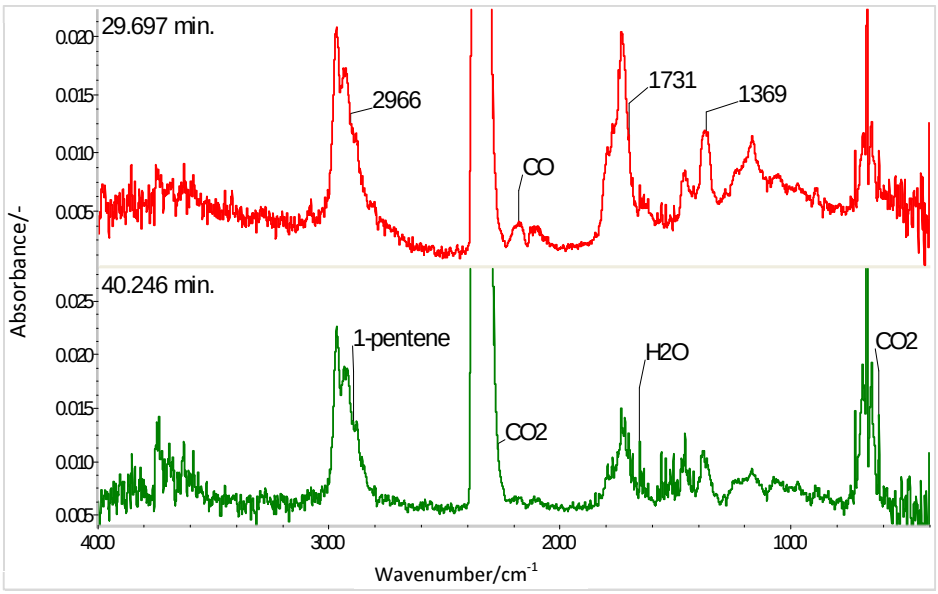

Figure 84 Selected spectra and peaks for the PP+NC analysis in air

Table 35 Possible volatiles for polypropylene with nanoclay, decomposition in air

Wavelength /cm^{-1}	**Possible Compounds**
2966	1-pentene, 2-propanone,
1731	4-methyl-2-pentanone, 4-methyl-2-pentene
1369	2-methyl-1-pentene, 2-pentanone,
	3-pentanone, 3-methyl-2-butanone, 3-methyl-2-pentanone
	pentene, benzaldehyde, ethanal, propanal, propenal
	2-butanal, benzaldehyde, propanol

6.1.3 Thermal Degradation products found from FTIR in Polypropylene Sample with Fire Retardant

In this part only FTIR data analysis is presented and no ThermaKin model is proposed as mechanism of thermal degradation of PP+FR is a long way from being understood.

Figure 85 presents spectra in nitrogen for PP+FR at different times. Most of the peaks are very similar to peaks coming from PP decomposition (possible hydrocarbons are listed in Table 35), however some new absorbances are also observed. Two new peaks are observed for ammonia and occurring at 964 and 933cm^{-1}. As explained for the PP+NC sample an extra peak is produced at 2296cm^{-1}, as this sample was tested in nitrogen it seems unlikely that the peak results from carbon dioxide. Isocyanates have characteristic peak occurring in this region, however as there are no comparison spectra in the library it is difficult to confirm this. In addition there are some peaks like 1066 cm^{-1} which can be possibly assigned to volatiles containing nitrogen.

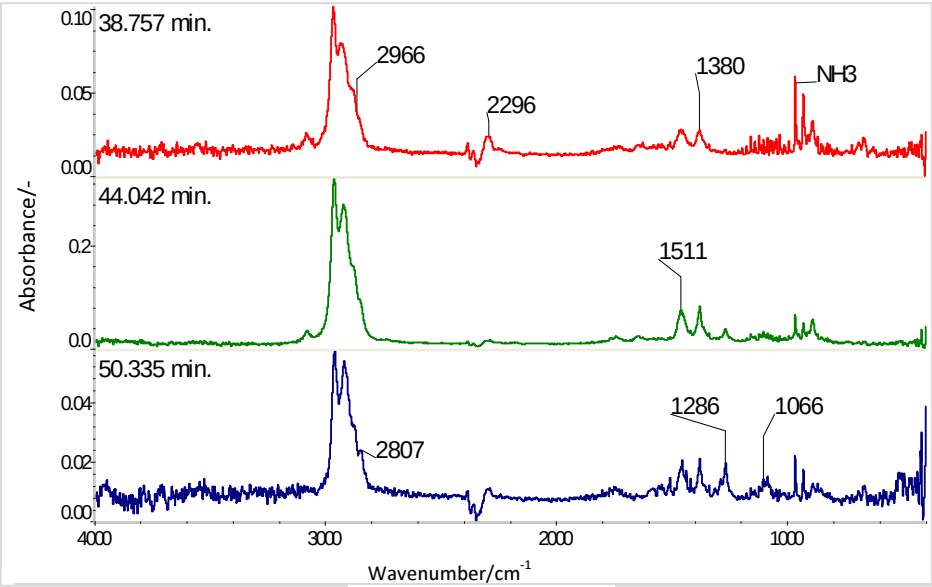

Figure 85 Selected spectra and peaks for the PP+FR analysis in nitrogen

Table 36 Possible volatiles for polypropylene with fire retardant, decomposition in nitrogen

Wavelength /cm^{-1}	**Compounds**
2966 1380	2-methyl-1-butene, 2-methyl-1-pentene 2-methyl-1-hexene, 2-methyl-1-heptene 2,3-dimethyl-1-butene, 2-methy;-butane 2-methyl-pentane, 2,3-dimethyl butane
2807 1066	N, N-diethylethanolamine N-methylaniline Triethylamine

Figure 86 presents spectra at different PP+FR decomposition times carried out in air. Compared to previous materials, the spectra look more complex and more bonds are observed. It seems that fire retardant changes the decomposition so that more volatiles are formed alongside the carbon monoxide and carbon dioxide and hydrocarbons already identified for polypropylene. An interesting peak is at 2297 cm^{-1} which indicates isocyanates presence, however, in order to determine if it is something other than carbon dioxide further analysis would be required. Additional peaks are observed at 2806, 1743, 1286, or 1057 cm^{-1}, compared to the PP sample, which corresponds to acrylamide or other group containing nitrogen. Possible volatiles are listed in Table 37.

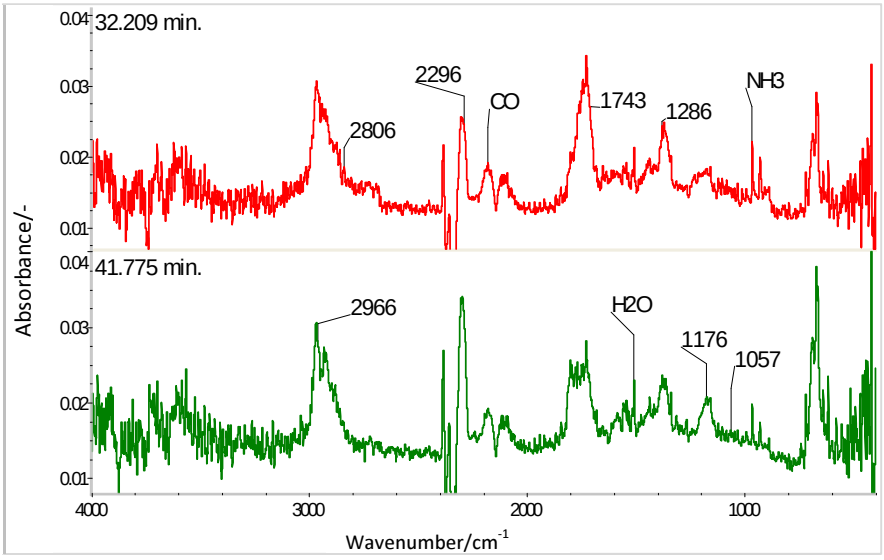

Figure 86 Selected spectra and peaks for the PP+FR analysis in air

Table 37 Possible volatiles for polypropylene with fire retardant decomposition in air

Wavelength /cm^{-1}	**Possible Compounds**
2966 2720 1176	2-methyl-1-pentene, 3-methyl-2-pentanone, 4-methyl-2-pentanone, 2-butanone, 2-pentanone, 3-pentanone, 2-propanol, Propanal, Propenal
2297	CHON peak
1057	N, N-diethylethanolamine
2806 1032	Triethanolamine
1743	N-methylformamide
plus all compounds found in PP sample tested in air from Table 31	

6.1.4 Thermal Degradation products found from FTIR in Polypropylene Sample with Nanoclay and Fire Retardant

Similarly to PP+FR also for PP+FR+NC a ThermaKin model has not been attempted, but the vapour phase FTIR data has been analysed for future reference.

Figure 87 presents spectra at different decomposition temperature/times for PP+FR+NC. Tests were carried out in nitrogen. It is seen that all peaks are combinations of all previously analysed samples: PP, PP+FR and PP+NC. Similar to the other samples, the hydrocarbon peaks remain very strong when decomposed in nitrogen compared to other products. Ammonia is observed with additional peaks at 1286, 868cm^{-1}. The peak at 2296 cm^{-1} indicates isocyanate presence, however it requires further analysis.

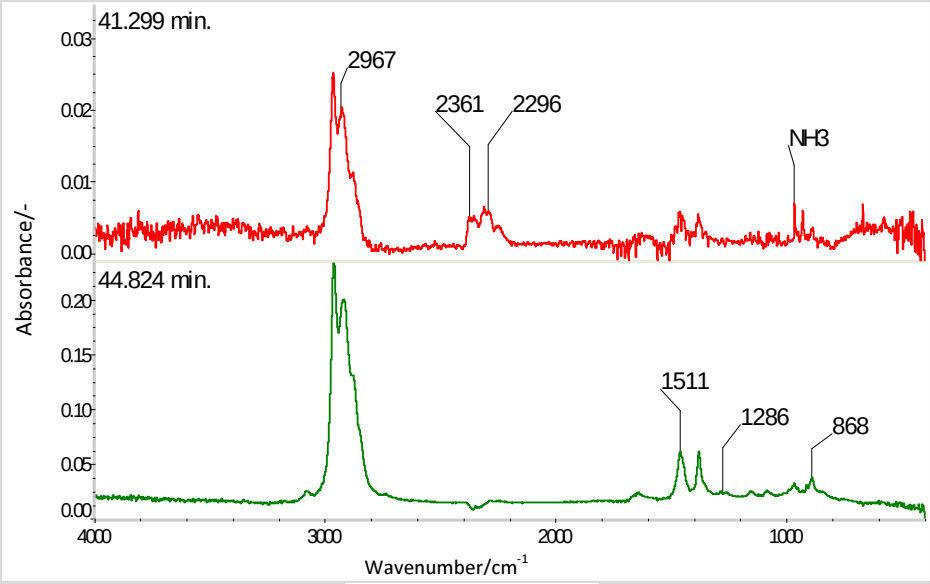

Figure 87 Selected spectra and peaks for the PP+FR+NC analysis in nitrogen

Figure 88 presents selected spectra and peaks for PP+FR+NC sample analysis in air. There is strong carbon monoxide peak as well as a peak occurring at 2296cm^{-1} which may be carbon dioxide or isocyanates (although it is much smaller compared to all other samples). The hydrocarbon peak (2967cm^{-1}) is much smaller compared to peak occurring at 1707cm^{-1}. In addition many small peaks are shown in 1400-1700 cm^{-1} region. This indicates a possible reduction of vapour phase fuel (hydrocarbon) by the FR/NC combination. As this spectrum is the most complex, the analysis is more difficult compared to previous samples. It seems that all peaks are combined spectra from PP, PP+FR and PP+NC samples and presented below.

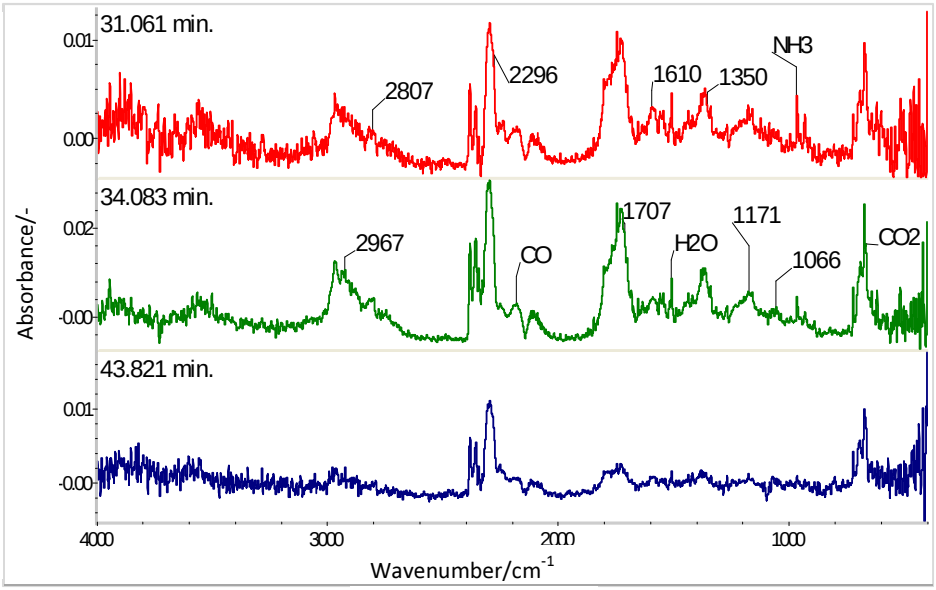

Figure 88 Selected spectra and peaks for the PP+FR+NC analysis in air

6.1.5 Further Analysis and Conclusions on Thermal Degradation of Polypropylene with Fire Retardant and Nanoclay

The shoulder at the end of thermal decomposition is important as it is indicative of residue formation which will protect the underlying polymer during burning. PP is very susceptible to oxidative degradation, and less than 1% O_2 is enough to achieve this. The decomposition of PP+NC is like the behaviour when all the O_2 has been stripped from the system, the behaviour of PP may result from small amounts of O_2 being desorbed from the furnace walls etc. Fire retardants frequently promote earlier decomposition, but in doing so form more stable residues (bigger shoulders). All samples except pure polypropylene or polypropylene together with nanoclay produce residues in air and nitrogen atmosphere.

Considering the results for TGA tests carried out **in nitrogen**, PP+NC shows very sharp decomposition compared to other samples. PP samples containing FR show an early onset of decomposition, but less residue at 500°C than in air.

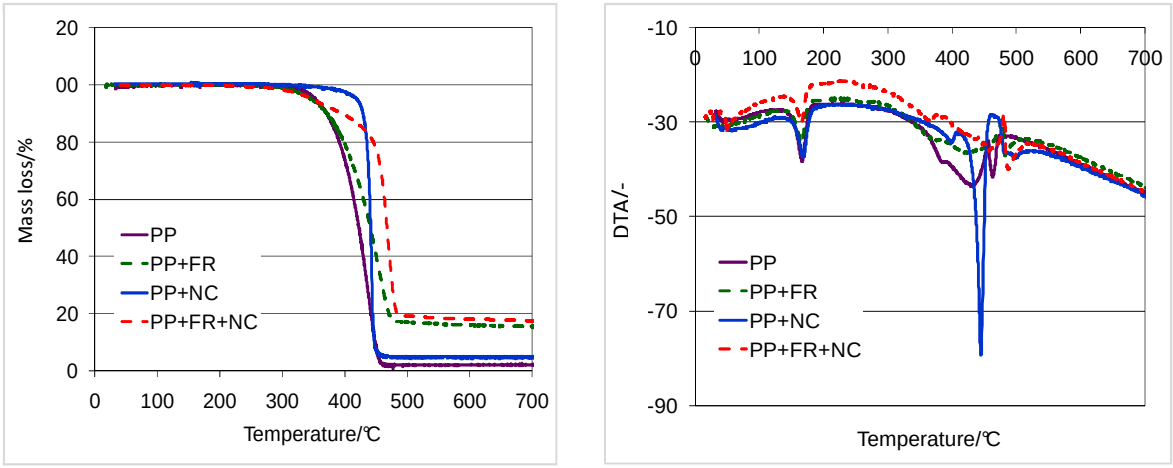

(a) (b)

Figure 89 TGA (a) and DTA (b) curves for PP samples carried out in nitrogen

The TGA results indicate that the nanoclay alone has little effect on the degradation of the polymer blend, whereas together with fire retardant it reduces the peak mass loss rate.

For PP in nitrogen, mostly monomers and randomly cut chain products are found. Samples with FR containing nitrogen and phosphorus in their structure release amines, amides and possibly isocyanates in both air and nitrogen. However, as FTIR analysis is not specified to a particular compound, further analysis like pyGCMS are required to identify nitrogen and phosphorus compounds. For the PP+NC sample in air, all profiles have lower absorbance than PP, reflecting the lower amount of hydrocarbon and organic compounds released during decomposition process; similarly not many nitrogen containing compounds are observed. In nitrogen, for the same sample, compounds are very similar to compounds obtained during PP decomposition. Finally for PP+FR+NC a mixture of compounds from PP, PP+FR and PP+NC are observed both in nitrogen and air.

Figure 90 shows the temperature/evolution profiles under nitrogen for hydrocarbons, ammonia and carbon dioxide. Hydrocarbon profiles for samples PP+NC and PP+FR have approximately the same peak temperature (~450°C). The lowest thermal stability is observed for the pure PP and the highest for the sample containing both the fire retardant and nanoclay. Similar to decomposition in air, ammonia is produced only from fire retarded samples as may be expected as a decomposition product of ammonium phosphate. The highest absorbance is observed for PP+FR.

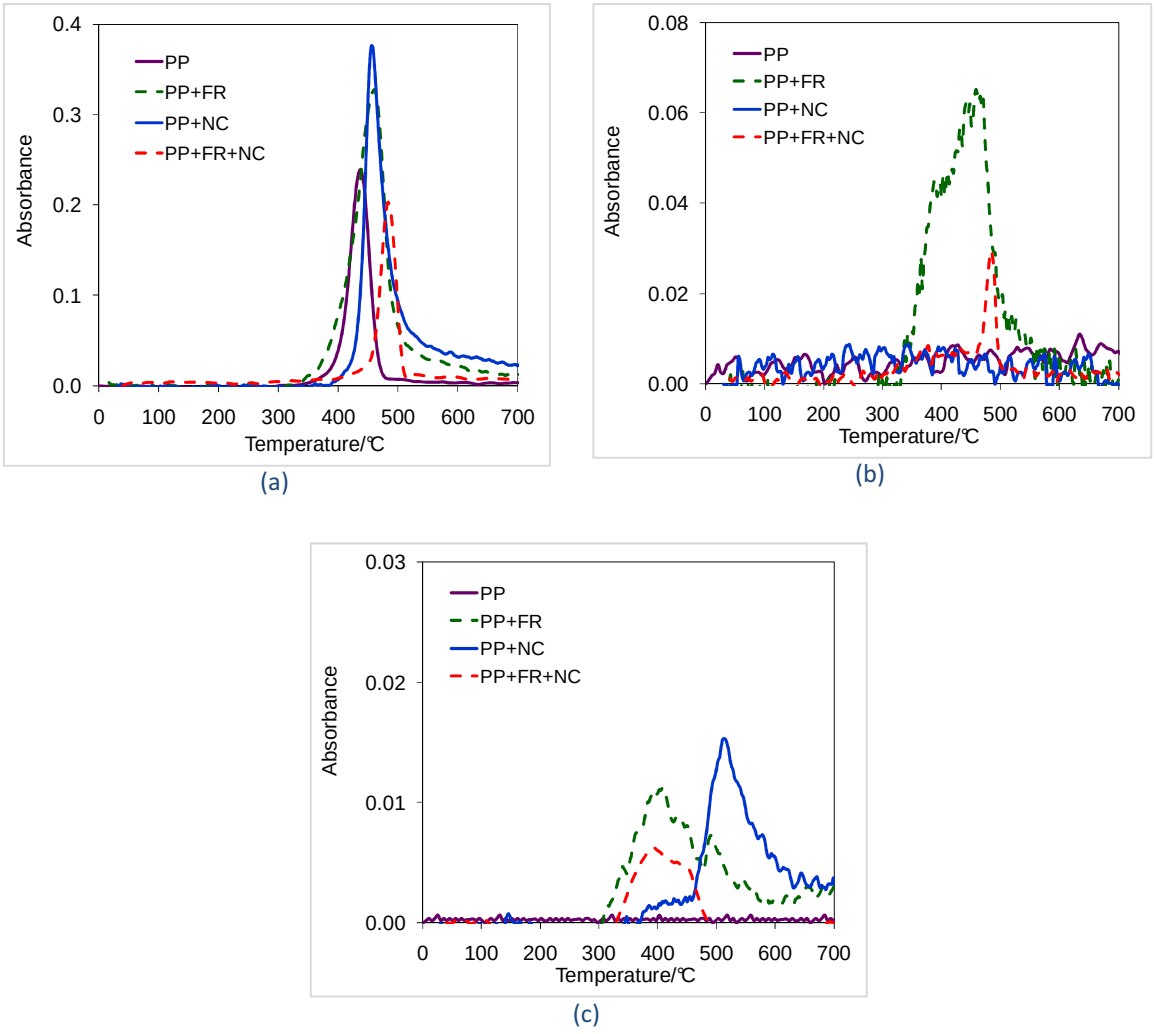

Figure 90 Pyrolysis products of PP under nitrogen: (a) Hydrocarbons (2967 cm^{-1}), (b) Ammonia (963 cm^{-1}) and (c) Isocyanates (2296 cm^{-1})

Possibly isocyanites evolved from all samples in nitrogen except PP. For fire retarded samples the peak maxima is shifted to lower temperatures (400°C) compared to the sample containing only nanoclay (~520°C). From the low temperature of evolution, it seems likely that the CO_2 is a decomposition product from the surfactant (organic coating) or APP, not a leak of air into the system.

Decomposition in air indicates the processes which may occur before ignition, while their absence or delay under nitrogen is indicative of a condensed phase decomposition mechanism. Figure 91 present TGA-DTA curves for all PP samples. Tests were carried out in air.

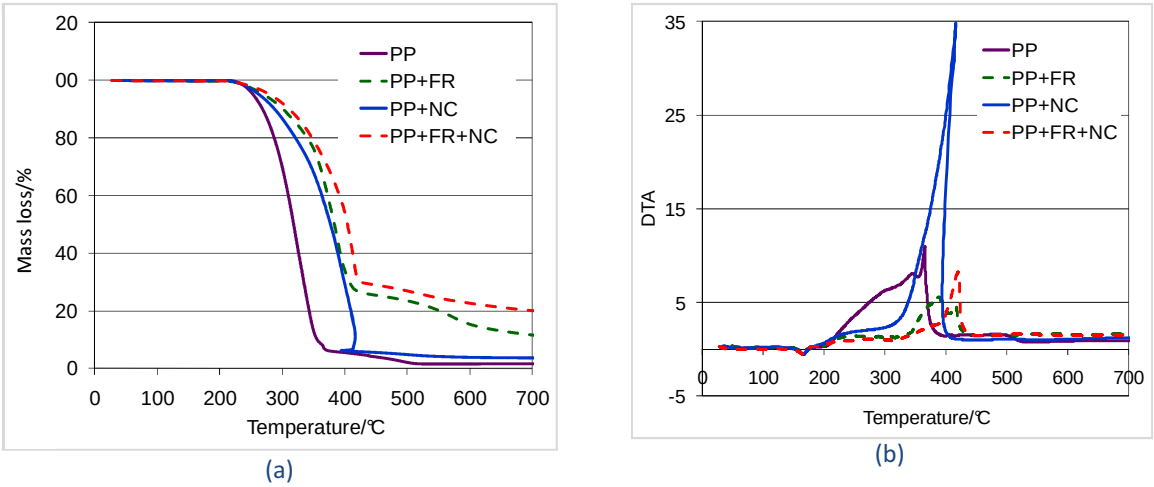

(a) (b)

Figure 91 TGA (a) and DTA (b) curves for PP samples carried out in air

The TGA shows significant enhancement of oxidative stability of the early decomposition stages of PP+NC and of PP+FR and PP+FR+NC. TGA in air shows a small char "shoulder" at 400-500°C for PP and PP+NC but a much larger shoulder for samples containing FR. The DTA in air shows a strong exotherm for PP+NC indicating that clay promotes surface oxidation reactions. The FR samples show the smallest exotherms.

In addition, analysis profiles for the major peaks were generated for identified compounds in air. Figure 92a shows the evolution of CO_2 (bend at 667 cm^{-1}) with temperature during pyrolysis in air for all samples. CO_2 production reaches a maximum at 335°C for PP and at approximately 390°C for PP+NC and PP+FR. The presence of FR hinders the onset temperature of reaction and also reduces CO_2 production. The presence of both FR and NC, not only reduces the carbon dioxide concentrations, but also produces products with the highest thermal stability compared to all other materials (the maxima are shifted to 440°C).

Figure 92b shows the CO (stretch at 2099 cm^{-1}) production profile for each material. CO production begins earliest at 230°C for PP, which reaches a maximum output at 315°C, which is only the decomposition onset temperature for the other materials. The CO production maxima for the PP with additives increase to 390°C for PP+NC and PP+FR and 440°C for PP+FR+NC.

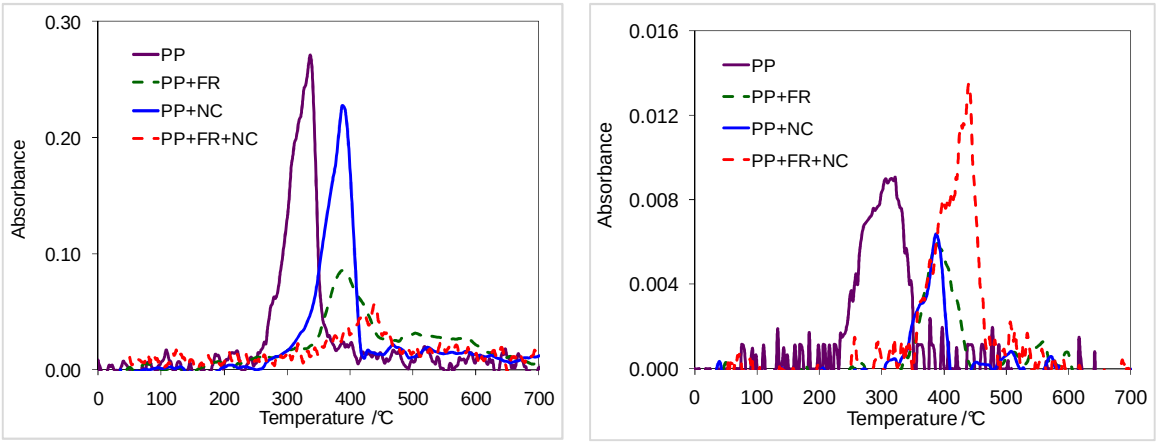

Figure 92(a) Carbon dioxide peak 667 cm^{-1}(b) Carbon monoxide peak 2099 cm^{-1}

Thus, it can be seen that the presence of FR or NC on their own hinders both the onset temperatures of reaction and decreases CO_2 and CO production. However, in combination, FR and NC increase the thermal stability and reduce CO_2 production, but increase CO production dramatically.

Hydrocarbon evolution is presented for each material in Figure 93a. Hydrocarbon production is highest for PP, followed by PP+NC, PP+FR and PP+FR+NC, where the lowest absorbance is observed. Similar to CO_2 production, the highest increase in thermal stability is observed for the combination of nanoclay and flame retardant (440°C). In the presence of FR or NC, the onset temperature of hydrocarbon production is around 390°C and for pure PP 330°C.

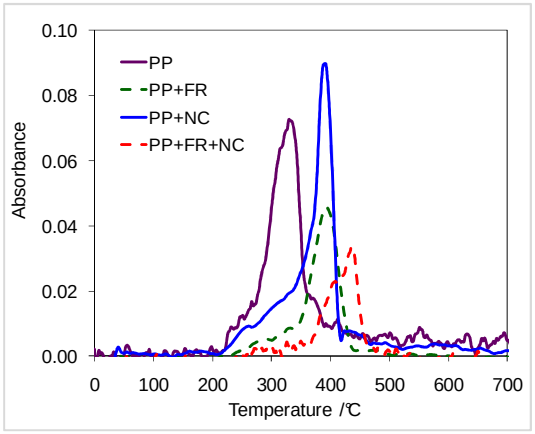

(a)

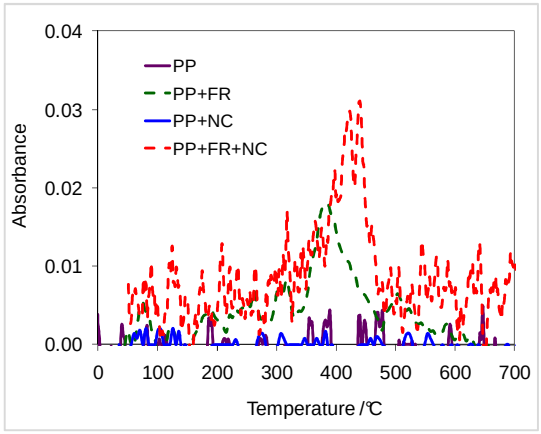

(b)

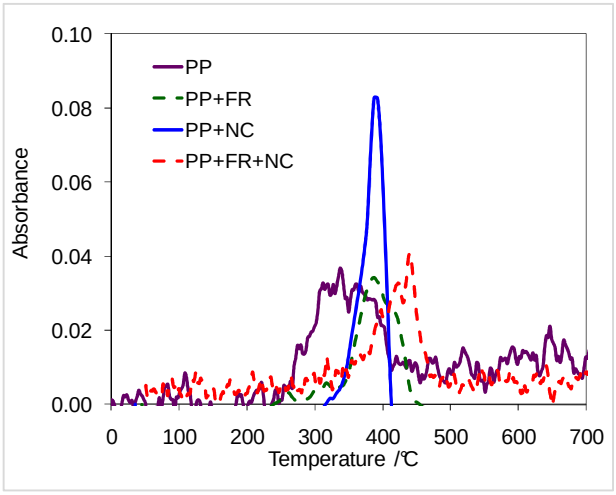

(c)

Figure 93 Pyrolysis products of PP in air: (a) hydrocarbons (2967 cm^{-1}). (b) ammonia (963 cm^{-1}) and (c) water (1509cm^{-1})

Figure 93(b) presents profiles for ammonia – a known decomposition product of the fire retardant ammonium polyphosphate. This nitrogen-containing volatile was observed with the two samples containing the ammonium polyphosphate flame retardant. Decomposition was observed at lower temperatures for the sample without NC, suggesting that the montmorillonite can exchange the ammonium ions for sodium, so protecting the ammonium ions from decomposition within the clay matrix. Alternatively, maybe more likely, the clay platelets, with very high aspect ratios hinder the escape of the ammonia, keeping it trapped for longer within the polymer matrix. It is interesting to note that even though the NC contains alkyl ammonium ions, ammonia is not detected, even at higher temperatures.

Water evolution appears to disrupt the protective layer, allowing the thermal decomposition in air to begin between 225 and 325°C for all materials.

6.1.6 FTIR Analysis of Minor Decomposition products for PP samples in air and nitrogen

Next to major products like carbon monoxide, carbon dioxide, hydrocarbons or ammonia other products were identified and presented in Figure 94. As discussed earlier, for some materials, there was a peak located at 2296cm^{-1}. There is a possibility of assigning this peak to isocyanates or other nitriles compounds which are formed during decomposition of PP+FR, PP+NC and PP+FR+NC samples. As some tests were carried out in nitrogen there is a small chance of it being carbon dioxide. However, as the TQ library does not have examples in a gas phase for isocyanates, additional techniques would be required to confirm these products. The highest peak (intensity) is observed for PP+FR+NC (test carried out in air) which has a sharp peak at 300 – 400°C. Similar to PP+FR+NC in air, the profile in nitrogen, shows much lower intensity. PP+FR sample carried out in air has two characteristics peaks between 300 – 700°C. A similar temperature range of isocyanate formation is observed for the sample tested in nitrogen; however there is weaker difference for two peaks and one broad profile is observed. PP+NC sample carried out in nitrogen shows intensity similar to PP+FR sample, however the temperature is shifted to higher range – around 450 - 550°C.

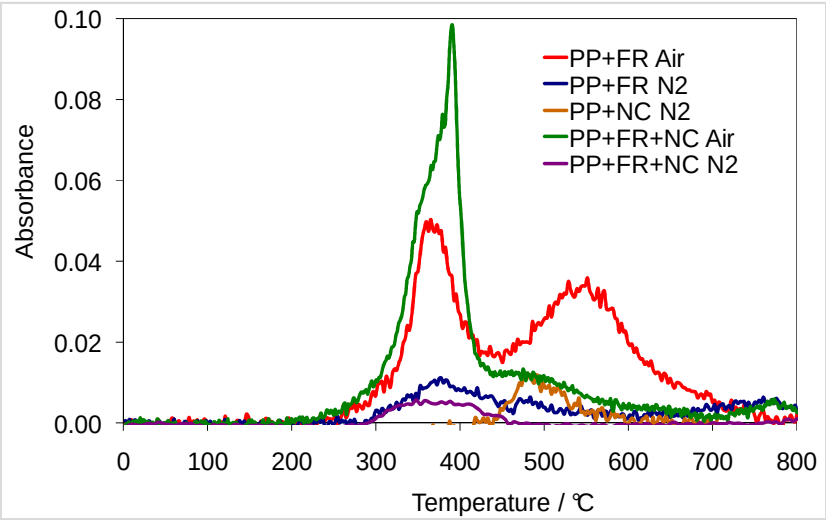

Figure 94 Temperature profile of isocyanates peak 2296cm^{-1}

6.2 STA—FTIR Study on the Thermal Degradation of EVA with Fire Retardant and Nanoclay

In this study, ethylene-vinyl acetate (EVA), fire retardant aluminium hydroxide $Al(OH)_3$ (ATH) and nanoclay (NC) were supplied by Kabelwerk Eupen AG/Belgium. The second mineral filler, magnesium hydroxide $Mg(OH)_2$ (MH), was supplied by Minelco, UK. Six formulations and compositions are presented in Table 38.

Table 38 Studied materials composition

Material	***Polymer/ %***	***Fire Retardant/ %***		***Nanoclay/ %***
		ATH	**MH**	**NC**
EVA	100			
EVA+ATH	32	68		
EVA+MH	32		68	
EVA+NC	95			5
EVA+ATH+NC	32	63		5
EVA+MH+NC	32		63	5

6.2.1 Thermal Decomposition of Mineral Fillers

In this part two mineral fillers are investigated separately as important contributors to overall material behaviour – Aluminium hydroxide $Al(OH)_3$ (often wrongly named and formulated as Alumina Trihydrate – ATH: $Al_2O_3 \cdot 3H_2O$) and Magnesium Hydroxide (MH: $Mg(OH)_2$)- bulk materials that are used as fire retardant fillers for polymers[112,113].These two materials account for more than 50% by weight of the world-wide sales of fire retardants; as much as 400 kt per annum is currently used. Most of this is low cost ATH that is used in thermosetting resins.

The ATH and MH powder was heated in air/nitrogen from 40°C to 900°C at a rate of 10°C/min. The sample masses were approximately 10mg. The thermogravimetric data collected in these tests is displayed in Figure 95. The mass loss rate data was calculated as a numerical differentiation of the total mass data, so the experimental curves may contain some random noise.

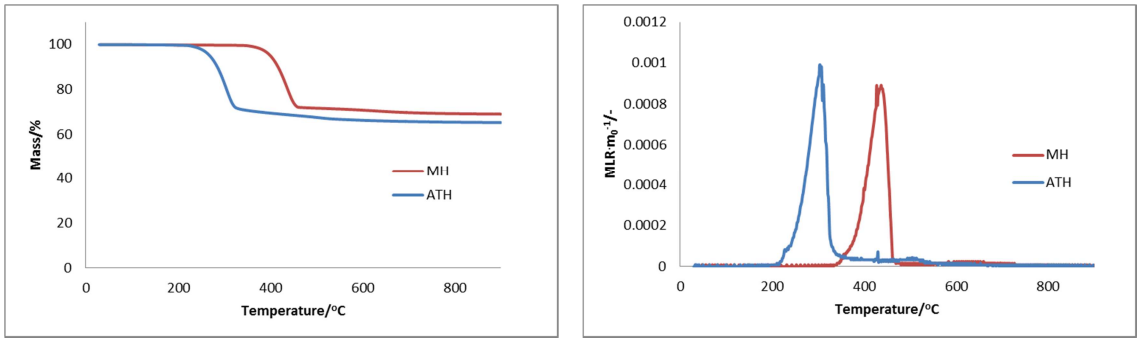

(a) (b)

Figure 95 TGA of ATH and MH (a) mass loss and (b) mass loss rate curve

The use of ATH is limited to those polymers processed below about 300°C while MH is stable above 300°C and thus can be used in polymers that must be processed at higher temperatures.

6.2.2 Fire Retardant Action of Mineral Fillers

The fire retardant action of aluminium hydroxide (ATH) and magnesium hydroxide (MH) are simpler that the complex chemistry of char formation or gas phase inhibition. Some additional analysis has been undertaken to better understand the importance of the different physical effects of these materials as fire retardants (published as part of this work in reference [119]).

Incorporation of any non-combustible filler will reduce the flammability of a polymer, by reducing the total amount of fuel, the rate of diffusion of oxygen into, and fuel from, the polymer bulk while increasing the heat capacity, thermal conductivity, reflectivity and emissivity. There may also be synergistic or antagonistic catalytic[114] or other surface effects associated with the filler, and effects on the polymer melt rheology[115]. In addition, certain inorganic materials decompose endothermically with the release of inert gases or vapour, enhancing the potential fire retardant effect. In order to be effective, the decomposition must

occur in a narrow window above the polymer processing temperature, but at or below its decomposition temperature. In practice most of the suitable materials are group II or III carbonates or hydroxides. They have three fire retardant effects, in addition to those of the inert fillers described above.

1. Endothermic decomposition, absorbing heat and therefore keeping the surrounding polymer cooler.
2. Production of inert diluent gases. Flaming reactions require a critical concentration of free radicals to be self-sustaining. If this concentration falls sufficiently, for example by the release of water or carbon dioxide, flame extinction will occur.
3. Accumulation of an inert layer on the surface of the decomposing polymer, shielding it from incoming radiation, and acting as a barrier to oxygen reaching the fuel, flammable pyrolysis products reaching the gas phase, and radiant heat reaching the polymer.

For example, aluminium hydroxide ($Al(OH)_3$), (which when used as a fire retardant, is commonly referred to as alumina trihydrate (ATH) and formulated as $Al_2O_3.3H_2O$, even though it is neither an alumina, nor a hydrate[116]), decomposes to form alumina (Al_2O_3) with the release of water. It breaks down endothermically forming water vapour, diluting the radicals in the flame, while the residue of alumina builds up to form a protective layer.

$$2\ Al(OH)_3\ (s) \xrightarrow{180\text{-}200°C} Al_2O_3(s) + 3\ H_2O(g)$$

$$\Delta H = +1.3\ kJ\ g^{-1}$$

It is worth noting that the heat capacity of organic polymers[84] vary from 0.9 to 2.1 $J\ K^{-1}g^{-1}$, thus the decomposition enthalpy of a fire retardant mineral filler is a factor of 1000 larger – the decomposition enthalpy of 1 g $Al(OH)_3$ is equal to the heat (q) required to raise the temperature of a mass (m) of 1.5 g of low density polyethylene (LDPE) from ambient temperature to decomposition (400°C)($\Delta\Theta$), assuming constant heat capacity (c_p) during heating, ($q = mc_p\Delta\Theta$, so q = 1.5 x 2.3 x 375 = 1.29 kJ).

An attempt to quantify the three contributions to fire retardancy (endotherm, gas and residue heat absorption) were found in a limited report by Rothon[115] for two mineral fillers, aluminium hydroxide ($Al(OH)_3$) and nesquehonite ($MgCO_3.3H_2O$). These ideas have been extended in an attempt to quantify the four physical contributions to the overall fire retardant effects of mineral fillers as shown in Table 39. In this way, any unexpected effects such as chemical interactions or changes of behaviour resulting from different filler morphologies may be more readily identified. In addition to the decomposition endotherm, the heat capacities of the filler, its solid residue, and its vapour phase products may be estimated for the temperature range over which they exist.

Table 39 Fire retardant effects of mineral fillers

Effect	How quantified
Diluting polymer in condensed phase	Heat capacity of the filler prior to decomposition
Endothermic decomposition of filler	Heat of decomposition
Presence of inert residue	Heat capacity of the residue after decomposition
Presence of diluent gases	Heat capacity of the diluent gases

However, the heat capacity of any material varies as a function of temperature, and particularly around any phase changes. For a single phase of a pure material this variation has been represented by a polynomial, giving the value of the heat capacity at any temperature. Integrating these values over the temperature range under consideration will give the best value of the heat required to raise temperature over that range. The heat capacity, C_p of a material is given by the Shomate equation[117, 118]

$$C_p = a + bT + cT^2 + dT^3 + e\,T^{-2}$$

Equation 18

The heat required to raise the temperature of a known quantity of substance over a temperature range is the sum of the heat capacities at each temperature. This used to be obtained by integration of the Shomate (or equivalent) equation with respect to T, but can also be integrated numerically using a spreadsheet. For example to heat $Mg(OH)_2$ from 25˚C to 300˚C (its decomposition temperature), its heat capacity is given by

$$C_p = 84.9 + 0.0744T - 6.89\cdot10^{-5}T^2 + 2.66\cdot10^{-8}T^3 - 2.17\cdot10^{6}T^{-2} \quad \text{in } JK^{-1}mol^{-1}$$

Therefore $C_{p\,298}$ = 77.2 J $K^{-1}mol^{-1}$ or $C_{p\,298}$ = 1.32 J $K^{-1}g^{-1}$
similarly $C_{p\,573}$ = 1.77 J $K^{-1}g^{-1}$

The heat required to raise 1g $Mg(OH)_2$ to its decomposition temperature at 300˚C is the area under the C_p vs T curve. However, within the errors associated with the approach outlined here, suitable selection of a representative value for C_p will give the heat requirement representative of the whole range. Thus a value of 1.44 JK^{-1} g^{-1} was used here. The same approach was used to determine the energy required to heat the resultant residue (such as MgO) from 300˚C to, for example, 600˚C, and for the gas phase diluents. Since the water and carbon dioxide will only be present in the gas phase above the filler decomposition temperature, no phase changes need be considered. The decomposition enthalpy of the filler may be determined experimentally, for example from differential scanning calorimetry (DSC), or obtained from the literature.

This approach is deliberately simplistic, allowing more subtle effects to be isolated from the quantifiable physical processes. In particular, the analysis involves the following assumptions:

- The thermal conductivity of the polymer composite is unaffected by the presence of the filler. This is not realistic, particularly if incorporation of the filler results in significant changes to the melt flow behaviour.
- The final temperature reached by the solid residues and the CO_2 and water in the gas phase do not vary significantly from one filler to another. This is discussed further.
- The heat capacity of the filler and residue is not affected by the presence of polymer.
- The decomposition endotherm of the filler is unaffected by incorporation into the polymer.
- The only effect of the solid residue is its ability to act as a heat sink (in practice it will also change the reflectivity and the absorption of radiant heat).
- The only effect of the gas phase diluent is an absorber of heat, neglecting any effects reducing the free radical concentration below a critical threshold.
- It takes no account of particle size or morphology of the filler, which have been shown to be important in experimental studies.

6.2.3 Calculation of the Physical Contribution to the Fire Retardant Effect

Table 40 Physical properties of potential fire retardant mineral fillers

Filler	Formula	T_{decomp} /°C	ΔH_{decomp} /J g^{-1}
Aluminium hydroxide	$Al_2O_3.3H_2O$	180-200	1300
Magnesium hydroxide	$Mg(OH)_2$	300-320	1450
Calcium hydroxide	$Ca(OH)_2$	430-450	1150
Nesquehonite	$MgCO_3.3H_2O$	70-100	1750
Hydromagnesite	$Mg_5(CO_3)_4(OH)_2.4H_2O$	220-240	1300
Huntite	$Mg_3Ca(CO_3)_4$	400	980
Ultracarb	Hydromagnesite/Huntite 60/40	220-400	1172
Boehmite	AlO(OH)	340-350	560

Table 40 shows a number of metal hydroxide and carbonates as potential fire retardant fillers, together with published estimates of their decomposition temperature ranges and endotherms. These data, together with the average values of heat capacities of the filler, its residue, and its gaseous decomposition products have been used to estimate the heat absorption by the filler (% Filler), the residue (% Residue), the evolved water vapour and carbon dioxide (%Gas) and the decomposition endotherm (% Decomposition Endotherm) shown in Table 41.

Table 41 Relative contribution of heat absorbing effects for potential mineral filler fire retardants

	Relative Contribution Fire Retardant Effects			
	% Filler	Endotherm	% Residue	%Gas
Aluminium hydroxide	9	55	13	23
Magnesium hydroxide	19	56	9	15
Calcium hydroxide	29	55	5	11
Nesquehonite	1	58	12	29
Hydromagnesite	10	56	14	21
Huntite	20	58	9	13
Ultracarb	14	57	12	18
Boehmite	18	46	20	15

In general the figures show broad similarities – in every case, the greatest contribution comes from the endothermic decomposition. The decomposition temperature clearly affects the relative contributions of the heat capacity of the filler, and those of the residue and gas. It can be seen that in some cases, e.g. $Al(OH)_3$, and $MgCO_3.3H_2O$, the heat capacities of the gas

phase products exceeds that of the condensed phase, where for others, e.g. $Mg(OH)_2$ and $Ca(OH)_2$ the solid phase contribution is greater. Comparing aluminium and magnesium hydroxide, it is evident that the difference between their relative effects arise from the higher decomposition temperature of $Mg(OH)_2$, giving a larger contribution to the heat capacity of the undecomposed filler, but a smaller contribution from the heat capacity of the residue that $Al(OH)_3$, and from the heat capacity of the greatest volume of water vapour released by the $Al(OH)_3$ – even though the energy for such a release is almost identical for both fillers.

As the data have all been calculated in energy units, the contribution to the individual fillers may also be compared in absolute terms. Figure 96 shows the energy absorption per gram of each of the processes undergone by the filler.

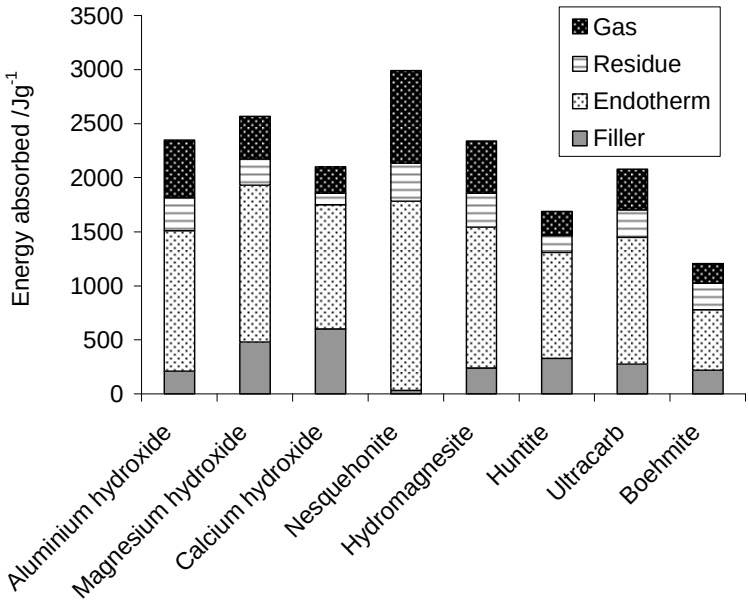

Figure 96 Absolute estimation of heat absorbed by potential fire retardant mineral fillers

The higher decomposition temperature of magnesium hydroxide and particularly the greater contribution of the filler, increase its energy absorbing capacity by about 250 J g^{-1}, compared to aluminium hydroxide, while the lower endotherm and smaller volatile heat capacity of calcium hydroxide also indicates inferior potential as a fire retardant.

It is evident from Figure 98 and Table 40 that endothermic decomposition accounts just over half of the fire retardant effect for the mineral fillers considered. For the example of

LDPE and $Al(OH)_3$ considered earlier, the total heat absorbed by 1g of filler could otherwise have heated almost 4g of LDPE to its decomposition temperature.

6.2.3.1 Modelling of ATH Thermal Decomposition in TGA

Decomposition of aluminium hydroxide (ATH) in air seems to be a two-step process as seen on Figure 95. The first step, between 200-345°C associated with about 27% of mass loss and second long tail degradation of about 8% of initial mass is visible in temperature range 345-725°C. Although the mass loss curve (Figure 95a) looks like single step of degradation of the ATH mass the MLR curve Figure 95b shows slight asymmetry of the main peak and also slow degradation of the mass at the end. According to these observations, a three reaction mechanism is proposed to model ATH behaviour in air and in N_2 using ThermaKin. In Figure 97 the solid line represents experimental data and dashed line ThermaKin fit curve.

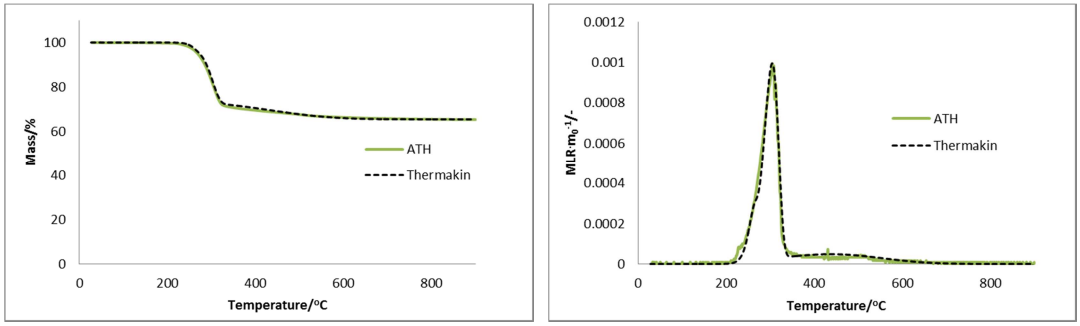

(a) (b)

Figure 97 ThermaKin fit of ATH in air/nitrogen (a) mass loss and (b) mass loss rate curve

Three reactions mechanism of degradation of ATH is presented in Table 42.

Table 42 Mechanism of ATH decomposition in air

Reaction 1 $ATH \rightarrow 0.97ATH_{residue1} + 0.03ATH_{volatiles1}$ $A = 6.58 \times 10^{19}\ sec^{-1}\ E_a = 2.2 \times 10^5\ J/mol$
Reaction 2 $ATH \rightarrow 0.75ATH_{residue1} + 0.25ATH_{volatiles1}$ $A = 8.94 \times 10^{12}\ sec^{-1}\ E_a = 1.65 \times 10^5\ J/mol$
Reaction 3 $ATH_{residue1} \rightarrow 0.9ATH_{residue2} + 0.1ATH_{volatiles2}$ $A = 1.93\ sec^{-1}\ E_a = 3.0 \times 10^4\ J/mol$

The mechanism has sequential reactions. The first reaction is responsible for the beginning of mass loss (it could loss from ATH surface) but much stronger reaction, 2, occurs at a slightly higher temperature and is competing with reaction 1 causing the biggest loss of mass (loss of water from within bulk). Reaction 3 acts to effectively decrease the tiny amount of mass at higher temperature leaving residue yield at 66% of original mass of the sample (possibly Boehmite formation). A three reaction mechanism was found to be the simplest curve that could encompass all the features of the curve. It is important to note that the reaction mechanism and the components included in the mechanism are not necessarily physically significant. The mechanism is intended to mathematically mimic the mass loss rate data in the simplest form possible and defines model-specific kinetics (Table42) that can reproduce the experimental curve. However as the ATH decomposition process is well understood[119] each component in the ThermaKin mechanism can be associated with real components and products. If taking into account surface loss as a first reaction in the ThermaKin mechanism, the next two reactions are:

Reaction 2: $2Al(OH)_3 \rightarrow 3H_2O + Al_2O_3$

Reaction 3: $2Al(OH)_3 \rightarrow 2AlOOH + 2H_2O$ (bohemite step)

6.2.3.2 Modelling of Magnesium Hydroxide Thermal Decomposition in TGA

The methodology and conditions used to pyrolyse magnesium hydroxide (MH) samples are the same as used with ATH described above. The thermogravimetric data collected in these tests is displayed Figure 95. The mass loss rate data was calculated as a numerical differentiation of the total mass data.

The shapes of ML and MLR curves of Magnesium Hydroxide (MH) look very similar to ATH. However the major difference is as the temperature of decomposition. MH starts to degrade in higher temperature and first step of 25% mass loss is visible in the temperature range of 325-455^{o}C. Another 5% of mass decomposes slowly until 825^{o}C. Also for this mineral filler a three reaction mechanism was proposed to model the decomposition behaviour. Figure 98 presents ThermaKin fit and experimental data.

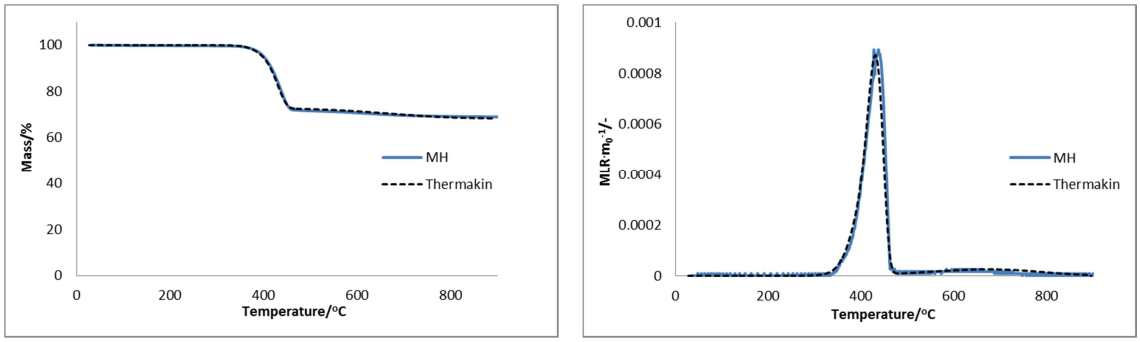

(a) (b)

Figure 98 ThermaKin fit of MH in nitrogen/air (a) mass loss and (b) mass loss rate curve

The experimental data is indicated by the solid line and the simulation data based on the reaction mechanism given in Table 43 is provided as the dashed line.

Table 43 Mechanism of MH decomposition in nitrogen/air

Reaction 1 $MH \rightarrow 0.97MH_{residue1} + 0.03MH_{volatiles1}$ $A = 8.97 \times 10^{13}\ sec^{-1}\ E_a = 2.0 \times 10^5\ J/mol$
Reaction 2 $MH \rightarrow 0.75MH_{residue1} + 0.25MH_{volatiles1}$ $A = 8.10 \times 10^{13}\ sec^{-1}\ E_a = 2.15 \times 10^5\ J/mol$
Reaction 3 $MH_{residue1} \rightarrow 0.94MH_{residue2} + 0.06MH_{volatiles2}$ $A = 1.33\ sec^{-1}\ E_a = 5.50 \times 10^4\ J/mol$

The mechanism has sequential reactions. The first reaction is responsible for the beginning of mass loss and reaction 2 occurs at a slightly higher temperature to compete with reaction 1 causing the biggest degradation of mass in whole mechanism. Reaction 3 acts to effectively decrease the tiny amount of mass (about 5%) at higher temperature leaving a residue yield of 69% of original mass of the sample. This model is assumed to be appropriate for both atmospheres air and nitrogen.

6.2.4 Thermal Degradation, Decomposition Products and Modelling of EVA

Experimental curves of EVA decomposition in nitrogen are presented in Figure 99.

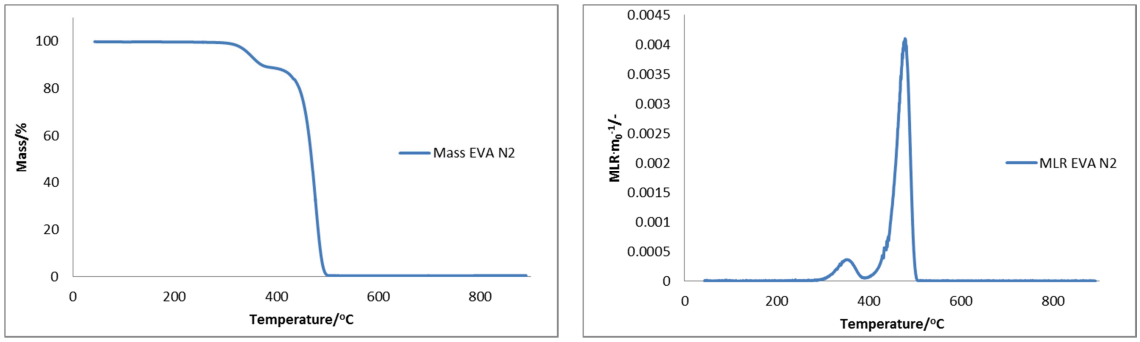

(a) (b)

Figure 99 TGA of EVA in nitrogen atmosphere (a) mass loss and (b) mass loss rate curve

Decomposition of EVA in nitrogen is a two-step process. MLR curve Figure 99b shows two isolated peaks.

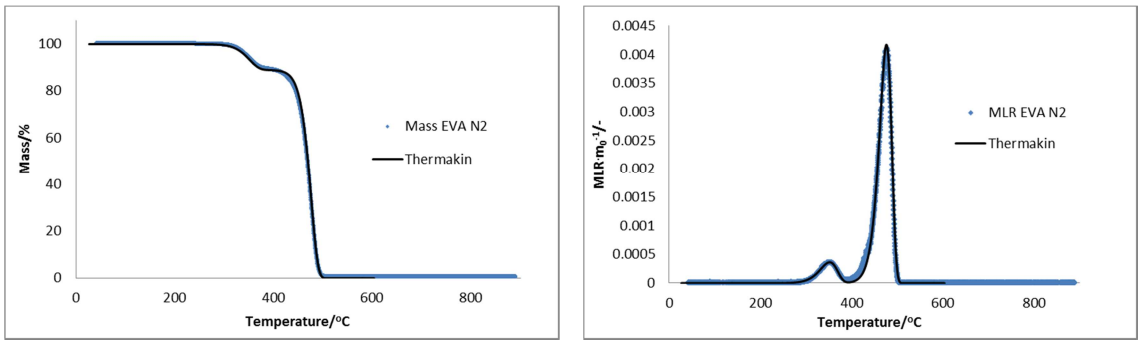

(a) (b)

Figure 100 Two reaction ThermaKin model of EVA decomposition in N_2 (a) mass loss and (b) mass loss rate curve

Table 44 Mechanism of EVA decomposition in N_2

Reaction 1	Reaction 2
$EVA \rightarrow 0.89EVA_{residue1} + 0.11EVA_{volatiles1}$	$EVA_{residue1} \rightarrow EVA_{volatiles2}$
$A = 6.11 \times 10^{11}\ sec^{-1}$ $E_a = 1.66 \times 10^5$ J/mol	$A = 1.27 \times 10^{22}\ sec^{-1}$ $E_a = 3.45 \times 10^5$ J/mol

Mechanism from Table 44 containing two reactions was proposed to model EVA behaviour in N_2. Volatile products from the reactions $EVA_{volatiles1and2}$ are detected by FTIR as shown in Figure 104. It is visible that acetic acid is present in the first reaction and eicosane in second one. ThermaKin solid line on Figure 100 showed good agreement with experimental data. EVA is non-charring polymer and no residue is left at the end of pyrolysis process.

The presence of oxygen makes changes to EVA decomposition as seen on Figure 101. In the first step not only acetic acid is released (as seen on FTIR spectrum in Figure 105), the process of decomposition slows showing a second and third type of residue.

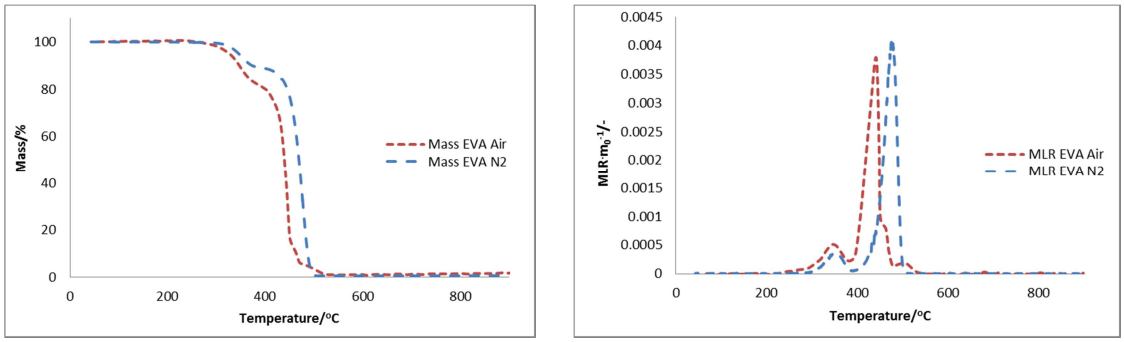

(a) (b)

Figure 101 Comparison of TGA EVA curves in air and nitrogen

Oxidation mainly accelerates the mass loss of EVA. Both curves look similar. Again two steps are present and two peaks on mass loss rate curves are dominant. Loss of mass in air starts a little bit earlier than in nitrogen. However, some part of the material is not degraded at temperatures below 500°C even in the presence of oxygen; that is why two small steps are visible at the end of reaction. Pyrolysis in nitrogen starts at higher temperature so the two last steps visible in air are overlapped by the second massive peak. Another interesting observation can be made based on the comparison of the heights of MLR peaks: the first MLR peak is higher in air than that in nitrogen but the second MLR peak in air is lower than that in nitrogen. Such a situation shows that at the lower temperature more EVA is lost in air than is observed in nitrogen, while at higher temperature correspondingly more rapid mass loss occurs in nitrogen. The idea of the EVA ThermaKin model in air is to maintain 2 pyrolysis reactions from the nitrogen simulation and to add another two reactions corresponding to oxidation mechanism.

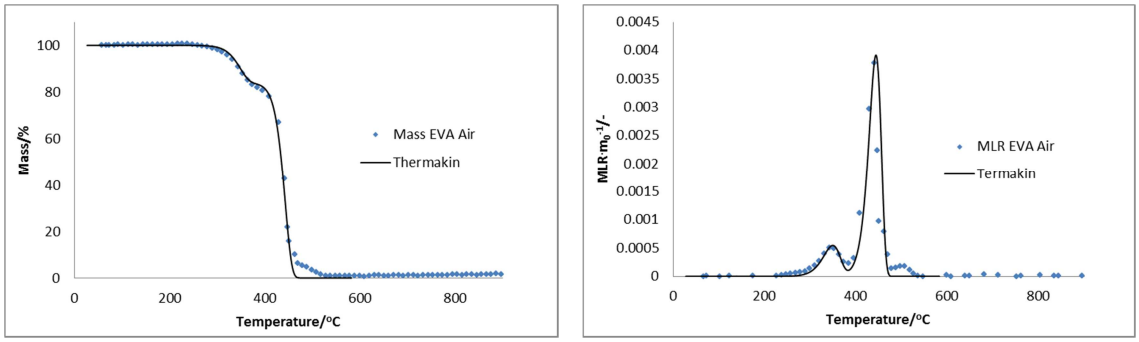

(a) (b)

Figure 102 Four Reaction ThermaKin model of EVA decomposition in air (a) mass loss and (b) mass loss rate curve

The solid line corresponds to the ThermaKin fit and the dotted line represents the experimental result.

Table 45 Four reaction mechanism of EVA decomposition in air

Reaction 1 Pyrolysis $EVA \rightarrow 0.89EVA_{residue1} + 0.11EVA_{volatiles1}$ $A = 6.11 \times 10^{11}\ sec^{-1}\ E_a = 1.66 \times 10^5\ J/mol$	Reaction 2 Pyrolysis $EVA_{residue1} \rightarrow EVA_{volatiles2}$ $A = 1.27 \times 10^{22}\ sec^{-1}\ E_a = 3.45 \times 10^5\ J/mol$
Reaction 1a Oxidation $EVA \rightarrow 0.65EVA_{residue1} + 0.35EVA_{volatiles1}$ $A = 5.25 \times 10^{11}\ sec^{-1}\ E_a = 1.72 \times 10^5\ J/mol$	Reaction 2a Oxidation $EVA_{residue1} \rightarrow EVA_{volatiles2}$ $A = 4.56 \times 10^{20}\ sec^{-1}\ E_a = 3.1 \times 10^5\ J/mol$

The four reaction mechanism, incorporating oxidation is provided in Table 45. Two oxidation reactions were included that were not present in the pyrolysis mechanism. The mechanism has parallel reactions that compete with reactions 1 and 2, respectively. The competitive reactions 1a and 2a act to effectively speed the pyrolysis process.

Table 46 The universal four reaction mechanism for EVA as a function of ambient oxygen volume fraction

Reaction 1 Pyrolysis $EVA \rightarrow 0.89EVA_{residue1} + 0.11EVA_{volatiles1}$ $A = 6.11 \times 10^{11}\ sec^{-1}\ E_a = 1.66 \times 10^5\ J/mol$	Reaction 2 Pyrolysis $EVA_{residue1} \rightarrow EVA_{volatiles2}$ $A = 1.27 \times 10^{22}\ sec^{-1}\ E_a = 3.45 \times 10^5\ J/mol$
Reaction 1a Oxidation $EVA \rightarrow 0.65EVA_{residue1} + 0.35EVA_{volatiles1}$ $\mathbf{A = 2.51x10^{10}[O_2\%]\ sec^{-1}}\ E_a = 1.72 \times 10^5\ J/mol$	Reaction 2a Oxidation $EVA_{residue1} \rightarrow EVA_{volatiles2}$ $\mathbf{A = 2.18\ x10^{19}[O_2\%]\ sec^{-1}}\ E_a = 3.1 \times 10^5\ J/mol$

The universal reaction mechanism from Table 46 was constrained by the requirement that the Arrhenius pre-exponential factor was a function of the ambient oxygen concentration, given in volumetric fraction, and the requirement that at 0% oxygen concentration this mechanism would revert to the pyrolysis mechanism in nitrogen. It should be noted that this model is tested only for oxygen level of 21%.

Figure 103 shows better ThermaKin fit of experimental data of EVA in air as two additional reactions were added as seen in Table 47. Four steps of the decomposition are captured.

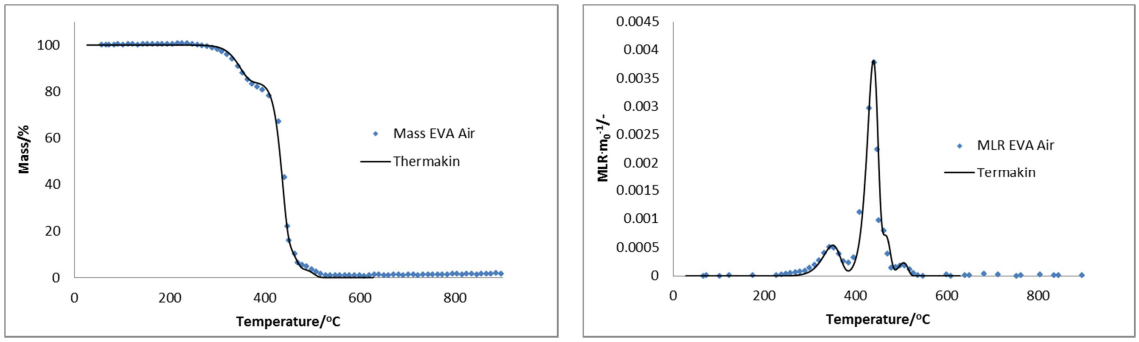

(a) (b)

Figure 103 Six reaction thermakin model of EVA decomposition in air (a) mass loss and (b) mass loss rate curve

Table 47 Six reaction mechanism of EVA decomposition in air

Reaction 1 Pyrolysis $EVA \rightarrow 0.89EVA_{residue1} + 0.11EVA_{volatiles1}$ $A = 6.11 \times 10^{11}\ sec^{-1}\ E_a = 1.66 \times 10^5$ J/mol	Reaction 2a Oxidation $EVA_{residue1} \rightarrow 0.19\ EVA_{residue2} + 0.81EVA_{volatiles2}$ $A = 4.07 \times 10^{24}\ sec^{-1}\ E_a = 3.6 \times 10^5$ J/mol
Reaction 1a Oxidation $EVA \rightarrow 0.65EVA_{residue1} + 0.35EVA_{volatiles1}$ $A = 2.85 \times 10^{11} sec^{-1}\ E_a = 1.69 \times 10^5$ J/mol	Reaction 3 Oxidation $EVA_{residue2} \rightarrow 0.25\ EVA_{residue3} + 0.75EVA_{volatiles3}$ $A = 3.20 \times 10^{26}\ sec^{-1}\ E_a = 4.0 \times 10^5$ J/mol
Reaction 2 Pyrolysis $EVA_{residue1} \rightarrow EVA_{volatiles2}$ $A = 1.27 \times 10^{22}\ sec^{-1}\ E_a = 3.45 \times 10^5$ J/mol	Reaction 4 Oxidation $EVA_{residue3} \rightarrow EVA_{volatiles4}$ $A = 6.15 \times 10^{29}\ sec^{-1}\ E_a = 4.7 \times 10^5$ J/mol

Two more reactions were added to 4 reactions mechanism to capture mass loss and mass loss rate curve of EVA in air at temperatures above 475^{o}C. It is apparent that two steps of mass decomposition are present at the end of TGA test.

Additionally, Table 48 presents universal six reactions model of EVA decomposition. Values of oxidation reactions' pre-exponential factors A are functions of oxygen concentration.

Table 48 The universal six reaction mechanism of EVA decomposition

Reaction description	Temp. (˚C)	Gas-phase products
Reaction 1 Pyrolysis $EVA \rightarrow 0.89EVA_{residue1} + 0.11EVA_{volatiles1}$ $A = 6.11 \times 10^{11}\ sec^{-1}\ E_a = 1.66 \times 10^5$ J/mol	300-375	Acetic acid
Reaction 1a Oxidation $EVA \rightarrow 0.65EVA_{residue1} + 0.35EVA_{volatiles1}$ **$A = 1.36 \times 10^{10}[O_2\%]\ sec^{-1}$** $E_a = 1.69 \times 10^5$ J/mol	260-360	CO_2, acetic acid
Reaction 2 Pyrolysis $EVA_{residue1} \rightarrow EVA_{volatiles2}$ $A = 1.27 \times 10^{22}\ sec^{-1}\ E_a = 3.45 \times 10^5$ J/mol	390-500	Eicosane
Reaction 2a Oxidation $EVA_{residue1} \rightarrow 0.19\ EVA_{residue2} + 0.81EVA_{volatiles2}$ **$A = 1.94 \times 10^{23}\ [O_2\%]\ sec^{-1}$** $E_a = 3.6 \times 10^5$ J/mol	360-450	H_2O, CO_2, CO, ethylene, heptane, 1-hexane, 1-heptene, acrolein, ethenal, propenal, 4-methyl-2-pentanone, 2-pentanone
Reaction 3 Oxidation $EVA_{residue2} \rightarrow 0.25\ EVA_{residue3} + 0.75EVA_{volatiles3}$ **$A = 1.53 \times 10^{25}\ [O_2\%]\ sec^{-1}$** $E_a = 4.0 \times 10^5$ J/mol	430-480	
Reaction 4 Oxidation $EVA_{residue3} \rightarrow EVA_{volatiles4}$ **$A = 2.94 \times 10^{28}\ [O_2\%]\ sec^{-1}$** $E_a = 4.7 \times 10^5$ J/mol	470-515	

6.2.4.1 FTIR Analysis of Evolved Condensable Products from EVA samples

FTIR Analysis was carried out very similarly to PP samples (section 6.1). First, the wavenumbers for all major peaks were selected and then compared to Omnic reference spectra[120] for different vapour phase volatiles. Major and minor products from all compounds were selected for the EVA sample degradation in nitrogen and air.

In nitrogen, the thermal degradation of EVA samples shows two distinct regions, which have been assigned to the loss of acetic acid at lower temperatures, followed by eicosane production at higher temperatures.

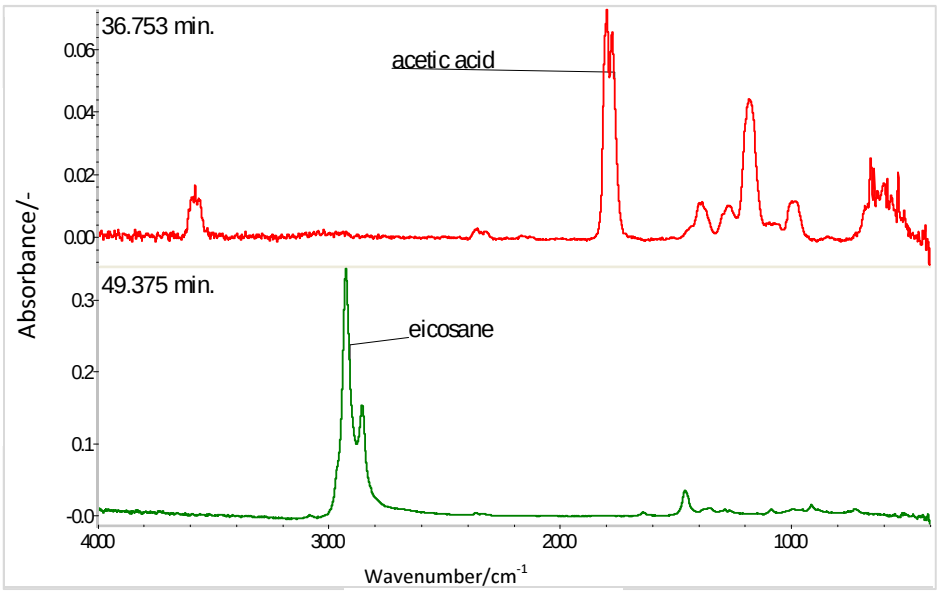

Figure 104 EVA selected spectra at different decomposition time carried out in nitrogen

Figure 105 presents selected FTIR spectra, in air, for EVA samples at different temperature/time regions.

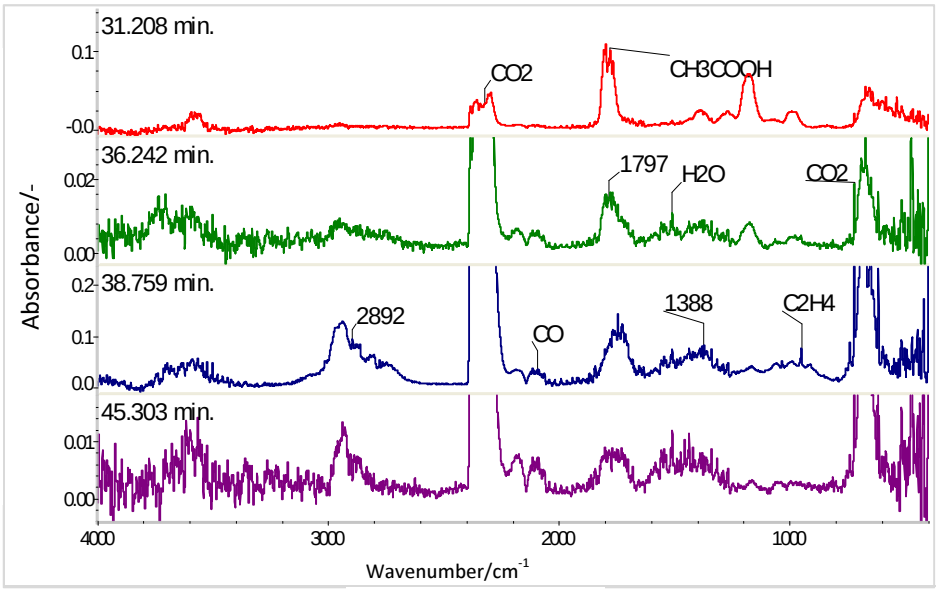

Figure 105 EVA selected spectra at different decomposition time carried out in air

For EVA four different spectra are presented in Figure 105. The obvious products from EVA decomposition are acetic acid (CH_3COOH), ethylene (C_2H_4), CO, CO_2, and H_2O. The peaks within 2998-2856 cm^{-1} indicate hydrocarbon presence (heptane, 1-hexene, 1-heptene); however it is difficult to assess what actual products are decomposed as their spectra are very similar.

The carbonyl region of 1815-1700 cm^{-1} provides some difficulty with identification of compounds as for all samples one broad peak shifts with temperature. For EVA the peak is shifted from 1815-1728 to 1796-1699 cm^{-1} at higher temperatures suggesting different volatiles generated. Acrolein, ethanal and propenal all fit into this wavenumber region. Additional peaks at 2998-2856 cm^{-1} suggest 4-methyl-2-pentanone or 2-pentanone may be present.

6.2.5 Thermal Degradation, Decomposition Products and Modelling of EVA with ATH

ATH normally decomposes at 190°C, whereas, when in an ethylene-vinyl acetate copolymer (EVA) in a common cable industry formulation, water does not start to be lost until the temperature reaches 250°C[121]. The loss of water can also have a deleterious effect, rupturing protective layers formed, for example, by the cross-linking of the conjugated polyene in EVA/ATH composites[122]. With some polymers, the resin and the additive might interact, and so one must be aware of these possibilities as these will influence the mode of action[123,111]. However, ThermaKin model of EVA+ATH would assume that there is no interaction between polymer and filler and the model would be constructed by the use of two independent mechanisms developed for EVA and ATH separately in previous sections.

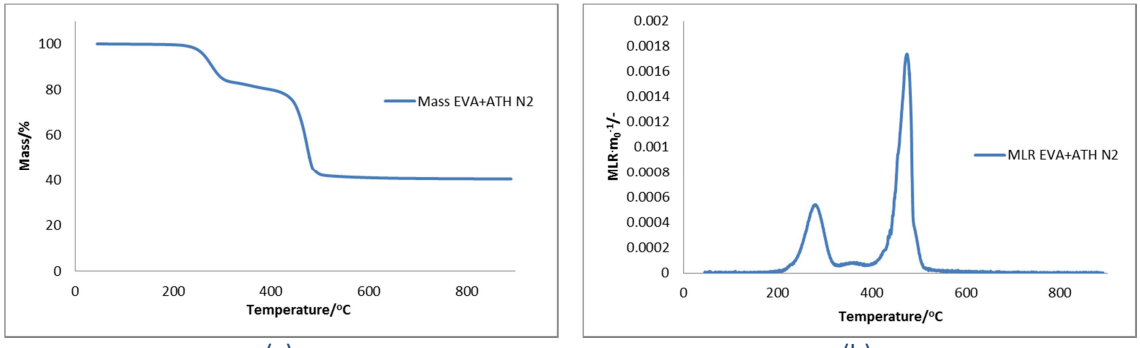

(a) (b)

Figure 106 TGA of EVA+ATH in N_2 (a) mass loss and (b) mass loss rate curve

Decomposition of EVA with Aluminium hydroxide (EVA+ATH) in nitrogen is presented in Figure 106. Three steps are observed - two major steps of degradation are observed and also one small peak just between at around 375°C as seen on Figure 106b. Figure 107 presents predictive ThermaKin model of EVA+ATH in nitrogen.

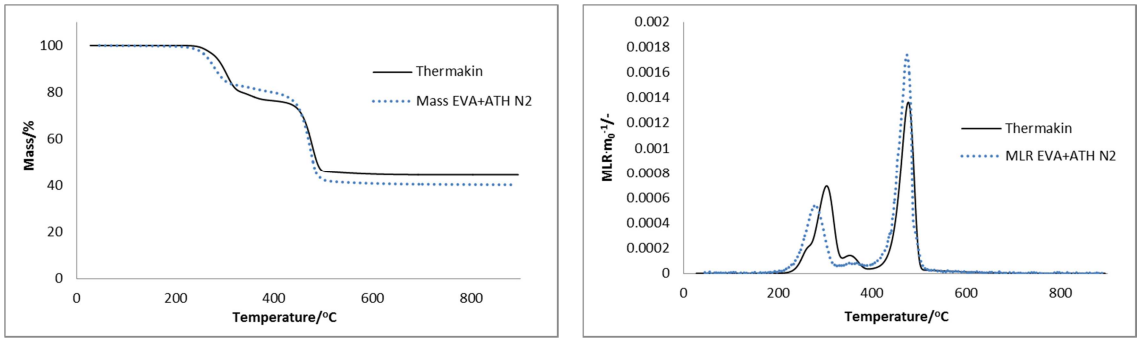

(a) (b)

Figure 107 ThermaKin fit of EVA+ATH in N_2 (a) mass loss and (b) mass loss rate curve

The mechanism of the EVA+ATH model was constructed from two independent models of EVA and ATH (see Table 47 for EVA and Table 42 for ATH reactions details). The proportions of polymer and the filler were kept as before: 32% and 68% respectively. The ThermaKin model of EVA+ATH captured all features of the reaction with satisfactory accuracy.

Decomposition of EVA with Aluminium hydroxide (EVA+ATH) in air is presented in Figure 108. MLR and ML curves in air have got similar structure to nitrogen one. There are two major steps of degradation and slow decomposition between 325-425°C.

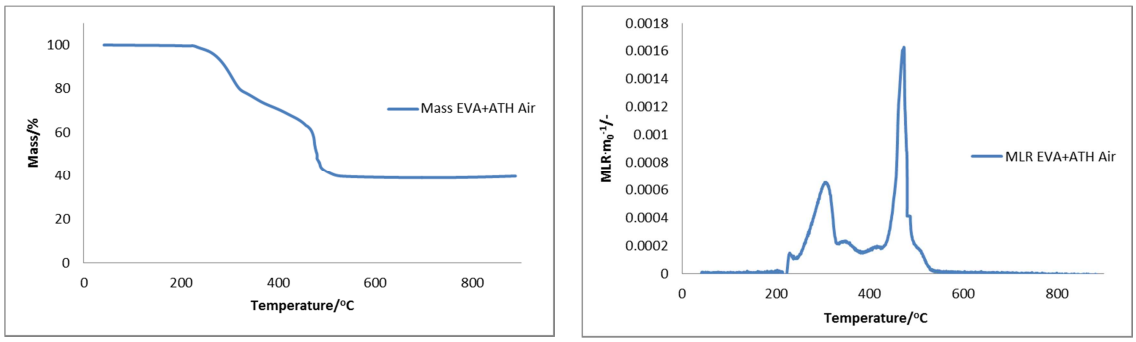

(a) (b)

Figure 108 TGA of EVA+ATH in air (a) mass loss and (b) mass loss rate curve

Figure 109 presents predictive ThermaKin model (solid line) of EVA+ATH in air.

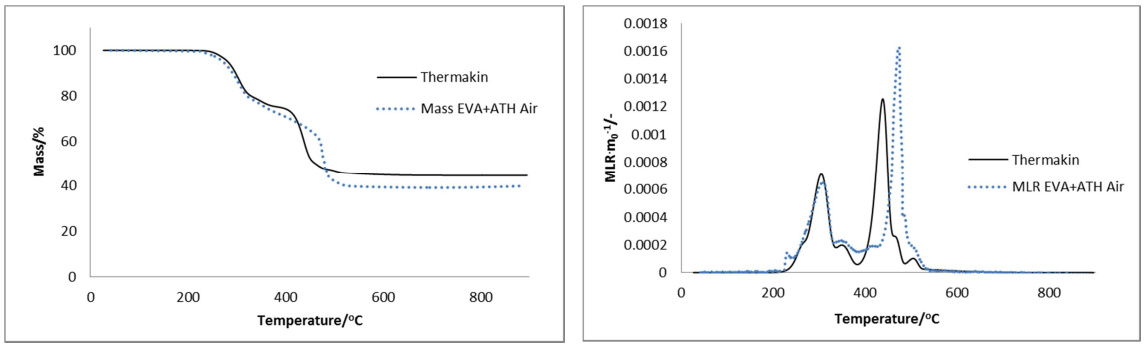

(a) (b)

Figure 109 ThermaKin fit of EVA+ATH in air (a) mass loss and (b) mass loss rate curve

The proportions of polymer and the filler were kept as stated: 32% and 68% respectively. ThermaKin model of EVA+ATH in nitrogen captured all features of the reaction with satisfactory accuracy. In air the second peak of ThermaKin model is shifted as seen on Figure 109. The delay of the second peak of EVA+ATH in air could be caused by transport of vapour products through the molten polymer. Model is based on two independent samples of EVA and ATH, a completely new material such as EVA+ATH was not fitted separately. ThermaKin model of EVA+ATH is strictly based on prediction. The kinetic parameters obtained are believed to be correct but transport phenomena such as gaseous diffusion causing delay needs further investigation.

As the model involves nine reactions and the mechanism is complex, it is recommended to trace each reaction contribution to mass loss rate as it is presented in Figure 110. The universal mechanism of the EVA+ATH model for nitrogen and air atmosphere was constructed from two independent models of EVA and ATH (in nitrogen and in air respectively – see Table 49 for reactions details). Oxidation reactions are built in such a way that a pre-exponential factor A is a function of oxygen concentration.

Table 49 The universal nine reaction mechanism of EVA+ATH decomposition

Reaction description	Temp. (˚C)	Gas-phase products
1) Reaction 1 ATH $ATH \rightarrow 0.97ATH_{residue1} + 0.03ATH_{volatiles1}$ $A = 6.58 \times 10^{19}\ sec^{-1}\ E_a = 2.2 \times 10^5$ J/mol	210-250	H_2O, CO_2
2) Reaction 2 ATH $ATH \rightarrow 0.75ATH_{residue1} + 0.25ATH_{volatiles2}$ $A = 8.94 \times 10^{12}\ sec^{-1}\ E_a = 1.65 \times 10^5$ J/mol	250-315	
3) Reaction 3 ATH $ATH_{residue1} \rightarrow 0.9ATH_{residue2} + 0.1ATH_{volatiles3}$ $A = 1.93\ sec^{-1}\ E_a = 3.0 \times 10^4$ J/mol	230-525	Hydrocarbons, eicosane
4) Reaction 1 Pyrolysis EVA $EVA \rightarrow 0.89EVA_{residue1} + 0.11EVA_{volatiles1}$ $A = 6.11 \times 10^{11}\ sec^{-1}\ E_a = 1.66 \times 10^5$ J/mol	210-310	H_2O, CO_2
5) Reaction 1a Oxidation EVA $EVA \rightarrow 0.65EVA_{residue1} + 0.35EVA_{volatiles1}$ **$A = 1.36 \times 10^{10}[O_2\%]\ sec^{-1}$** $E_a = 1.69 \times 10^5$ J/mol	275-365	Acetic acid, H_2O, CO_2, CO,
6) Reaction 2 Pyrolysis EVA $EVA_{residue1} \rightarrow EVA_{volatiles2}$ $A = 1.27 \times 10^{22}\ sec^{-1}\ E_a = 3.45 \times 10^5$ J/mol	310-375	H_2O, CO_2, acetone
7) Reaction 2a Oxidation EVA $EVA_{residue1} \rightarrow 0.19\ EVA_{residue2} + 0.81EVA_{volatiles2}$ **$A = 1.94 \times 10^{23}\ [O_2\%]\ sec^{-1}$** $E_a = 3.6 \times 10^5$ J/mol	370-435	Acetic acid, H_2O, CO_2, CO, hydrocarbons, ethylene
8) Reaction 3 Oxidation EVA $EVA_{residue2} \rightarrow 0.25\ EVA_{residue3} + 0.75EVA_{volatiles3}$ **$A = 1.53 \times 10^{25}\ [O_2\%]\ sec^{-1}$** $E_a = 4.0 \times 10^5$ J/mol	420-480	
9) Reaction 4 Oxidation EVA $EVA_{residue3} \rightarrow EVA_{volatiles4}$ **$A = 2.94 \times 10^{28}\ [O_2\%]\ sec^{-1}$** $E_a = 4.7 \times 10^5$ J/mol	425-520	

The reactions order from 1 to 9 is indicated as observed in Figure 110.

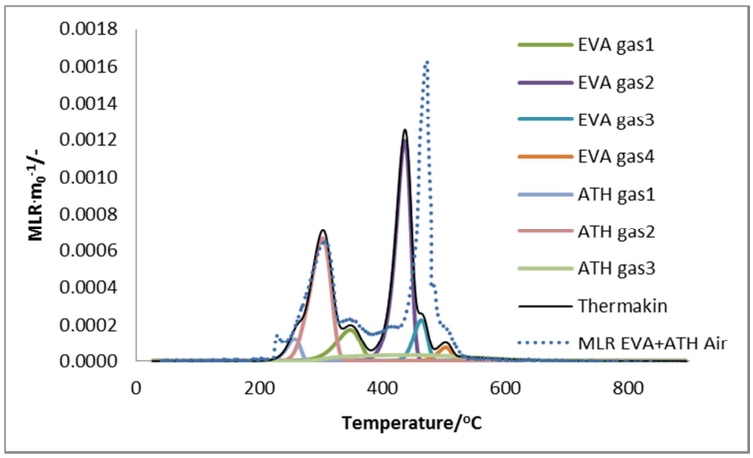

Figure 110 Contribution of each ThermaKin reaction to MLR curve predicting behaviour of EVA+ATH in air

6.2.5.1 FTIR Analysis of Evolved Condensable Products from EVA and ATH samples

For samples containing ATH, Figure 111, acetic acid production is not clearly seen during the decomposition process. The main volatiles released are water, carbon dioxide and hydrocarbons (eicosane) at higher temperatures.

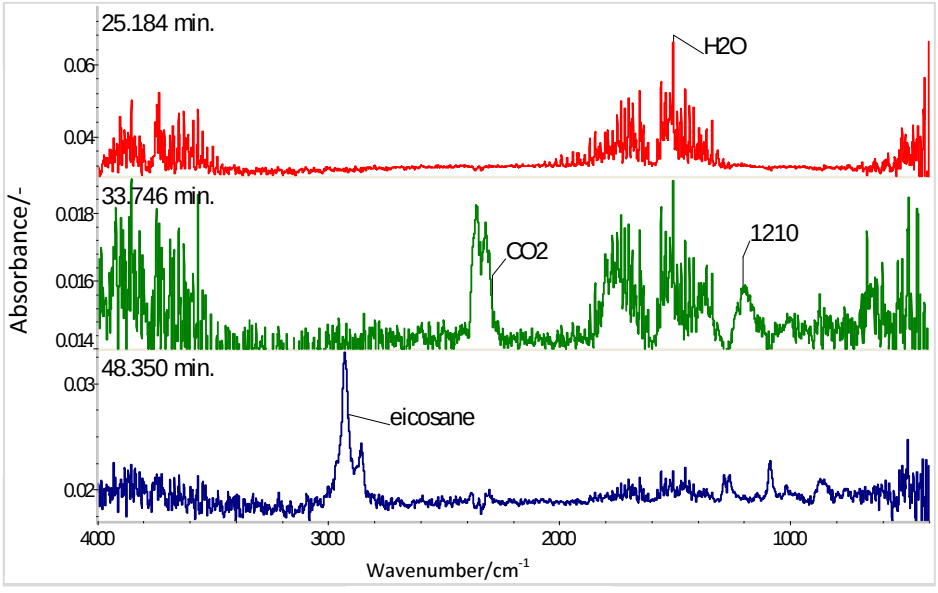

Figure 111 EVA+ATH selected spectra at different decomposition time carried out in nitrogen

Samples containing ATH (Figure 112) have two decomposition steps in air. There is no significant difference between these two samples in terms of the peak positions, which means

that the same volatiles are found. Compared to previous samples, the noticeable difference is only a significant reduction in the visibility of peaks corresponding to CH_3COOH. Additionally to acetic acid, CO, CO_2, H_2O is found. Hydrocarbons and other volatiles within regions 2998-2856 cm^{-1} and 1815-1700 cm^{-1}, similarly to EVA and EVA+NC samples, are also possibly present.

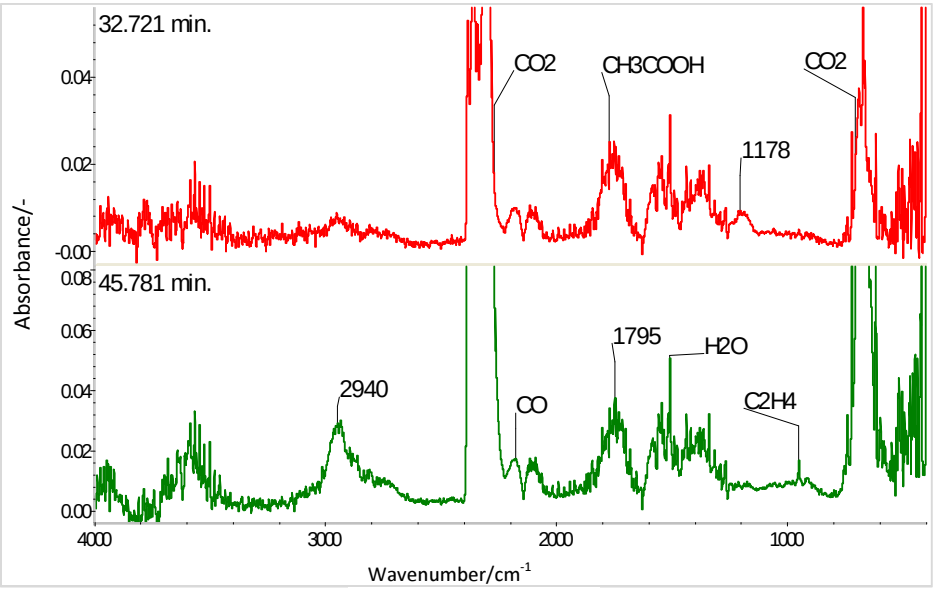

Figure 112 EVA+ATH selected spectra at different decomposition time carried out in air

6.2.5.2 Modelling of EVA with MH

Magnesium Hydroxide is stable up to 300°C and thus can be used in polymers that must be processed at higher temperatures. MH effectiveness comes from the fact that it decomposes endothermically and consumes a large amount of heat. Additionally, water dilutes any volatiles, thus decreasing the possibility of ignition. MH decomposition begins near 340°C, and consumes 1450 joules per gram of MH. There is some tendency for MH to catalyse the degradation of some polymers; in unsaturated polyester resins it can act as a chain extender, affecting resin rheology[111].

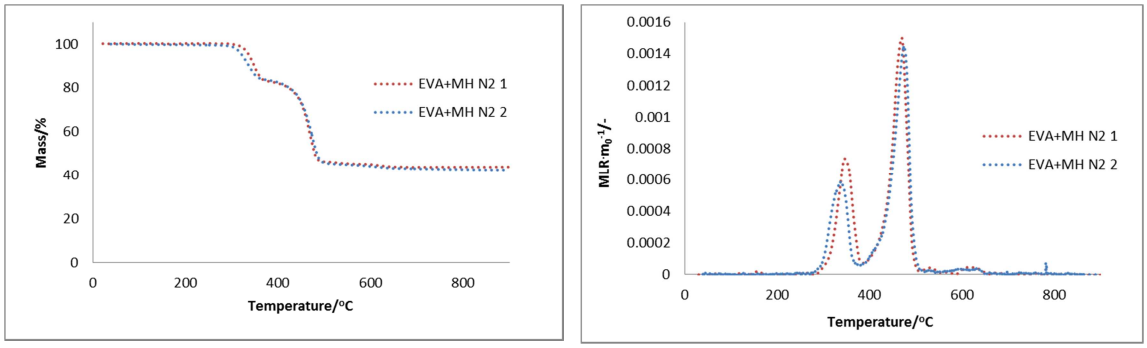

(a) (b)

Figure 113 TGA of EVA+MH in N_2 (a) mass loss and (b) mass loss rate curves

TGA experimental results of EVA+MH in nitrogen are presented in Figure 113. Two steps of decomposition are observed. In Figure 114 the solid line presents the predictive ThermaKin model of EVA+MH in nitrogen while the dotted lines represent experimental data.

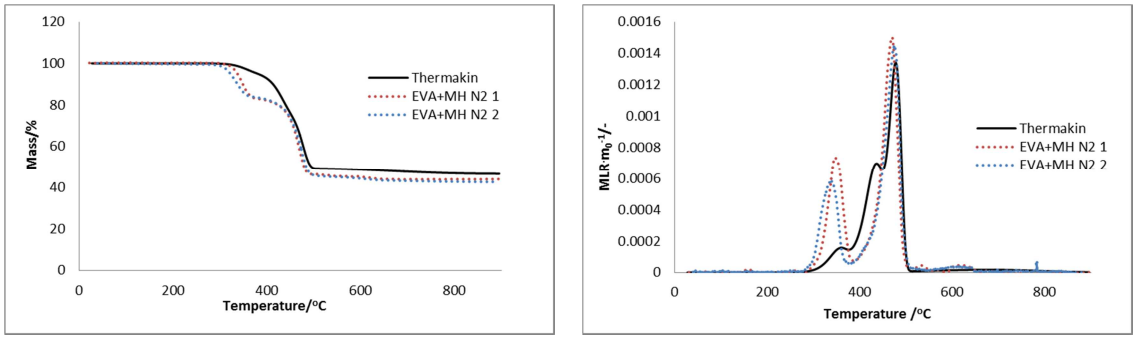

(a) (b)

Figure 114 ThermaKin fit of EVA+MH in N_2 (a) mass loss and (b) mass loss rate curves

The mechanism of the EVA+MH model of decomposition in nitrogen was constructed from two independent models of EVA and MH (see Table 44 for EVA and Table 43 for MH reactions details). The quantitative proportion of polymer and the filler was kept as required: 32% and 68% respectively. The ThermaKin model of EVA+MH captured features of the second step of decomposition with satisfactory accuracy, but the first degradation step was not covered by the model. However, partial decomposition of the first peak is visible on Figure 114b. The reason for the lack of agreement between the model and the first decomposition step could be explained by the fact that for EVA+MH mass loss at 365°C was 16% which was three times more than the mass lost in EVA and MH in separate experiments added together. ThermaKin model was constructed from two independent models of EVA and MH so it was impossible to degrade more mass than the sum of these two.

Table 50 ThermaKin performance on EVA, MH and EVA+MH in N_2

Sample	EVA*0.32	MH*0.68	EVA(32%)+MH(68%)
TGA mass loss at 365°C	11%*0.32=3.5%	2%*0.68=1.3%	16%
ThermaKin mass loss at 365°C	3.5%	1.3%	4%
Difference of mass lost between ThermaKin and TGA	0	0	12%

Magnesium hydroxide as a filler seems to change EVA properties as a polymer because proportionally more mass was degraded in first step (365°C) of EVA+MH than it was for pure EVA and pure MH together over the same temperature range. To improve the model's performance more reactions could be added to the mechanism. In Figure 115 it is easier to trace each reaction's contribution to mass loss rate.

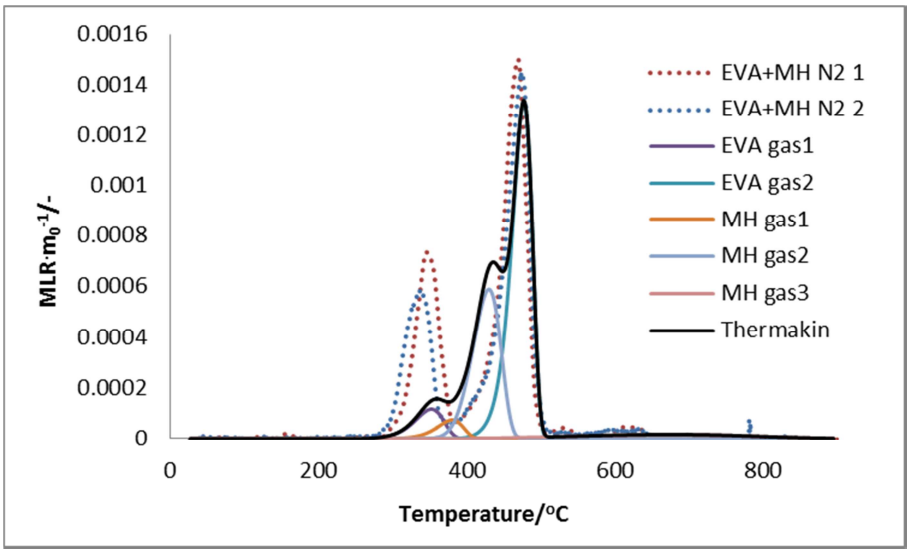

Figure 115 Contribution of each ThermaKin reaction to the mass loss rate in nitrogen

Decomposition of EVA with magnesium hydroxide (EVA+MH) in air is presented in Figure 116. MLR and ML curves in air have similar structure to those in nitrogen. There are two major steps of degradation and slow decomposition between 390-410°C.

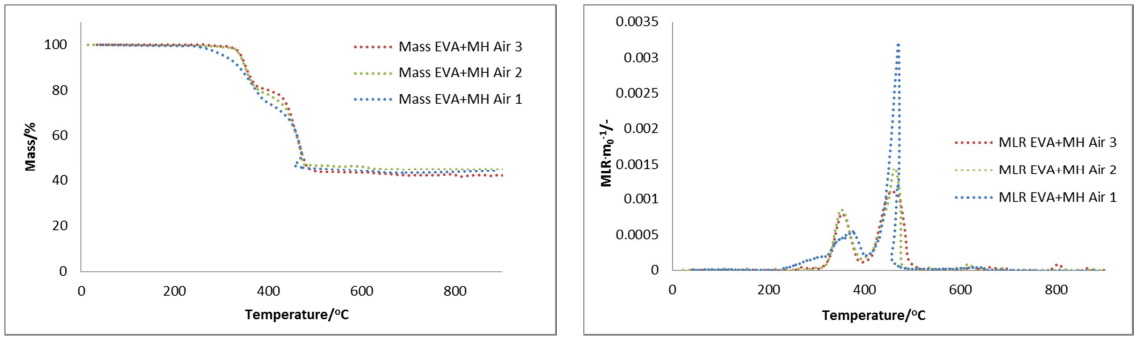

(a) (b)

Figure 116 TGA of EVA+MH in air (a) mass loss and (b) mass loss rate curves

The solid line on Figure 117 presents the predictive ThermaKin model of EVA+MH in air. Similar to nitrogen the location of the first step of mass loss was captured but the amount of mass lost was not predicted well. The second decomposition step was predicted at satisfactory level.

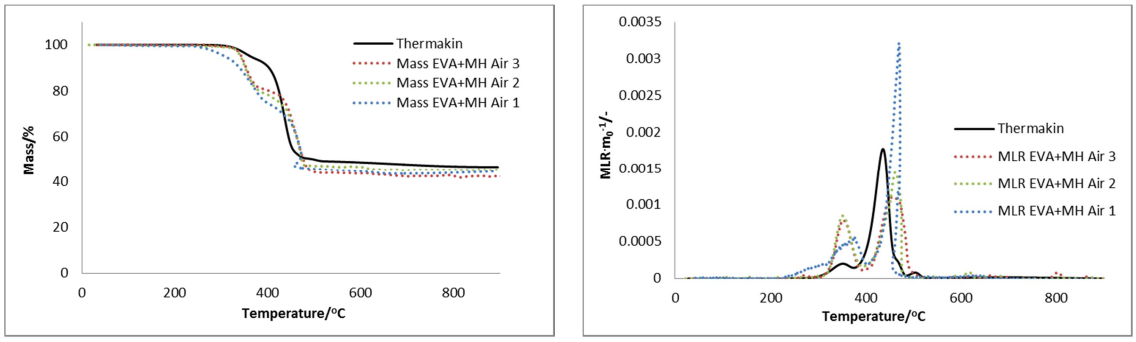

(a) (b)

Figure 117 ThermaKin fit of EVA+MH in air (a) mass loss and (b) mass loss rate curve

Universal nine reaction mechanism of the EVA+MH model of thermal decomposition in nitrogen and air atmosphere was constructed. Two independent models of EVA and MH were used for this purpose. Both atmospheres nitrogen and air were investigated - see Table 51 for reactions details). ThermaKin model of EVA+MH in nitrogen and also in air was not able to capture all features of the first reaction step but second step was predicted with satisfactory accuracy. In air ThermaKin fit of second peak of MLR is shifted to lower temperature as seen on Figure 117b but such prediction could be acceptable as well. It is worth noting that experimental tests uncertainties could also affect the results – model is based on two independent samples of EVA and MH, a completely new material such as EVA+MH was not fitted separately. ThermaKin model of EVA+MH is strictly based on

prediction. Experimental results of EVA+MH were scattered what could also affect the final result.

Table 51 The universal nine reaction mechanism of EVA+MH decomposition

Reaction description	Temp. (˚C)	Gas-phase products
1) Reaction 1 Pyrolysis EVA EVA → 0.89$EVA_{residue1}$ + 0.11$EVA_{volatiles1}$ A = 6.11 x 10^{11} sec^{-1} E_a = 1.66 x 10^5 J/mol	275-360	Water, carbon dioxide, carbon monoxide, acetic acid, acetone
2) Reaction 1a Oxidation EVA EVA → 0.65$EVA_{residue1}$ + 0.35$EVA_{volatiles1}$ **A = 1.36x10^{10}[O_2%] sec^{-1}** E_a = 1.69x10^5 J/mol	300-400	
3) Reaction 1 MH MH → 0.97$MH_{residue1}$ + 0.03$MH_{volatiles1}$ A = 8.97 x 10^{13} sec^{-1} E_a = 2.0 x 10^5 J/mol	325-455	
4) Reaction 2 MH MH → 0.75$MH_{residue1}$ + 0.25$MH_{volatiles1}$ A = 8.10 x 10^{13} sec^{-1} E_a = 2.15 x 10^5 J/mol	350-450	
5) Reaction 2 Pyrolysis EVA $EVA_{residue1}$ → $EVA_{volatiles2}$ A = 1.27 x 10^{22} sec^{-1} E_a = 3.45 x 10^5 J/mol	360-450	
6) Reaction 2a Oxidation EVA $EVA_{residue1}$ → 0.19 $EVA_{residue2}$ + 0.81$EVA_{volatiles2}$ **A = 1.94x10^{23} [O_2%] sec^{-1}** E_a = 3.6 x 10^5 J/mol	400-430	
7) Reaction 3 Oxidation EVA $EVA_{residue2}$ → 0.25 $EVA_{residue3}$ + 0.75$EVA_{volatiles3}$ **A = 1.53x10^{25} [O_2%] sec^{-1}** E_a = 4.0 x 10^5 J/mol	400-460	
8) Reaction 4 Oxidation EVA $EVA_{residue3}$ → $EVA_{volatiles4}$ **A = 2.94x10^{28} [O_2%] sec^{-1}** E_a = 4.7 x 10^5 J/mol	460-500	Hydrocarbons, ethylene, dodecane, eicosane, carbon monoxide, carbon dioxide, acetic acid
9) Reaction 3 MH $MH_{residue1}$ → 0.94$MH_{residue2}$ + 0.06$MH_{volatiles2}$ A = 1.33 sec^{-1} E_a = 5.50 x 10^4 J/mol	450-825	

6.2.5.3 FTIR Analysis of Evolved Condensable Products from EVA and MH samples

In nitrogen, for EVA+MH, water is observed at lower temperatures and at higher temperatures small amounts of acetic acid are found, followed by eicosane formation during the last decomposition step (Figure 118).

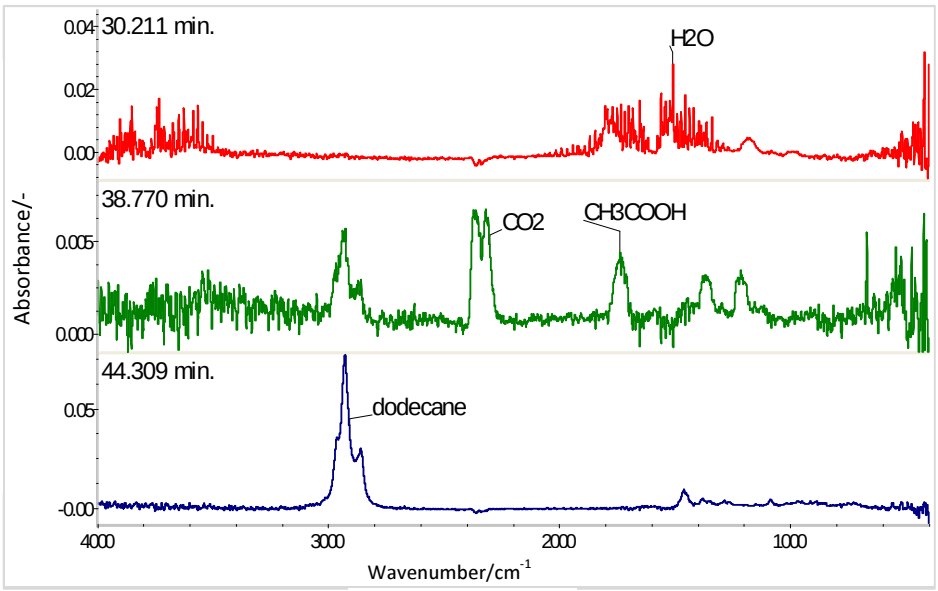

Figure 118 EVA+MH selected spectra at different decomposition time carried out in nitrogen

In air, samples containing magnesium hydroxide, Figure 119, have higher intensities for the peak corresponding to water and no clear spectrum for acetic acid, compared to EVA or EVA+NC samples. The most dominant volatiles found are hydrocarbons, C_2H_4, CO, CO_2, and H_2O.

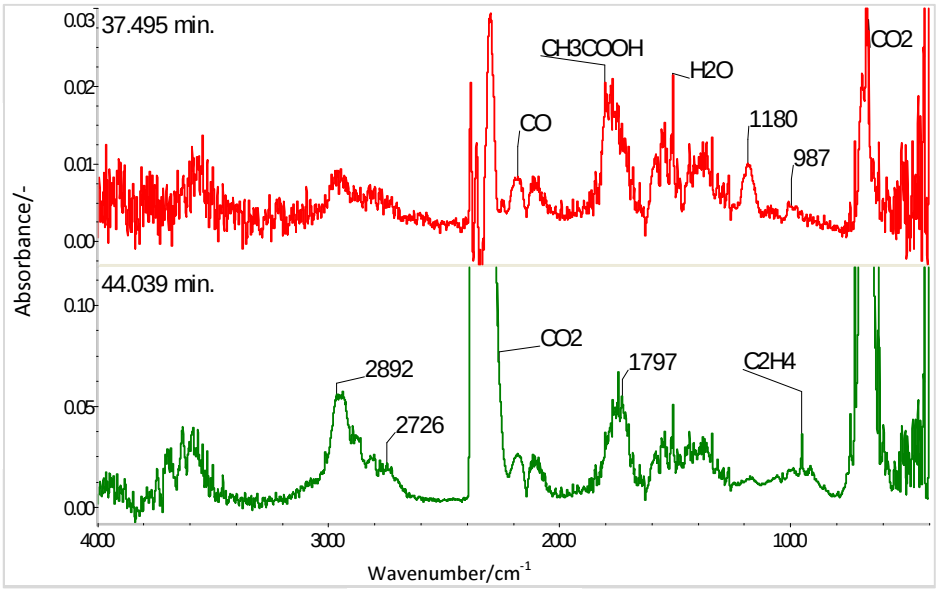

Figure 119 EVA+MH selected spectra at different decomposition time carried out in air

6.2.6 Thermal Degradation, Decomposition Products and Modelling of EVA with Nanoclay

This case is similar to PP+NC approach - the model assumed that the nanoclay was well-dispersed in EVA and a separate decomposition mechanisms for the polymer and nanofiller were not considered. It has been reported that when a well-dispersed system is obtained, loadings of 3 to 5% are sufficient to cause a large increase in mechanical strength and a significant reduction in the rate of peak heat release[111]. In other words, the EVA+NC model is entirely independent of the EVA model.

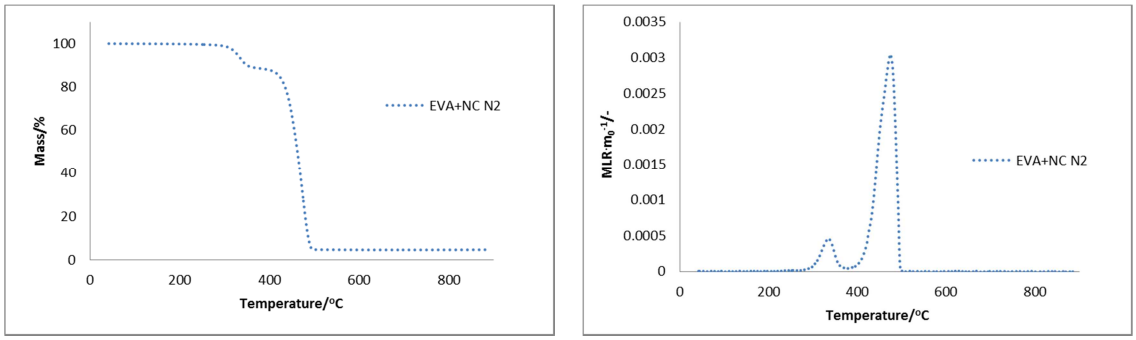

(a) (b)

Figure 120 TGA of EVA+NC in nitrogen atmosphere (a) mass loss and (b) mass loss rate curve

The decomposition of EVA+NC in nitrogen is a two-step reaction as seen in Figure 120. MLR curve shows two isolated peaks. A mechanism containing two reactions is proposed to model EVA+NC behaviour in N_2.

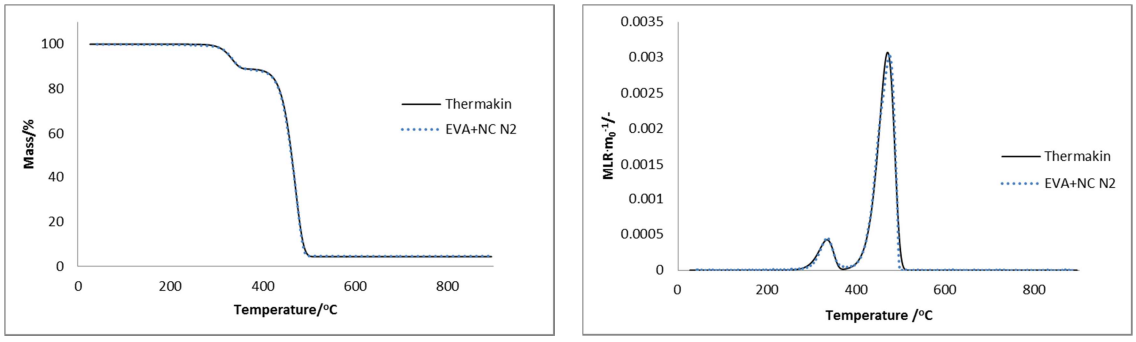

(a) (b)

Figure 121 Two reactions ThermaKin model of EVA+NC decomposition in N_2 (a) mass loss and (b) mass loss rate curve

The two reaction ThermaKin mechanism from Table 52 is sufficient to capture all the features of the experimental data as seen in Figure 121. Black solid lines represent

ThermaKin's fit and dark blue dots represent experimental data. EVA+NC leaves a 5% residue at the end of the pyrolysis process.

Table 52 Mechanism of EVA+NC decomposition in N_2

Reaction description	Temp. (˚C)	Gas-phase products
Reaction 1 $EVA\_NC \rightarrow 0.89EVA\_NC_{residue1} + 0.11EVA\_NC_{volatiles1}$ $A = 8.03 \times 10^{13}\ sec^{-1}\ E_a = 1.85 \times 10^5\ J/mol$	265-365	Acetic acid
Reaction 2 $EVA\_NC_{residue1} \rightarrow 0.05EVA\_NC_{residue2} + 0.95EVA\_NC_{volatiles2}$ $A = 1.74 \times 10^{16}\ sec^{-1}\ E_a = 2.6 \times 10^5\ J/mol$	365-495	Dodecane

In Figure 122 it is possible to observe how presence of oxygen changes EVA+NC's thermal decomposition behaviour.

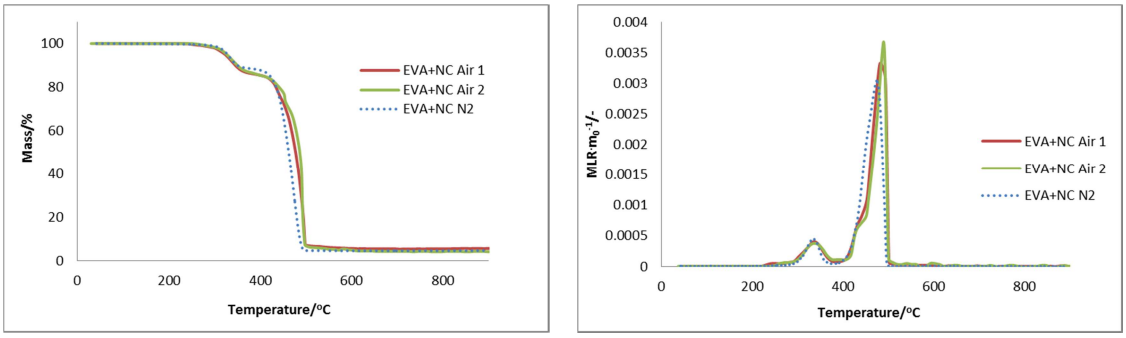

(a) (b)

Figure 122 Comparison of TGA EVA+NC curves in air and nitrogen

As seen in Figure 122, oxidation slightly delays the mass loss of EVA+NC. Both curves look similar. Again two steps are present and two peaks in the mass loss rate curves are dominant. Degradation of mass in air starts at the same time as in nitrogen, presumably because the nanoclay platelets cover the surface and protect it from attack by oxygen. Pyrolysis in nitrogen is a very similar process to pyrolysis in air. However this time the mechanism is not universal and separate models were built for each atmosphere.

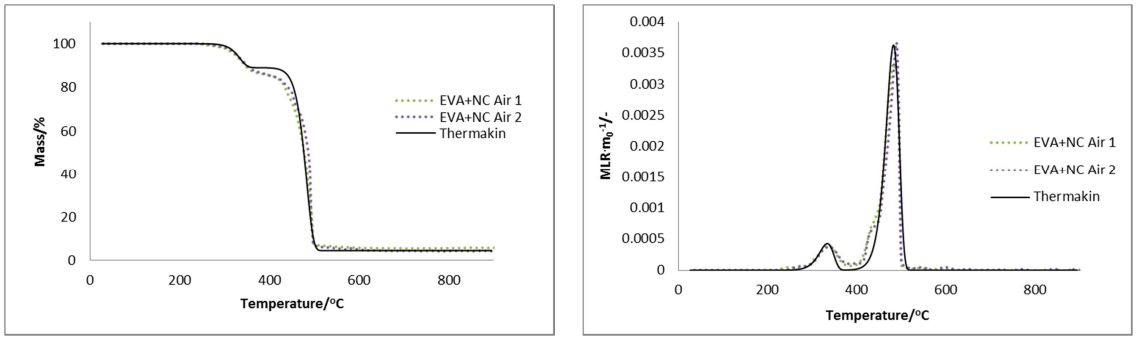

(a) (b)

Figure 123 Four Reaction ThermaKin model of EVA+NC decomposition in air (a) mass loss and (b) mass loss rate curve

The two reaction ThermaKin mechanism from Table 53 is able to reflect EVA+NC thermal decomposition behaviour in air with relatively high accuracy. The solid line of ThermaKin's fit in Figure 123 is a good approximation of mass loss, except for the area at the beginning of second decomposition step (~425°C). To keep the model mechanism simple, no more reactions were added.

Table 53 Two reaction mechanism of EVA+NC decomposition in air

Reaction description	Temp. (˚C)	Gas-phase products
Reaction 1 Oxidation (same as Pyrolysis) $EVA\_NC \rightarrow 0.89EVA\_NC_{residue1} + 0.11EVA\_NC_{volatiles1}$ $A = 6.11 \times 10^{11}\ sec^{-1}\ E_a = 1.66 \times 10^5\ J/mol$	265-360	Acetic acid, CO_2
Reaction 2 Oxidation $EVA\_NC_{residue1} \rightarrow 0.05EVA\_NC_{residue2} + 0.95EVA\_NC_{volatiles2}$ $A = 1.42 \times 10^{20}\ sec^{-1}\ E_a = 3.2 \times 10^5\ J/mol$	395-505	Acetic acid, CO_2, CO, H_2O, hydrocarbons, heptane, 1-hexene, 1-heptene, 4-methyl-2-pentanone or 2-pentanone, acrolein, ethanal or propenal

It is worth noting that nanoclay makes significant impact on kinetic parameters when added to PP but when added to EVA such dramatic changes were not observed, as seen in Table 52 and Table 53. In nitrogen, the pre-exponential factor *A* of EVA+NC is decreased, relative to EVA, the opposite to that observed for PP+NC. Values of activation energy seem to remain at a stable level. In air, the frequency factor *A* is increased when nanoclay is added to EVA, by approximately 9 orders of magnitude (for PP 7 orders of magnitude), while, again, the activation energy is hardly changed.

6.2.6.1 FTIR Analysis of Evolved Condensable Products from EVA and Nanoclay Samples

For EVA+NC, Figure 124, acetic acid is released at lower temperatures, followed by dodecane production at higher temperatures.

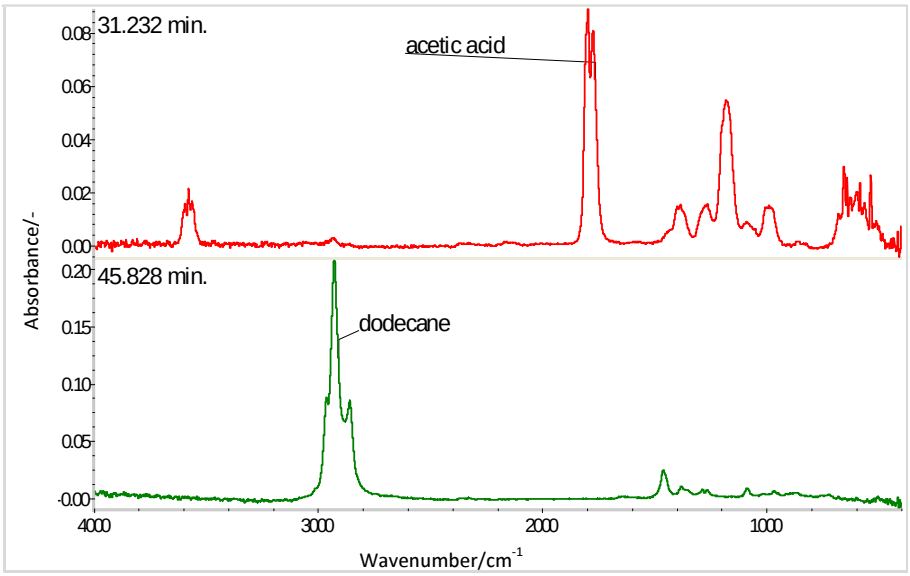

Figure 124 EVA+NC selected spectra at different decomposition time carried out in nitrogen

For the EVA+NC sample in air, Figure 125, the same products are observed for the two decomposition steps, as for EVA, and CH_3COOH together with CO, CO_2, H_2O and hydrocarbons are released. Similarly to EVA sample, the peaks within 2998-2856 cm^{-1} indicate heptane, 1-hexene, or 1-heptene presence. Additionally, 4-methyl-2-pentanone or 2-pentanone may be also present. The carbonyl region of 1815-1700 cm^{-1} suggests acrolein, ethanal or propenal, however in order to confirm their existence further analysis is required.

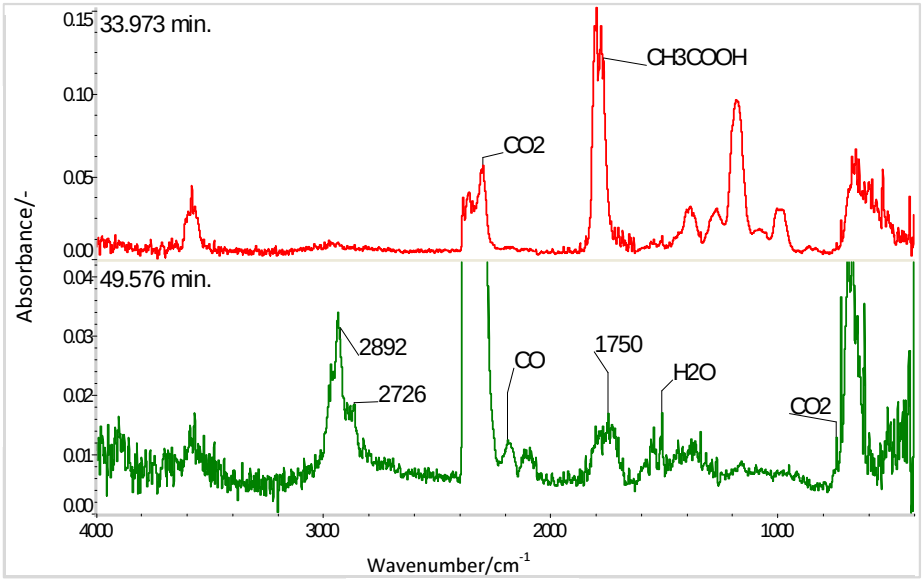

Figure 125 EVA+NC selected spectra at different decomposition time carried out in air

6.2.7 Thermal Degradation, Decomposition Products and Modelling of EVA+NC+ATH

Experimental data of the thermal decomposition of EVA+NC+ATH in N_2 is presented in Figure 126.

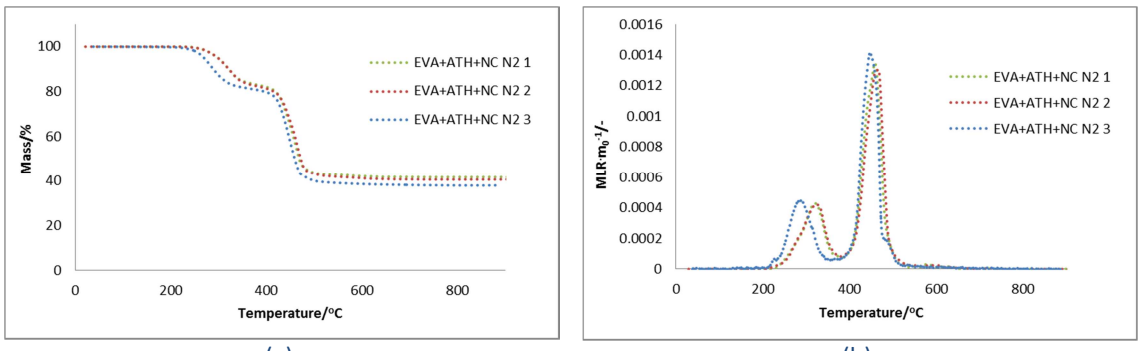

(a) (b)

Figure 126 TGA of EVA+NC+ATH in N_2 (a) mass loss and (b) mass loss rate curves

Two decomposition steps are observed. Figure 127 presents a predictive ThermaKin model of EVA+NC+ATH in nitrogen displayed as a solid line. Dotted lines represent experimental data.

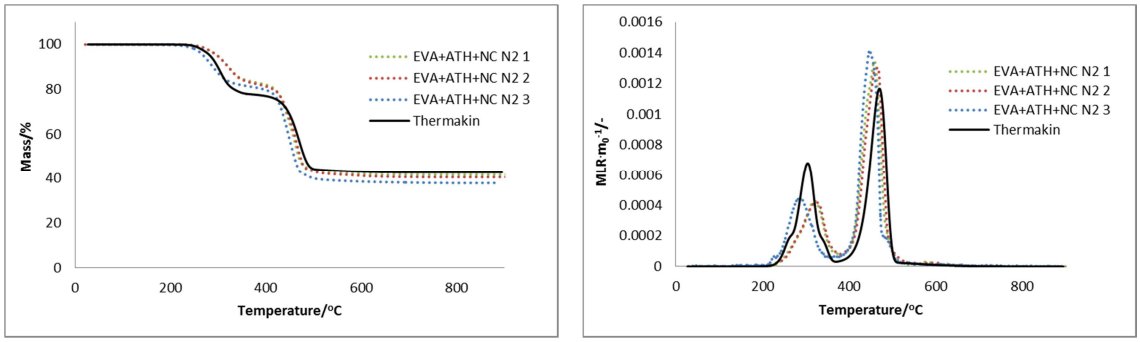

(a) (b)

Figure 127 ThermaKin fit of EVA+NC+ATH in N_2 (a) mass loss and (b) mass loss rate curves

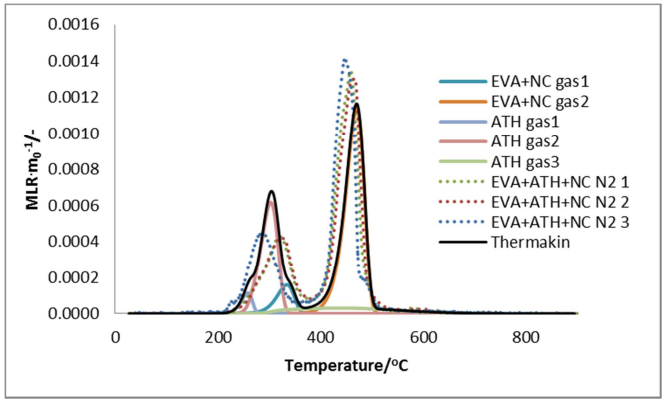

Figure 128 Contribution of each ThermaKin reaction to the mass loss rate in N_2

Figure 128 highlights the contribution of each ThermaKin reaction from Table 54 to overall mass loss rate. Dotted lines are experimental, solid lines are from ThermaKin.

Table 54 The five reaction mechanism of EVA+NC+ATH decomposition in N_2

Reaction description	Temp. (˚C)	Gas-phase products
1) Reaction 1 ATH $ATH \rightarrow 0.97ATH_{residue1} + 0.03ATH_{volatiles1}$ $A = 6.58 \times 10^{19}$ sec^{-1} $E_a = 2.2 \times 10^5$ J/mol	210-260	H_2O
2) Reaction 2 ATH $ATH \rightarrow 0.75ATH_{residue1} + 0.25ATH_{volatiles1}$ $A = 8.94 \times 10^{12}$ sec^{-1} $E_a = 1.65 \times 10^5$ J/mol	225-335	
3) Reaction 1 Pyrolysis EVA+NC $EVA\_NC \rightarrow 0.89EVA\_NC_{residue1} + 0.11EVA\_NC_{volatiles1}$ $A = 8.03 \times 10^{13}$ sec^{-1} $E_a = 1.85 \times 10^5$ J/mol	270-360	CO, CO2, acetic acid, acetone
4) Reaction 3 ATH $ATH_{residue1} \rightarrow 0.9ATH_{residue2} + 0.1ATH_{volatiles2}$ $A = 1.93$ sec^{-1} $E_a = 3.0 \times 10^4$ J/mol	280-550	
5) Reaction 2 Pyrolysis EVA_NC $EVA\_NC_{residue1} \rightarrow 0.05EVA\_NC_{residue2} + 0.95EVA\_NC_{volatiles2}$ $A = 1.74 \times 10^{16}$ sec^{-1} $E_a = 2.6 \times 10^5$ J/mol	370-500	Nonane

The mechanism of the EVA+NC+ATH model in nitrogen was constructed from two independent models of EVA+NC and ATH as it is presented in Table 54. The ThermaKin model of EVA+NC+ATH captured features of the ML and MLR curves with satisfactory accuracy. However experimental data shows some scatter, and the model seems to fit the average experimental results.

Decomposition of EVA with aluminium hydroxide (EVA+NC+ATH) in air is presented in Figure 129. MLR and ML curves in air have similar structures to those in nitrogen. There are two major steps of degradation and slow decomposition between 325-425°C.

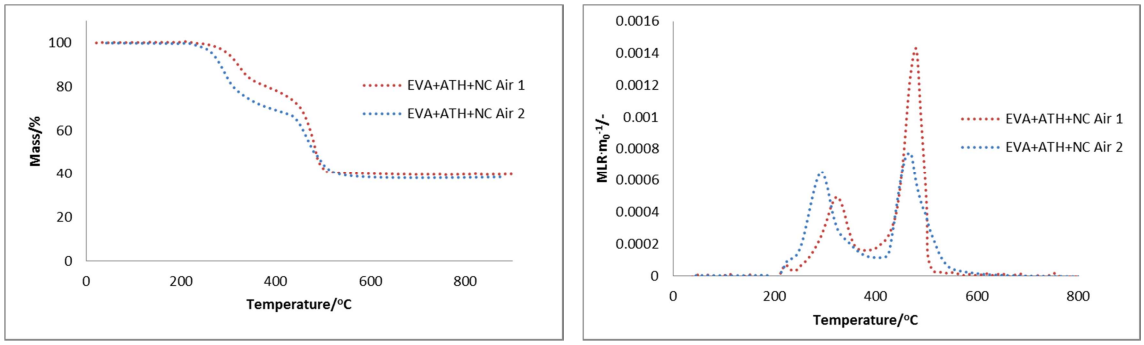

(a) (b)

Figure 129 TGA of EVA+NC+ATH in air (a) mass loss and (b) mass loss rate curves

Figure 130 presents predictive ThermaKin model of EVA+NC+ATH in air. The solid line corresponds to the model approximation and dotted lines represent experimental data collected in air.

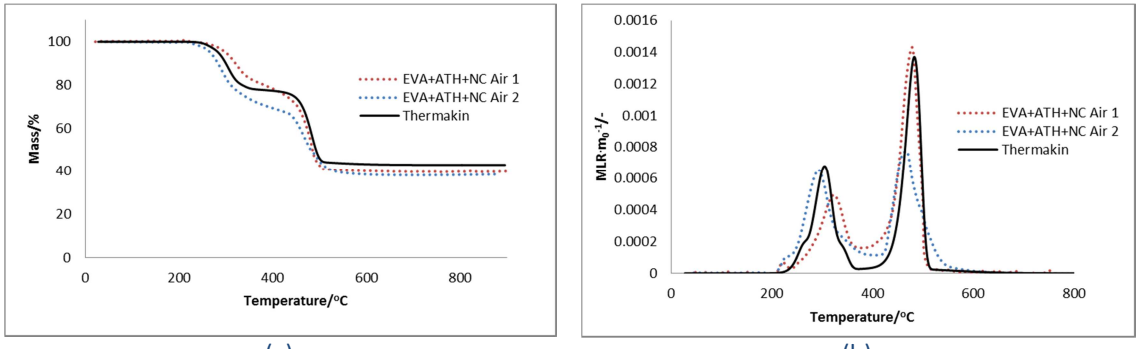

(a) (b)

Figure 130 ThermaKin fit of EVA+NC+ATH in air (a) mass loss and (b) mass loss rate curve

As the model mechanism is complex, Figure 131 is a magnified version of MLR curve with additional information showing the contribution of each reaction from Table 55.

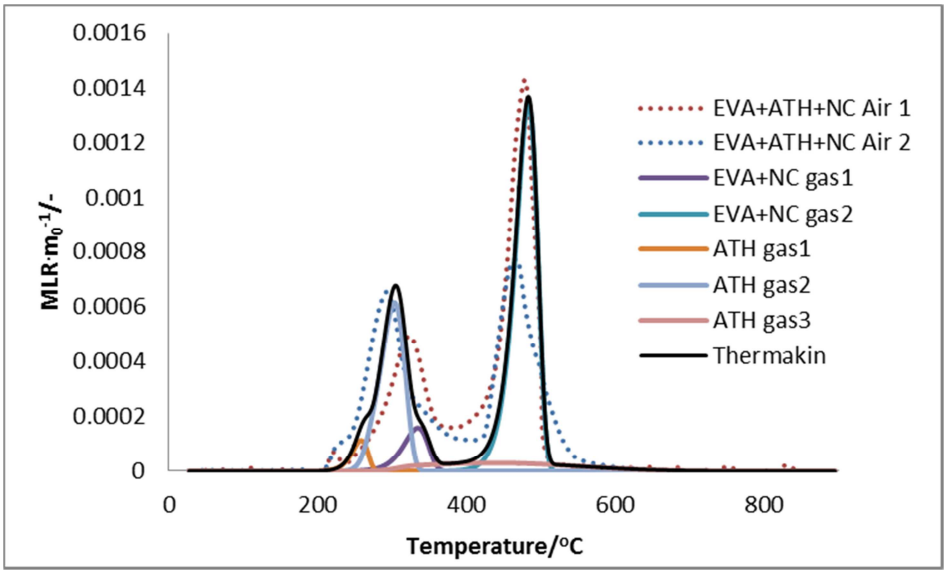

Figure 131 Contribution of each ThermaKin reaction to the mass loss rate in air

Although repeatability of TGA results was not very good the model still predicted MLR behaviour at satisfactory level.

Table 55 The five reaction mechanism of EVA+NC+ATH decomposition in air

Reaction description	Temp. (˚C)	Gas-phase products
1) Reaction 1 ATH $ATH \rightarrow 0.97ATH_{residue1} + 0.03ATH_{volatiles1}$ $A = 6.58 \times 10^{19}\ sec^{-1}\ E_a = 2.2 \times 10^5\ J/mol$	200-255	H_2O
2) Reaction 2 ATH $ATH \rightarrow 0.75ATH_{residue1} + 0.25ATH_{volatiles1}$ $A = 8.94 \times 10^{12}\ sec^{-1}\ E_a = 1.65 \times 10^5\ J/mol$	225-315	CO_2, CO, H_2O, acetic acid
3) Reaction 1 Pyrolysis EVA+NC $EVA\_NC \rightarrow 0.89EVA\_NC_{residue1} + 0.11EVA\_NC_{volatiles1}$ $A = 8.03 \times 10^{13}\ sec^{-1}\ E_a = 1.85 \times 10^5\ J/mol$	260-360	
4) Reaction 3 ATH $ATH_{residue1} \rightarrow 0.9ATH_{residue2} + 0.1ATH_{volatiles2}$ $A = 1.93\ sec^{-1}\ E_a = 3.0 \times 10^4\ J/mol$	250-550	
5) Reaction 2 Oxidation EVA_NC $EVA\_NC_{residue1} \rightarrow 0.05EVA\_NC_{residue2} + 0.95EVA\_NC_{volatiles2}$ $A = 1.42 \times 10^{20}\ sec^{-1}\ E_a = 2.2 \times 10^5\ J/mol$	390-530	hydrocarbons (heptane, 1-hexene, 1-heptene, ethylene)

6.2.7.1 FTIR Analysis of Evolved Condensable Products from EVA+NC+ATH samples

Similarly to other samples, EVA+ATH+NC (Figure 132) is the sample where acetic acid production is not clearly seen during the decomposition process. The main volatiles released are water, carbon dioxide and nonane at higher temperatures.

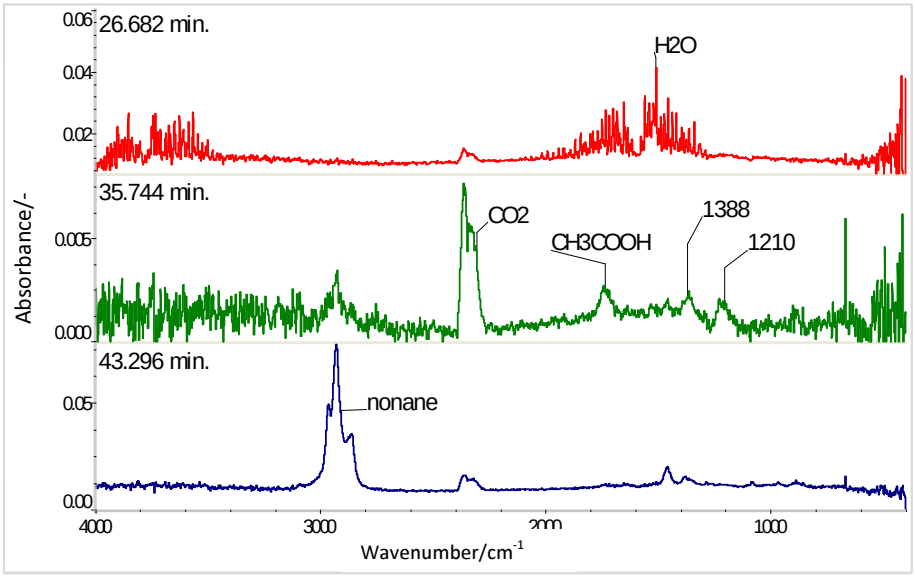

Figure 132 EVA+ATH+NC selected spectra at different decomposition time carried out in nitrogen

For EVA+ATH+NC in air two different spectra are presented in Figure 133. The obvious products from EVA+ATH+NC decomposition are CH_3COOH, C_2H_4, CO, CO_2, and H_2O. The peaks within 2998-2856 cm^{-1} indicate hydrocarbon presence (heptane, 1-hexene, 1-heptene).

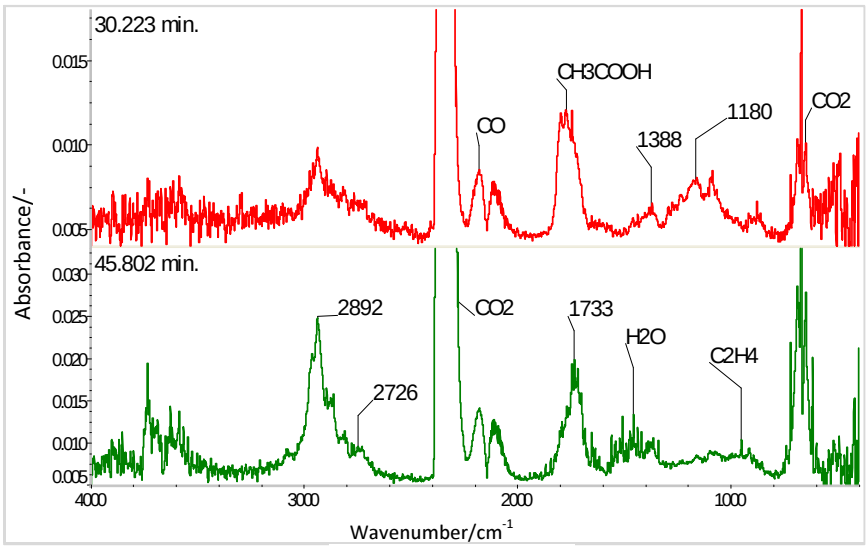

Figure 133 EVA+ATH+NC selected spectra at different decomposition time carried out in air

6.2.8 Thermal Degradation, Decomposition Products and Modelling of EVA+NC+MH

Experimental data of thermal decomposition of EVA with magnesium hydroxide and nanoclay (EVA+NC+MH) in nitrogen is presented in Figure 134.

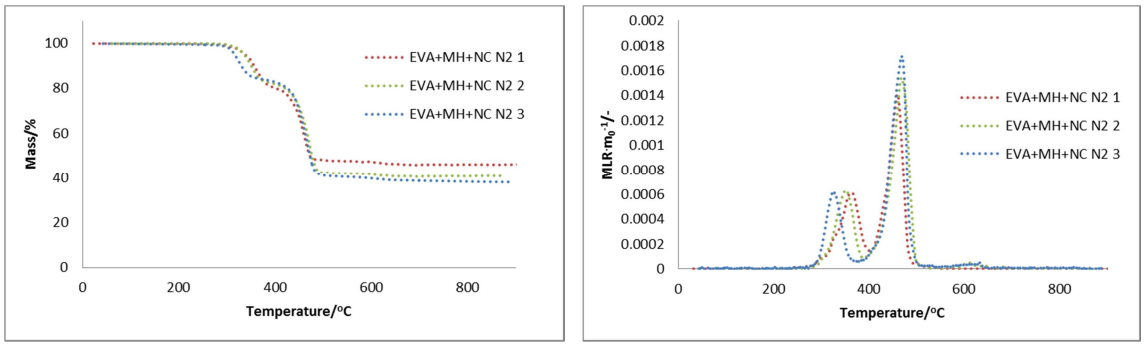

(a) (b)

Figure 134 TGA of EVA+NC+MH in N_2 (a) mass loss and (b) mass loss rate curves

Two mass loss steps are observed. Figure 135 presents a predictive ThermaKin fit of EVA+NC+MH in nitrogen. The solid line represents the model prediction and the dotted lines show the experimental results.

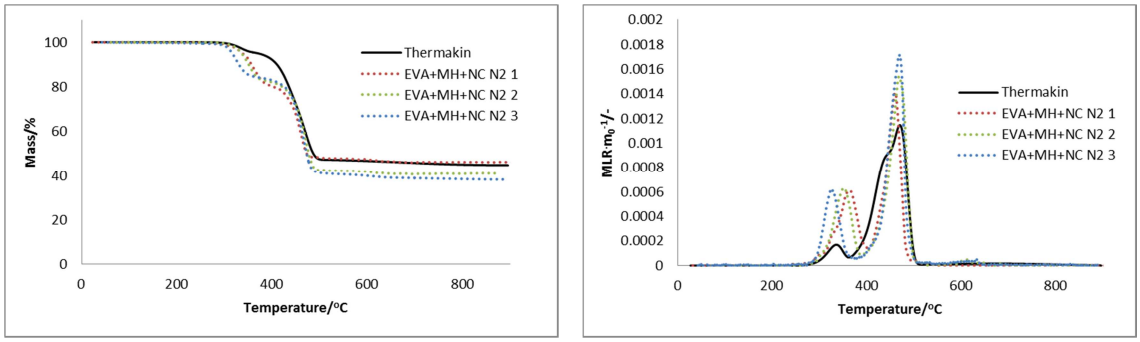

(a) (b)

Figure 135 ThermaKin fit of EVA+NC+MH in N_2 (a) mass loss and (b) mass loss rate curves

The model contains two independent mechanisms (EVA+NC and MH) which combined together contribute to a model a new material (EVA+NC+MH) prediction as shown in Figure 135.

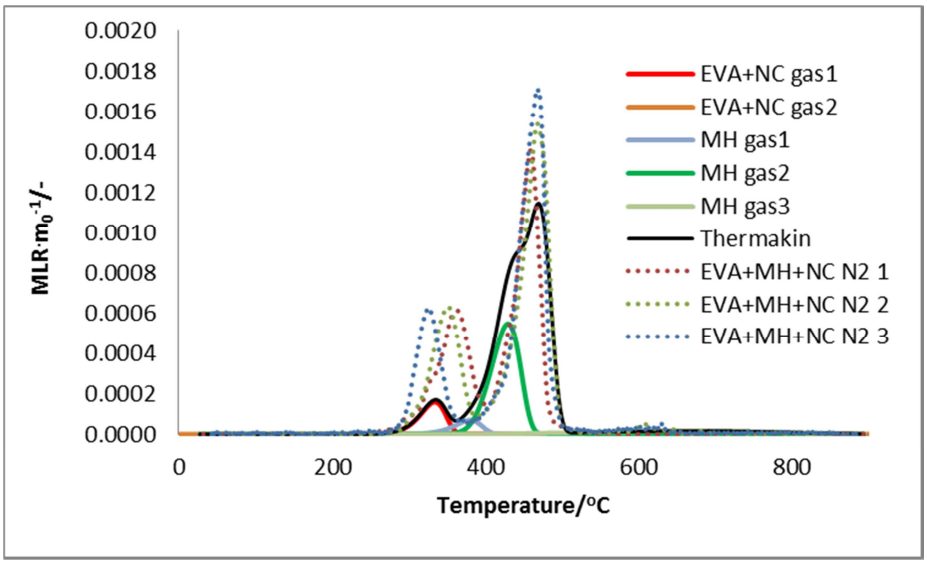

Figure 136 Contribution of each ThermaKin reaction to the mass loss rate in N_2

Similar situation to that with EVA+MH has been observed in this case. Magnesium hydroxide affects also EVA+NC thermal behaviour at the early stage of decomposition. Mainly water was detected by FTIR at around 350°C as shown in Figure 140 (corresponding to the first peak of mass loss rate curve). Again it is difficult to explain that more mass was degraded from EVA+NC+MH than from EVA+NC and MH. Possibly decomposition of MH stopped the early release of acetic acid from EVA+NC and in the same time some extra water degraded from MH.

Table 56 The five reaction mechanism of EVA+NC+MH decomposition in N_2

Reaction description	Temp. (˚C)	Gas-phase products
1) Reaction 1 Pyrolysis EVA+NC $EVA\_NC \rightarrow 0.89EVA\_NC_{residue1} + 0.11EVA\_NC_{volatiles1}$ $A = 8.03 \times 10^{13}\ sec^{-1}\ E_a = 1.85 \times 10^5$ J/mol	270-360	H_2O
2) Reaction 1 MH $MH \rightarrow 0.97MH_{residue1} + 0.03MH_{volatiles1}$ $A = 8.97 \times 10^{13}\ sec^{-1}\ E_a = 2.0 \times 10^5$ J/mol	315-390	
3) Reaction 2 MH $MH \rightarrow 0.75MH_{residue1} + 0.25MH_{volatiles2}$ $A = 8.10 \times 10^{13}\ sec^{-1}\ E_a = 2.15 \times 10^5$ J/mol	370-445	CO_2, acetic acid, acetone
4) Reaction 2 Pyrolysis EVA_NC $EVA\_NC_{residue1} \rightarrow 0.05EVA\_NC_{residue2} + .95EVA\_NC_{volatiles2}$ $A = 1.74 \times 10^{16}\ sec^{-1}\ E_a = 2.6 \times 10^5$ J/mol	410-495	Dodecane
5) Reaction 3 MH $MH_{residue1} \rightarrow 0.94MH_{residue2} + 0.06MH_{volatiles3}$ $A = 1.33\ sec^{-1}\ E_a = 5.50 \times 10^4$ J/mol	400-620	CO_2, H_2O

The mechanism containing 5 reactions described in Figure 50 was constructed from two independent models of EVA+NC and MH. The ThermaKin model EVA+NC+MH captured of the second step of decomposition with satisfactory accuracy, while the first degradation step was recognised but did not fit entirely with the model Figure 136. The reason for lack of agreement with the model for the first decomposition step could be explained by surprisingly high level of decomposition in first peak. Adding magnesium hydroxide seems to change EVA+NC properties, because proportionally more mass was degraded in first step (at 325°C) of EVA+NC+MH than it was for EVA+NC and pure MH together, over the same temperature range.

Decomposition of EVA+NC+MH in air is presented on Figure 137. The MLR and ML curves in air have a similar structure to those in nitrogen. There are two major steps of degradation.

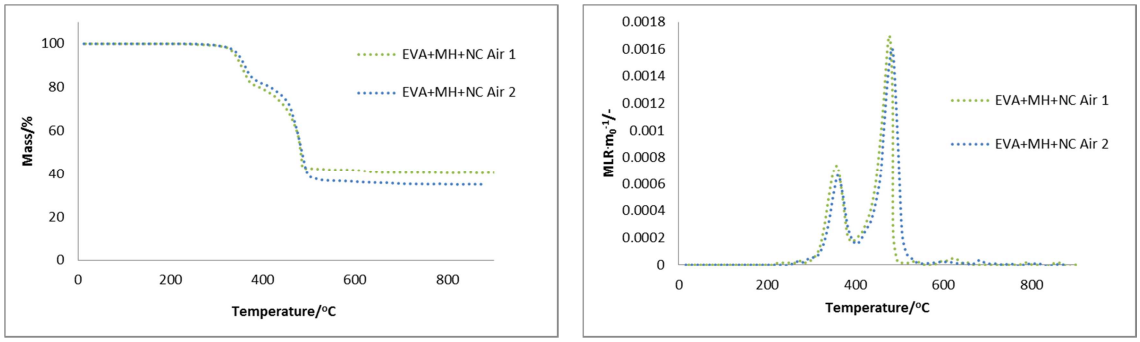

(a) (b)

Figure 137 TGA of EVA+NC+MH in air (a) mass loss and (b) mass loss rate curves

Figure 138 presents predictive ThermaKin model of EVA+NC+MH in air.

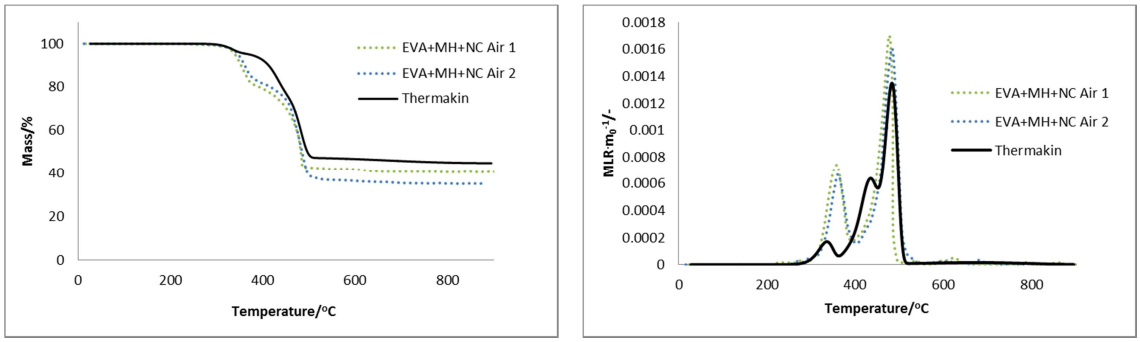

(a) (b)

Figure 138 ThermaKin fit of EVA+NC+MH in air (a) mass loss and (b) mass loss rate curve

On Figure 139 it is easy to trace all reactions contributions to mass loss rate data.

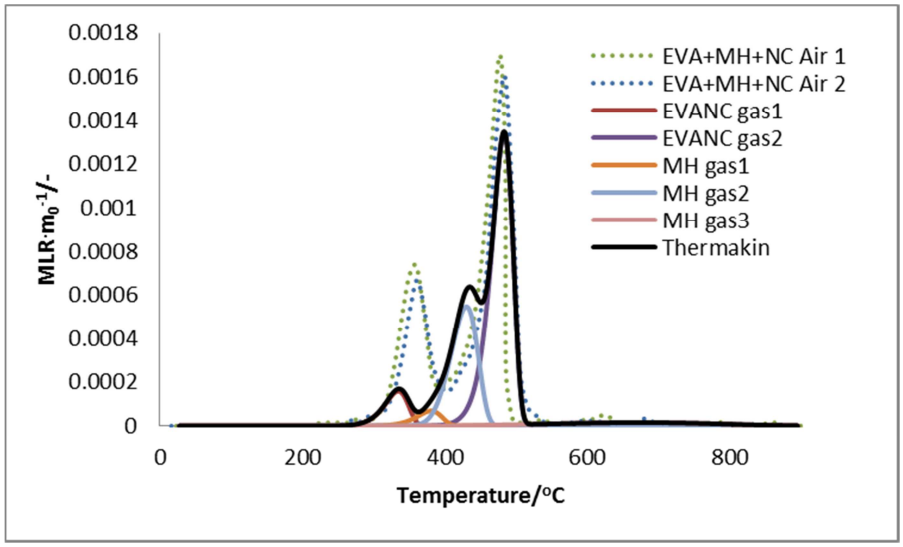

Figure 139 Contribution of each ThermaKin reaction to the mass loss rate in air

Modelling problem of MH as filler also refers to EVA+MH+NC in air. Again it was difficult to encompass first peak of mass loss rate by the 5 reaction model. Probably there is a strong interference between EVA+NC and MH. Possible volatile products can be found in Figure 141.

Table 57 The five reaction mechanism of EVA+NC+MH decomposition in air

Reaction description	Temp. (˚C)	Gas-phase products
1) Reaction 1 Pyrolysis EVA+NC $EVA\_NC \rightarrow 0.89EVA\_NC_{residue1} + 0.11EVA\_NC_{volatiles1}$ $A = 8.03 \times 10^{13}\ sec^{-1}\ E_a = 1.85 \times 10^5$ J/mol	270-360	H_2O
2) Reaction 1 MH $MH \rightarrow 0.97MH_{residue1} + 0.03MH_{volatiles1}$ $A = 8.97 \times 10^{13}\ sec^{-1}\ E_a = 2.0 \times 10^5$ J/mol	350-390	
3) Reaction 2 MH $MH \rightarrow 0.75MH_{residue1} + 0.25MH_{volatiles1}$ $A = 8.10 \times 10^{13}\ sec^{-1}\ E_a = 2.15 \times 10^5$ J/mol	360-450	
4) Reaction 2 Oxidation EVA_NC $EVA\_NC_{residue1} \rightarrow 0.05\ EVA\_NC_{residue2} + 0.95EVA\_NC_{volatiles2}$ $A = 1.42 \times 10^{20}\ sec^{-1}\ E_a = 3.2 \times 10^5$ J/mol	390-530	Hydrocarbons, ethylene, CO, CO_2, H_2O, methanol
5) Reaction 3 MH $MH_{residue1} \rightarrow 0.94MH_{residue2} + 0.06MH_{volatiles2}$ $A = 1.33\ sec^{-1}\ E_a = 5.50 \times 10^4$ J/mol	350-580	H_2O

6.2.8.1 FTIR Analysis of Evolved Condensable Products from EVA+NC+MH samples

In nitrogen, Figure 140, for EVA+NC+MH very similar products are observed compared to EVA+MH. Water is observed at lower temperatures. Then, at higher temperatures small amounts of acetic acid are found, followed by hydrocarbon formation during the last decomposition step.

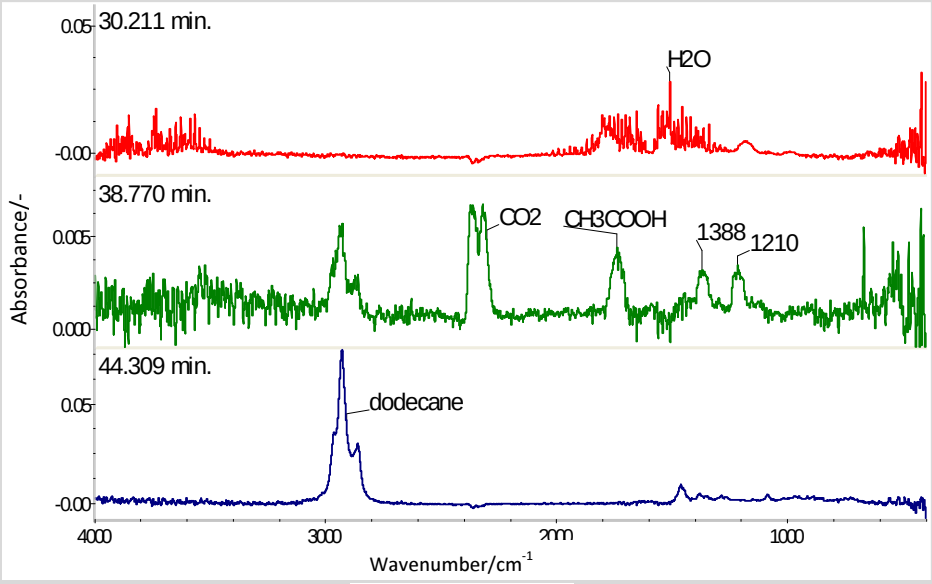

Figure 140 EVA+NC+MH selected spectra at different decomposition time carried out in nitrogen

Similar to samples containing magnesium hydroxide, EVA+NC+MH in air (Figure 141) have higher intensities for the peak corresponding to water and no clear spectrum for acetic acid. Similarly to EVA+MH sample, the most dominant volatiles found are hydrocarbons, C_2H_4, CO, CO_2, and H_2O.

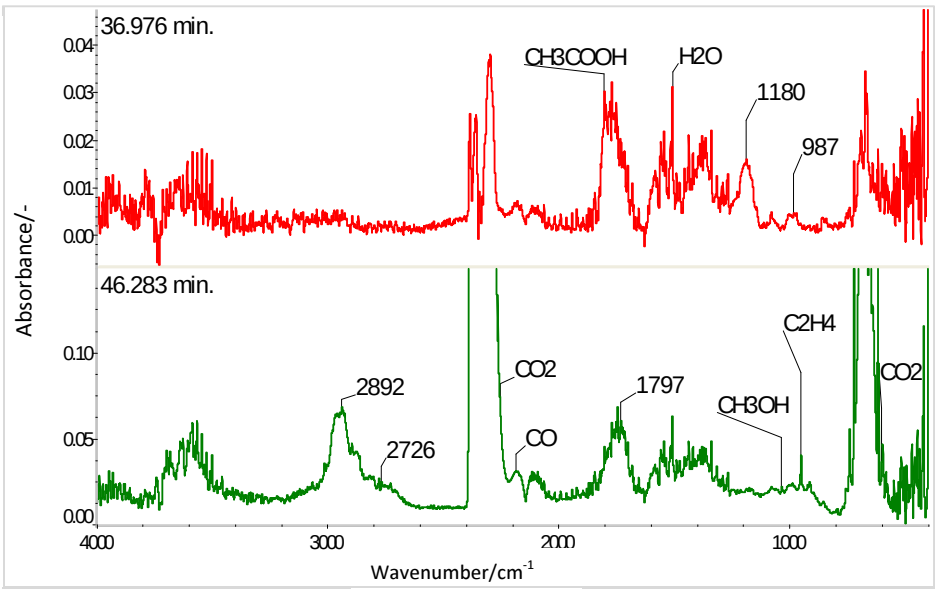

Figure 141 EVA+NC+MH selected spectra at different decomposition time carried out in air

FTIR spectra contain potential gas phase products; however sometimes it was difficult to assign particular volatiles to particular reaction in ThermaKin model as very often reactions overlapped. Then products were displayed on FTIR graphs at temperatures which showed the strongest infrared peaks. When ThermaKin mechanism involved reactions (which not overlapped) it was possible to distinguish gas products. Possibly pyGCMS could answer with higher precision which volatile has been released at each particular temperature.

6.2.9 Summary of Thermal Degradation of EVA with Fire Retardant and Nanoclay

The behaviour of EVA and additives was also investigated by TGA–FTIR under a nitrogen atmosphere. TGA mass losses together with Gram-Schmidt profiles (GS) (the sum of the total evolved gases detected by the spectrometer from FTIR) and degradation temperatures are presented in Figure 142 and Table 58.

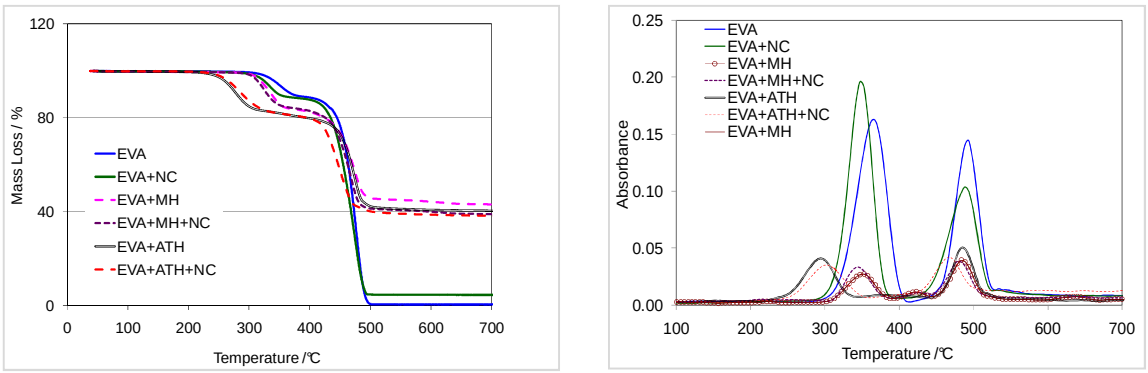

Figure 142 TGA mass losses (a) and FTIR Gram-Schmidt (b) profiles under nitrogen atmosphere

There are two consecutive decomposition steps observed except for EVA+MH and EVA+MH+NC where three Gram-Schmidt peaks are present, indicating the greater thermal stability of $Mg(OH)_2$ over $Al(OH)_3$.

Table 58 FTIR degradation temperatures from Gram-Schmidt profiles for the major peaks, and TGA mass losses under nitrogen atmosphere

	FTIR Degradation Temperature (°C)		**TGA Mass Loss (%)**	
	First peak	Second (Third) Peak	First peak	Second (Third) Peak
EVA	357	483	11	88
EVA + NC	342	483	11	83
EVA + MH	347	412 (483)	16	(38)
EVA + MH + NC	337	417 (478)	16	(43)
EVA + ATH	292	488	19	39
EVA + ATH + NC	297	463	19	41

For the first main decomposition peak, all samples have lower decomposition temperatures compared to EVA. EVA and EVA+NC have the highest thermal stability. For the second (third) main degradation peak the samples containing metal hydroxide alone have slightly greater thermal stabilities (Table 58), while those containing nanoclay have lower or equal thermal stabilities to the base polymer.

Figure 143 - Figure 146 presents FTIR profiles for water, acetic acid, and hydrocarbons in nitrogen. These profiles show evolution of water and acetic acid in the early stages, followed by hydrocarbons.

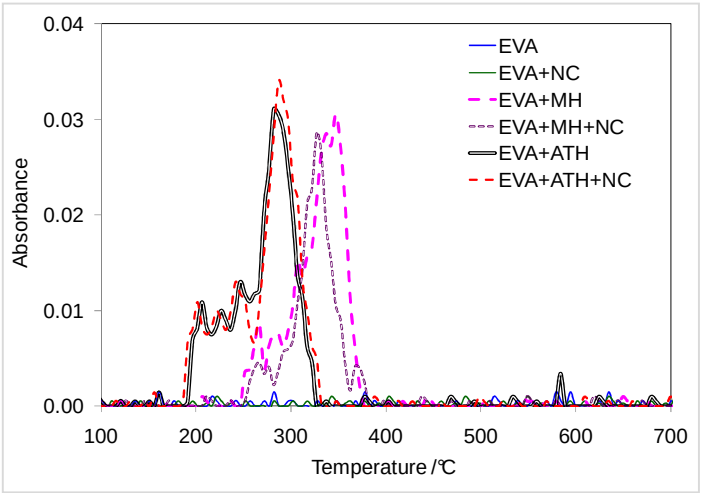

Figure 143 Water profile for EVA samples in nitrogen

At 250°C the protective layer on the EVA samples was ruptured by water evolution from the hydroxide decomposition, Figure 143. The intensities are similar for both samples; however ATH and ATH+NC release water at lower temperatures (250°C) compared to MH and MH+NC samples (350°C). For EVA and EVA+NC there is no evolution of water.

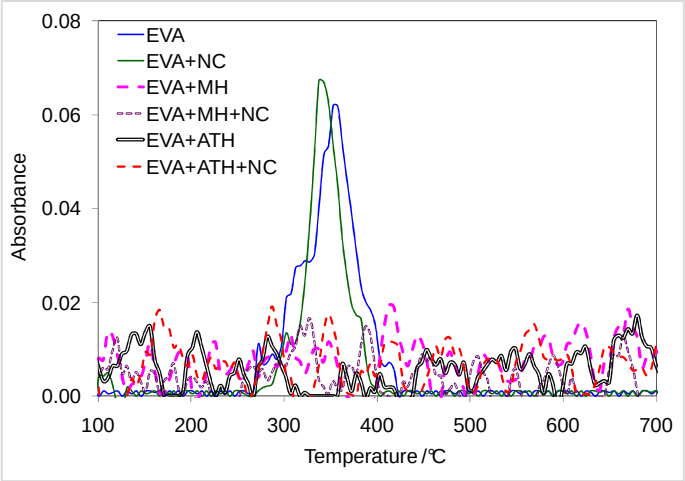

Figure 144 Acetic acid profile for EVA samples in nitrogen

It is generally accepted that the first stage of EVA decomposition is chain stripping with loss of acetic acid. At 345°C in pristine EVA, the major peak in the GS profile is assigned to acetic acid, Figure 144. Similarly it is in EVA+NC where the intensity of the first peak is higher. Remarkably no acetic acid peak is observed for any of the formulations containing metal hydroxides (ATH + MH). In the past, acetic acid was converted to acetone by passing over heated calcium oxide. The resulting aluminium oxide and magnesium oxide are believed to show the same catalyctic properties.

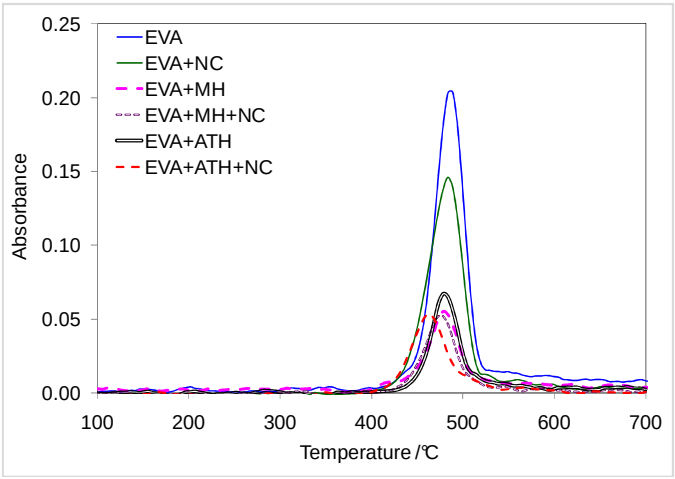

Figure 145 Hydrocarbon profile for EVA samples in nitrogen

At 460°C hydrocarbon compounds dominate and have much higher intensities (6-8 times greater) compared to other volatiles, Figure 145. Except for EVA+ATH+NC, which shows a peak hydrocarbon decomposition at 460°C, all the other materials show a peak in the main fuel production stage around 485°C. The higher peaks for EVA and EVA+NC correspond to the higher polymer content of these samples. At 500°C a reduced amount of all evolved materials is still observed and at higher temperatures evidence of char formation is presented.

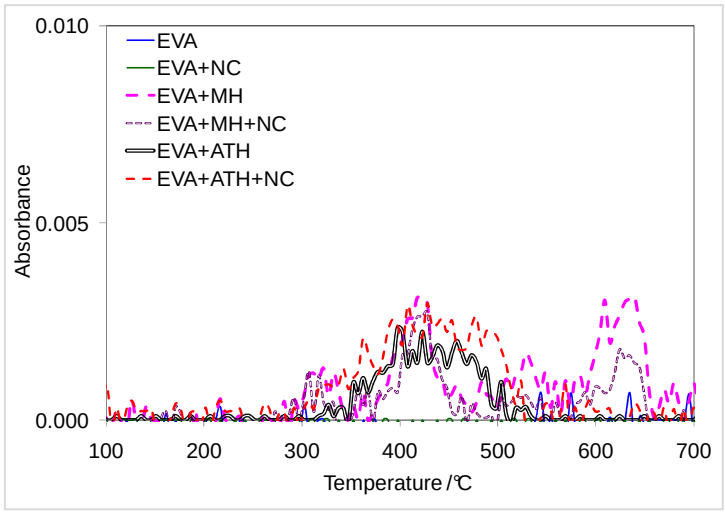

Figure 146 Carbon dioxide profile for EVA samples in nitrogen

Carbon dioxide is observed only for fire retarded samples, Figure 146. There are broader peaks observed for samples EVA+ATH and EVA+ATH+NC (~420°C), whereas for EVA+MH and EVA+MH+NC two peaks are observed; first at temperatures similar to the previous samples, and the second peak at ~630°C.

Figure 147 presents FTIR Gram–Schmidt profiles and TGA mass loss curves for all samples tested in air. Mass losses and FTIR degradation temperature for the main decomposition steps are presented in Table 59.

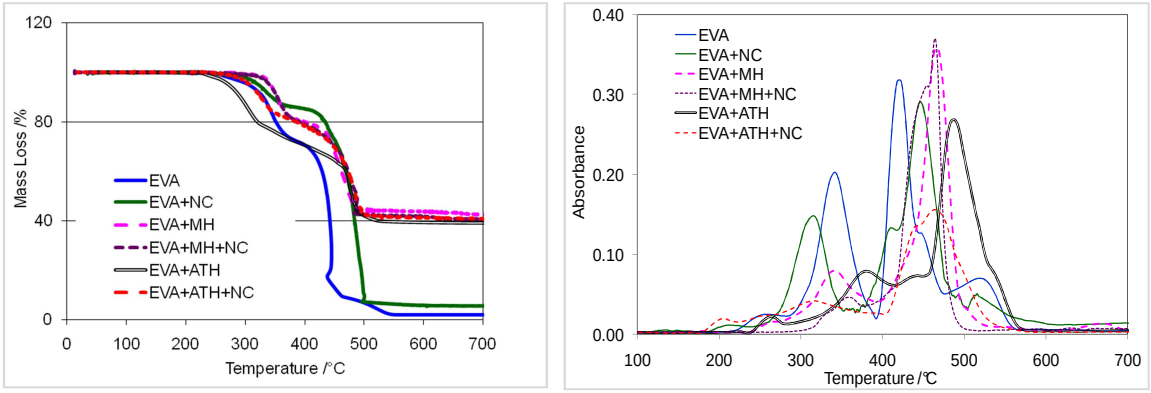

(a) (b)

Figure 147 TGA mass losses (a) and FTIR Gram-Schmidt (b) profiles under air atmosphere.

TGA and FTIR curves obtained for EVA and EVA+NC in air, similarly to nitrogen, shows that addition of nanoclay does not seem to change the thermal stability of the first degradation peak of EVA. However, there is a noticeable difference between these two samples for the second peak (where the most of volatiles are released) observed at 420-480°C where the temperature difference is around 50°C for approximately the same mass losses. This has been described elsewhere as the oxidation of the conjugated polyene, and its resulting carbonaceous residue. These studies support Beyer's assertion that the nanocomposite exhibits a significant increase in thermal stability, giving nitrogen-like decomposition[124].

Very similar TGA and FTIR curves for EVA+MH and EVA+MH+NC are observed. For these samples, the thermal stability is improved compared to EVA or EVA+NC with higher degradation temperatures, Table 59. Samples containing ATH show very similar characteristics compared to EVA+MH and EVA+MH+NC.

Table 59 FTIR degradation temperatures from Gram-Schmidt profiles, and TGA mass losses under air atmosphere for the major peaks

	FTIR Degradation Temperature/°C		**TGA Mass Loss/%**	
	First peak	Second Peak	First peak	Second Peak
EVA	347	427	18	74
EVA + NC	347	478	14	79
EVA + MH	390	483	19	36
EVA + MH + NC	380	473	18	39
EVA + ATH	409	454	16	44
EVA + ATH + NC	(342)*	468	(15)*	44

*small peak

For EVA and EVA+NC samples, the major peak in the GS profile is assigned to acetic acid at ~310°C and ~335°C respectively (Figure 148). The lower polymer loading in presence of ATH or MH masks the deacetylation of all other samples (EVA+ATH, EVA+MH, EVA+ATH+NC and EVA+MH+NC); acetic acid is not clearly seen (much harder to see for samples containing ATH than MH). However, unlike the results in nitrogen, its absence cannot be confirmed.

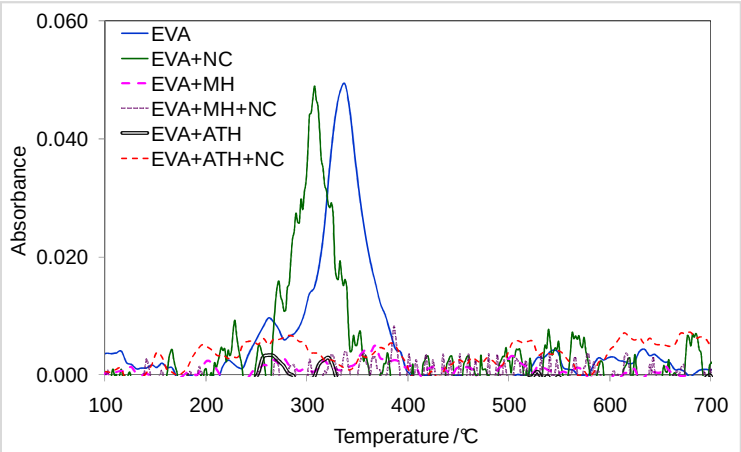

Figure 148 Acetic acid profile for EVA samples in air

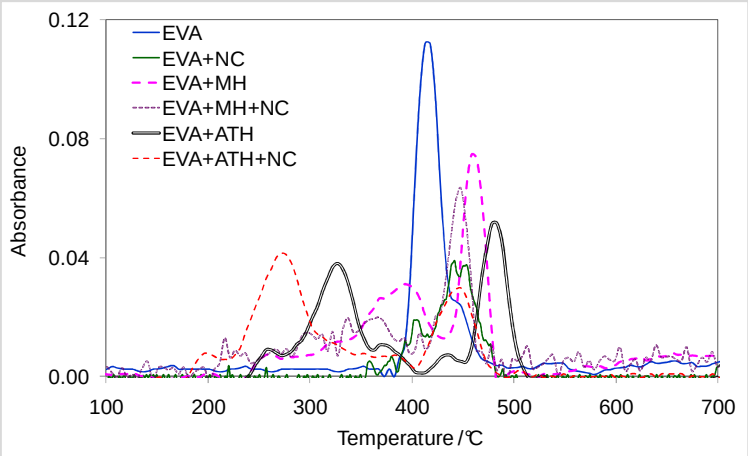

Figure 149 Water profile for EVA samples in air

The intensities for H_2O profiles are presented in Figure 149. Water results from both endothermic decomposition of filler (ATH or MH) and as an oxidation of the polymer. Both stages of polymer decomposition chain stripping with loss of acetic acid and oxidation of the unsaturated polyene may result in water formation. For EVA and EVA+NC one major peak is observed, having maxima at 415°C and 450°C. In air, at ~220°C the protective layer on the EVA samples is failing in the presence of ATH or MH, as it is ruptured by escaping water vapour[121] and two peaks are observed. The first peak, occurring at ~325°C for EVA+ATH and ~387°C for EVA+MH, followed by a smaller peak at ~480°C and ~460°C.

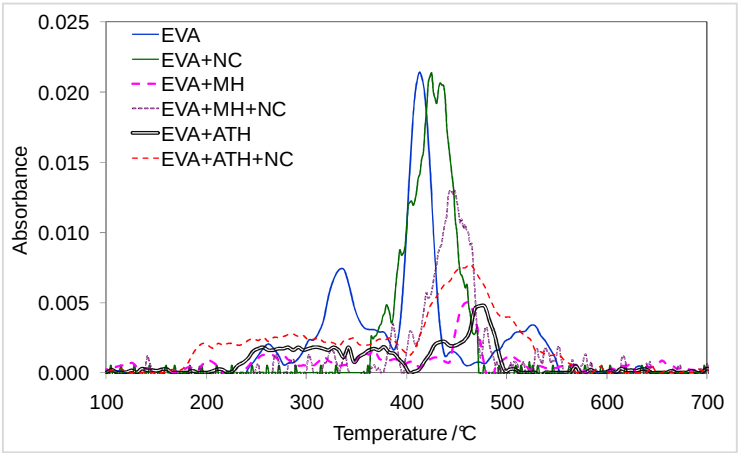

Figure 150 Carbon monoxide profile for EVA samples in air

A small release of carbon monoxide for all materials except EVA and EVA+NC is observed at 250-375°C, Figure 150, followed by major peaks, shifted towards higher temperatures in the following order: EVA+MH+NC (at ~445°C), EVA+ATH+NC, EVA+MH, and EVA+ATH (~480°C). For

EVA, three peaks are seen at ~332°C, maximum at ~412°C and the smallest peak at ~520°C. EVA+NC has only one broad peak observed at ~430°C.

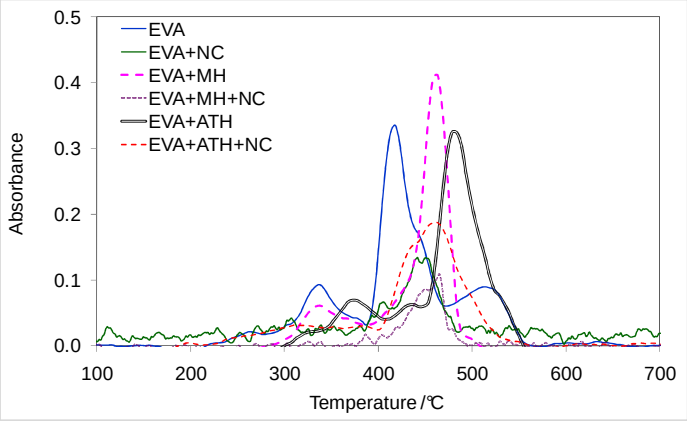

Figure 151 Carbon dioxide profile for EVA samples in air

Compared to carbon monoxide and water profiles, carbon dioxide is formed over the same temperature range (Figure 151). For all samples containing NC one major peak is observed occurring at similar temperatures around 450°C. Fire retarded samples (EVA+MH, EVA+ATH) have a much broader first peak occurring over a wider temperature range (300-425°C) compared to other samples. The effects of ATH and MH are observed and formation of a protective layer slows down the rate of decomposition until the temperature reaches ~460°C for EVA+MH, and ~480°C for EVA+ATH, where the major peak is produced. EVA has three peaks. The first peak at ~335°C, followed by the major peak around ~420°C and the third peak with a much smaller intensity occurring at ~520°C.

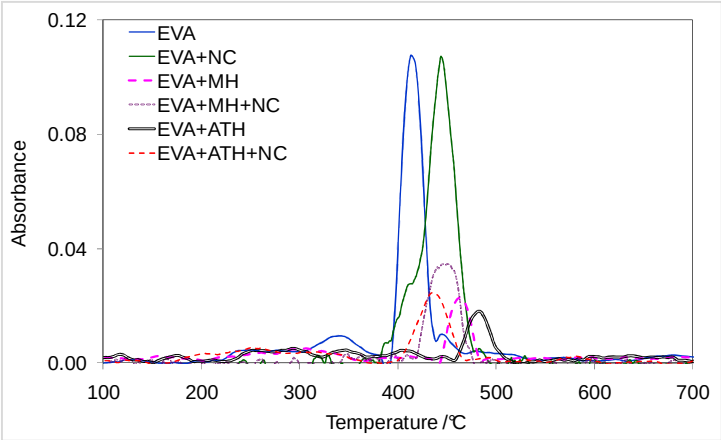

Figure 152 Hydrocarbons profile for EVA samples in air

After the loss of acetic acid, the remaining now unsaturated poly(ethylene-co-acetylene) undergoes scission at allylic positions (allylic bond – double bond at end of chain). Between 400 and 500°C, the hydrocarbon peak is present for all samples (Figure 152). Hydrocarbon formation for EVA starts at ~330°C and reaches maximum at ~415°C. All samples containing NC have one peak where maxima are observed at similar temperatures (~450°C). The highest thermal stabilities are seen for fire retarded samples (EVA+ATH, EVA+MH).

6.2.10 FTIR minor products for EVA samples in nitrogen

Additionally, to acetic acid, water and hydrocarbons, also strong FTIR peak is observed possibly for acetone for samples containing either ATH or MH, but absent in samples of EVA and EVA+NC. Together with the reference and sample spectra acetone presence is presented in Figure 153.

This peak reaches maxima at 38 min. for samples containing MH and at 36-37 min. for samples containing ATH. This is significantly hotter than the acetic acid release from EVA and EVA+NC around 350°C.

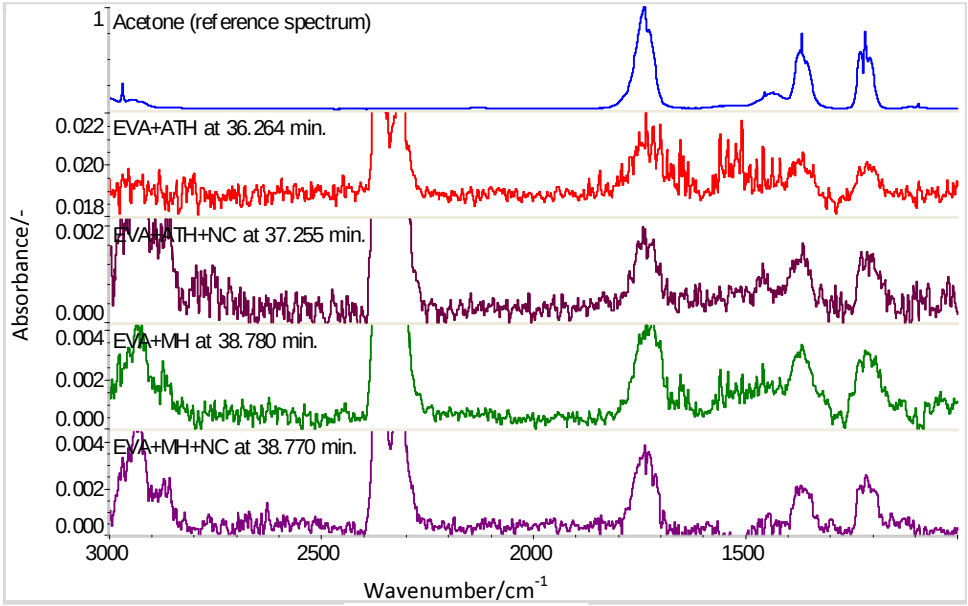

Figure 153 Acetone FTIR spectra found in samples under nitrogen atmosphere

There are no profiles presented for acetone, as other volatiles fit within the same wavenumber regions (water, ketones, aldehydes, hydrocarbons etc.) which makes difficult to

generate profiles purely assigned to acetone presence. In addition, the absorbances for this species are very low, compared to other decomposition products and peaks are shifted to a higher temperature, making harder to isolate it.

6.2.11 Conclusions of Thermal Degradation of EVA samples with Fire Retardants and Nanoclay

In a summary:

<u>In Nitrogen</u>

- Studies by TGA, in nitrogen, show an increased thermal stability for all samples compared with EVA where char is not present. For the first degradation peak, addition of ATH shows mass loss at lower temperature then MH samples. However, looking at the second peak where the most volatiles are formed, all samples show the higher thermal stability compared to pristine EVA or EVA+NC.

- In nitrogen, at 250°C the protective layer on the EVA samples is failing in the presence of ATH or MH due to water vapour produced from the decomposing ATH or MH compromising its integrity. The intensities are similar for both samples; however ATH and ATH+NC release water at lower temperatures compared to MH and MH+NC samples.

- For EVA and EVA+NC there is no corresponding evolution of water, and the first mass loss stage is assigned to acetic acid release. At higher temperatures, the beneficial effect of flame retardants is seen. Addition of MH or ATH inhibits acetic acid evolution. In samples containing ATH, acetic acid is not detected (suggesting high conversion rates on the fresh alumina surface).

- At 460°C hydrocarbon compounds dominate and have much higher intensities (6-8 times greater) as the unsaturated polyene decomposes. At 500°C a small amount of evolved materials is still observed and at higher temperatures there is evidence of char formation for all samples except EVA.

- Also in inert atmosphere there are CO_2 peaks released from fire retarded samples.

In Air

- Compared to pristine EVA, addition of nanoclay did not change the temperature of the first degradation peak. However, there is a noticeable difference between these two samples for the second peak (the main fuel production step) observed at 420-480°C where the nanoclay raised the temperature of the second stage by 50°C with approximately the same mass loss. Similar profiles are found for fire retarded samples containing MH or ATH. For these samples, the thermal stability is improved compared to EVA or EVA+NC with higher degradation temperatures, and lower mass losses as well as the presence of approximately 30% char. Lower mass losses are mainly due to the release of water.

- Under oxidative conditions, the most significant bands are due to acetic acid, carbon monoxide, carbon dioxide, water, and hydrocarbon release. The initial degradation step involves the formation of acetic acid which is clearly observed for EVA and EVA+NC. The presence of ATH or MH masks the deacetylation of all other samples and acetic acid evolution is not observed. Compared to EVA and EVA+NC samples there is a significant reduction in the peaks corresponding to CH_3COOH. Similar to samples containing magnesium hydroxide, EVA+ATH and EVA+ATH+NC have higher intensities for the peak corresponding to water and no clear evidence for acetic acid.

- Within the same temperature range CO_2 and CO are released. The major peaks for CO and CO_2 production, towards higher temperatures, are in the same order for both of these gases suggesting both gases originate from the same source, presumably polymer oxidation. Looking at the major peak, EVA has the major peak, followed by the EVA+NC peak (~450°C). For EVA+ATH+NC, EVA+MH+NC, and EVA+MH samples, the peak occurs at similar temperatures ~465°C. The highest temperature is presented by peak belonging to EVA+ATH (~475°C).

- At the same and higher temperatures water, ethylene, methanol, and hydrocarbons are also observed. Water could result from endothermic decomposition of filler (ATH or MH) or from oxidation of the polymer. For EVA and EVA+NC one major peak is observed which is in the middle of two peaks observed for all other samples. In the presence of ATH or MH, the protective layer on the EVA samples is failing, as it is ruptured by escaping water vapour. Water

release occurring at lower temperatures is observed for samples containing nanoclays and fire retardants. EVA+ATH and EVA+MH seem to have higher temperatures when water is released.

- After the loss of acetic acid, the remaining, now unsaturated, poly(ethylene-co-acetylene) undergoes scission at allylic positions. For all polymers one peak is observed, occurring between 400 and 500°C. The maximum hydrocarbon peak occurs at similar temperatures for EVA and samples containing nanoclay. The highest thermal stabilities are seen for fire retarded samples (EVA+ATH, EVA+MH).

- In air there is no evidence for acetone formation.

6.3 Summary

Several, micro scale decomposition numerical models of fire retarded polymers (PP+NC, EVA+NC, EVA+ATH, EVA+MH, EVA+NC+ATH, EVA+NC+MH), mineral fillers (ATH, MH) and pure polymers (PP, EVA) have been presented. Complexity of decomposition of different materials has been captured with various levels of accuracy. The best fits were done for homogenous samples such as a PP, EVA, ATH, and MH and also for polymers with additives such as PP+NC and EVA NC. Propositions of four predictive models were also attempted. The idea of prediction was to combine independent mechanisms developed for EVA, EVA+NC, ATH and MH to reproduce results of EVA+ATH, EVA+MH, EVA+NC+ATH and EVA+NC+MH. Two predictive models of the samples which contained ATH were fully successful – whole decomposition processes were captured. Modelling of materials with MH occurred to be more challenging as only partial agreement was obtained.

STA-FTIR data analysis combined with ThermaKin numerical simulations showed a new ways of building and understanding thermal decomposition mechanisms. Numerical models which reproduced the experimental results with high accuracy could be treated as kind of confirmation that decomposition mechanisms were relatively well understood. When the agreement between the model and the experiment was unsatisfactory some constructive conclusions were made and new ideas for further investigation initiated.

7 CONCLUSIONS AND FUTURE WORK

The initial aim of this project was to enhance our understanding of the laboratory analysis techniques and data analysis methods used to study fire behaviour. In particular, thermogravimetric analysis is generally recognised as the most important technique for investigating the thermal decomposition behaviour of complex materials, such as polymer composites. The development of fire-safe materials, either new, high thermal stability polymers, or existing polymers containing fire retarded additives, depends on a proper understanding of the processes of decomposition and gasification. However, the decomposition curves, obtained in air or nitrogen, often show evidence of multiple, competing processes. These cannot be characterised from the mass loss data alone. This thesis describes two approaches for improving our understanding of thermal decomposition.

The first was to improve the quality of the chemical information from TGA through the use of FTIR gas analysis. This provides a spectrum of all the decomposition products typically every 10°C over the heating period. On occasions, the spectra alone provides the essential clues relating the chemical processes to particular mass loss steps, without further analysis. More often the spectra overlayed with individual absorptions of several different species, with very different intensities, produces a data set so complex that days or weeks are required to fully analyse a single thermal decomposition experiment. The parameters for these experiments have been optimised, and the necessary compromise between better chemical resolution (at $0.5cm^{-1}$) or better temporal (or thermal) resolution (at $4cm^{-1}$) has been identified. The next stage of this process is the acquisition of calibration data specific to the instrument, recorded under the optimum conditions. This time consuming task was deemed to be outside the scope of the current work.

The second approach was to use the 1-dimensional pyrolysis model, ThermaKin, to better understand the processes occurring during thermal decomposition. This allows the individual reactions occurring during polymer decomposition (competing reactions, volatile formation and transport, temperature sensitivity through Arrhenius parameters, etc.) to be simulated simulatanously, in order to create approximate models of the actual processes occurring during TGA.

In summary, the main thrust of this work has been to understand the behaviour of materials in a variety of different tests conditions in terms of the mechanism of its thermal decomposition by a combination of chemical analysis and proposing theoretical, numerical models. Further research directions have been also outlined as a means of providing the next steps towards developing materials with enhanced fire safety. While numerical modelling of pure polymer decomposition, using ThermaKin and other techniques, is well established, the approach described here is novel in fact it has opened the door to predictive modelling of fire retarded polymer composites.

7.1 Experimental Data Acquisition Methods

A detailed investigation of STA-FTIR data acquisition methods has been described in this work. Sample mass, heating rates, gas flow, scanning time and resolution were investigated to obtain the best data quality for future processing. Thermal decomposition products of polymers with fire retardant additives were analysed in depth to demonstrate the great potential, abilities, advantages and disadvantages of STA-FTIR fire retardant investigation methodology. The results themselves were used to build and validate the numerical models.

Using copolymers based on acrylonitrile monomer, which show a number of distinct chemical species in the infrared spectrum (unlike polypropylene for example) parameter optimisation of the STA-FTIR experiment was undertaken and led to useful information concerning the sensitivity and limitations of the STA-FTIR technique.

7.2 Numerical Models Based on Experimental Results

Modelling methodology was developed and described in detail in this work. As a result, several micro-scale and bench-scale ThermaKin models were developed and presented, based on the data obtained during this research. The main assumption in modelling was to propose as simple mechanisms as possible, however in practice this resulted in different levels of complexity. In some cases, a single reaction was enough to reflect the thermal decomposition of a material but sometimes up to nine reactions were required to encompass all features of the pyrolysis phenomenon. Some numerical approximations were constructed to fit actual mass loss data of a single compound, like EVA or ATH, separately and then used to recognize and predict its contribution to the decomposition of more complex materials like EVA+ATH. Also, universal

mechanisms of decomposition of materials were proposed, in order to predict behaviour in different testing conditions such as changing atmospheres from nitrogen to various concentrations of oxygen (cardboard model) or changing heating rates, as performed for PAN modelling.

The study on cardboard showed the necessity to first understand the heat transfer problem, which required the development of the non-homogenous model, and then to break down the complex thermal analysis data into a set of competing and sequential reactions, able to represent the decomposition, gasification and char formation processes occurring. This complex problem provided a unique introduction to the methods and approaches of ThermaKin modelling, and represents the first successful model of cardboard pyrolysis, contributing to better understanding of the behaviour cardboard boxes in warehouse fires.

The study on polypropylene with nanoclay and ammonium polyphosphate fire retardant illustrates the potential of the combined STA-FTIR/ThermaKin approach. Modelling the decomposition of PP alone showed evidence for several competing reactions, which could not be explained by the simple chemistry and identical repeating units of polypropylene. Further FTIR analysis showed only minor differences in the decomposition products occurring in the different decomposition stages. Incorporation of nanoclay led to a single, very sharp decomposition stage, much more consistent with simultaneous bond cleavage of all identical bonds at the same temperature, and thus could be considered closer to "idealised PP decomposition". At this stage, it is not clear why such a dramatic change occurred, but three possibilities have been considered:

1) The gas transport properties of the polymer matrix are reduced by the nanoclay, inhibiting the escape of fuel and the uptake of any available oxygen

2) The maleic anhydride groups grafted onto the PP chain are stabilised by the organoclay, and are no longer the first sites of decomposition

3) The clay changes the decomposition pathway of PP.

The EVA/ATH and EVA/MH study shows the greatest potential to use ThermaKin and FTIR to understand the thermal decomposition of this industrially important (cable sheathing)

formulation. FTIR analysis shows the effect of additives, or their decomposition products, such as Al_2O_3 or MgOH, on the decomposition of EVA and the resultant acetic acid formation, changing the chemistry leading to production of acetone and CO_2 from the EVA composite. The interactions between the decomposing mineral filler and polymer have been shown through the failure of the simplistic analysis[119] and the reaction steps required in ThermaKin for EVA/MH to be important to thermal decomposition process.

This work presents the potential of the ThermaKin framework and gives guidelines how to use it. All micro-scale models of polymers (also with additives) presented here, are the base for developing bench-scale burning models, as was done for cardboard.

7.3 Future Work

The STA-FTIR technique showed great potential for analysing thermal decomposition processes of polymeric materials. Following experimental parameter optimisation the STA-FTIR technique has still one area for improvement – quantitative analysis. At the moment FTIR is used to identify gas phase products, but in the future it will be calibrated and quantitative algorithms will be developed to give full information about the composition of the gas phase decomposition products.

The cardboard model is still under development, so far the universal pyrolysis mechanism in nitrogen and in different oxygen concentration atmospheres has been proposed. Time to ignition is captured but the flaming stage and oxidation of the char are still under construction.

The ThermaKin pyrolysis mechanisms of fire retarded polymers described in Chapter 6 could be extended to bench scale combustion models.

ThermaKin itself can be also improved. At the moment, ThermaKin has no optimisation algorithms to find kinetic parameters and manual iteration is required. The simple optimisation algorithm described in Chapter 5 will be implemented into ThermaKin code to improve its efficiency.

The second important upgrade of ThermaKin framework is to develop visualisation technique for the output file. The first attempt has been already completed and presented in

section 5.2.7. but this still needs to be improved. At the moment only temperatures profiles, and thickness of the sample are visualised. Concentrations of each component in the modelled material will be visualised as well. Ideally the visualisation process should be automated and not require manual data processing.

Finally it would be very useful to test and validate a 2-dimensional version of ThermaKin, able to simulate, for example, the IMO LIFT (ISO 5658) apparatus.

APPENDIX A

VBA code transforming ThermaKin Output for Tecplot 360 Input format. The output Thermakin file should be paste to Sheet1.

```
Sub tec()
Application.DisplayAlerts = False
Dim A As Long
Dim B As Long
Dim C As Long
Dim D As Long
Dim F As Long
Dim G As Long
Dim H As Long
Dim i As Long

   Rows("1:26").Select
   Selection.Delete Shift:=xlUp
   Columns("A:B").Select
   Selection.Copy
   Sheets("Sheet2").Select
   ActiveSheet.Paste
   Sheets("Sheet1").Select
   Cells.Select
   Application.CutCopyMode = False
   Selection.ClearContents
   Range("A1").Select
   Sheets("Sheet2").Select
   Selection.Cut
   Sheets("Sheet1").Select
   ActiveSheet.Paste
   Selection.AutoFilter
   ActiveSheet.Range("$A$1:$B$1048576").AutoFilter Field:=1, Criteria1:=">=0", _
      Operator:=xlOr, Criteria2:="=Tim*"
   Selection.Copy
   Sheets("Sheet2").Select
   Range("B1").Select
   ActiveSheet.Paste
   A = ActiveSheet.Range("B1:C1").CurrentRegion.Rows.Count
   Range("A1").Select
   ActiveCell.FormulaR1C1 = "1"
   Range("A2").Select
   ActiveCell.FormulaR1C1 = "2"
   Range("A1:A2").Select
   Selection.AutoFill Destination:=Range("A1:A" & A)
```

```
Range("A1:A" & A).Select
Columns("A:C").Select
Selection.AutoFilter
ActiveSheet.Range("$A$1:$C$1048576").AutoFilter Field:=2, Criteria1:= _
   "Time [s] ="
Selection.Copy
Sheets("Sheet3").Select
ActiveSheet.Paste
Rows("1:1").Select
Application.CutCopyMode = False
Selection.Insert Shift:=xlDown, CopyOrigin:=xlFormatFromLeftOrAbove
Range("A1").Select
ActiveCell.FormulaR1C1 = "lp"
Range("B1").Select
ActiveCell.FormulaR1C1 = "t  "
Range("C1").Select
ActiveCell.FormulaR1C1 = "time"
Range("D1").Select
ActiveCell.FormulaR1C1 = "Layers"
B = ActiveSheet.Range("B1:C1").CurrentRegion.Rows.Count
Range("D2").Select
ActiveCell.FormulaR1C1 = "=R[1]C[-3]-RC[-3]-1"
Range("D2").Select
Selection.AutoFill Destination:=Range("D2:D" & B)
Range("D2:D" & B).Select
Sheets("Sheet2").Select
Selection.AutoFilter
Columns("A:A").Select
Selection.Delete Shift:=xlToLeft
C = ActiveSheet.Range("A1:B1").CurrentRegion.Rows.Count
Sheets("Sheet3").Range("A" & B + 1).Value = C + 1
Range("A1").Select
Sheets("Sheet2").Select
Columns("B:B").Select
Application.CutCopyMode = False
Selection.Insert Shift:=xlToRight, CopyOrigin:=xlFormatFromLeftOrAbove
   i = B
    Do While i > 1
   i = i - 1

       Sheets("Sheet3").Select
        D = ActiveSheet.Range("D1").Offset(i, 0)
       H = ActiveSheet.Range("A1").Offset(i, 0)

       Range("F3").Select
       ActiveCell.FormulaR1C1 = "Zone T=""zone " & i & """"
```

```
Range("F4").Select
ActiveCell.FormulaR1C1 = "STRANDID=0, SOLUTIONTIME=0"
 Range("F5").Select
 ActiveCell.FormulaR1C1 = "I=" & D & ", J=2, K=1, ZONETYPE=ORDERED"
 Range("F6").Select
ActiveCell.FormulaR1C1 = "DATAPACKING=POINT"
 Range("F7").Select
 ActiveCell.FormulaR1C1 = "DT=(SINGLE,SINGLE)"
Range("F3:H7").Select
Selection.Copy

Sheets("Sheet2").Select
 Rows(H & ":" & H).Select
Application.CutCopyMode = False
Selection.Delete Shift:=xlUp
Sheets("Sheet3").Select
Selection.Copy
Sheets("Sheet2").Select
 Selection.Insert Shift:=xlDown

  F = H + 5

 Sheets("Sheet2").Select
Range("B" & F).Select
 ActiveCell.FormulaR1C1 = "0.1"
Range("B" & F + 1).Select
ActiveCell.FormulaR1C1 = "0.1"
  Range("B" & F & ":" & "B" & F + 1).Select
          Selection.AutoFill  Destination:=Range("B"  &  F  &  ":"  &  "B"  &  F  +  D  -  1),
Type:=xlFillDefault

 Range("A" & F & ":" & "C" & F + D - 1).Select
  Range("C" & F + D - 1).Activate
Selection.Copy

 Rows(F & ":" & F).Select
 Selection.Insert Shift:=xlDown

 Range("B" & F).Select
 Application.CutCopyMode = False
ActiveCell.FormulaR1C1 = "0"
 Range("B" & F + 1).Select
ActiveCell.FormulaR1C1 = "0"
 Range("B" & F & ":B" & F + 1).Select
 Selection.AutoFill Destination:=Range("B" & F & ":B" & F + D - 1),   Type:=xlFillDefault
```

```
Loop

Sheets("Sheet1").Select
Selection.AutoFilter
Cells.Select
Selection.ClearContents
Range("A1").Select
Sheets("Sheet2").Select
Range("A1").Select
Columns("A:C").Select
Selection.Cut
Sheets("Sheet1").Select
ActiveSheet.Paste
Range("A1").Select
Sheets("Sheet2").Select
Range("A1").Select
Sheets("Sheet3").Select
Cells.Select
Selection.ClearContents
Range("A1").Select
Sheets("Sheet2").Select
Cells.Select
Selection.Delete Shift:=xlUp
Range("A1").Select
Sheets("Sheet3").Select
Cells.Select
Selection.Delete Shift:=xlUp
Range("A1").Select
Sheets("Sheet1").Select
G = ActiveSheet.Range("A1:C1").CurrentRegion.Rows.Count
Range("A1:C" & G).Select
Range("C" & G).Activate
Selection.Copy
```

APPENDIX B

VBA code extracting temperature profiles from ThermaKin output file. The ThermaKin output file should be paste to Sheet1 in Excel.

```
Sub temp()

    Rows("1:26").Select
    Selection.Delete Shift:=xlUp
    Columns("C:L").Select
    Selection.ClearContents
    Columns("A:B").Select
    Selection.AutoFilter
   ActiveSheet.Range("$A$1:$B$1047722").AutoFilter Field:=1, Criteria1:=">0", _
   Operator:=xlOr, Criteria2:="=Ti*"
    Selection.Copy
    Sheets("Sheet2").Select
    Range("A1").Select
    ActiveSheet.Paste
    Columns("A:A").Select
    Application.CutCopyMode = False
    Selection.Insert Shift:=xlToRight, CopyOrigin:=xlFormatFromLeftOrAbove
    A = ActiveSheet.Range("B1:C1").CurrentRegion.Rows.Count

    Range("A1").Select
    ActiveCell.FormulaR1C1 = "1"
    Range("A2").Select
    ActiveCell.FormulaR1C1 = "2"
    Range("A1:A2").Select
    Selection.AutoFill Destination:=Range("A1:A" & A)
    Range("A1:A" & A).Select
    Columns("B:B").Select
    Selection.AutoFilter
    Columns("B:B").Select
    Selection.AutoFilter
    ActiveSheet.Range("$B$1:$B$1047722").AutoFilter Field:=1, Criteria1:= _
       "Time [s] ="
    Columns("A:C").Select
    Selection.Copy
    Sheets("Sheet3").Select
    Range("A1").Select
    ActiveSheet.Paste
    Rows("1:1").Select
    Application.CutCopyMode = False
    Selection.Insert Shift:=xlDown, CopyOrigin:=xlFormatFromLeftOrAbove
```

```
Range("A1").Select
ActiveCell.FormulaR1C1 = "Lp"
Range("B1").Select
ActiveCell.FormulaR1C1 = "T "
Range("C1").Select
ActiveCell.FormulaR1C1 = "Time"
Range("D1").Select
ActiveCell.FormulaR1C1 = "Layers"

Range("E1").Select
ActiveCell.FormulaR1C1 = "Lower TC"
Range("F1").Select
ActiveCell.FormulaR1C1 = "Middle TC"
Range("G1").Select
ActiveCell.FormulaR1C1 = "Middle TC L"
Range("H1").Select
ActiveCell.FormulaR1C1 = "Middle TC U"
Range("I1").Select
ActiveCell.FormulaR1C1 = "Upper TC"
Range("J1").Select
ActiveCell.FormulaR1C1 = "Upper TC L"
Range("K1").Select
ActiveCell.FormulaR1C1 = "Upper TC U"
Range("M1").Select
B = ActiveSheet.Range("B1:C1").CurrentRegion.Rows.Count
Range("E1:K1").Select
Selection.Copy
Range("L1").Select
ActiveSheet.Paste
Range("D2").Select
Application.CutCopyMode = False
Range("D2").Select
ActiveCell.FormulaR1C1 = "=R[1]C[-3]-RC[-3]-1"
Range("D2").Select
Selection.AutoFill Destination:=Range("D2:D" & B)
Range("D2:D" & B).Select
Range("E2").Select
ActiveCell.FormulaR1C1 = "=ROUND(Sheet3!R2C4*(1-0.686)+RC1, 0)"
Range("E2").Select
Selection.AutoFill Destination:=Range("E2:E" & B)
Range("E2:E" & B).Select
Range("F2").Select
ActiveCell.FormulaR1C1 = "=ROUND(Sheet3!R2C4*(1-0.821)+RC1, 0)"
Range("F2").Select
Selection.AutoFill Destination:=Range("F2:F" & B)
Range("F2:F" & B).Select
```

```
Range("G2").Select
ActiveCell.FormulaR1C1 = "=ROUND(Sheet3!R2C4*(1-0.814)+RC1, 0)"
Range("G2").Select
Selection.AutoFill Destination:=Range("G2:G" & B)
Range("G2:G" & B).Select
Range("H2").Select
ActiveCell.FormulaR1C1 = "=ROUND(Sheet3!R2C4*(1-0.827)+RC1, 0)"
Range("H2").Select
Selection.AutoFill Destination:=Range("H2:H" & B)
Range("H2:H" & B).Select
Range("I2").Select
ActiveCell.FormulaR1C1 = "=ROUND(Sheet3!R2C4*(1-0.991)+RC1, 0)"
Range("I2").Select
Selection.AutoFill Destination:=Range("I2:I" & B)
Range("I2:I" & B).Select
Range("J2").Select
ActiveCell.FormulaR1C1 = "=ROUND(Sheet3!RC4*(1-0.984)+RC1, 0)"
Range("K2").Select
ActiveCell.FormulaR1C1 = "=ROUND(Sheet3!R2C4*(1-0.995)+RC1, 0)"
Range("J2:K2").Select
Selection.AutoFill Destination:=Range("J2:K" & B)
Range("J2:K" & B).Select
Range("L2").Select
Sheets("Sheet3").Select
Range("L2").Select
ActiveCell.FormulaR1C1 = "=VLOOKUP(RC[-7],Sheet2!C1:C3,3,FALSE)"
Range("L2").Select
Selection.AutoFill Destination:=Range("L2:R2"), Type:=xlFillDefault
Range("L2:R2").Select
Selection.AutoFill Destination:=Range("L2:R" & B)
Range("L2:R" & B).Select
Range("M2").Select
ActiveCell.FormulaR1C1 = "=VLOOKUP(RC[-7],Sheet2!C1:C3,3,FALSE)"
Range("L2").Select
Sheets("Sheet3").Select
Cells.Select
Selection.Copy
Selection.PasteSpecial Paste:=xlPasteValues, Operation:=xlNone, SkipBlanks _
   :=False, Transpose:=False
Application.CutCopyMode = False
Sheets("Sheet1").Select
Selection.AutoFilter
Cells.Select
Selection.ClearContents
Range("A1").Select
Sheets("Sheet2").Select
```

```
    Selection.AutoFilter
    Cells.Select
    Selection.ClearContents
    Range("A1").Select
    Sheets("Sheet3").Select
    Range("C:C,L:R").Select
    Range("L1").Activate
    Selection.Copy
    Sheets("Sheet1").Select
    Selection.PasteSpecial Paste:=xlPasteValues, Operation:=xlNone, SkipBlanks _
        :=False, Transpose:=False
    Sheets("Sheet3").Select
    Cells.Select
    Selection.ClearContents
    Range("A1").Select
    Sheets("Sheet1").Select
    Range("A1").Select
    Columns("A:A").Select
    Selection.NumberFormat = "0"
    Columns("B:H").Select
    Selection.NumberFormat = "0"
    Range("A1:H" & B - 1).Select
    'Range("H" & B - 1).Activate
    ActiveSheet.Shapes.AddChart.Select
    ActiveChart.SetSourceData Source:=Range("'Sheet1'!$A$1:$H$" & B - 1)
    ActiveChart.ChartType = xlXYScatterSmoothNoMarkers
    Rows(B & ":" & B).Select
    Selection.ClearContents
    Range("A1").Select
    Sheets("Sheet2").Select
    Cells.Select
    Selection.Delete Shift:=xlUp
    Range("A1").Select
    Sheets("Sheet3").Select
    Cells.Select
    Selection.Delete Shift:=xlUp
    Range("A1").Select
    Sheets("Sheet1").Select
    Range("A1").Select
End Sub
```

APPENDIX C

ThermaKin input files for cardboard model.

Component file	Condition file
COMPONENT: CB_A STATE: S DENSITY: 10000 0 0 0 HEAT CAPACITY: 5230 -6.71 0.011 2 CONDUCTIVITY: 0.08 0 5e-11 3 TRANSPORT: 1e-5 0 0 0 EMISSIVITY & ABSORPTION: 0.67 100 COMPONENT: CB_B1 STATE: S DENSITY: 567 0 0 0 HEAT CAPACITY: 1800 0 0 0 CONDUCTIVITY: 0.08 0 5e-11 3 TRANSPORT: 1e-5 0 0 0 EMISSIVITY & ABSORPTION: 0.67 100 COMPONENT: CB_B2 STATE: S DENSITY: 39 0 0 0 HEAT CAPACITY: 1800 0 0 0 CONDUCTIVITY: 0.08 0 5e-11 3 TRANSPORT: 1e-5 0 0 0 EMISSIVITY & ABSORPTION: 0.67 100 COMPONENT: CB_C1 STATE: S DENSITY: 510 0 0 0 HEAT CAPACITY: 1560 0 0 0 CONDUCTIVITY: 0.08 0 6e-10 3 TRANSPORT: 1e-5 0 0 0 EMISSIVITY & ABSORPTION: 0.67 100 COMPONENT: CB_C2 STATE: S DENSITY: 35 0 0 0 HEAT CAPACITY: 1560 0 0 0 CONDUCTIVITY: 0.08 0 6e-10 3 TRANSPORT: 1e-5 0 0 0 EMISSIVITY & ABSORPTION: 0.67 100	OBJECT TYPE: 1D OBJECT STRUCTURE ********** THICKNESS: 0.00064 TEMPERATURE: 300 MASS FRACTIONS: CB_B1 0.98 CB_A 0.02 THICKNESS: 0.0032 TEMPERATURE: 300 MASS FRACTIONS: CB_B2 0.98 CB_A 0.02 THICKNESS: 0.00064 TEMPERATURE: 300 MASS FRACTIONS: CB_B1 0.98 CB_A 0.02 THICKNESS: 0.0024 TEMPERATURE: 300 MASS FRACTIONS: CB_B2 0.98 CB_A 0.02 THICKNESS: 0.00064 TEMPERATURE: 300 MASS FRACTIONS: CB_B1 0.98 CB_A 0.02 THICKNESS: 0.015 TEMPERATURE: 300 MASS FRACTIONS: KAOWOOL 1

```
COMPONENT:      CB_ch1
STATE:          S
DENSITY:        189  0  0  0
HEAT CAPACITY:  1280  0  0  0
CONDUCTIVITY:   0.08  0  6e-10  3
TRANSPORT:      1e-5  0  0  0
EMISSIVITY & ABSORPTION:  0.9  100

COMPONENT:      CB_ch2
STATE:          S
DENSITY:        13  0  0  0
HEAT CAPACITY:  1280  0  0  0
CONDUCTIVITY:   0.08  0  6e-10  3
TRANSPORT:      1e-5  0  0  0
EMISSIVITY & ABSORPTION:  0.9  100

COMPONENT:      CB_ch3
STATE:          S
DENSITY:        111  0  0  0
HEAT CAPACITY:  1280  0  0  0
CONDUCTIVITY:   0.08  0  6e-10  3
TRANSPORT:      1e-5  0  0  0
EMISSIVITY & ABSORPTION:  0.9  100

COMPONENT:      CB_ch4
STATE:          S
DENSITY:        8  0  0  0
HEAT CAPACITY:  1280  0  0  0
CONDUCTIVITY:   0.08  0  6e-10  3
TRANSPORT:      1e-5  0  0  0
EMISSIVITY & ABSORPTION:  0.9  100

COMPONENT:      CB_g_1
STATE:          G
DENSITY:        10000  0  0  0
HEAT CAPACITY:  2398  -1.6  0.0016  2
CONDUCTIVITY:   -0.0075  8e-5  0    1
TRANSPORT:      1e-5  0  0  0
EMISSIVITY & ABSORPTION:  0.67  100

COMPONENT:      CB_g_2
STATE:          G
DENSITY:        174  0  0  0
HEAT CAPACITY:  1560  0  0  0
CONDUCTIVITY:   0.08  0  5e-11  3
```

```
OBJECT BOUNDARIES
*****************

TOP BOUNDARY

MASS TRANSPORT: YES
CB_g_1  LIN  0.05  0
CB_g_2  LIN  0.05  0

OUTSIDE TEMP TIME PROG: 300  0
CONVECTION COEFF:  10

EXTERNAL RADIATION: YES
TIME PROG1:  2e4  0  1e10
TIME PROG2:  0  0  0
REPEAT:  NO
ABSORPTION MODE: MAX

FLAME: YES
IGNITION MASS FLUXES:
CB_g_2  8.3e-4
OUTSIDE TEMP:  2270
CONVECTION COEFF:  8.58
RADIATION:  0

BOTTOM BOUNDARY

MASS TRANSPORT:  NO

OUTSIDE TEMP TIME PROG:  300  0
CONVECTION COEFF:  0

EXTERNAL RADIATION:  NO

FLAME:  NO

INTEGRATION PARAMETERS
**********************

ELEMENT SIZE:  5e-5
TIME STEP:    0.01
DURATION:     150

OUTPUT FREQUENCY:
ELEMENTS:   1
```

TRANSPORT: 1e-5 0 0 0 EMISSIVITY & ABSORPTION: 0.67 100 COMPONENT: KAOWOOL STATE: S DENSITY: 256 0 0 0 HEAT CAPACITY: 1070 0 0 0 CONDUCTIVITY: 0.0519 -4e-5 1e-7 2 TRANSPORT: 1e-30 0 0 0 EMISSIVITY & ABSORPTION: 0 1000 MIXTURES S SWELLING: 0 L SWELLING: 0 G SWELLING LIMIT: 1e-30 PARALL CONDUCTIVITY: 0.5 PARALL TRANSPORT: 0.5 REACTION: CB_A + NOCOMP -> NOCOMP + CB_g_1 STOICHIOMETRY: 1 0 0 1 ARRHENIUS: 6.14e0 2.35e4 HEAT: -24.45e5 0 0 0 TEMP LIMIT: L 300 REACTION: CB_B1 + NOCOMP -> CB_C1 + CB_g_2 STOICHIOMETRY: 1 0 0.9 0.1 ARRHENIUS: 7.95e9 1.3e5 HEAT: -17e3 0 0 0 TEMP LIMIT: L 300 REACTION: CB_B2 + NOCOMP -> CB_C2 + CB_g_2 STOICHIOMETRY: 1 0 0.9 0.1 ARRHENIUS: 7.95e9 1.3e5 HEAT: -17e3 0 0 0 TEMP LIMIT: L 300 REACTION: CB_C1 + NOCOMP -> CB_ch1 + CB_g_2 STOICHIOMETRY: 1 0 0.37 0.63 ARRHENIUS: 2e11 1.6e5 HEAT: -10.71e4 0 0 0 TEMP LIMIT: L 300 REACTION: CB_C2 + NOCOMP -> CB_ch2 + CB_g_2 STOICHIOMETRY: 1 0 0.37 0.63 ARRHENIUS: 2e11 1.6e5 HEAT: -10.71e4 0 0 0	TIME STEPS: 100

TEMP LIMIT: L 300 REACTION: CB_ch1 + NOCOMP -> CB_ch3 + CB_g_2 STOICHIOMETRY: 1 0 0.59 0.41 ARRHENIUS: 2.61e-2 1.7e4 HEAT: 0 0 0 0 TEMP LIMIT: L 300 REACTION: CB_ch2 + NOCOMP -> CB_ch4 + CB_g_2 STOICHIOMETRY: 1 0 0.59 0.41 ARRHENIUS: 2.61e-2 1.7e4 HEAT: 0 0 0 0 TEMP LIMIT: L 300	

REFERENCES

1. G. Rein, C. Lautenberger, A.C. Fernandez-Pello, J.L. Torero and D.L. Urban, Application of genetic algorithms and thermogravimetry to determine the kinetics of polyurethane foam in smouldering combustion, Combustion and Flame, 146, pp. 95-108, 2006.
2. S.I. Stoliarov, R.E Lyon. Thermo-kinetic model of burning. Federal Aviation Administration Technical Note DOT/FAA/AR-TN08/17, 2008.
3. S.C. Moldoveanu, Analytical pyrolysis of synthetic organic polymers, Techniques and Instrumentation in Analytical Chemistry, Volume 25, Elsevier, Oxford, 2005.
4. M. Blazs, Review, Recent trends in analytical and applied pyrolysis of Polymers, Journal of Analytical and Applied Pyrolysis, 39, pp. 1-25, 1997.
5. D.M. Price, S.P. Church, FTIR evolved gas analysis of the decomposition products of cellulose diacetate, Thermochimica Acta, 294, pp. 107-112, 1997.
6. A. Gopferich, Mechanism of polymer degradation and erosion, Biomaterials, 23, pp. 103-114, 1996.
7. M. Partini, R. Pantani, FTIR analysis of hydrolysis in aliphatic polyesters, Polymer Degradation and Stability, 92, pp. 1491-1497, 2007.
8. C.A. Wilkie, TGA/FTIR: an extremely useful technique for studying polymer degradation, Polymer Degradation and Stability, 66, pp. 301-306, 1999.
9. R.G. Davidson, Enhancement of evolution profiles in pyrolysis-evolved gas-infrared spectroscopy of polymers, Journal of Analytical and Applied Pyrolysis, 16, pp. 143-152, 1989.
10. P.C. Uden, Nomenclature and Terminology for Analytical Pyrolysis (IUPAC recommendations 1993), J. Anal. Appl. Pyrol., 31, pp. 251-256, 1995.
11. E.M. Anderson, I. Ericsson, Samples from ng to mg in pyrolysis—gas chromatography, Journal of Analytical and Applied Pyrolysis, 2, pp. 97-107, 1980.
12. J.V. Gulmine, P.R. Janissek, H.M. Heise, L. Akcelrud, Polyethylene characterization by FTIR, Polymer Testing, 21, pp. 557–563, 2002.
13. L.C. Speitel, Fourier Transform Infrared Analysis of Combustion Gases, Office of Aviation Research, Washington, D.C. 20591 US Department of transportation, Federal Aviation Administration, DOT/FAA/AR-01/88, 2001.
14. ISO 19702:2004 Analysis of fire gases using Fourier infra-red technique- FTIR, 2004.
15. T. Hakkarainen, E. Mikkola, J. Laperre, F. Gensous, P. Fardell, Y. Le Tallec, C. Baiocchi, K. Paul, M. Simonson, C. Deleu, E. Metcalfe, Smoke gas analysis by Fourier Transform Infrared Spectroscopy – summary of the SAFIR project results, Fire and Materials, 24, pp. 101–112, 2000.
16. J. Golebiewski, A. Galeski, Thermal stability of nanoclay polypropylene composites by simultaneous DSC and TGA, Composites Science and Technology, 67, pp. 3442–3447, 2007.
17. J. Ma, Z. Qi, Y. Hu, Synthesis and characterization of polypropylene clay nanocomposites, J Appl Polym Sci, 82, pp. 3611–7, 2001.
18. M. Zanetti, G. Camino, P. Reichert, R. Mulhaupt, Thermal behaviour of poly(propylene) layered silicate nanocomposites, Macromol Rapid Comm, 22, pp. 176–80, 2001.
19. Y. Tang, Y. Hu, L. Song, R.W. Zong, Z. Gui, Z.Y. Chen, W. Fan, Preparation and thermal stability of polypropylene/montmorillonite nanocomposites, Polymer Degradation and Stability, 82, pp. 127–31, 2003.

20. J.G. Zhang, D.D. Jiang, C.A. Wilkie, Polyethylene and polypropylene nanocomposites based upon an oligomerically modified clay, Thermochim Acta, 430, pp. 107-113, 2005.
21. W. Gianelli, G. Ferrara, G. Camino, G. Pellegatti, J. Rosenthal, R.C. Trombini, Effect of matrix features on polypropylene layered silicate nanocomposites, Polymer, 46, pp. 7037–7046, 2005.
22. F.C. Chiu, S.M. Lai, J.W. Chen, P.H. Chu, Combined effects of clay modifications and compatibilizers on the formation and physical properties of melt-mixed polypropylene/clay nanocomposites, J. Polym Sci B Polym Phys, 42, pp. 4139–4150, 2004.
23. M.A. Gomez, S. Menargues, TGA/FTIR study of the evolution of the gases evolved in the catalytic pyrolysis of ethylene-vinyl acetate copolymers.Comparison among different catalysts, Polymer Degradation and Stability, 89, pp. 454-460, 2005.
24. M. Herrera, G. Matuschek and A. Kettrup, Thermal degradation studies of some Aliphatic polyamides using hyphenated Techniques (TG-MS, TG-FTIR), Journal of Thermal Analysis and Calorimetry, 59, pp. 385-394, 2000.
25. B.N. Jang, C.A. Wilkie, The effect of clay on the thermal degradation of polyamide 6 in polyamide 6/clay nanocomposites, Polymer, 46, pp. 3264–3274, 2005.
26. J.M. Cervantes-Uc, J.V. Cauich-Rodrıguez, H. Vazquez-Torres, A. Licea-Claverıe, TGA/FTIR study on thermal degradation of polymethacrylates containing carboxylic groups, Polymer Degradation and Stability, 91, pp. 3312-3321, 2006.
27. A. Chowdhurya, P.R. Thompsonb, S.J. Milnea, TGA–FTIR study of a lead zirconate titanate gel made from a triol-based sol–gel system, Thermochimica Acta, 475, pp. 59–64, 2008.
28. V. Berbenni, A. Marini, G. Bruni, T. Zerlia, TG/FT-IR: an analysis of the conditions affecting the combined TG/spectral response, Thermochimica Acta, 258, pp. 125-133, 1995.
29. T. Rogaume, L. Bustamante Valencia, E. Guillaume, F. Richard, J. Luche, G. Rein, J. L. Torero, Development of the Thermal Decomposition Mechanism of Polyether Polyurethane Foam Using Both Condensed and Gas-Phase Release Data, Combustion Science and Technology, 183:7, 627-644, 2011.
30. ASTM D7309: Standard Test Method for Determining Flammability of Plastics and Other Solid Materials Using Microscale Combustion Calorimetry. ASTM International, West Conshohocken, PA, USA, 2007.
31. R.E. Lyon, R.N. Walters, Pyrolysis Combustion Flow Calorimeter, Journal of Analytical and Applied Pyrolysis, 71, pp.27-46, 2004.
32. R.E. Lyon, R. Walters, A Microscale Combustion Calorimeter, US Department of Transport. Report Number: DOT/FAA/AR-01/117, Federal Aviation Administration, 2002.
33. ISO 5660-1: 1993. Fire Tests on Building Materials and Structures. Part 15-Method for Measuring the Rate of Heat Release of Products, 1993.
34. V. Babrauskas, The Cone Calorimeter, Chapter 3: Section 3. In SFPE Handbook of Fire Protection Engineering. 2nd Edition, 2nd Ed.; C.L. Beyler, R.L.P. Custer, P.J. DiNenno, D. Drysdale, J.R. Jr. Hall, W.D. Walton, J.M. Watts, Eds.; National Fire Protection Association: Qunicy, 1995.
35. B. Karlsson, J.G. Quintiere, J. G., Enclosure Fire Dynamics, CRC Press, New York, USA, 2000.
36. B. Schartel, T.R. Hull, Development of fire-retarded materials—Interpretation of cone calorimeter data, Fire and Materials, 31, pp. 327–354, 2007.
37. H. Zhang, Fire-Safe Polymers and Polymer Composites. US Department Of Transport. Report Number: DOT/FAA/AR-04/11. Federal Aviation Administration, 2004.

38. ASTM Standard E 1354-04, Standard Test Method for Heat and Visible Smoke Release Rates for Materials and Products Using an Oxygen Consumption Calorimeter American Society for Testing and Materials, West Conshohocken, PA, 2004.
39. ASTM Standard E 906-06, Standard Test Method for Heat and Visible Smoke Release Rates for Materials and Products Using a Thermopile Method American Society for Testing and Materials, West Conshohocken, PA, 2006.
40. C. L. Beyler, M.M. Hirschler, Thermal decomposition of polymers. National Institute of Standards and Technology, Chapter 7, pp. 1-110 - 1-131, 2001.
41. C.L. Beyler, M.M. Hirschler, Thermal Decomposition of Polymers, SFPE Handbook of Fire Protection Engineering, 2nd Ed.; C.L. Beyler, R.L.P. Custer, P.J. DiNenno, D. Drysdale, J.R. Jr. Hall, W.D. Walton, J.M. Watts, Eds.; National Fire Protection Association: Qunicy, pp 99-117, 1995.
42. M.M. Hirschler, Chemical aspects of thermal decomposition of polymeric materials, in Fire Retardancy of Polymeric Materials, 1st Ed.; A.F. Grand, C.A. Wilkie, Eds. Marcel Dekker Inc: New York, pp 27-79, 2000.
43. C.F. Cullis, M.M. Hishler, The combustion of organic polymers, Oxford University Press, New York, 1981.
44. R.M. Ziff, E.D. McGrady, Kinetics of polymer degradation, Macromolecules, 19, pp. 2513-2519, 1986.
45. D. Purser, A.A. Stec, R. Hull, Fire Toxicity, Effects of the material and fire conditions on toxic product yields, Chapter 14, A.A. Stec and R. Hull (Editors), CRC Press, Cambridge, 2010.
46. F. Samyn, S. Bourbigot, C. Jama, S. Bellayer, S. Nazare, R. Hull, A. Castrovinci, A. Fina, G. Camino, Crossed characterisation of polymer-layered silicate (PLS) nanocomposite morphology: TEM, X-ray diffraction, rheology and solid-state nuclear magnetic resonance measurements, European Polymer Journal, 44, pp. 1642-1653, 2008.
47. C. Shih-Hsuan, W. Wun-Ku, Dynamic flame retardancy of polypropylene filled with ammonium polyphosphate, pentaerythritol and melamine additives, Polymer, 39, pp. 1951-1955, 1998.
48. S.A. Hedrick, S.S.C. Chuan, Temperature programmed decomposition of polypropylene: in situ FTIR coupled with mass spectroscopy study, Thermochimica Acta, 315, pp. 159-168, 1998.
49. R. Bernstein, S.M. Thornberg, R.A. Assink, D.M. Mowery, M.K. Alam, A.N. Irwin, J.M. Hochrein, D.K. Derzon, S.B. Klamo, R.L. Clough, Insights into oxidation mechanisms in gamma-irradiated polypropylene, utilizing selective isotopic labeling with analysis by GC/MS, NMR and FTIR, Nuclear Instruments and Methods in Physics Research Section B: Beam Interactions with Materials and Atoms, 265, pp. 8-17, 2007.
50. S. Zhang, A.R. Horrocks, A review of flame retardant polypropylene fibres, Progress in Polymer Science, 28, pp. 1517-1538, 2003.
51. C.A. Harper, Handbook of Plastics Technologies: The Complete Guide to Properties and Performance, McGraw-Hill Professional, 2nd Edition, 2006.
52 T.R. Hull, A.A. Stec, A. May, Fire retardant mechanism of acrylonitrile copolymers containing nanoclay, Fire and Polymers V – Materials and concepts for Fire Retardancy, ACS Symposium Series 1013, Ch 9, pp. 118-147, Oxford Univeristy Press, 2009.
53. L.T. Memetea, N.C. Billingham, E.T.H Then, Hydroperoxides in polyacrylonitrile and their role in carbon-fibre formation, Polym Degradation and Stability, 47, pp. 189-201, 1995.

54 A. Biedunkiewicz, P. Figiel, M. Sabara, Pyrolysis and oxidation of PAN in dry Air, Thermoanalytical Methods, Materials Science, 17, No. 1, 2011.
55. A.R. Horrocks, J. Zhang, M.E. Hall, Flammability of polyacrylonitrile and its copolymers. II: Thermal behaviour and mechanism of degradation, Polymer International, 33, pp. 303-314, 1994.
56. M.C. Costachea, D.D. Jianga and C.A. Wilkie, Thermal degradation of ethylene–vinyl acetate coplymer nanocomposites, Polymer, 46, pp. 6947-6958, 2005.
57. A. Marcilla, , A. Gómez and S. Menargues, TG/FTIR study of the thermal pyrolysis of EVA copolymers, Journal of Analytical and Applied Pyrolysis, 74, pp. 224-230, 2005.
58. T.R. Hull, D. Price, Y. Liu, C.L. Wills, J. Brady, An investigation into the decomposition and burning behaviour of Ethylene-vinyl acetate copolymer nanocomposite materials, Polymer Degradation and Stability, 82 pp. 365–371, 2003.
59. M.C. Costache, D.D. Jiang, C.A. Wilkie, Thermal degradation of ethylene–vinyl acetate coplymer nanocomposites, Polymer, 46, pp. 6947–6958, 2005.
60. N.S. Allen, M. Edge, M. Rodriguez, C. M. Liauw, E. Fontan, Aspects of the thermal oxidation of ethylene vinyl acetate copolymer, Polymer Degradation and Stability, 68, pp. 363-371, 2000.
61. A.D. Cross, An Introduction to Practical Infra-Red Spectroscopy, Butterworths Scientific Publications, 1960
62. P.R. Griffiths, J.A de Haseth, Fourier Transform Infrared Spectrometry, 2nd Edition, Wiley Interscience, John Wiley and Sons, Inc Publication New Jersey, 2007.
63. Excerpted from OMNIC Help, Thermo Electron Corporation, 2006.
64. B. Stuart, W.O. George, P.S. McIntyre, Modern Infrared Spectroscopy, Editor: D.J. Ando, University of Greenwich, 1998.
65. A.R. Horrocks, P.D Price and M. Akalin, FTIR analysis of gases evolved from cotton and flame retarded cotton fabrics pyrolysed in air, Polymer Degradation and Stability, 52, pp. 205-213, 1996.
66. H. Yan, W.R. Cannon and D.J. Shanefield, Thermal Decomposition Behaviour of Poly(propylene carbonate), Ceramics International, 24, pp.433-439, 1998.
67. A. Marcilla, A. Gomez, S. Menargues, TGA/FTIR study of the evolution of the gases evolved in the catalytic pyrolysis of ethylene-vinyl acetate copolymers, Comparison among different catalysts, Polymer Degradation and Stability, 89, pp. 454-460, 2005.
68. A. Soufiani, J.P. Martin, J.C. Rolon, L. Brenez, Sensitivity of Temperature and Concentration Measurements in Hot Gases from FTIR Emission Spectroscopy Journal of Quantitative Spectroscopy and Radiative Transfer, 73, pp. 317-327, 2002.
69. F. Eigenmann, M. Maciejewski, A. Baiker, Quantitative calibration of spectroscopic signals in combined TG-FTIR system, Thermochimica Acta, 440, pp. 81–92, 2006.
70. M. Mittleman, Quantitative TG/IR, Thermochimica Acta, 166, pp. 301-308, 1990.
71. L.C.K. Liau, T.C.K. Yang, D.S. Viswanath, Approach to quantitative analysis of dynamic mixture IR spectra using TG/FT-IR, Appl. Spectrosc., 51, pp. 905-909, 1997.
72. M.F. Cai, R.B. Smart, Quantitative analysis of N-methyl-2-pyrrolidinone in coal extracts by TGA-FTIR, Energy Fuels, 7, pp. 52-56, 1993.
73. A. Kurt, K. Demirelli, Thermal degradation of block copolymers of ethyl methacrylate with styrene synthesized by atom transfer radical polymerization method, Turkish Journal of Science and Technology, 4, pp. 65-72, 2009.

74. BS EN ISO 11358:1997 or BS 2782-1: Method 127A:1997, Plastics -Thermogravimetry (TG) of polymers -General principles, 1997.
75. C. Lautenberger, E. Kim, N. Dembsey, C. Fernandez-Pello, The Role of Decomposition Kinetics in Pyrolysis Modeling – Application to a Fire Retardant Polyester Composite, Fire Safety Science 9: 1201-1212, 2008.
76. A. Matala, S. Hostikka, and J. Mangs, Estimation of pyrolysis model parameters for solid materials using thermogravimetric data, Fire Safety Science 9: 1213-1223, 2009.
77. J.E.J. Staggs, A theory for quasi-steady single-step thermal degradation of polymers, Fire and Materials, 22, 1998, pp. 109-118, 1998.
78. J. Zhang, M.A. Delichatsios, S. Bourbigot, Experimental and numerical study of the effects of nanoparticles on pyrolysis of polyamide 6 (PA6) nanocomposite in the cone calorimeter, Combustion and Flame, 156, pp. 2056-2062, 2009.
79. F. Jia, E.R. Galea, M.K. Patel, The numerical simulation of the non-charring pyrolysis process and fire development within a compartment, Applied Mathematical Modelling, 23, pp. 587-607, 1999.
80. C. Lautenberger, "Gpyro – A Generalized Pyrolysis Model for Combustible Solids – Users' Guide," Version 0.700, February 19, 2009.
81. K. B. Mc Grattan, S. Hostikka, J. E. Floyd, H. R. Baum, and R. G. Rehm, Fire Dynamics Simulator (Version 5), Technical Reference Guide, Volume 1: Mathematical Model. NIST Special Publication 1018-5, National Institute of Standards and Technology, Gaithersburg, Maryland, October 2007.
82. S.I. Stoliarov, S. Crowley, R.E. Lyon, G. T. Linteris, Prediction of the burning rates of non-charring polymers, Combustion and Flame, 156, pp. 1068-1083, 2009.
83. S.S. Rahatekar, M. Zammarano, S. Matko, K.K. Koziol, M.H. Windle, T. Kashiwagi, J.W. Gilman, Effect of carbon nanotubes and montmorillonite on the flammability of epoxy nanocomposites, Polymer Degradation and Stability, 95, pp. 870-879, 2010.
84. S.I. Stoliarov, N. Safronava, R.E. Lyon, The effect of variation in polymer properties on the rate of burning, Fire and Materials, 33, pp. 257-271, 2009.
85. E.S. Oztekin, S.B. Crowley, R.E. Lyon, S. I. Stoliarov, Sources of Variability in Fire Test Data: A case study on Poly(aryl ether ether ketone) (PEEK); Combustion and Flame (Elsevier); accepted.
86. S.I. Stoliarov, R.E. Lyon, Thermo-kinetic model of burning for pyrolyzing materials. Proceedings of the Ninth International Symposium on Fire Safety Science, Karlsruhe, Germany, 2008.
87. R.E. Lyon, J.G. Quintiere, Criteria for piloted ignition of combustible solids, Combustion and Flame, 151, pp. 551–559, 2007.
88. J. G. Quintiere, Principles of Fire Behaviour, 1997, Delmar. Albany, NY.
89. D. Drysdale, An Introduction to Fire Dynamics, 2nd Edition. John Wiley and Sons, Chichester, 1999.
90. R.E. Lyon, N. Safronava, S.I. Stoliarov, The role of thermal decomposition kinetics in the burning of polymers, Proceedings of the 12th International Conference on Fire Science and Engineering, INTERFLAM, UK, 2010.
91. P. Patel, T.R. Hull, A.A. Stec, R.E. Lyon, Influence of physical properties on polymer flammability in the cone calorimeter, , Special Issue: Selected papers from the 2010 International Symposium on Flame Retardant Materials & Technologies, China, Polymers for Advanced Technologies September, 22, pp. 1100-1107, 2011

92. T. Ohlemiller, T. Shields, One- and two-sided burning of thermally thin materials, Fire and Materials, 17, pp. 103-110, 1993.
93. M.I. Nelson, J. Brindley, A.C. McIntosh, The dependence of critical heat flux on fuel and additive properties: A critical mass flux model, Fire Safety Journal, 24, pp. 107-130, 1995.
94. M.I. Nelson, J. Brindley, A.C. McIntosh, Polymer ignition, Mathematical and Computer Modelling, 24, pp. 39-46, 1996a.
95. M.I. Nelson, J. Brindley, A.C. McIntosh, Ignition properties of thermally thin materials in the cone calorimeter: A critical mass flux model, Combustion Science and Technology, 113-114, pp. 221--241, 1996b.
96. M.I. Nelson, J. Brindley, A.C. McIntosh, Ignition properties of thermally thin thermoplastics - The effectiveness of inert additives in reducing flammability, Polymer Degradation and Stability, 54, pp. 255-267, 1996c.
97. M.I. Nelson, J. Brindley, A.C. McIntosh, The effect of heat sink additives on the ignition and heat release properties of thermally thin thermoplastics, Fire Safety Journal, 28, pp. 67-94, 1997.
98. J.E.J. Staggs, M.I. Nelson, A critical mass flux model for the flammability of thermoplastics, Combustion Theory and Modelling, 5, pp. 399-427, 2001.
99. R.E Lyon, N. Safronava, S. I. Stoliarov, The thermal decomposition kinetics in the burning of polymers, Proceedings of the 12th International Conference on Fire Science and Engineering, INTERFLAM, UK, 2010.
100. Encyclopeadia Britannica, http://www.britannica.com/EBchecked/topic/492712/heat-of-reaction
101. P.J. DiNenno (ed.) SFPE Handbook of Fire Protection Engineering. National Fire Protection Association: Quincy, MA, 2002.
102. M. Chaos, M.M. Khan, S.B. Dorofeev, Inert and oxidative pyrolysis of a lignocellulosic material: Corrugated cardboard, 7th US National Technical Meeting of the Combustion Institute, Atlanta, 2011.
103. T. Kashiwagi, T.J. Ohlemiller, K. Werner, Effects of external radiant heat flux and ambient oxygen concentration on nonlaming gasification rates and evolved products of white pine, Combustion and Flame, pp. 331-345, 1987.
104. B. Moghtaderi, The state-of-the-art in pyrolysis modelling of lignocellulosic solid fuels, Fire and Materials, pp. 301-334, 2006.
105. C. Davida, S. Salvadora, J.L. Diriona, M. Quintard, Determination of a reaction scheme for cardboard thermal degradation using thermal gravimetric analysis, Journal of Analytical Applied Pyrolysis, pp. 67-, 2003.
106 R. E. Lyon, N. Safronava, E. Oztekin, A simple method of determining kinetic parameters for materials in fire models, *Fire Safety Science* 10: 765-777. 10.3801/IAFSS.FSS.10-765, 2011.
107. http://www.grc.nasa.gov/WWW/CEAWeb/ceaHome.htm, curator: Dr. M. J. Zehe, NASA Official: Dr. M. J. Zehe, last updated: 02/03/2010
108. M. F. Ashby, Materials and the environment. Eco-informed material choice. s.l. Chapter 12: Butterworth-Heinemann, 2009. ISBN: 978-1-85617-608-8 pp.356.
109. L. Bustamante Valencia. Experimental and Numerical Investigation of the Thermal Decomposition of Materials at Three Scales: Application to Polyether Polyurethane Foam used in Upholstered Furniture, Doctoral dissertation, ENSMA, Poitiers, France, 2009.
110. F. Samyn, S.C. Jama, S. Bellayer, S. Nazare, R. Hull, A. Fina, A. Castrovinci, G. Camino

Characterisation of the dispersion in polymer flame retarded nanocomposites, European Polymer Journal, 44, pp. 1631–1641, 2008.
111. M. Le Bras, S. Bourbigot, S. Duquesne, C. Jama, C. Wilkie, Fire Retardancy of Polymers: New Applications of Mineral Fillers. Cambridge, UK: Royal Society of Chemistry, pp. 1-15, 2005.
112. W.E. Horn, Jr., Fire Retardancy of Polymeric Materials, A.F. Grand and C.A. Wilkie (Eds.), Marcel Dekker, New York, pp. 285–352, 2000.
113. P.R. Hornsby, Fire retardant fillers for polymers, International Materials Reviews, 46, 199-210, 2001.
114. T. R. Hull, R. E. Quinn, I. G. Areri, D. A. Purser, Combustion toxicity of fire retarded EVA. Polymer Degradation and Stability, *77* (2), 235-242, 2002.
115. R. N. Rothon, , Effects of Particulate Fillers on Flame Retardant Properties of Composites, Chapter 6 in Rothon R. N. (Ed) Particulate-Filled Polymer Composites, 2nd Edition, Rapra Technology, Shawbury, UK, 2003.
116. W. E. Horn, Inorganic hydroxides and hydroxycarbonates: Their function and use as flame retardants, Chapter 9 in *Fire Retardancy of Polymeric Materials*, Ed Grand, A. and Wilkie, C.A., Marcel Dekker, New York, 2000.
117. C. H. Shomate, High-temperature Heat Contents of Magnesium Nitrate, Calcium Nitrate and Barium Nitrate. J. Am. Chem. Soc., *66*, 928–929, 1944.
118. NIST chemistry webbook, http://webbook.nist.gov/chemistry/
119. T.R. Hull, A. Witkowski, L. Hollingbery, Fire retardant action of mineral fillers, Polymer Degradation and Stability 96, pp. 1462-1469, 2011.
120. Omnic, Vapour Phase FTIR library, 2010.
121. K. McGarry, J. Zilberman, T. R. Hull, W. D. Woolley, Decomposition and Combustion of EVA and LDPE alone and when Fire Retarded with ATH, Polymer International, 49, 1193-1198, 2000.
122. J. Zilberman, T.R. Hull, D. Price, G.J. Milnes, F. Keen, Flame Retardancy of Some Ethylene-Vinyl Acetate Copolymer-Based Formulations, *Fire and Materials*, , 24, 159-164, 2000.
123 P.R. Hornsby, The application of hydrated mineral fillers as fire retardant and smoke suppressing additives for polymers, Macromolecular Symposia, 108, 203-219, 1996.
124. G. Beyer, Flame retardant properties of EVA-nanocomposites and improvements by combination of nanofillers with aluminium trihydrate, Fire Materials, 25, pp. 193–197, 2001.